UiO : Department of Geosciences
University of Oslo

Reservoir quality evaluation of the Jurassic successions of the Bjørnøyrenna Fault Complex, Norwegian Barents Sea.

Examples from Havis, Iskrystall, Skavl and Drivis discoveries.

Sofia M. Villanueva Q.
Master Thesis, Spring 2018

Reservoir quality evaluation of the Jurassic successions of the Bjørnøyrenna Fault Complex, Norwegian Barents Sea.

Examples from Havis, Iskrystall, Skavl and Drivis discoveries.

SOFIA M. VILLANUEVA Q.

Master Thesis in Geosciences
Petroleum Geology and Petroleum Geophysics (PEGG)
30 credits

Department of Geosciences
Faculty of Mathematics and Natural Sciences

UNIVERSITY OF OSLO

01.06.2018

2018
Reservoir quality evaluation of the Jurassic successions of the Bjørnøyrenna Fault complex, Norwegian Barents Sea. *Examples from Havis, Iskrystall, Skavl and Drivis discoveries*.
Sofia M. Villanueva Q
Supervisor: Nazmul Haque Mondol
http://www.duo.uio.no
Printed: Reprosentralen, University of Oslo

Preface

This thesis is part of the ‘‘*Trias North - Reconstructing the Triassic Northern Barents Shelf*’ project and is submitted to the Department of Geosciences, University of Oslo (UiO), in the candidacy of the M.Sc. in Petroleum Geology and Petroleum Geophysics (PEGG).

This research has been performed at the Department of Geosciences, University of Oslo, during the period of January to May 2018 under the supervision of Nazmul Haque Mondol, Associate Professor, Department of Geosciences, University of Oslo, Norway.

Acknowledgments

I would like to express my gratitude to my supervisor Nazmul Haque Mondol for his patience, valuable guidance, and encouragement through the entire research.

I am very thankful to Ph.D. candidates Honore Dzekamelive Yenwongfai and Jørgen André Hansen for taking part f their time to guide me and helping me in the best way possible when it was needed, and for the discussions we had that helped me for a better understanding.

I would also like to thank my friends and classmates that I have met during this journey, especially Miriam, Trisha, Waqas, and Ludvig. To my dearest friends Veronica, Valeria, Oswellin, Angelica, Silvana, Diana, Jorge and Roberto for been there any time despite the distance and for all your support.

A special thanks to the Department of Geosciences for allowing me been part of the program, for all my teachers and their enthusiasm, that made these two years and enriching experience.

Finally, this special part goes to my parents and my grandpa (Tito). Thank you for encouraging me to come to Oslo, for giving me your love, caring, support and guidance every day during this experience despite the long distance. To Markus for been an amazing support in all the possible ways, for all the patience and love you have given me. To my uncle and aunt, Youssef and Aida, for taking care of me and making me feel at home. I feel so blessed for having you all in my life, I love you.

Gracias Divina Pastora and Sagrado Corazón de Jesús.

Thanks, Venezuela for been my first home, you will always be in my heart.

Abstract

The Norwegian Barents Sea is considered a prospective but very challenging area in terms of hydrocarbon exploration despite recording higher success rate compared to both Norwegian Sea and the North Sea. This study focuses on the reservoir characterization of the Jurassic successions within the Bjørnøyerenna Fault Complex (BFC), using petrophysical analysis, rock physics diagnostic, and AVO modeling based on the information from six exploration wells 7219/8-1S, 7219/8-2 (Iskrystall), 7219/9-1, 7220/7-1 (Havis), 7220/7-2 (Skavl), and 7220/7-3 (Drivis) in the area. A special emphasis is given on Jurassic Stø and Nordmela Formations since both have proven good reservoir properties and hydrocarbon discoveries.

Through the petrophysical analysis, potential reservoir intervals are identified and analyzed in terms of reservoir properties (e.g. net-to-gross, porosity, shale volume, and saturation). The Jurassic reservoir of the Stø Formation exhibits good reservoir quality, with an average water saturation (Sw) < 3% (hydrocarbon saturation 97%), average porosity (φ) ~20%, shale volume (Vshale) ~16%, and consequently a net-to-gross of about 90%. The well 7220/7-3 (Drivis), has shown the best reservoir properties of porosity 22%, shale volume 16%, water saturation 5% and the thickest net pay of 74.8m. The Nordmela Formation has lower quality due to an increase in the shale content. The upper section of the formation is the only unit that has proper reservoir qualities and proven hydrocarbon zone. The average porosity is 16%, but it varies from 10% - 20%, the water saturation ranges from 16% to 37%, and the shale volume is defined between 13% and 20%. This formation has been the thickest formation recorded in the studied wells, where well 7220/7-3 (Drivis) has the best reservoir properties and thickest net pay zone (~48.04m), followed by neighboring well 7219/8-2 (Iskrystall).

The usage of published Vp versus depth trends allowed the estimation of uplift in the study area from ~870 m (BSF) to 1100 m (BSF), which combined with the rock physic cement models and the shear versus density crossplot to identify the areas influenced by the mechanical and chemical compaction, and the degree of cementation. In overall quartz and siderite cement have been observed within the Stø and Nordmela Formations, however, the level of cementation varies according to their maximum burial depth. In well 7219/8-2 (Iskrystall) the Stø and Nordmela Formations have the maximum burial depth of 3513 m (BSF) and 3560 m (BSF) respectively, before the uplift. Therefore, they have been experienced greater quartz cementation in comparison to the surrounding wells- The results are well correlated with the rock physics diagnostic results where low porosity, high Mu-Rho (μρ), and high Vp values are observed. On the other hand, well 7220/7-3 (Drivis), where the formations are expected bury at the shallowest depth have low cementation (less influence of chemical compaction) compared to the other wells. The Vp/Vs versus AI and LMR rock physics templates work well to discriminate lithology and fluid, showing a clear separation between the gas sands and the cap rock shales.

AVO forward modeling combined with the fluid substitution from Gassman's equations, helped to analyze the significant changes on the AVO signatures when fluid saturation (both water and oil/gas) is varied. The AVO anomalies of the Stø Formation of wells 7220/7-1 (Havis) and 7219/8-2 (Iskrystall) classified as a class II and IIP gas sands, while a weak class II anomaly is attributed for well 7220/7-3 (Drivis) since the formation is located at relatively shallow depth and the reservoir sands are less consolidated and cemented. Finally, the AVO anomaly of the Stø Formation of well 7219/9-1 describes as class I. The results of this study indicates that the Drivis discovery (7220/7-3) has better reservoir properties and thickest net pay in comparison to the well-known Havis discovery (7220/7-1).

Contents

List of Figures

List of tables

Nomenclature

- AI: Acoustic Impedance
- AVO: Amplitude Variation with Offset
- BSF: Below Sea Floor
- CMP: Common Mid-Point
- CIG: Common Image gather
- (R)KB: (Relative to) Kelly Bushing
- K: Bulk modulus
- k: Permeability
- GPa: Giga pascal
- mD: Milli Darcy
- BSF: below the sea floor
- N/G: Net-to-gross ratio
- V_p: P-wave velocity
- V_s: S-wave velocity
- V_{sh}: Shale volume
- R_w: Water resistivity
- S_w: Water saturation
- ϕ: Porosity
- μ: Shear modulus
- λ: Incompressibility (Rock physics)
- ρ: Density
- ν: Poisson's ratio
- TOC: Total organic carbon.
- LMR: Lambda-Mu-Rho
- TWT: two way travel time.
- PHIT: Total porosityChapter 1. Introduction

Chapter 1: Introduction

1.1 Background and Motivation

The Greater Barents Sea is considered one of the largest epicontinental seas at the north-western continental shelf of Eurasia, with an aerial extent of 1.3 million km^2 and the average water depth of 300m (Doré, 1995). It is located in an intracratonic setting with the Norwegian mainland to the south, the archipelagos of Novaya Zemlya to the east, Franz Josef Land to the northeast, and Svalbard to the north-west (Fig. 1.1).

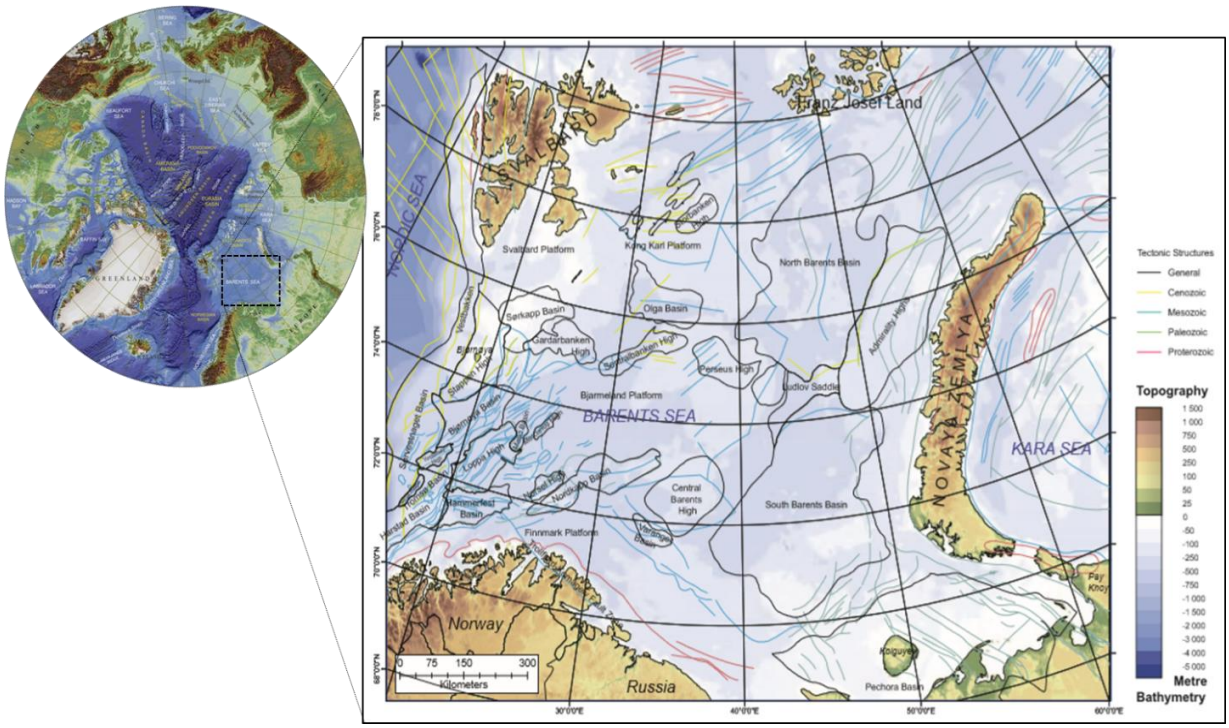

Figure 1.1: Location of the Greater Barents Sea with elevation for topography and bathymetry scale (m) and regional faults are labeled by color according to stratigraphic time (modified from Smelror et al., 2009).

According to the United States Geological Survey (USGS), about 30% of the world's undiscovered gas and 13% of the world's undiscovered oil can be located in the Arctic, mostly offshore. It is estimated that the Barents Sea Basin has 5.3 billion barrels of oil (BBO) undiscovered, and 184 trillion cubic feet (TCF) of undiscovered gas (Gautier et al., 2009)

In the Norwegian Barents Sea, hydrocarbon exploration began in 1970. Nevertheless, it was until 1980 when exploration activities were developed in the southern part of the Norwegian Barents Sea, with the main targets in Triassic to Middle Jurassic successions (Lundschien et al., 2014; Smelror et al., 2009). In this area, several discoveries have been made, including two hydrocarbon fields: Snøhvit, Goliat, and some noticeable discoveries such as Skugard, Havis and Drivis. The Johan Castberg field and Wisting are the two fields under the development plans. The Johan Castberg field proven volumes are estimated between 400 to

650 million barrels of oil and consist of the three discoveries Skrugrard (year 2011), Havis (year 2012), and Drivis (year 2014) (Statoil ASA, 2017, now Equinor).

Even though exploration has been taken place for almost 47 years, the knowledge about the petroleum potential is still uncertain. The undiscovered resources in the Barents Sea have increased from 50 to 65 percent of the total undiscovered resources on the Norwegian Continental Shelf since new information from the northeastern part has been collected after the agreement with Russia (NPD, 2017a). So far substantial reserves of hydrocarbon (mostly natural gas) have been found within the Norwegian Barents Sea, nevertheless the uplift and erosion events from the Cenozoic Era assumed to have affected the hydrocarbon potential in the area, causing leakage, seal failure, formation of empty traps, and redistribution of the hydrocarbon (Doré et al.,1996; Ohm et al., 2008).

A better understanding of the reservoir qualities and seismic response might help to reduce the uncertainty and risks associated with exploration success in the Norwegian Barents Sea. Therefore, the analysis and interpretation of well log data through petrophysical analysis, the application of advanced rock physics diagnostic techniques and AVO forward modeling, could contribute for a better understanding of the geological evolution and to characterize the potential reservoir, source and cap rocks in the area.

1.1 Research Objectives

The aim of this study is to investigate and analyze the reservoir quality of the Jurassic successions in the Bjørnøyrenna Fault Complex (BFC), more specifically in the Skavl (well 7220/7-2), Drivis (well 7220/7-3), Havis (well 7220/7-1), and Iskrystall (well 7219/8-2) discoveries, using six exploration and appraisal wells in the study area (Fig. 1.3). The main tasks consist as follow:

- Study published literature in order to understand the major geological events that have affected the petroleum systems in the area. In addition, to understand the scope of the applying methods and their limitations.

- Detail analysis of well log data, to identify the zone of potential reservoirs by employing petrophysical analysis to estimate porosity, permeability, shale volume, net-to-gross, net pay, and water saturation.

- Utilize rock physics diagnostic technique, to establish a link between elastic parameters and geological processes (e.g. maximum burial, uplift, compaction, and cementation).

- Use seismic AVO forward modeling, to investigate lithology and fluid sensitivity of target horizons and to classify their type based on the Intercept and Gradient (I-G crossplot) response.

- Discuss the uncertainties and limitations of the different methods applied in this study.

1.2 Study Area

The study area is located within the Bjørnøyrenna Fault Complex (BFC) in the Norwegian Barents Sea. The Polhem Sub-platform and Loppa High limit the study area to the east, Ringvassøy-Loppa Fault Complex and Trømsø Basin to the south, and the Bjørnøya Basin in the northwest (Fig. 1.2 and Fig. 1.3).

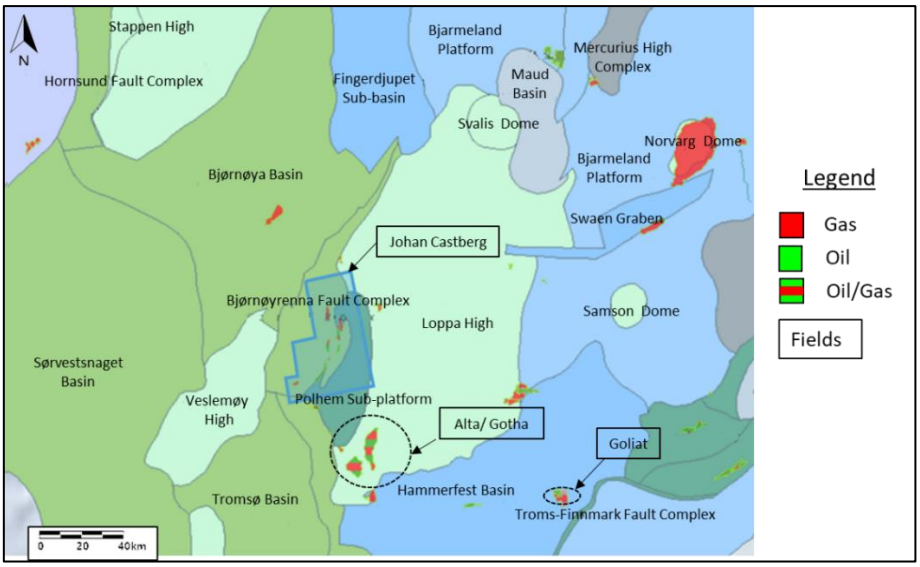

Figure 1.2: General overview and main structural elements in and around the study area. The blue polygon indicates the location of the study area (modified from NPD, 2018)

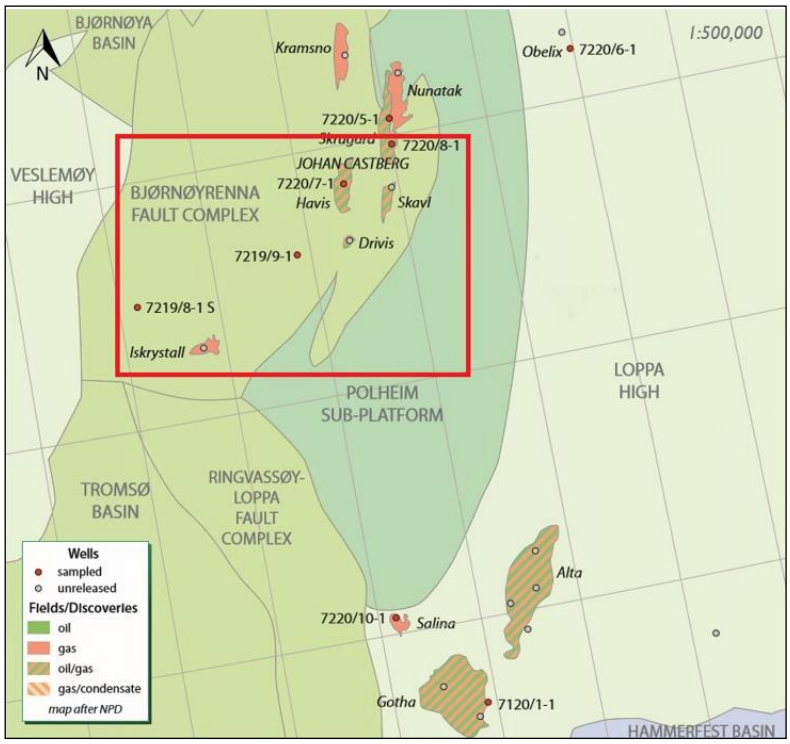

Figure 1.3: An enlarged view in and around the study area shows the investigated wells and discoveries (modified from APT, 2016)

1.3 Database and Software

The available data consist of six exploration and appraisal wells located in the Bjørnøyrenna Fault Complex, as shown in Figure 1.3. Three of the wells 7220/7-1, 7220/7-3, and 7220/7-2 are located to the west of the Polheim Sub-Platform and are associated to the Havis, Drivis, and Skavl discoveries, respectively. Meanwhile, wells 7219/8-1S, 7219/8-2, and 7219/9-1 are positioned on the southwestern part of the BFC, where the Iskrystall discovery corresponds to the well 7219/8-2. An overview of the well information and available measured log data is provided in Tables 1.1 and 1.2.

Table 1.1: General information on the studied wells. Wells are arranged from the northeast (left) to the southwest (right).

Well	7220/7-1	7220/7-2	7220/7-3	7219/9-1	7219/ 8-1S	7219/ 8-2
Discovery	Havis	Skavl	Drivis			Iskrystall
Content	Oil / Gas	Oil / Gas	Oil / Gas	Dry	Dry	Gas
OWC	1956m	-	1604m	-	-	-
GOC	1828m	1150m	1516m	-	-	-
MD (m)	2231.4896	1854.708	2095.8048	4312.96	4617.125	3424.7328
KB (m)	40	31	31	23	24	31
Water depth (m)	365	349	345	356	369	344
Bottom hole temp. (°C)	72	-	-	145	165	122
1st level with HC	Middle Jurassic	Late Triassic	Middle Jurassic	-	-	Middle Jurassic
1st level with HC, formation	Stø	Fruholmen	Stø	-	-	Stø
2nd level with HC	Early Jurassic	Early Jurassic	Early Jurassic	-	-	Early Jurassic
2nd level with HC, formation	Nordmela	Tubåen	Nordmela	-	-	Nordmela

Well log correlations are performed using Petrel software (Version 2016.2; Schlumberger Limited). An industry popular software IP (Interactive Petrophysics version 4.4.2017.57: LR Senergy) is used to carry petrophysical analysis. Finally, the rock physics diagnostics and seismic AVO forward modeling are performed using Hampson-Russell Software (Version HRS10.2; CGG).

Table 1.2: Availability of well log data within the six studied wells. Wells are arranged from the northeast (left) to the southwest (right).

Well	7220/7-1	7220/7-2	7220/7-3	7219/9-1	7219/ 8-1S	7219/ 8-2
Gamma Ray (API)	✓	✓	✓	✓	✓	✓
Caliper (in)	✓	✓	✓	✓	✓	✓
Bit Size (in)	✓	✓	✓			✓
Density (g/cc)	✓	✓	✓	✓	✓	✓
Density Correc (g/cc)	✓	✓	✓	✓	✓	✓
Neutron (v/v)	✓	✓	✓	✓	✓	✓
Sonic P (US/F)	✓	✓	✓	✓	✓	✓
Sonic S (US/F)	✓	×	✓	×	×	✓
Res. Shallow (ohmm)	✓	✓	✓	✓	✓	✓
Res. Medium (ohmm)	✓	✓	✓	✓	✓	✓
Res. Deep (ohmm)	✓	✓	✓	✓	✓	✓
SP	×	×	×	×	×	×
PE (B/E)	✓	✓	✓	×	×	✓
GR Spectral (ppm)	✓	×	✓	×	×	✓

1.4 Limitations

This study is conducted in approximately five months; as a consequence, this limited time does not allow to do thin section analysis and core examination, instead that information is gathered from published data to describe sedimentology and depositional environment. Moreover, in this study the mechanical and chemical compaction have not been executed in great detail.

In terms of well log data, the original well log data from the density and neutron log required editing and correction before further studies can be performed. Furthermore, the current database has measured S-wave velocity only available in three wells (well 7220/7-1, 7220/7-3, and 7219/8-2) limiting the data for the rock physics diagnostic and AVO modeling analysis only to those wells.

Due to time restrictions, real seismic data are not included in the study. The lack of the seismic data limited the AVO analysis, since the obtained results are based only on well logs and synthetic seismic data and cannot be correlated with real seismic anomalies.

1.5 Chapter Descriptions

The first chapter consists of a general introduction of the study. It contains background information about the study area, motivation for conducting this study in the Bjørnøyrenna Fault Complex (BFC), available well log data and software, and the limitations that are encountered during the research.

Chapter 2 summarizes the geological information of in and around the study area, based on gathered information from published literature. The regional tectonic and depositional patterns

(e.g.: mainly structural elements, stratigraphy, petroleum system, uplift, erosion, and their influences on hydrocarbon production) are briefly discussed in the chapter.

In chapter 3, the methodology and theoretical background compiled from published papers and books are presented. The basic principles and description of the geophysical techniques such as petrophysical analysis, rock physics diagnostics, and AVO modeling are provided, including relevant equations and empirical relations.

The fourth chapter presents the results and discussion of the petrophysical analysis. The reservoir properties (e.g.: lithology, shale volume, total and effective porosities, permeability, fluid saturation, and net-to-gross) are determined, within the Jurassic intervals in order to define the potential reservoir using the data from wells 7220/7-1, 7220/7-2, 7220/7-3, 7219/8-1S, 7219/8-2 and 7219/9-1.

The results and discussion of the rock physics diagnostics are presented in chapter 5. Several standard rock physics crossplots (e.g.: Porosity (φ) versus Vs, LMR and Vp/Vs versus AI) are generated to extract information about lithology, compaction, cementation, and hydrocarbon saturation. This advanced technique provides valuable information to establish links between the reservoir rock properties and the geological processes. Nevertheless, the study only includes wells that have measured Vs (7220/7-1, 7220/7-3, and 7219/8-2), since the predicted Vs has serious limitations to accurately characterize the reservoir zones.

Chapter 6 includes the results of sensitivity analysis of AVO modeling when different parameters, such as wavelet or fluid saturation are changed. In addition, the AVO forward modeling results and discussion on top of the Stø reservoir intervals are shown. The wells 7220/7-1, 7220/7-3, 7219/8-2, and 7219/9-1 are used in this section to evaluate changes in the AVO response when variations in depth, thickness, and shaliness are involved.

Finally, in chapter 7, a summary of the results from the petrophysical analysis, rock physics diagnostics, and AVO modeling applied to the study are discussed to conclude the research outcomes.

Chapter 2: Geological setting

2.1 Regional tectonic and geologic evolution

After the Caledonian Orogeny event, the geological history of the Norwegian Barents Sea was dominated by three major rift phases: Late Devonian-Carboniferous, Middle Jurassic-Early Cretaceous, and Early Tertiary (Fig. 2.1) (Faleide et al., 1993a; Glørstad-Clark et al. 2010).

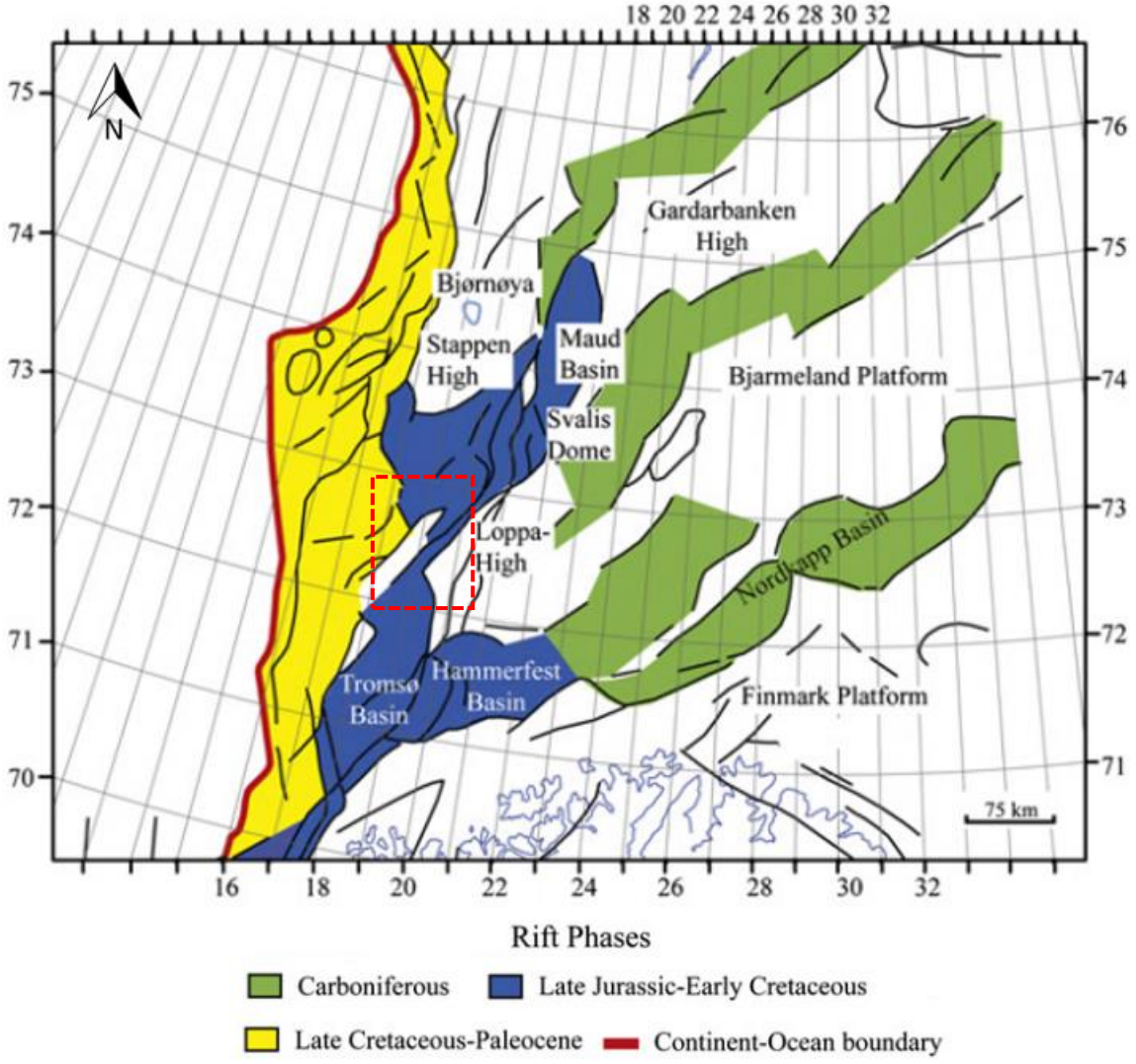

Figure 2.1: Structural timing of events affecting the western Barents Sea. The red polygon indicates the study area (adapted from Glørstad-Clark et al. 2011).

During Late Paleozoic times most of the Barents Sea was affected by crustal extension. The later extension was characterized by general westward migration of the rifting, formation of well-defined rifts and pull-apart basins in the southwest, and at the north a development of a belt of strike-slip faults.

The Caledonian Orogeny, in the Ordovician, was the result of the collision between Eurasia and Laurentia, and consequent closing of the Lapetus Ocean. This process was followed by extension in Late Paleozoic, which resulted in most of the Barents Shelf being covered by a regional sag basin. Moreover, uplift in the east side from Permian to Early Triassic, the onset of the Uralian Orogeny changed the physiology and sediment deposition patterns on the basin, giving rise to a material influx towards the west through the Triassic (Henriksen et al., 2011).

The collapse between the newly formed Caledonian and Uralian orogenic belts and progressive break-up stages of the Pangean supercontinent had influenced in the Barents Sea from Late Paleozoic to Mesozoic times. These episodes are recognizable in the Early-Middle Devonian, Carboniferous, Permian, Triassic and late Jurassic-Early Cretaceous.

Moreover, major rift basins traversing the Barents Shelf, intervening a series of platforms, and structural highs were the result of these events (Doré, 1995).

In addition, during Late Paleozoic and Early Mesozoic, a local continental deposition took place in the syn- and post-orogenic collapse basins, while marine sedimentation was dominating from the Late Paleozoic to the present day. This marine depositional environment was highly influenced by the specific tectonic setting and the climatic factors (Doré, 1995; Heafford, 1988).

2.1.1 Late Devonian - Carboniferous rifting

During Late Devonian to Carboniferous times, the tectonic activity in the Barents Sea was characterized by rifting episodes and the collapse of the Caledonian Orogeny (Henriksen et al., 2011b).

In the Late Devonian, a switch in the compressional regime to a shear system and strike-slip movement in the Artic-North Atlantic region controlled the early post-orogenic sedimentation in the Barents Sea (Gabrielsen et al., 1990; Gudlaugsson et al., 1998; Smelror et al., 2009).

This tectonic event was followed by an extensional event during Late Devonian to Carboniferous, which it is related to the initiation of the Atlantic rift system between Norway and Greenland, as a response to the plate divergence and lithospheric stretching. This lead to the formation of interconnected extensional basins, filled with syn-rift deposits, separated by fault-bounded highs and north-easterly orientation in the main rift zones (Gudlaugsson et al., 1998; Henriksen et al., 2011).

Several sedimentary basins, such as Tromsø, Bjørnøya, and Nordkapp were the result of this extensional episode (Gudlaugsson et al., 1998).

2.1.2 Middle Jurassic – Early Cretaceous Rifting

The Middle Jurassic period was characterized by a regional NW-SE extension and minor strike-slip along the deep-seated structural lineaments and development of deep basin in the western part of the Loppa High (Clark et al., 2014; Faleide et al., 1993).

Furthermore, during Middle-Late Jurassic the rift event in the Barents Sea occurred through the Hammerfest and Bjørnøya Basins, along preexisting frameworks. This caused block faulting in east and northeast direction and deposition of Upper Jurassic shales in restricted basins between the faulted blocks. Loppa High was uplifted in the Late Jurassic – Early Cretaceous inverting the Late Triassic to Middle Jurassic depocenter (Faleide et al., 1993; Gabrielsen et al., 1990).

This tectonic activity culminated in the Early Cretaceous was followed by rapid thermal subsidence and infill of the Bjørnøya, Tromsø and Harstad Basins with Cretaceous succession (Kolmule Formation) due to crustal stretching and thinning within the area (Faleide et al.,1993).

2.1.3 Late Cretaceous-Paleocene rifting

The Late Cretaceous period was dominated by the opening of the Labrador Sea, and regional subsidence in the North Atlantic Rift Basins. Most of these deep basins ended at the De Geer Zone, where pull apart basin formed due to dextral oblique-slip in the Wandel Sea, northeast Greenland, and southwestern Barents Sea (Clark et al., 2014; Faleide et al., 1993)

Additionally, during the period it was also found evidence of wrench forming structures along the major faults, suggesting compressional deformation (Gabrielsen et al., 1990).

By the Cretaceous-Paleocene transition an uplift of the wider Barents platform relative to Tromsø and Bjørnøya Basin was identified; moreover, inversion of local depocenters, folding, reverse faulting and thrusting were developed in the Bjørnøyrenna Fault Complex. Finally, the Paleocene period was characterized by the shift from a rift regime to a shear regime associated with the De Geer System (Clark et al., 2014; Faleide et al., 1993; Gabrielsen et al., 1990; Glørstad-Clark et al., 2014).

2.2 Structural Elements

The Barents Sea can be divided into an eastern and western province, due to the considerable difference in time, trend and magnitude during their development (Fig. 2.2).

On one hand, the eastern province was influenced by Late Paleozoic tectonism with minimal deformation in post-Jurassic times, displaying E-W and WNW-ESE trending faults, and thicker Upper Paleozoic and Mesozoic sequences.

On the other hand, the western province was affected by active tectonic throughout Late Mesozoic and Cenozoic times, with deposition of thicker Cretaceous, Paleogene and Neogene sediments in the Harstad, Tromsø and Bjørnøya Basins, and faults trending NNE-SSW, NE-SW and N-S (Faleide et al., 1993; NPD, 2014).

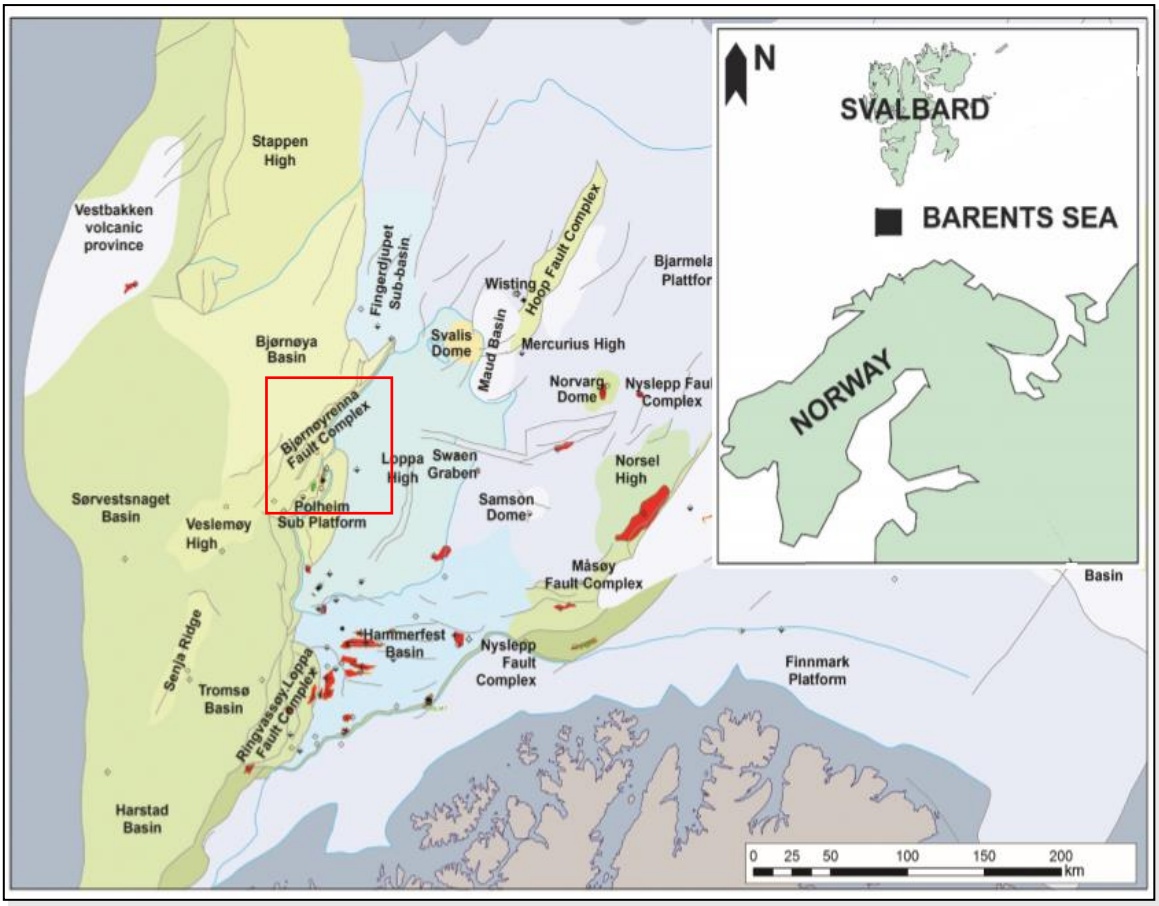

Figure 2.2: Main tectonic features of southwestern Barents Sea. The study area is defined by the red rectangle (modified from Fanavoll et al., 2014).

2.2.1 Loppa High

The Loppa high is considered as a positive tectonic element, that resembles a diamond-shaped structure. This structure had been influenced by several phases of uplift, subsidence, tilting, and erosion. During the Early Triassic, it was an uplifted, tilted ridge structure, onlapped by sediments until the Middle Triassic. It is also characterized by a very thick Upper Triassic sediments of the Snadd Formation (Gabrielsen et al, 1990).

2.2.2 Bjørnøyrenna Fault Complex

The studied Bjørnøyrenna Fault Complex defines the transitional zone between the Loppa High to the southeast and the deep Cretaceous basins to the northwest (Gabrielsen et al., 1997). Based on its geometry, it can be subdivided into four major segments (Fig. 2.3). The subareas I-III separated from the north-west margin of the Loppa High, are characterized by a graben and horsts system. Meanwhile, the grabens from the subarea IV have flower-like geometries (Gabrielsen et al., 1990, 1997).

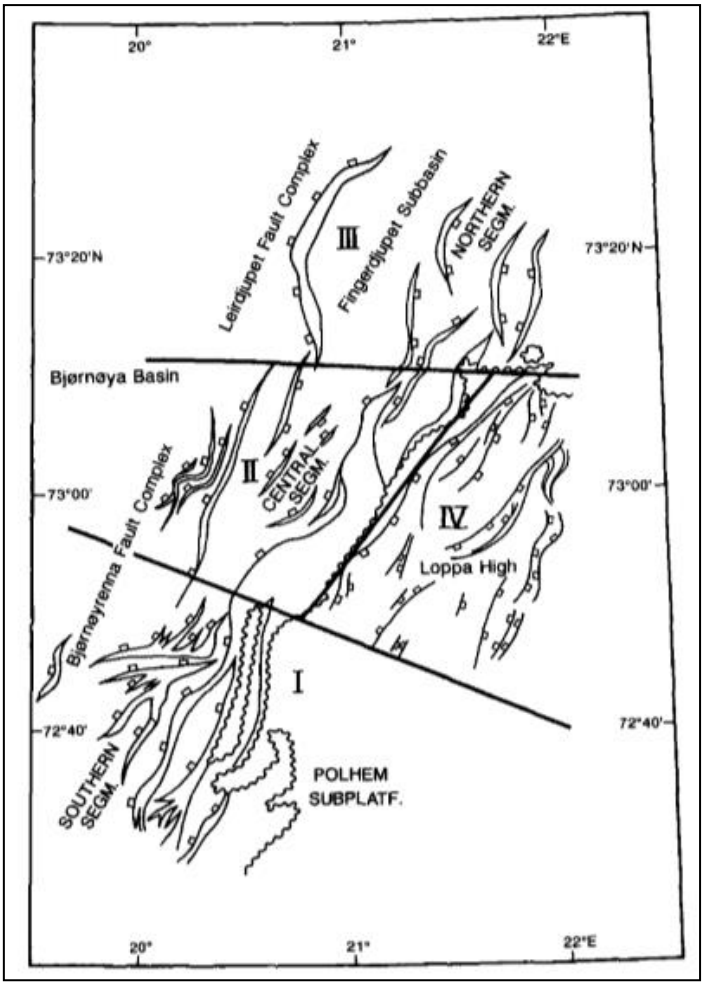

Figure 2.3: Structural map of the Bjørnøyrenna Fault Complex subareas (Gabrielsen et al., 1997).

The NE-SW trend of the Bjørnøyrenna Fault Complex is the result of an extensional process of the Ringvassøy – Loppa Fault Complex in the Early Cretaceous. Nevertheless, the subsidence along the fault complex was interrupted in the Hauterivian-Aptian by left-lateral transtension. Finally, it was inverted during Late Cretaceous-Early Tertiary. Both episodes caused relatively intense deformation (Gabrielsen et al., 1997)

It exhibits very complex geometry with signs of inversion, deformed footwall block planes, domal features, and reverse faults; with all the major structures developed in a major subsidence episode during the Early Cretaceous (Gabrielsen et al., 1997). Across the complex, a vertical displacement along the faults was identified at 3 and 6 seconds (TWT) on the Upper Triassic level (Fig. 2.4**).** However, the throw terminates to the North and South (Gabrielsen et al., 1990).

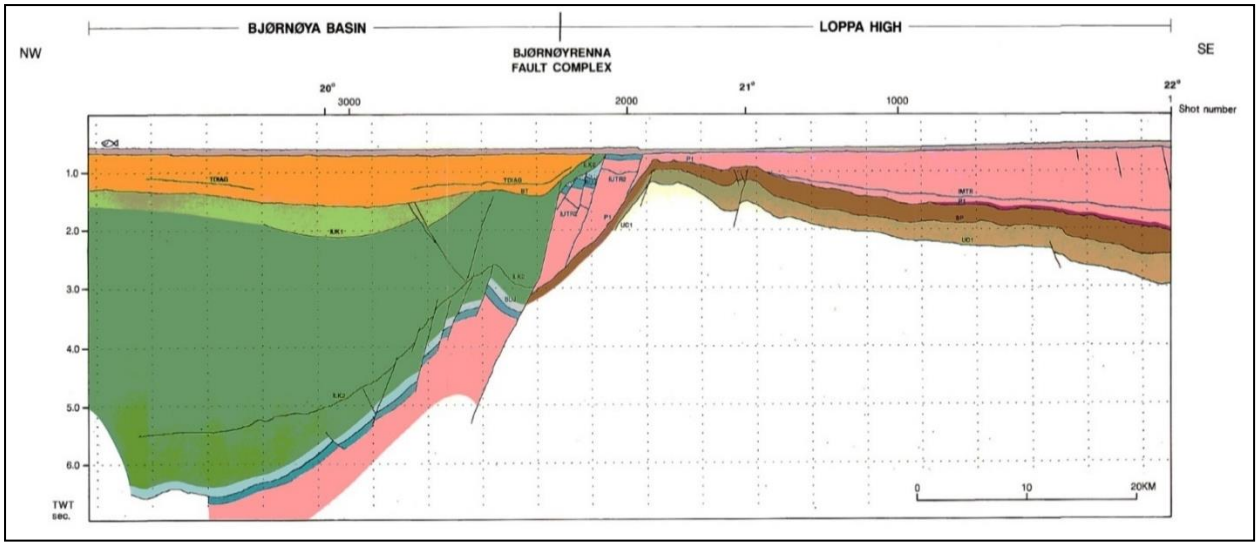

Figure 2.3: Bjørnøyrenna Fault Complex stratigraphy (Profile D-10-84). Color codes: Grey (Quaternary), Orange (Tertiary), Yellow Green (Upper Cretaceous), Green (Lower Cretaceous), Light blue and blue (Base of Upper Jurassic), Pink (Triassic), Violet (Top Permian), Brown (Base of Permian), Olive (Carboniferous) (Modified from Gabrielsen et al., 1990).

2.2.3 The Polhem Subplatform

The Polhem Subplatform, which used to be part of the Loppa High, is bordered by the Ringvassøy–Loppa Fault Complex to its southwest, and by the Bjørnøyrenna Fault Complex to the northeast.

This sub-platform forms the block-faulted area between the stable eastern part of the Loppa High and the Bjørnøyrenna and Ringvassøy-Loppa Fault Complexes. Most of the faults are considered listric formed in Late Jurassic-Early Cretaceous, with a detachment surface below Triassic. Additionally, the rotated fault blocks have an N-S orientation, delineated by an array of down-to-the-west normal faults (Gabrielsen et al., 1990; Indrevær et al., 2016).

2.2.4 Bjørnøya Basin

The Bjørnøya basin is interpreted as a prograding system with a highly thinned crust, aborted during Mesozoic times. This Cretaceous sag basin lies beneath a deep-seated metamorphic lower crust (Gernigon et al., 2014).

The basin underwent rapid subsidence in Cretaceous times, with an extensive deformation along the Bjørnøyrenna Fault Complex and Stappen High (Doré, 1995). The upper part of the succession was heavily eroded while the center of the basin is quite stable (Gabrielsen et al., 1990; Faleide et al., 1993).

2.3 General Stratigraphy

During the Carboniferous, the southwestern area of the Barents Sea was dominated by conglomerates, sandstones, and shale deposits; however, by Mid-Carboniferous to late Permian limestones and evaporites were controlling the deposition. A shift to a deltaic depositional

environment occurred in the Rhaetian to early Toarcian, followed by a transgressional process and deposition of shallow marine sheet sands (Gabrielsen et al., 1997).

The Cretaceous and Tertiary sequences, located in transition between the Bjørnøya Basin and the Loppa High, are represented by marine claystones and shales with occasional calcareous strata, siltstones, and tuffs.

Nevertheless, Mesozoic and Cenozoic strata were partly removed by erosion during the Loppa High uplift, so Quaternary strata could be found directly on top of Triassic sediments (Gabrielsen et al., 1990).

The lithostratigraphic chart of Triassic and Jurassic presented in Figure 2.5, encompass the Sassendalen Group (Subgroup Ingøydjupet), the Kapp Toscana Group (Subgroups Realgrunnen and Storfjorden), and the lower Adventdalen Group (equivalent to Teistengrunnen Group, and it is summarized by Dalland et al. (1988), Klausen et al. (2015), and Halland et al. (2014) on the following section.

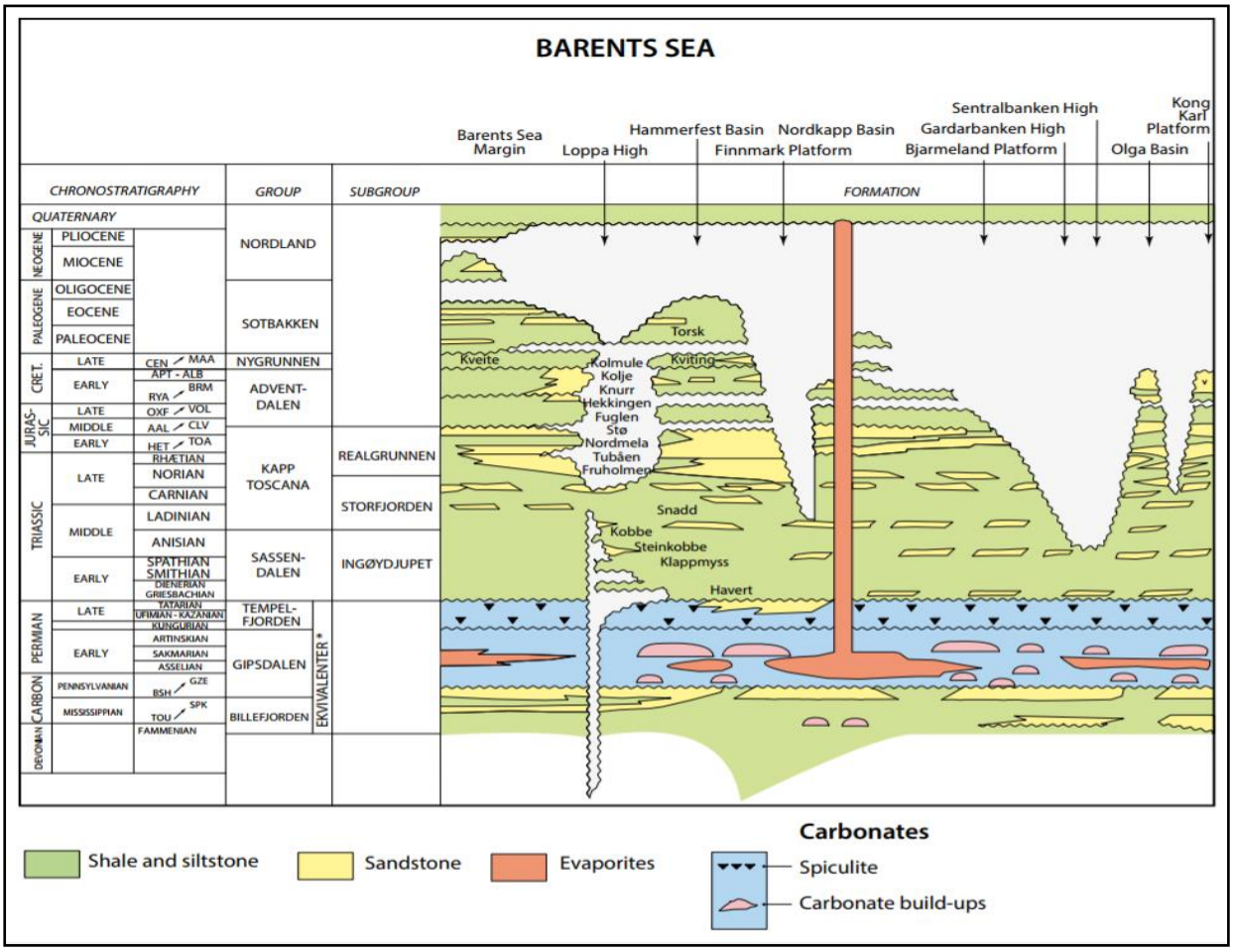

Figure 2.5: Lithostratigraphy of the Barents Sea (Halland et al., 2014). Stratigraphy of western Loppa High, Polheim Sub-Platform, Bjørnøyrenna Fault Complex, Bjørnøya and Tromsø Basins.

2.3.1 Stratigraphy of Western Loppa High, Polheim Sub-Platform, Bjørnøyrenna Fault Complex, Bjørnøya and Tromsø Basins

The depositional history of the western Barents Sea began in Early Devonian (Lochkovian) when it was directly overlying crystalline sediments. After the Caledonian breakdown in Lochkovian, continental siliciclastic sediments were deposited in intracratonic and foreland basins (Fig. 2.6**)** (Gudlaugsson et al., 1998).

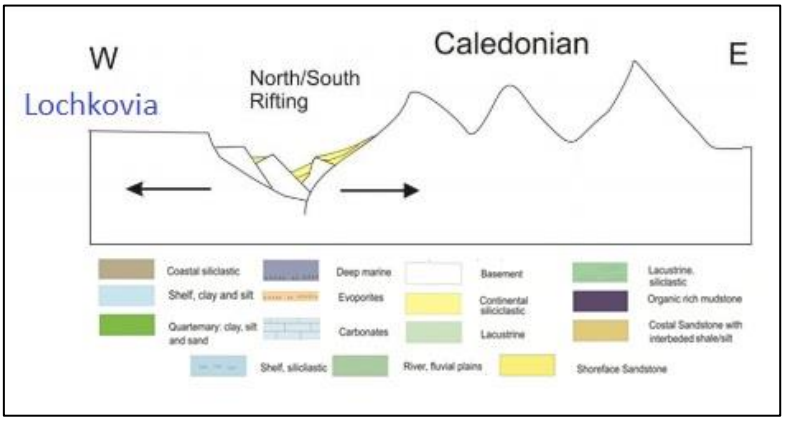

Figure 2.6: Geological evolution during Early Devonian (Larsen, 2011).

During Middle Carboniferous (Fig. 2.7), the depositional system change from a regime governed by clastic sediments to fluvial deposits controlled by river systems. Finally, at the end of this period, Moscovian, the continuous sea level rising from the east allowed the formation of evaporites and carbonates (Gudlaugsson et al., 1998; Smelror et al., 2009).

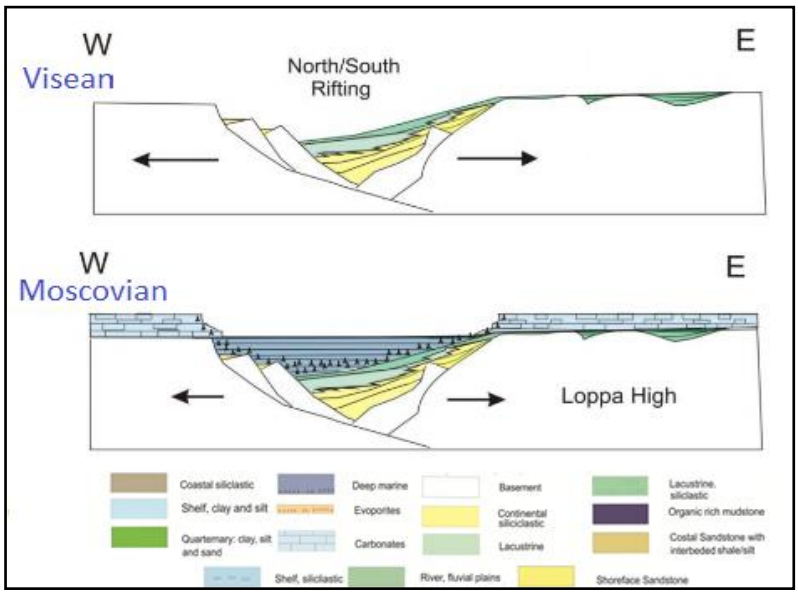

Figure 2.7: Geological evolution from Visean to Moscovian (Larsen, 2011).

In Early-Middle Triassic, Induan and Ansian age, the Loppa High was uplifted and eroded due to the rifting in the Loppa High and Bjørnøyrenna Fault Complex (Fig. 2.8). As a consequence,

siliciclastic shelf deposits were continuously deposited, while in the deep basins the presence of restricted anoxic environments allowed the accumulation of organic-rich sediments (Kobbe Formation).

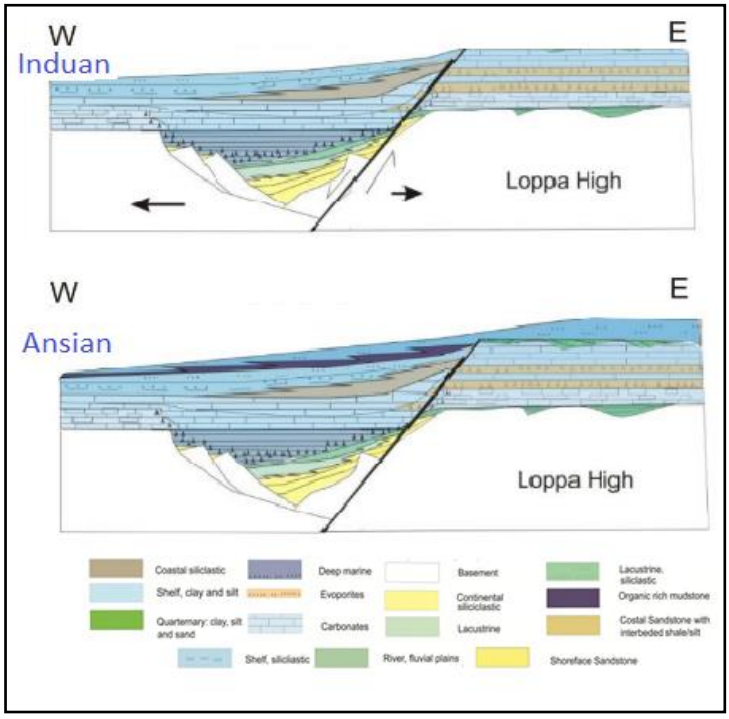

Figure 2.8: Geological evolution from Induan to Ansian (Larsen, 2011).

Due to uplift and erosion of the Loppa High in Early Jurassic (Hettangian), coastal sand deposits with interbedded sequences of marine shales from flooding periods could be found in the western margin of the Loppa High (Fig. 2.9).

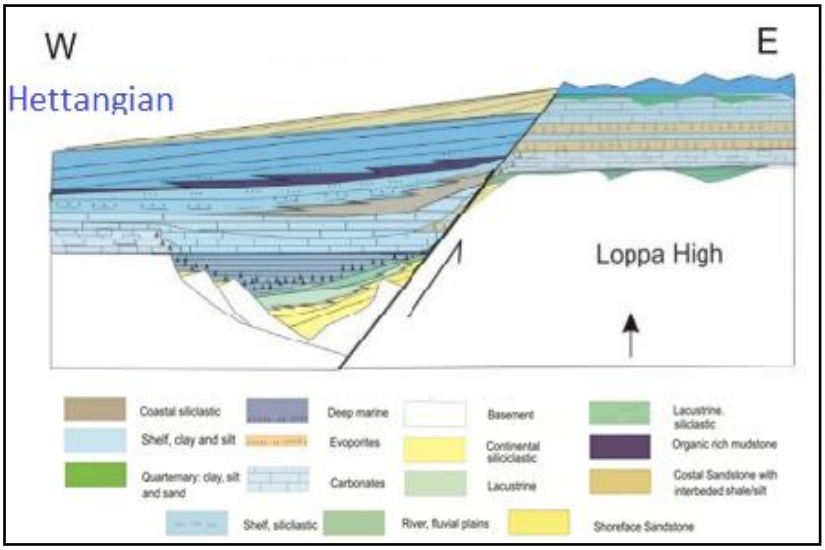

Figure 2.9: Geological evolution Hettangian (Larsen, 2011).

In Early to Middle Cretaceous times (Fig. 2.10), the continuous subsidence of the Tromsø and Bjørnøya Basins and upliftment at the east part caused a larger accumulation of syn-rift sedimentary wedges deposits, dominated by clay and silt over the Bjørnøyrenna Fault Complex, Bjørnøya and Tromsø Basin (Gudlaugsson et al., 1998; Smelror et al.,2009).

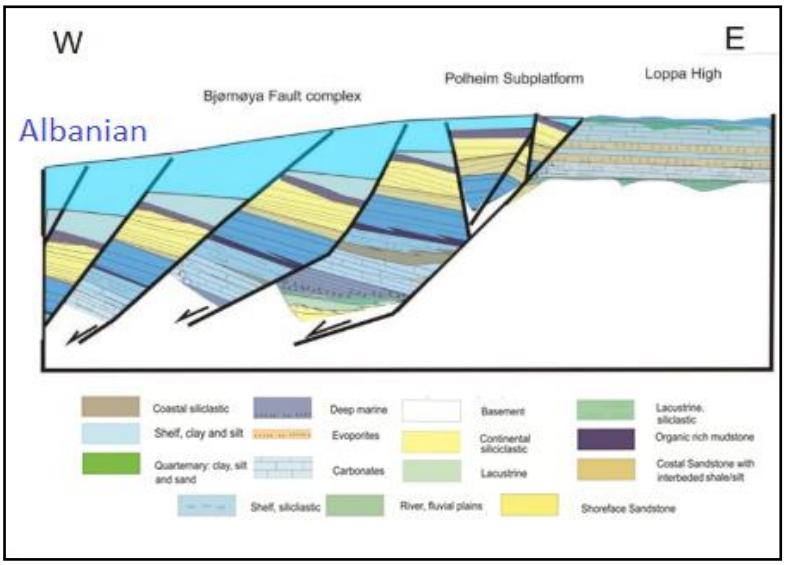

Figure 2.10: Geological evolution Albanian. (Larsen, 2011)

During Early Tertiary (Eocene) a progressive sedimentation occurred in the west, due to the North Atlantic break up. Deposits were preserved in the Bjørnøyrenna Fault Complex and Tromsø Basin, while in the Loppa High these sediments were eroded by post -Eocene processes (Fig. 2.11).

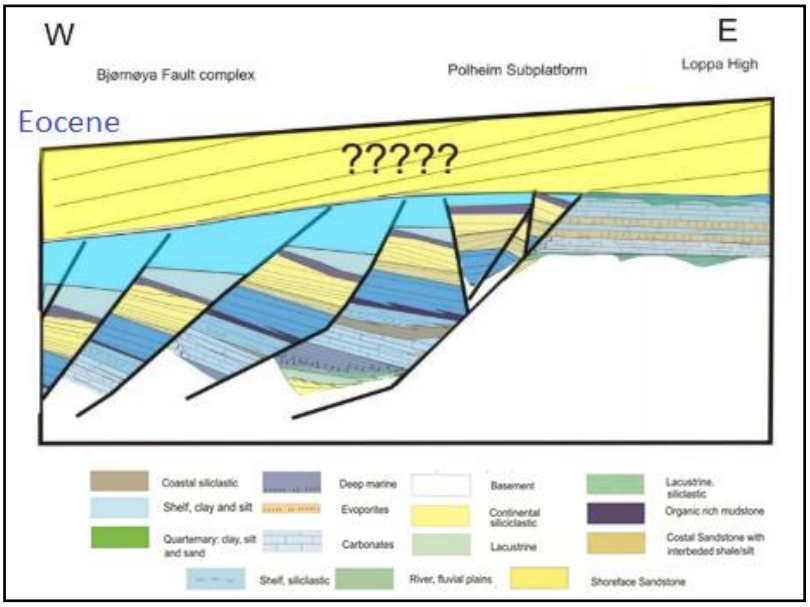

Figure 2.11: Geological evolution in Eocene time (Larsen, 2011)

Finally, in Late Tertiary and Quaternary, the entire Barents Sea was uplifted and several glaciations had eroded around 1000 to 1500 m of sediments (Fig. 2.12).

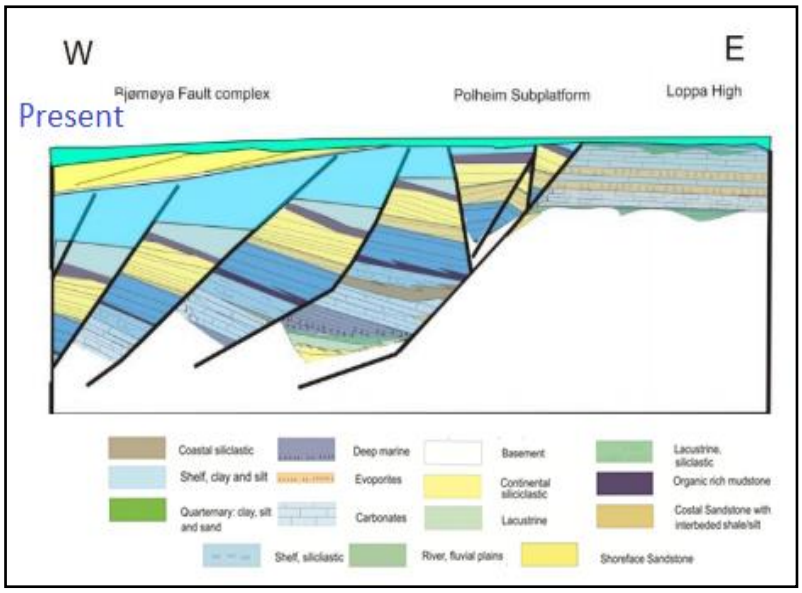

Figure 2.12: Geological evolution present time (Larsen, 2011).

2.3.2 Sassendalen Group

The group can be divided into the Ingøydjupet Subgroup which consists of three formations: Havert, Klappmyss, and Kobbe. The Ingøydjupet Subgroup consists of black shale and claystone with thin grey silt- and sandstones, in the upper parts, with minor carbonate and coal interbeds. It has been interpreted as a marine environment in the lower parts of the subgroup and in the upper parts deltaic sequences over an extensive, low relief depositional basin (Dalland et al., 1988; Halland et al., 2014; Klausen et al., 2015).

- **Havert Formation**

The Havert Formation, Griesbachian to Dienerian, is typically made up of medium to dark grey shales with minor grey siltstones and thin sandstones beds, which include two generally coarsening upwards sequences. Toward Hammerfest Basin, the unit is more continuous silty shale with a very weak upwards-coarsening trend.

This formation has been interpreted as marginal to open marine environments and coastal environments to the south and southeast.

- **Klappmyss Formation**

The Klappmyss Formation, Smithian to Spathian age, is described as medium to dark grey shales, passing upwards into interbedded shales, siltstones, and sandstones. Generally, the formation thickness becoming finer northwards from the southern margins of the Hammerfest Basin.

The formation is associated with marginal -to- open marine environments, with renewed northwards coastal progradation following the mentioned Early Smithian transgression.

- **Kobbe Formation**

The Kobbe Formation, Anisian age, consists of base shale which changes upward to interbedding of shale, siltstone, and carbonate-cemented sandstone.

The depositional environment was interpreted as shallow to open marine, with a renewed coastal progradation from the north- to the northwest. The shale base of the unit defines a transgressive pulse, which is followed by a build-out of clastic marginal marine regimes from southern coastal areas.

2.3.3 Kapp Toscana Group

The Kapp Toscana Group can be divided into two subgroups:

a) The Storfjorden subgroup that includes immature sandstones and mudstones from the Snadd Formation, deposited in coastal to marine environments in the Early-Late to Medium- Late Triassic.

b) The Realgrunnen subgroup, that comprises mature sandstones, shales and coal of the Fruholmen, Tubåen, Nordmela and Stø Formations (Dalland et al., 1988; Klausen et al.,2015; Halland et al., 2014).

- **Snadd Formation**

Ladinian to early Norian age, the Snadd Formation has a base of grey shales that is coarsening upwards into shales with interbeds of grey siltstones and sandstones. Additionally, the lower part consists of limestone interbeds, and coaly lenses in the upper part, with red-brown shales defining the top of the formation.

The depositional environment is interpreted as a distal marine to deltaic progradation. The depositional characteristic varied temporally and spatially according to the position of the coastline and the sediment input source.

- **Fruholmen Formation**

The age of the formation is from Norian to Rhaetian. The Formation is composed of grey to dark grey shales passing upwards into interbedded sandstones, shales, and coals. Sandstones dominate the middle part of the formation, while the upper part is dominated by shales.

Depositionally this has been interpreted in terms of the transition from open marine shales to coastal and fluvial dominated sandstones, with flood-plain deposition. (Fig. 2.13).

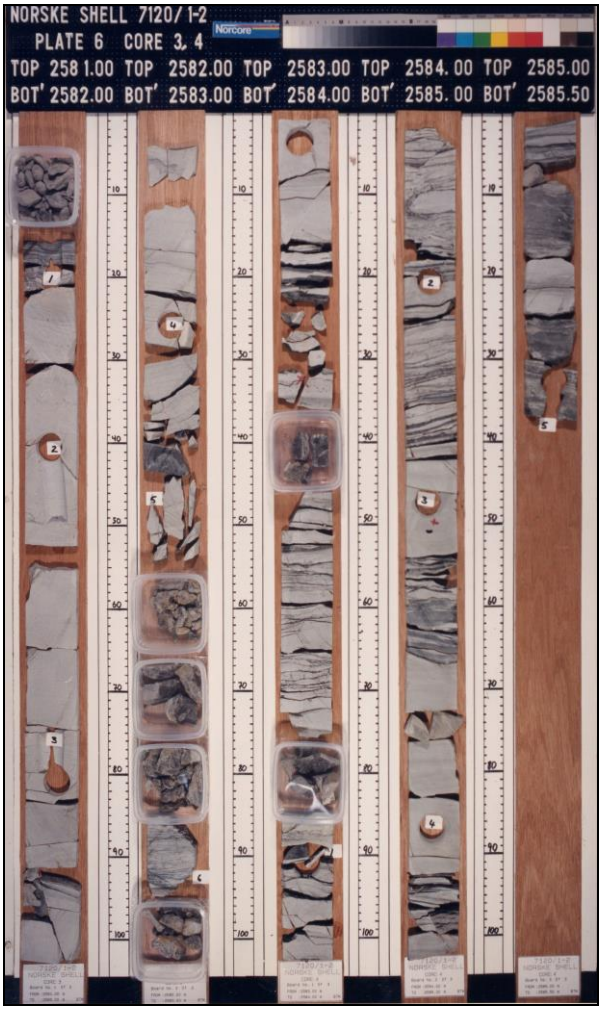

Figure 2.13: Core photographs of the Fruholmen Formation 2581 to 2585 (m MDKB) from well 7120/1-2 (NPD, 2017b).

- **Tubåen Formation**

The formation defined from Late Rhaetian to early Hettangian times is dominated by sandstones with some shales and minor coal deposits, commonly located near the southeastern basinal margins, and discontinues in the northwest. Meanwhile, the upper and lower sand-rich units are separated by a shale interval.

The sand units of the formation were associated with fluvio-deltaic deposits (tidal inlet and/or estuarine). The marine shales represent distal environments to the northwest, and coals in the southeast-involved backbarrier- lagoonal environment (Fig. 2.14**)**.

Figure 2.14: Core photographs of the Tubåen Formation 2506 to 2508 (m MDKB) from well 7121/5-1 (NPD, 2017b).

- **Nordmela Formation**

The Nordmela Formation is from Sinemurian to Late Pliensbachian. It consists of interbedded siltstones, sandstones, shales and claystones with individual minor coals; with the sandstones dominating upwards.

The formation is interpreted as tidal flat to flood-plain environment sandstones representing estuarine and tidal channels.

- **Stø Formation**

From Late Pliensbachian to Bajocian times, the Stø Formation is described as moderately to well-sorted sandstones, with thin units of shale and siltstone. Phosphatic lag conglomerates are found in some wells, especially in upper parts of the unit

The corresponding depositional environments involved prograding coastal regimes associated with the sand deposits, while regional transgressive pulses are represented by shale and siltstone intervals (Fig. 2.15).

Figure 2.15: Core photographs of the Stø Formation (2400-2405 m MDKB) from well 7121/5-1 (NPD, 2017b).

2.3.4 Adventdalen Group

The group is dominated by dark marine mudstones, locally including deltaic and shelf sandstones as well as carbonate of the Fuglen, Hekkingen, Knurr, Kolje and Kolmule Formations (Dalland et al., 1988; Klausen et al.,2015; Halland et al., 2014).

- **Fuglen Formation**

The Fuglen Formation, Late Callovian to Oxfordian age, contains pyritic dark brown shales with interbedded white-to-brownish grey limestones.

Depositionally, the formation is thought to be deposited in a marine environment during highstand events with ongoing tectonic movements **(**Fig. 2.16).

Figure 2.16: Core photographs of the Fuglen Formation (1365-1370 m MDKB) from well 7321/9-1 (NPD, 2017b).

- **Hekkingen Formation**

This formation is from Late Oxfordian-Early Kimmeridgian to Ryazanian times. The lithology is composed of brownish-grey to very dark grey shale and claystone with thin interbeds of limestone, dolomite, siltstone, and sandstone.

The depositional environment has been identified as deep marine under anoxic conditions. Local barriers to circulation by Kimmerian movements caused the anoxic conditions (Fig. 2.17). A correlation of each of the mentioned formations through the six wells are displayed in Figure 2.18.

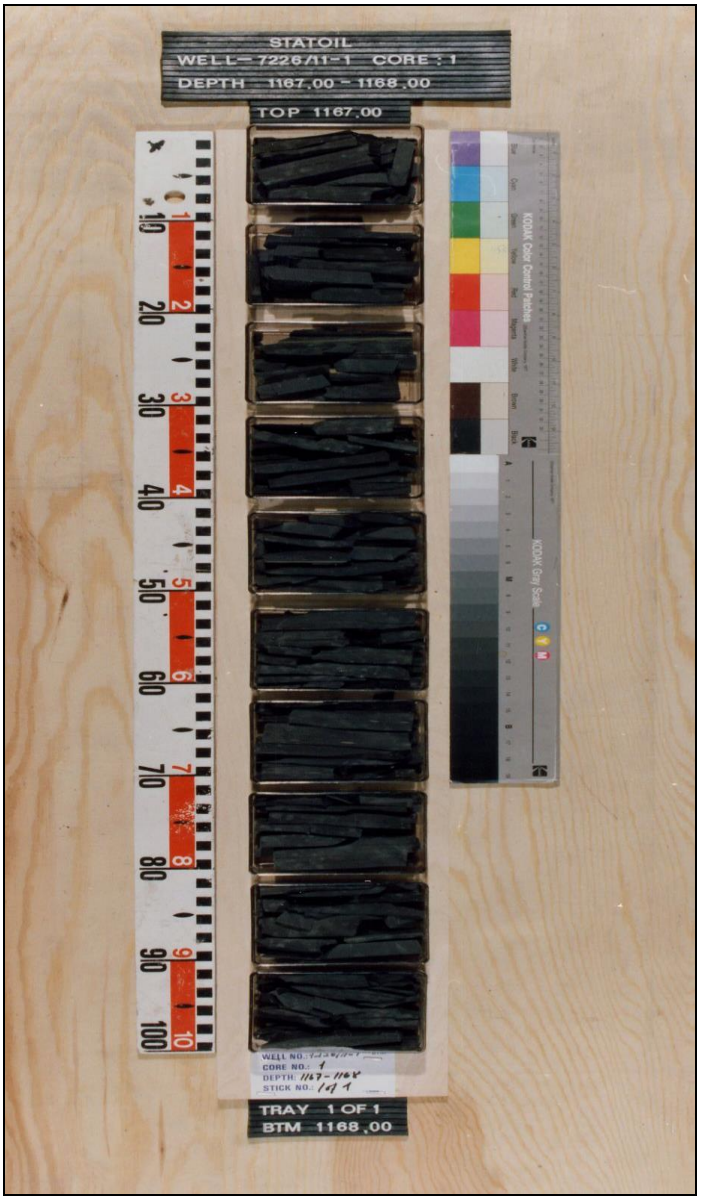

Figure 2.17: Core photographs of the Hekkingen Formation (1167-1168 m MDKB) from well 7226/11-1 (NPD, 2017b).

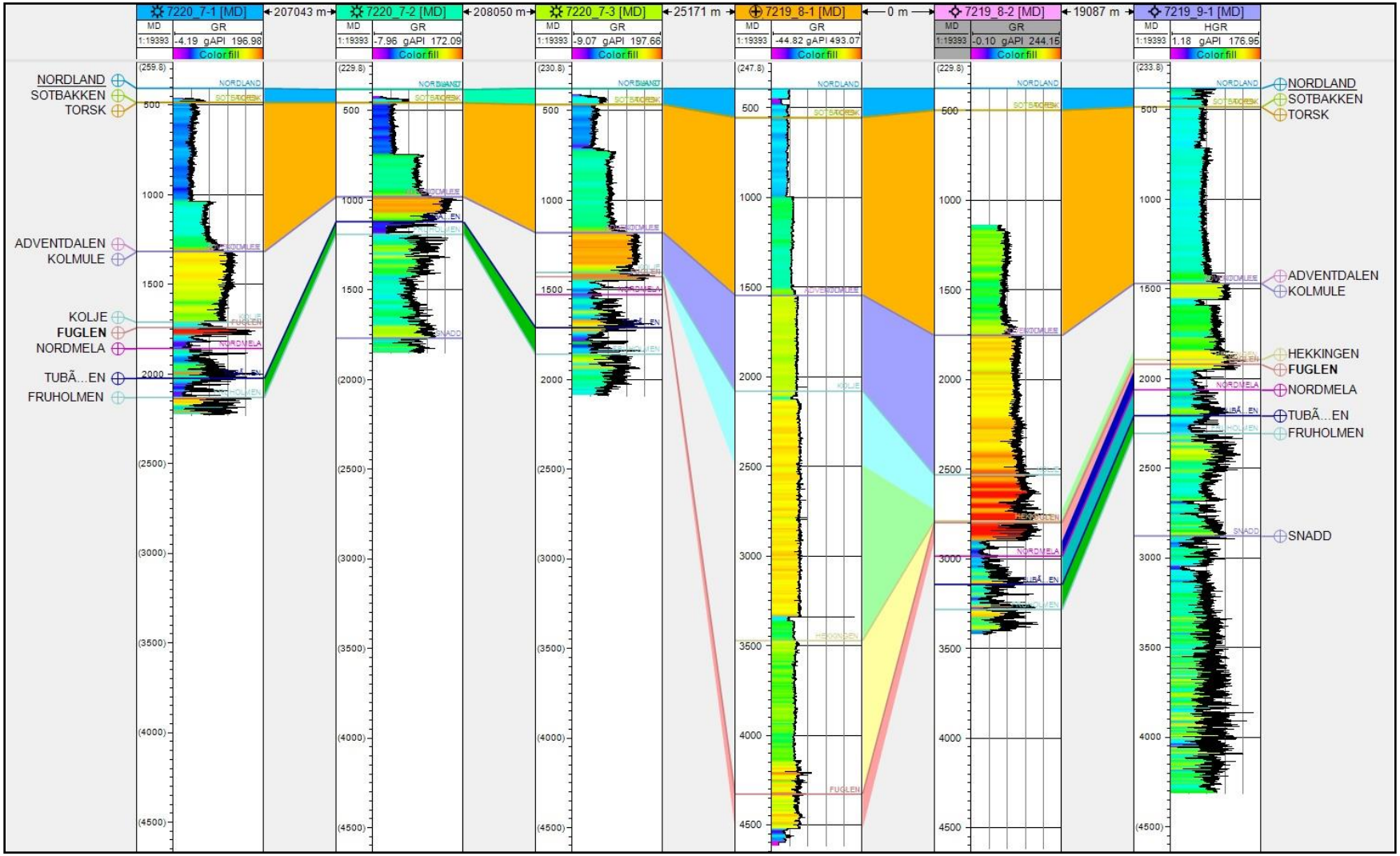

Figure 2.18: Well correlation of the six wells used in the study

2.4 Petroleum System

A petroleum system is a natural system that involves all of the essential elements and processes needed for oil and gas accumulations. The essential elements are source, reservoir, seal or cap rock in the form of a trap and overburden rock; while the processes include: trap formation and the generation-migration-accumulation of petroleum.

In order for the petroleum accumulation to happen all the elements and processes must be placed correctly in time and space (Magoon and Dow, 1994)

The Barents Sea consists of a complex system of source, reservoir, and cap rocks present at different stratigraphic levels from Paleozoic to Cenozoic times. Sandstones from Triassic and Jurassic successions have been considered the main exploration target within the Norwegian Barents Sea. Meanwhile, shales from the Upper Jurassic, as Hekkingen and Fuglen Formations, are considered the main oil and gas source (Lundschien et al., 2014; Ohm et al., 2008).

2.4.1 Source Rock

A source rock is a sedimentary rock, commonly shale or limestone, and rich in organic matter that is subjected to high temperature for a considerable time. This rock is capable of generating and/or expelling hydrocarbons in suitable temperature and pressure conditions (Ohm et al., 2008).

The Barents Sea constitutes a multi-source rock system. The potential source rocks have been identified at all stratigraphic intervals from the Carboniferous to the Cretaceous (Figure 2.19 and Table 2.1). The Hekkingen and Fuglen Formations are the most well known dark, organic-rich shales in the area, which are the major oil/gas source. Unfortunately, the Hekkingen shales did not realize their full generation potential due to maturity problems, i.e: did not reach the right temperature for oil generation. This unit is believed to have matured enough for hydrocarbon production only in a small area at the western margin of the Hammerfest Basin and along the western edge of the Loppa High (Doré, 1995).

However, it has been proven that shales from the Permian, Carboniferous, Triassic, and Middle to Lower Jurassic have potential to generate gas. (Ohm et al., 2008).

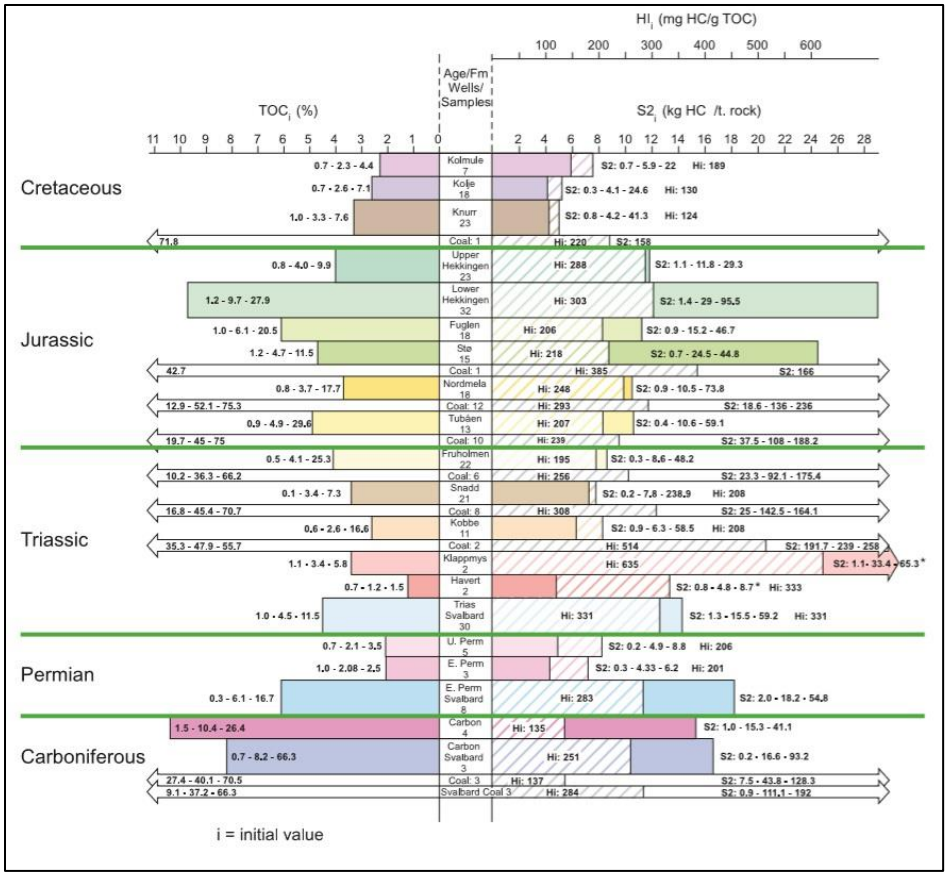

Figure 2.19: Representation of the source rock system in the Barents Sea. Indications of their respective quality (TOC, S2, Hydrogen index) are displayed (Ohm et al., 2008).

Table 2.1: Petroleum source rocks in the greater Barents Sea (Henriksen et al., 2011)

Age	Formations	Common thickness (m)	Kerogen type	TOC (%)	Hydrogen index, HI (mg g^{-1} TOC)
Barremian	Kolje	<30	II–II/III	1-7	130
Kimmeridgian	Hekkingen	10-250	II/III	<20	300
Carnian–Norian	Snadd		III-I	<5	300-500
Ladinian	Snadd	1-15	II	6	200-590
Anisian	Kobbe	5-20	II-II/III	2-8	180-350
Olenekian	Klappmyss	<100	III/II	3.5	200-330
Devonian	Domanic	20-60	II	8-10	300-450

2.4.2 Reservoir Rocks

A reservoir rock is a subsurface body that has sufficient porosity and permeability to store and transmit fluids. In general sedimentary rocks, sandstones, are the most common reservoir rocks due to the high porosity.

In the Barents Sea, the Triassic and Jurassic reservoirs are widely distributed (Fig. 2.20 and 2.21). They could be found in Bjørnøya, Hammerfest and Nordkapp Basins. Most of these sandstone reservoirs from the Snadd, Kobbe, and Klappmyss Formations are associated with a prograding coastal/delta front, which includes estuaries and fluvial channel (Doré, 1995; NPD, 2017c; Stephenson et al., 1995). However, these rocks are limited by the lack of clean sand and poor reservoir quality, low permeability, and porosity. As a consequence, minor gas accumulation could be found (Doré, 1995; Stephenson et al, 1995).

Furthermore, in the Norwegian Barents Sea about 70% to 80% of the hydrocarbon resources are located in the Lower-Middle Jurassic sandstones of Nordmela, Tubåen, Stø, and Fruholmen Formations which are assumed to be coastal/delta front deposits (Fig. 2.20 and 2.21).

The major discoveries represented by Snøhvit, Albatross, and Askeladden have a major reservoir sandstone of Lower- Middle Jurassic of Stø Formation, which has excellent reservoir properties (porosity and permeability) (Doré, 1995).

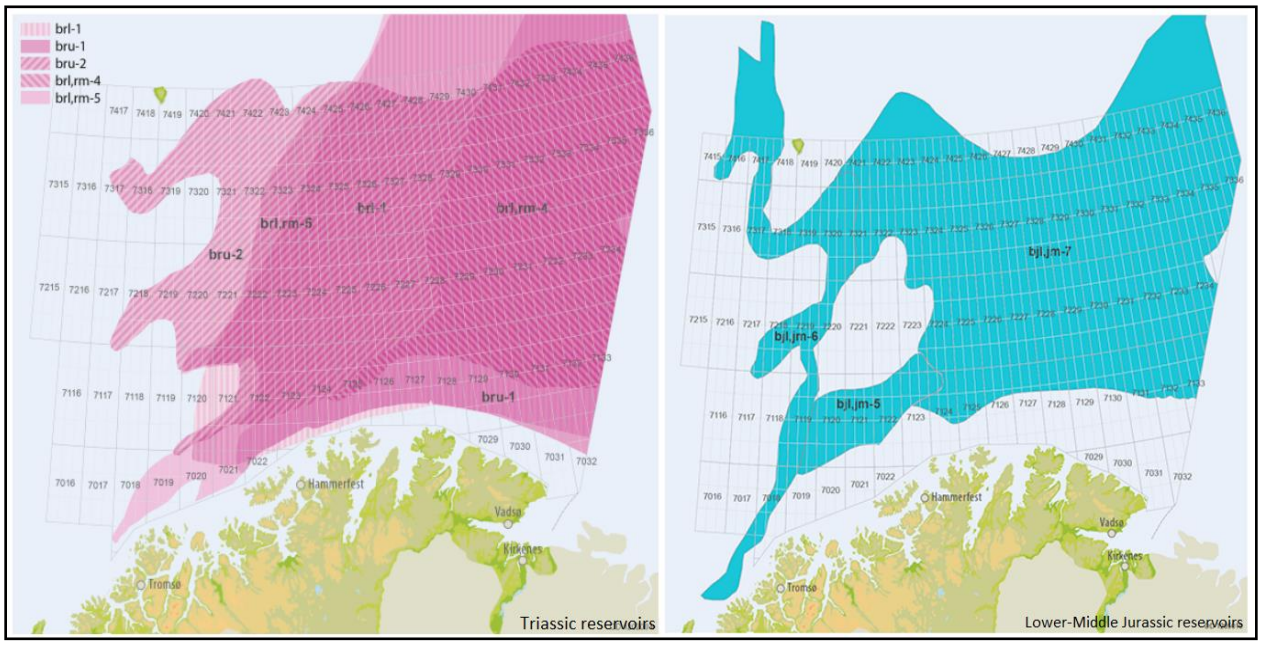

Figure 2.20: Map of the Triassic and Lower-Middle Jurassic plays in the Norwegian Barents Sea (NPD, 2017c).

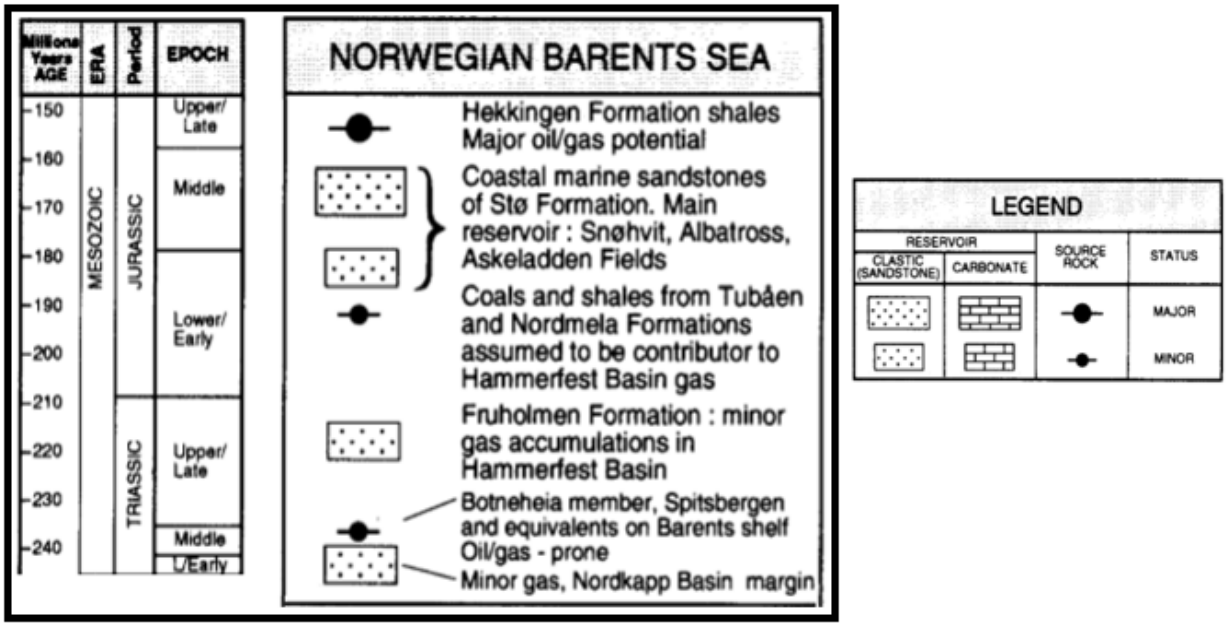

Figure 2.21: Potential reservoir and source rocks of Triassic and Jurassic successions of the Norwegian Barents Sea (modified from Dore, 1995).

2.4.3 Cap rock and trap

The Hekkingen and Fuglen Formations are considered the cap rocks in the Barents Sea for Lower-Middle Jurassic sandstones, however, shales from older formations, e.g. intra-Triassic, also have the potential to seal Triassic reservoir rocks

Additionally, the traps system is considered mainly stratigraphic but rotated fault blocks, horst structures, and traps formed in relation to salt are also common.

The Jurassic traps are generally fault-bounded positive blocks and salt diapers, while the Triassic traps consist of fault-bounded and domal structures, with sealing facilitated by the intra-Triassic shales (Doré, 1995).

2.4.4 Effect of uplifting and Erosion in Hydrocarbon Accumulation.

Uplift and erosion processes in sedimentary basins can have a wide range of consequences, both positive and negative, on hydrocarbon prospectivity. In case of the Norwegian Barents Sea, petroleum system has been influenced by substantial periods of uplift and erosion, being the Cenozoic event, the most significant since it is assumed to affect the commercial petroleum accumulations (Ohm et al, 2008; Doré, 1995). Figure 2.22 provides a representation of the total amount of uplift in different areas of the Norwegian Barents Se based on vitrinite reflectance (maturity) results.

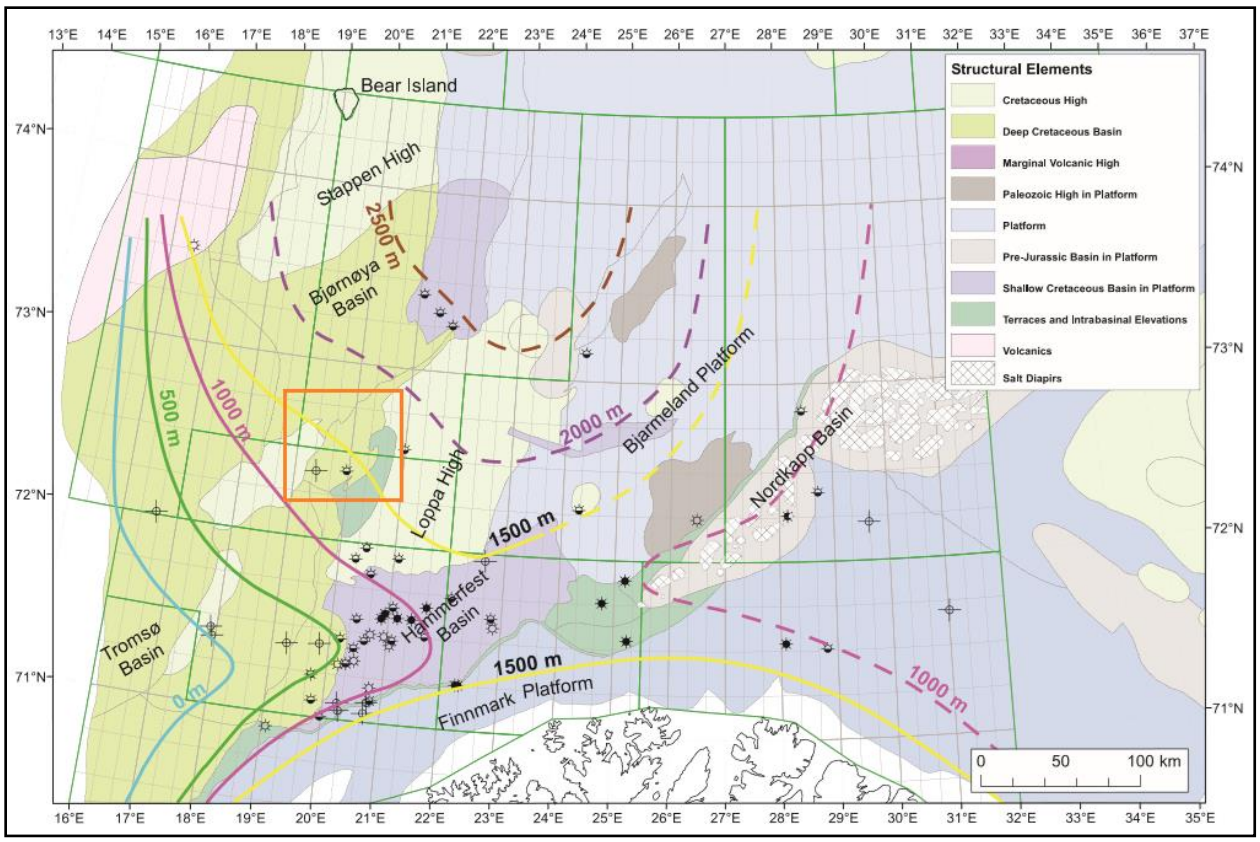

Figure 2.22: Uplift estimation map according to the vitrinite data (modified from Ohm et al., 2008). The study area is marked by the orange polygon.

Both processes have occurred in two distinct periods. The first could be linked to the opening of the Norwegian Greenland Sea; while post-Miocene glaciations are considered as the other main period (Nyland et al., 1992). Up to 3 km of sediments are assumed to have been removed in the areas where the influence was significant, 1.5 up to 2km in the western Barents Sea, although the accuracy of timing of events and thickness of the eroded section has not yet completely agreed upon (Doré and Jensen 1996; Faleide, et al., 2010)).

Negative effects associated with these processes are briefly listed below (Doré, 1995; Doré and Jensen, 1996; Ohm et al., 2008):

- Tilting, as result of differential uplift, originated spillage and seal breaching of pre-existing oil accumulation.

- Changes in structural altitude could have created new structural traps, which might be empty if the upliftment caused petroleum generation to cease.

- The exsolution between oil and gas and gas expansion due to pressure decrease caused the expulsion of oil from the traps if it assumed that the preexisting structures were filled to spill.

- Cooling of the source rock was the responsible for the subsequent cessation of hydrocarbon generation.

- Failure in the seal. Traps with a less well-developed top seal could have a high chance of retaining oil in uplifted areas. These traps classified as type II and III, allow the gas to leak through the seal, thus the oil column is not displaced below the spill point (Fig. 2.23).

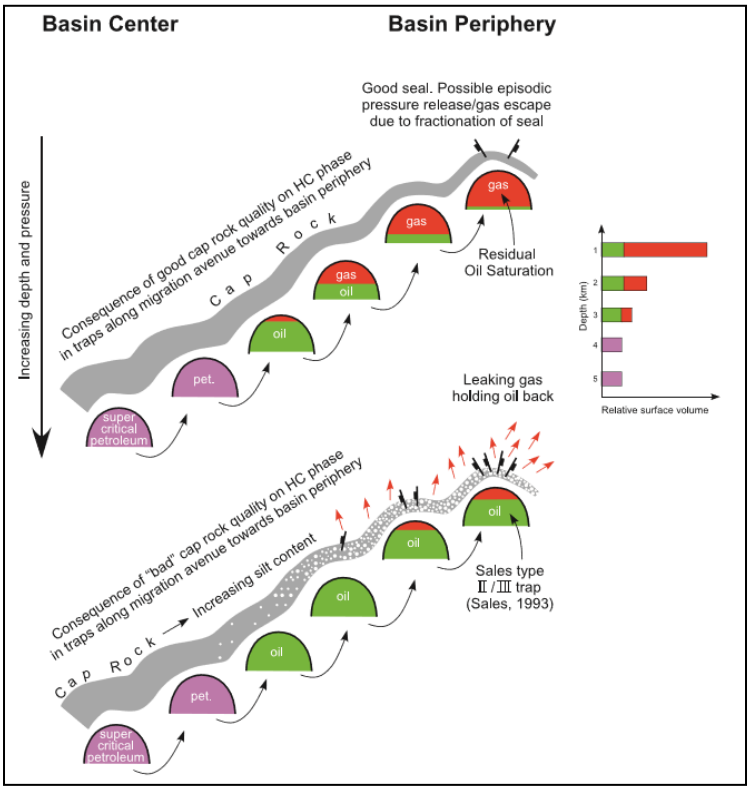

Figure 2.23: Schematical representation of hydrocarbon phase and cap rock quality (modified from Ohm et al., 2008).

Nevertheless, uplift, erosion, and pressure release are not necessarily devastating for oil accumulations; some of the positive effects are listed below.

- Areas that have undergone late Cenozoic uplift will contain source rocks that were buried deeper, and thus will be more thermally mature than expected from their present depth (Doré and Jensen, 1996).

- Rapid deposition of eroded sediments, in the areas, caused an accelerated maturation of source rocks enhancing the hydrocarbon generation and secondary migration due to rapid burial.

- Even though it is known that shales seal tends to fail during uplift and erosion processes there are other ductile seals, like evaporites, which can retain their sealing capacity despite the amount of uplift and deformational episode.

  The effectiveness of a good and a bad cap rock quality in terms of hydrocarbon retention could vary according to their classification (Fig. 2.23). Class I traps only contain gas, but due to the excess sealing capacity, it will not leak oil. What is more, during uplift, the gas might be flushed. Class II traps contains both hydrocarbons; it could spill oil, and leak gas. However, during uplift, it might gain additional capacity for oil.

  Finally, Class III traps are filled with oil. These traps leak both oil and gas and spill neither, due to uplift traps might modestly loose or gain capacity for oil (Sales, 1993)

As seen in Figure 2.22, the estimated uplift in the study area is approximately ~1000 m based on the vitrinite reflectance data. Nevertheless, studies carried by Baig et al., 2016 proposed net exhumation maps based on a combination of well log data (sonic logs), shot gathers, and maturity data. From then exhumation values for the Bjørnøyrenna Fault Complex are range from ~800 to 1200 m. The lowest values are displayed in the southwest of the area and the highest towards the southeast (Fig. 2.24).

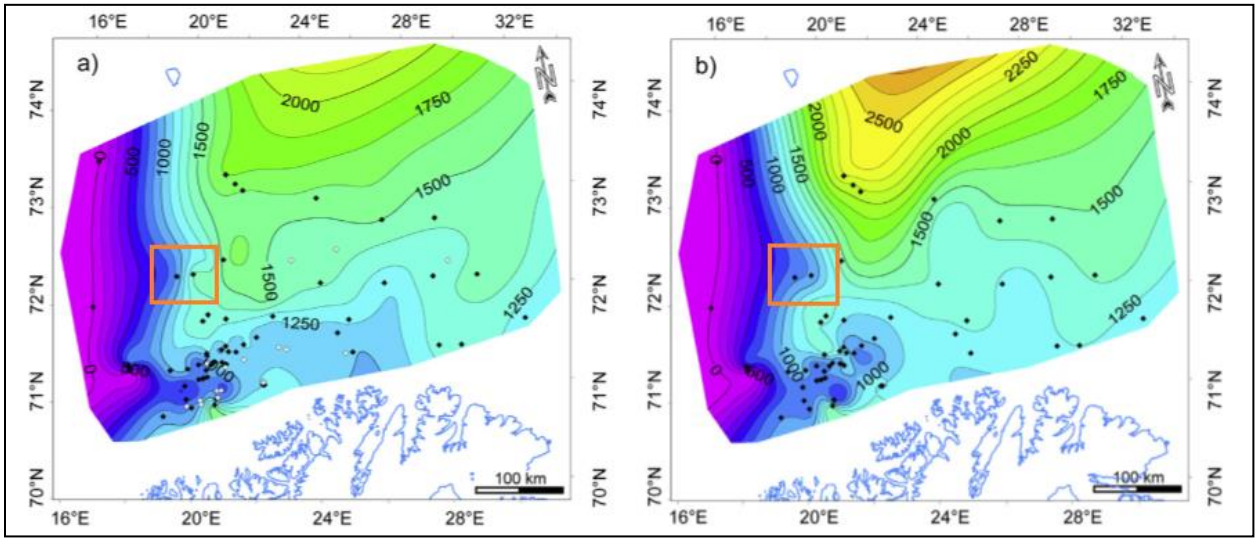

Figure 2.24: Net exhumation map of the Barents Sea. a) From sonic log data, and b) From vitrinite reflectance (modified from Baig et al., 2016). The location of the study area is marked by the orange polygon.

An estimation of the uplift performed in this study and is summarized in Table 2.2 for all the wells and for the Jurassic reservoirs (Table 2.3 and 2.4). These results are obtained through the analysis of the velocity-depth trends and further comparison with experimental compaction trends such as

Smectite, Kaolinite, Silt – Kaolinite 50:50 from Marcussen et al., 2010; Mondol et al., 2007; Storvoll et al., 2005 (Figure 2.25 and some Figures in Appendix A). Although many uncertainties are involved in this type of study due to lateral variation in facies, temperature and pressure variation, the results were similar to previous studies (Baig et al., 2016; Ohm et al., 2008).

Table 2.2: Uplift and geothermal gradient values for the studied well log data.

Well	Final vertical depth (MD) [m_RKB]	Final vertical depth (MD) [m SBF]	Kelly bushing (m)	Water depth (m)	BHT (°C)	Thermal Gradient (°C/km)	Uplift (m)
7220/7-1	2231.49	1826.49	40	365	72	36.44	1100
7220/7-2	1854.71	1474.71	31	349	-	35	1200
7220/7-3	2095.8	1709.8	41	345	-	35	1050
7219/8-1	4617.13	4424.13	24	369	165	37.95	900
7219/8-2	3424.73	3049.73	31	344	122	38.29	950
7219/9-1	4312.97	3933.97	23	356	145	35.75	980

Tabla 2.3: Depth estimation for the Stø Formation before and after uplift.

	Stø Formation				
	Present Depth		Maximum burial depth		
Well	**Top (m BSF)**	**Bottom (m BSF)**	**Top (m BSF)**	**Bottom (m BSF)**	**Thickness (m)**
72207-1	1376	1452	2486	2562	76
72207-2	-	-	-	-	-
72207-3	1072	1150	2122	2200	78
7219/8-1	4128	-	5028	-	-
7219/8-2	2523	2610	3473	3560	87
7219/9-1	1572	1683	2552	2663	111

Tabla 2.4: Depth estimation for the Nordmela Formation before and after uplift.

	Nordmela Formation				
	Present Depth		Maximum burial depth		
Well	**Top (m BSF)**	**Bottom (m BSF)**	**Top (m BSF)**	**Bottom (m BSF)**	**Thickness (m)**
72207-1	1452	1618	2552	2718	166
72207-2	-	-	-	-	-
72207-3	1150	1334	2200	2384	184
7219/8-1	-	-	-	-	-
7219/8-2	2610	2796	3560	3746	158
7219/9-1	1827	1926	2807	2906	144

The estimation of the thermal gradient for each well is estimated using the following formula:

$$G = \frac{T_2 - T_1}{Z_2 - Z_1} \qquad \text{Eq. 2.1}$$

Where G is the geothermal gradient (°C/Km), T_2 is the Bottom Hole Temperature (BHT), T_1 measured the temperature of the sediments at the sea bottom (4°C), Z_2 and Z_1 are measured depth below the sea floor (Km). However, T2 is not available for well 7220/7-2 and 7220/7-3, therefore the geothermal gradient is interpolated from the neighboring wells 7220/7-1 and 7219/9-1.

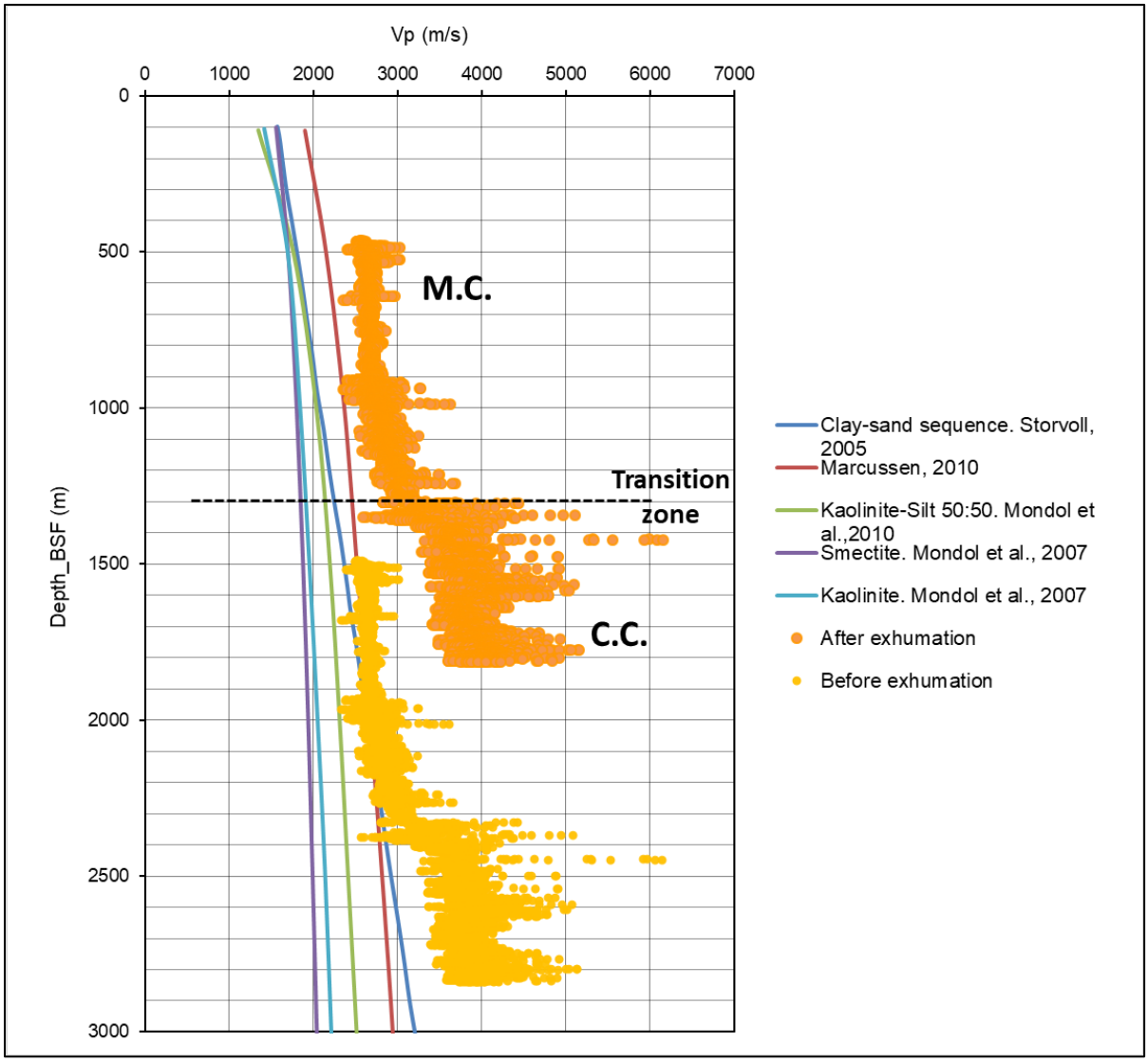

Figure 2.25: Vp vs depth crossplot for well 7220/7-1. Compared to published Vp depth trends (Marcussen et al., 2010; Mondol et al., 2007; Storvoll et al., 2005). The uplift is estimated for well 7220/7-1.

Chapter 3: Research Methodologies and Theoretical Background

3.1 Workflow

This study focuses on reservoir characterization by employing three different techniques. The first task focuses on petrophysical analysis, followed by rock physics diagnostic, and AVO modeling. A summary of the workflow including the main and secondary tasks are displayed in Figure 3.1.

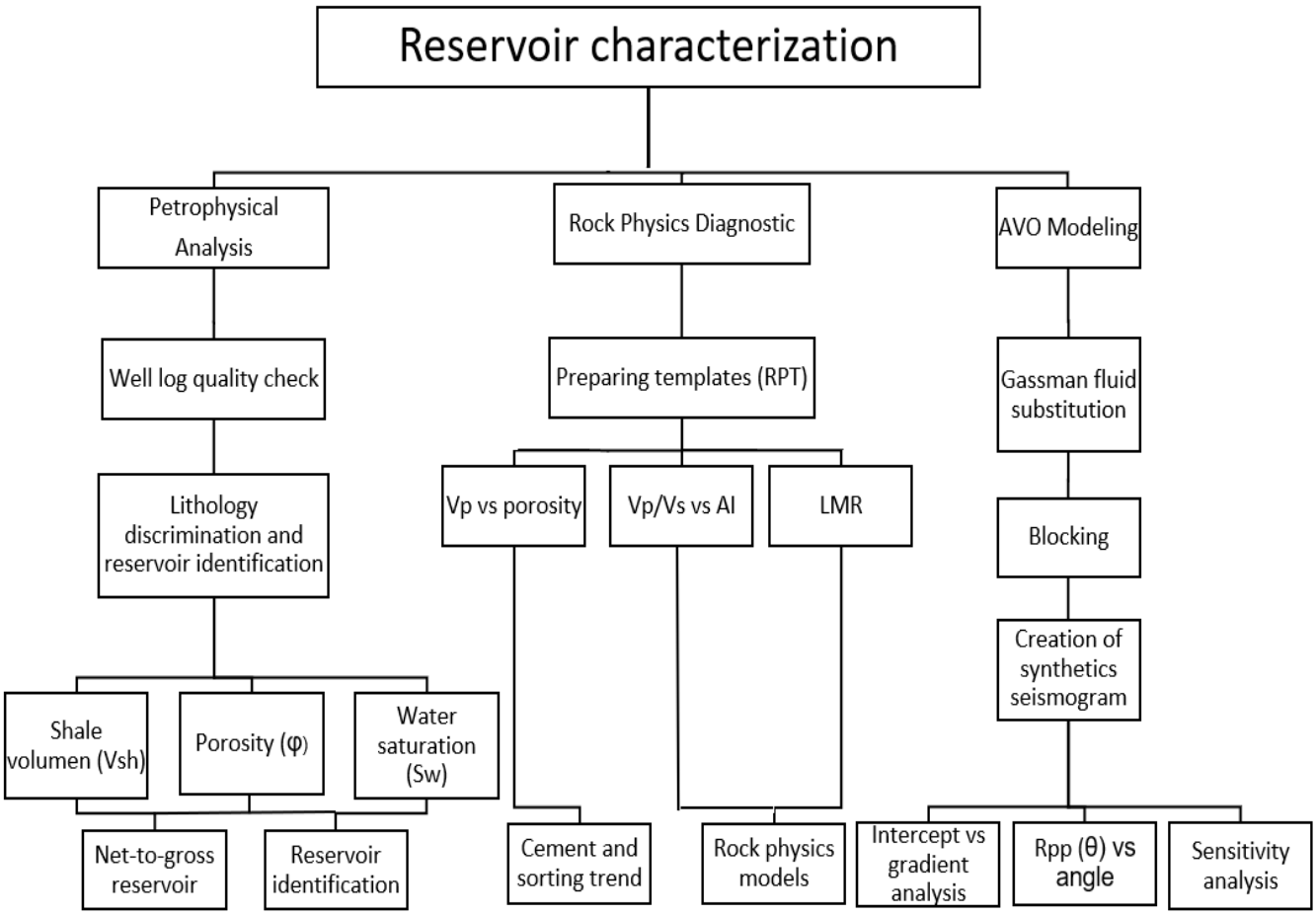

Figure 3.1: Summarize workflow employed during the reservoir characterization.

3.2 Petrophysical Analysis

The petrophysical analysis is a method that uses well log data to evaluate and predict the reservoir quality. This method encompasses the determination of special parameter like shale volume, net-to-gross ratio, porosity (φ), and water saturation (Sw) of the drilled section.

A transformation of the well log measurements into reservoir properties by establishing a relationship between selected logs and combining their information is very important for increasing confidence in the interpretation since there are uncertainties and limitations for all of the wells. However, including core data, thin section and gas chromatographic analysis will increase the accuracy of the study.

In Figure 3.2, composite log plot of well 7220/7-1 (Havis) is displayed showing an overview of the available well log data, and their organization into groups according to the study purpose (e.g: the first group includes gamma ray (GR), bit size and caliper for shale volume (Vsh) estimation).

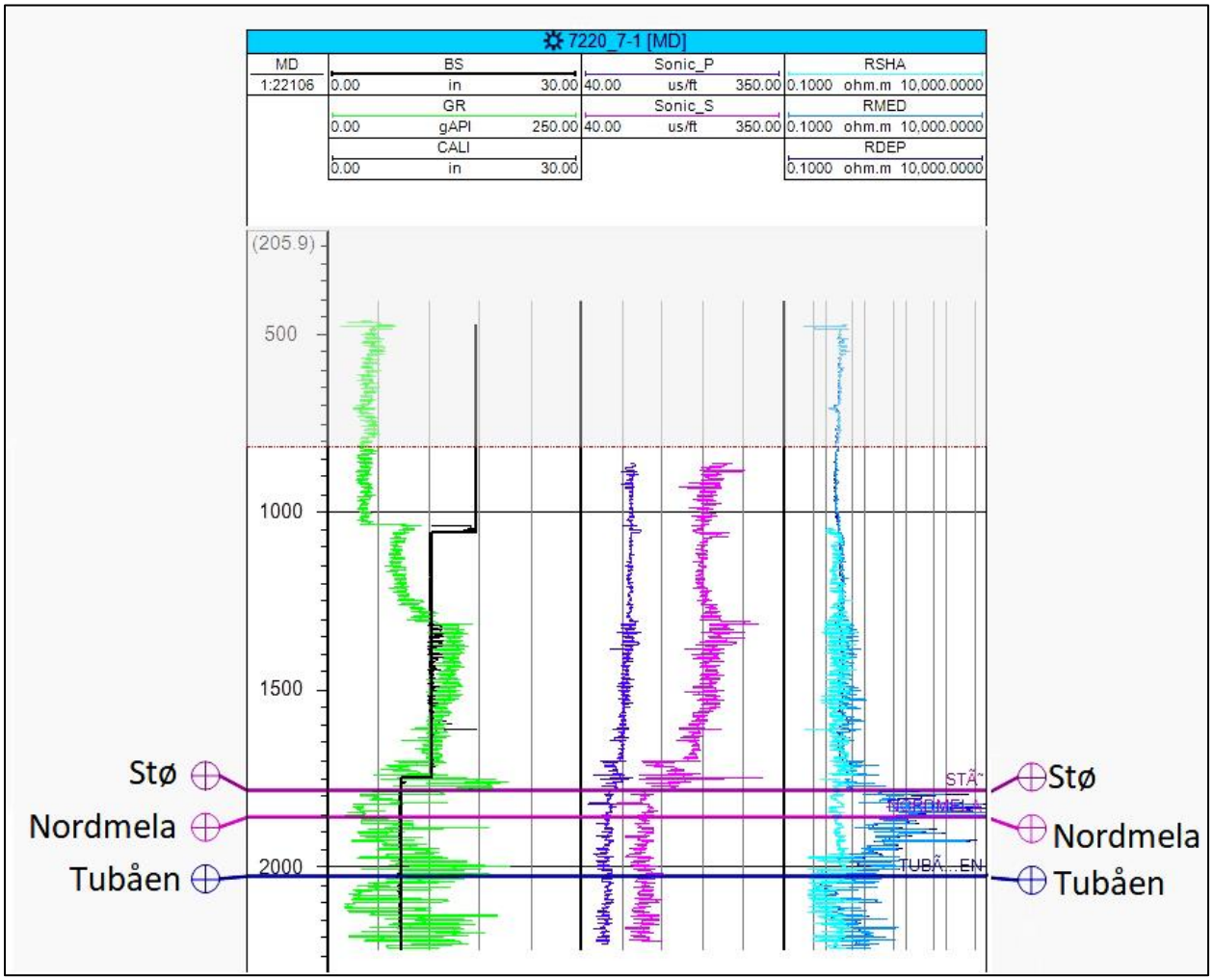

Figure 3.2: Overview of logs included in a composite display from well 7220/7-1 (Havis).

3.2.1 Lithology Discrimination

The main purpose of lithology discrimination is to classify sedimentary rocks discriminating types between lithologies such as sandstone, shale, limestone, dolomite, etc.

The most common method is to use gamma ray (GR) and neutron-density overlay to identify lithology and shaliness, based on the radioactive response and crossover, respectively. This can also be supported by the caliper log to identify areas of caving (brittle shales) and mudcake (porous rocks) effects.

The photoelectric (Pe) log, which is supplementary of the density log can be used as an additional lithology indicator since it records the absorption of low energy gamma rays within the formation. The recorded values are directly related to the atomic number of the formation (Z) and are mildly affected by pore volume or fluid content. (AAPG, 1994).

The Pe index is commonly scaled on a range between 0 and 10 b/e (barns/electron) and in Table 3.1 summaries the Pe absorption index values of common rock-forming minerals (Mondol, 2015b)

Table 3.1: Photoelectric index values of common rock-forming minerals (modified from Mondol, 2015b)

	Pe	**ρ_b (gr/cm^3)**
Quartz	1.81	2.65
K-feldspar	2.86	2.62
Calcite	5.08	2.71
Dolomite	3.14	2.87
Shale	3.42	2.65
Shaly sand	2.70	2.41
Muscovite	2.40	3.29
Anhydrite	5.10	2.98
Pure water	0.358	1.00
Salt water (NaCl 120,000 ppm)	0.81	1.19
Oil	0.13	0.97

3.2.2 Spectral Gamma ray (SGR)

Spectral Gamma Ray (SGR) is a logging tool used to quantify the clay type, volume, and mineralogy within the formation by measuring the natural gamma radiations and splitting it according to the contribution of each major radioisotopic sources: Thorium, Uranium, and Potassium (Hall, 2013; Klaja and Dudek, 2016).

SGR log is commonly displayed as the three curves of thorium (ppm), uranium (ppm) and potassium (%). Potassium (K) is common in many type of sediment that bears K-feldspar, micas or clay. Thorium (Th) is concentrated in the sand and silt-sized heavy minerals as Zircon, Monazite or fine-grained fraction in association with selected clay minerals. Uranium(U) occurs within the heavy minerals but also can be concentrated in anoxic sediments. Moreover, sediment composition and the sorting effects of sedimentary processes and environment can be distinguished based in the relation between the main elements such as Th/K and Th/U (Davies and Elliott, 1996; Doveton, 1994).

The potassium-thorium crossplot is used to recognize the different clay minerals and differentiate between micas and K-feldspar. The ratio is a relative measure of the potassium richness and thorium (Fig. 3.3), and according to the value the clay would be classified as it is indicated on Table 3.2.

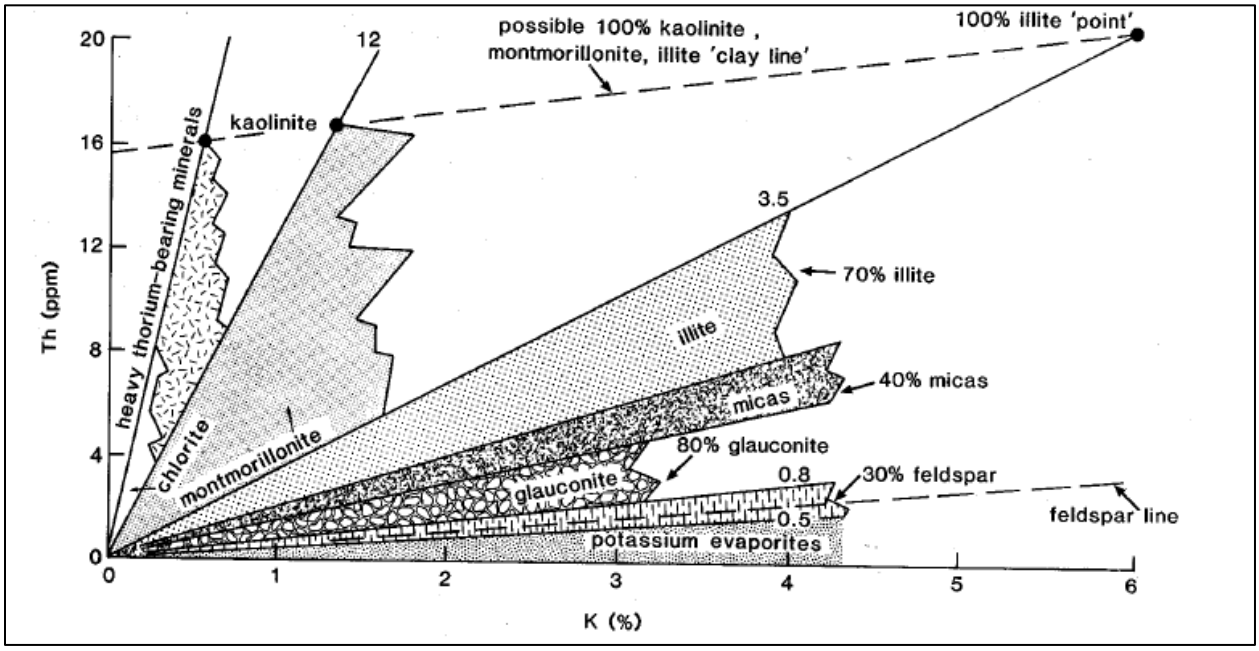

Figure 3.3: Thorium/ potassium crossplot for clay identification using spectral gamma ray data (Glover, 2013).

Table 3.2: Clay mineral classification according to the Th/K ratio from (Klaja and Dudek, 2016).

Clay Mineral	Th/K range
Feldspar	0.5 - 0.6
Glauconite	0.6 – 1
Micas	1 – 2
Illite	3 – 3.5
Mixed layer	>3.5

The thorium-uranium ratio (Th/U) is commonly applied during geochemical facies recognition since it is an indicator of redox potential. This ratio according to Adams and Weaver (1958) Th/U ratio is strongly linked to depositional environment, when the value is less than 2 (uranium-rich) the depositional environment is commonly marine; by contrast, if the value is larger than 7 the uranium has been mobilized by weathering and/or leaching, indicating an oxidizing condition that represents possible terrestrial environment (Fig. 3.4)

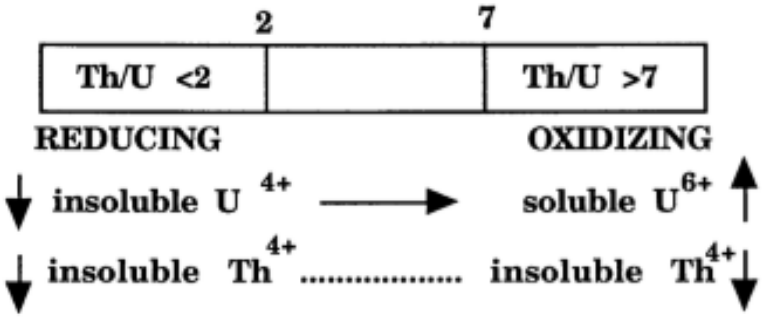

Figure 3.4: Relation between Th/K ratio and redox potential, with boundary Th/U ratio values suggested by Adams and Weaver (1958).

3.2.3 Shale Volume (Vsh) Estimation

As mentioned earlier, Gamma Ray (GR) is a log that measures the natural gamma radiation originated from potassium, uranium and thorium isotopes within the formation. This log is used as lithology indicator since shales display the highest gamma values; while halite, anhydrite, clean sandstone, limestone, and dolomite have the lowest values (Mondol, 2015b).

Once the lithologies are defined the estimation of the shaliness (Vsh) can be done. This parameter is considered a threshold value that helps to distinguish reservoir rock from the non-reservoir rock. Knowing the amount of shale or clay is also useful since it is established that it affects the reservoir quality by reducing the permeability and porosity. In addition, the water saturation calculation is

also affected by the same factor since Archie's equation do not work properly in shaly sandstones (Ellis and Singer, 2008)

The simplest method for Vsh estimation is through the gamma ray log by employing Equation 3.1:

$$I_{gr} = \frac{GR_{log} - GR_{min}}{GR_{max} - GR_{min}} \qquad \text{E.q. 3.1}$$

Where I_{gr} is the Gamma Ray Index, GR_{log} is the Gamma Ray value of a formation, GR_{min} is the minimum Gamma Ray (clean sand line), and GR_{max} is the maximum Gamma Ray (shale line).

This relationship assumes a linear estimation between the shale volume and the gamma ray index ($I_{gr} = V_{sh}$). However, several non-linear relationships (Asquith and Krygowski, 2004a; Mondol, 2015b) based on the geography of the area and the age of the formation are used (Table 3.3).

Table 3.3: Non-linear equations for shale volume estimation.

Authors	Equation
Larionov (1969) 'Young rock'	$V_{sh} = 0.083 \times \left(2^{3.7 I_{gr}} - 1\right)$
Larionov (1969) 'Old rock'	$V_{sh} = 0.33 \times \left(2^{2 I_{gr}} - 1\right)$
Steiber (1970)	$V_{sh} = I_{gr} \div \left(3 - 2 \times I_{gr}\right)$
Clavier et al. (1971)	$V_{sh} = 1.7 - \left[3.38 - \left(I_{gr} + 0.7\right)^2\right]^{\frac{1}{2}}$

In this study, an interpretation of the gamma ray response on each formation on all the wells is done to determine the sand and shale baseline varying from well to well. The sandstone baseline is determined by a thick/clean sandstone section with a minimum GR value, and a maximum value of GR in the shale section neglecting the organic-rich shales intervals due to the high gamma response.

A representation of the shale volume estimation using the information from the gamma ray is displayed in Figure 3.5 for the Stø and Nordmela Formations. Moreover, a quality control of the results is compared with the shale volume obtained by employing the neutron and density measurements.

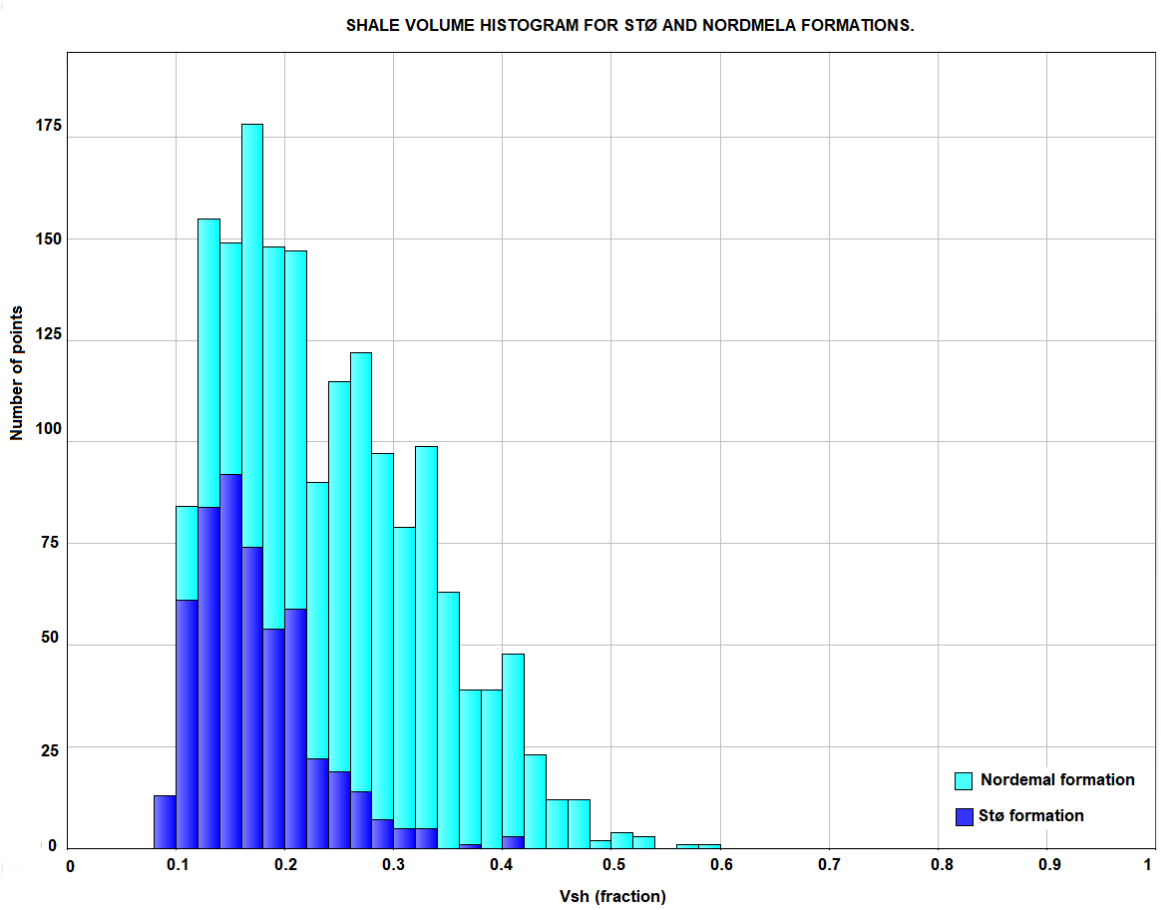

Figure 3.5: Shale volume histogram for well 7220/7-3 (Drivis) for the Stø and Nordmela Formations.

3.2.4 Net-to-Gross Estimation

Net-to-gross is a term that applies to the ratio between the volume of the producible reservoir rock to the total volume of the reservoir rock. The importance of net-to-gross is to find the potential zones in the reservoir for hydrocarbon exploitation. Moreover, several terms are proposed by Worthington and Cosentino (2005) that involves different levels of ”net” thickness related to the “gross” reservoir thickness (Fig.3.6).

- **Gross interval**: It is the whole sedimentary package that is going to be evaluated. It includes the reservoir and non-reservoir zone.

- **Net sand**: it is the interval that might have good reservoir properties. This is defined by the shale volume (V_{sh}).

- **Net reservoir**: this comprises the net sand interval that contributes reservoir quality, high porosity. The cut-off is defined by the porosity (φ).

- **Net pay**: this term includes the net reservoir interval that contains substantial hydrocarbon quantities. This is defined by the water saturation (S_w) cut-off.

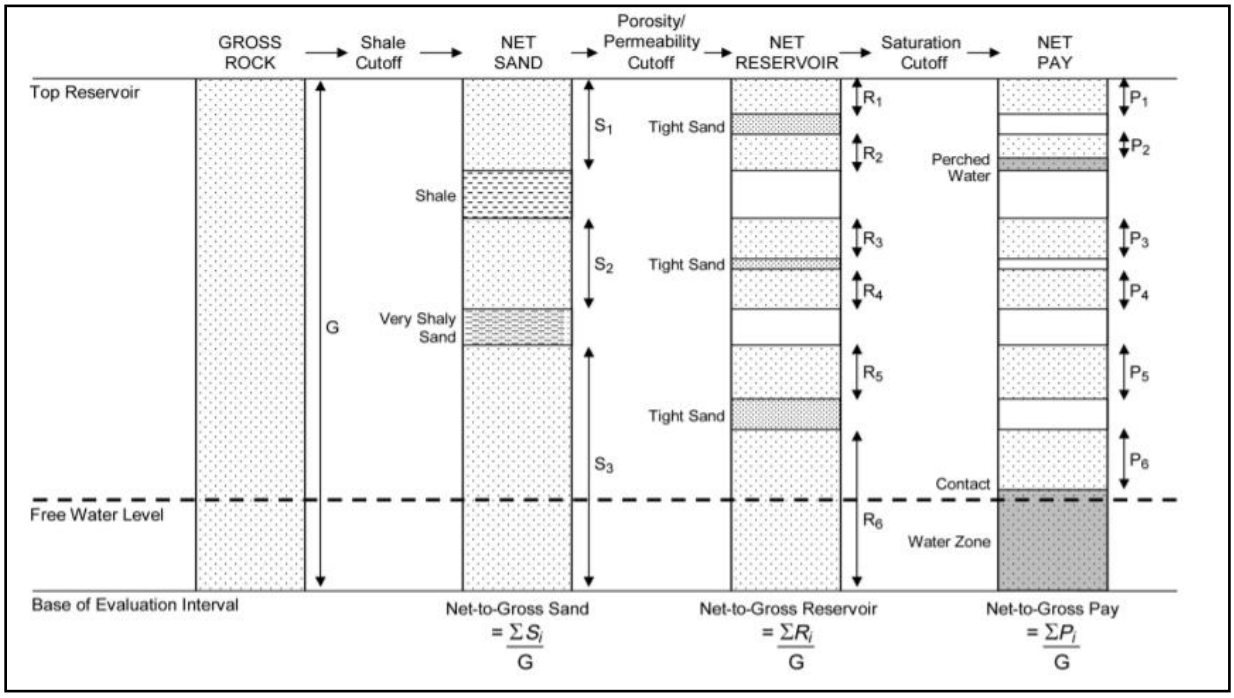

Figure 3.6**:** Schematic representation of different net terms and their cut-offs (Worthington and Cosentino, 2005).

A compiled cut-offs selection from Worthington and Cosentino (2005) work for sandstones, are shown in Table 3.4.

Table 3.4: Proposed cut-off values for sandstones (Worthington and Cosentino, 2005)

Parameter	Range of values (Cut-off)
V_{sh}	≤ 0.3-0.5
φ	≥ 0.08-0.06
S_w	≤0.5-0.6

3.2.5 Porosity Estimation

Porosity is the percentage of the pore volume within a rock volume which may or may not be connected and can contain fluids (Schulumberger Limited, 2017).

Evaluating this parameter is an important task for reservoir characterization. The porosity can be estimated using the information from neutron (NPHI), density (DPHI), and/or sonic log (SPHI).

Most of these logs do not measure the porosity directly. The sonic log uses acoustic measurement, while the neutron and density logs use nuclear measurement. These logs, in general, are affected by the lithology but combining them provides a reliable porosity estimation (φ) (Mondol, 2015b).

3.2.4.1 Total porosity and Effective porosity

Several types of porosity terms such as total and effective porosity are defined based on the degree of connecting of the pores.

Total porosity refers to the total pore space of the rock, including the sealed-off pore as well the connected ones (Manger, 1963). Effective porosity is the interconnected pores. Therefore, the effective porosity is used in the petrophysical analysis for reservoir calculation.

Figure 3.7. shows the different rock components and relevant porosity terms

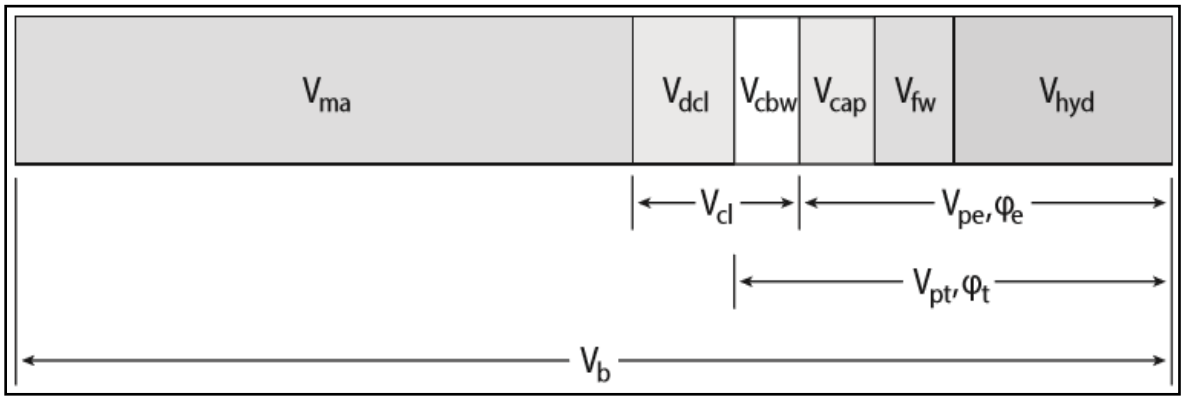

Figure 3.7: Relative amounts of the various volumes (V) and porosity (φ) terms. V_{ma} =matrix volume, V_{dcl} is the dry clay volume, V_{cl} is the wet clay volume, V_{cbw} is the clay bound water volume, V_{cap} is the capillary bound (irreducible) water volume, V_{fw} is the free water volume, V_{hyd} is the hydrocarbon volume, Vb is the bulk volume, φ is the porosity, φ_e is the effective porosity, and φ_t is the total porosity (Ellis and Singer, 2008).

3.2.5 Sonic Porosity (φ_S)

The sonic log is considered a porosity log that measures interval transit time or slowness of a compressional sound wave that travels inside the formation. The transit time unit is μs/ft, and it represents the inverse of velocity (m/s).

The measure of this log can be interpreted in term of the porosity according to Wyllie's time average equation (1958) (Asquith and Krygowski, 2004b):

$$\varphi_S = \frac{\Delta t_{log} - \Delta t_{matrix}}{\Delta t_{fl} - \Delta t_{matrix}} \qquad \text{Eq.3.2}$$

Where φ_S is the computed sonic porosity, Δt_{matrix} is the interval transit time of solid phase (minerals), Δt_{fl} is the interval transit time of the fluid, and Δt_{log} is the interval transit time measured.

The time average equation provides good porosity estimation in well-cemented sandstone with low porosity. However, in case of highly porous unconsolidated sand Wyllie's equation overestimates the porosity. In order to solve this, the compaction factor is added to the original equation (Rider and Kennedy, 2011):

$$\varphi_S = \frac{\Delta t_{log} - \Delta t_{matrix}}{\Delta t_{fl} - \Delta t_{matrix}} \times \frac{1}{C_p} \qquad \text{Eq. 3.3}$$

Where $C_p$is the compaction factors,

An alternative equation for porosity estimation is proposed by Raymer-Hunt-Gardner (1980):

$$\varphi_S = \frac{5}{8} \times \frac{\Delta t_{log} - \Delta t_{matrix}}{\Delta t_{log}} \qquad \text{Eq. 3.4}$$

Standard values use in Wyllie or Raymer's equations for porosity calculation are represented in Table 3.5

Table 3.5: Acoustic transit time values for common reservoirs and lithologies (Petrowiki, 2015).

	Transit time
Sandstone	55 μs/ft
Shale	44 μs/ft
Anhydrite	54 μs/ft
Brine	189 μs/ft
Oil	238 μs/ft

3.2.6 Density Porosity (φ_D)

The density log consists of an induced radiation tool. It emits gamma ray radiations through the formation and measures how much radiation returns to the sensor. The measures obtained are the bulk density (g/cm^3), which are a function of the fluid and matrix densities. From these readings, porosity values can be calculated using the Equation 3.5 (Asquith and Krygowski, 2004b; Mondol, 2015b):

$$\varphi_D = \frac{\rho_{matrix} - \rho_{log}}{\rho_{matrix} - \rho_{fl}} \qquad \text{Eq.3.5}$$

Where φ_D is the computed density porosity, ρ_{matrix} is the density of solid phase (rock), ρ_{fl} is the fluid density, and ρ_{log} is the bulk density measured log.

The values for the matrix and the fluid must be chosen correctly in order to get accurate porosity estimation. The wrong selection of the value can easily over/underestimate the porosity. especially the matrix density which has a bigger impact on the estimated porosity (Asquith, and Krygowski, 2004b)

The presence of gas in the pores can significantly alter the density porosity since the gas has a very low density an overestimation of porosity will happen (Mondol, 2015b).

3.2.7 Neutron Porosity (NPHI)

A neutron log measures the amount of hydrogen in the formation since it is often found in the form of water or hydrocarbons inside the pore spaces thereby the porosity can be estimated. The log output is based on a limestone model, and the common units of the reading is % or decimal (Mondol,2015b).

Nevertheless, gas and shale have a particular effect on the logs measurements. High clay content gives high porosity estimation due to shale effect. The presence of hydrogen in OH groups and clay bound water inside the shale matrix influence the measurements. Porosity underestimation occurs when the pores spaces are filled with gas (called: gas effect) since it contains less hydrogen atom per volume than water or oil (Mondol, 2015b; Rider and Kennedy, 2011).

3.2.8 Porosity from Neutron-Density Combination (φ_{ND})

Neutron-density logs are generally displayed on compatible scales considering a limestone matrix for lithology discrimination and gas identification.

On one hand, this type of scale separation of neutron and density curve is used to discriminate lithology or the presence of gas. In case of a gas bearing formation, low apparent neutron porosity and low-density reading would be displayed. On the other hand, shale intervals would have the opposite behavior (Asquith and Krygowski, 2004b).

The combination of both neutron and density porosity may provide a true porosity value and it can be calculated by the following equation:

$$\varphi_{ND} = \sqrt{\frac{\varphi_N^2 + \varphi_D^2}{2}} \qquad \text{Eq. 3.6}$$

Where φ_{ND} is the average neutron and density porosity, φ_N is the neutron porosity, and φ_D is density porosity.

3.2.9 Water Saturation (Sw)

Water saturation is defined as the portion of the pore space that is filled with water, expressed in fraction or percentage.

Log derived saturation is based on the resistivity log. The resistivity log measures the resistance to the flow of electric current. Most of the conduction occurs in the liquid phase and depends on the porosity, permeability, fluid and salt content. Therefore, resistivity values are considered the major hydrocarbon indicator since it displays an increase in the formation resistivity in the deep and medium log (Mondol, 2015b).

The determination of the water saturation (Sw) is achieved through Archie's law (Eq. 3.7):

$$S_w = \sqrt[n]{\frac{a * R_w}{R_t * \varphi^m}} \qquad \text{Eq. 3.7}$$

Where, S_w is the water saturation, a is the tortuosity factor, m is the cementation factor, n is the saturation exponent, R_w is the formation water resistivity, φ is the porosity, and R_t is the formation resistivity (from deep resistivity log) (Ellis and Singer, 2008).

Archie's equation works properly under a simple, uniform pore system, filled with saline water; but in case of a shaly or heterogeneous formation, it cannot be directly used. For shaly formation, correction for clay bound water must be done (Ellis and Singer, 2008).

An important value that must be calculated is the formation water resistivity (Rw). This term can be estimated from the SP log. Unfortunately, the SP log is not included in the studied well log data. In this study, Rw is estimated from the log in water-filled zones (Sw=100%), assuming that the bulk density (Ro) is equal to the formation resistivity (Rt).

3.3 Rock Physics Diagnostics

The rock physics technique provides a link between geophysical measurements (e.g. P-wave velocity, S-wave velocity, bulk density, and acoustic impedance) with reservoir parameters (e.g. porosity, water saturation, shale volume, and lithology); providing a better understanding of the reservoir qualities and properties (Avseth et al., 2010). Moreover, rock physics is also applied to predict seismic response to assumed overburden properties and conditions.

Rock physics commonly uses crossplots, in which elastic parameters are plotted against geological reservoir parameters, and then compared to theoretical models.

3.3.1 Rocks Physics Cement Models

The rock physics correlates velocity and porosity to predict the microstructure (texture) and type of rock by adjusting an effective-medium theoretical model to a trend in the data (Avseth et al., 2010). The most common theoretical models are the contact cement model, friable sand model, and the constant cement model. These are used to explain the velocity-porosity-pressure behavior in reservoir sands (Fig. 3.8)

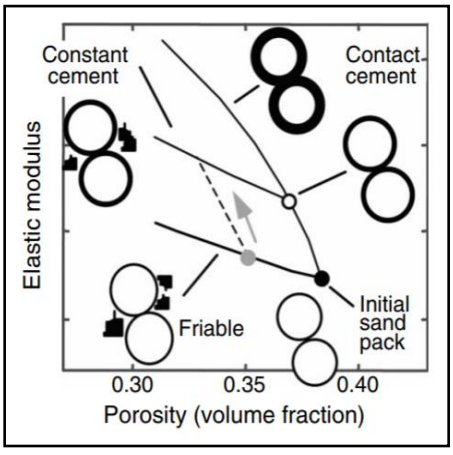

Figure 3.8: Representation of three effective-medium cement models for reservoir sands.

3.3.1.1 The Friable Sand Model

The friable sand model is also known as the unconsolidated line, introduced by Dvorkin and Nur (1996), described the variation in the velocity-porosity relationship due to the sorting. The model assumes that sorting deteriorates by smaller grains deposited within the pores, as a consequence, the porosity decrease, and the rock stiffness slightly increase.

The two “end members” consists of well-sorted packed sand, with a critical porosity of 40%, and on the other side a zero porosity sand which has moduli of the mineral (Fig. 3.9). The elastic moduli of the critical porosity is calculated by the Hertz-Mindlin theory, assuming an elastic spherical grain package under confining pressure conditions. While the other ”endpoint” is adapted to the mineral properties. The moduli between both “end members” are then interpolated using the lower Hashin-Shtrikman bound (Avseth et al., 2010).

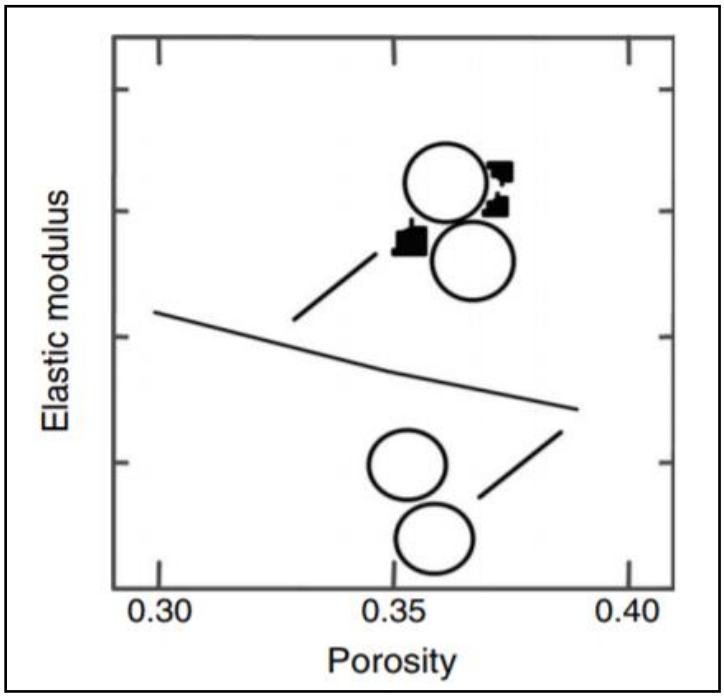

Figure 3.9: Schematic representation of the friable sand model (Avseth et al., 2010).

3.3.1.2 The Contact- Cement Model

The contact-cement model assumes a uniform deposition of cement layer on the grain’s surface, which rapidly reinforced the stiffness of the sand due to the contact cement (Fig. 3.10). This causes a velocity increase with a small decrease in porosity from the initial cementation stage. This model describes a diagenetic trend for sandstones (Avseth et al., 2010)

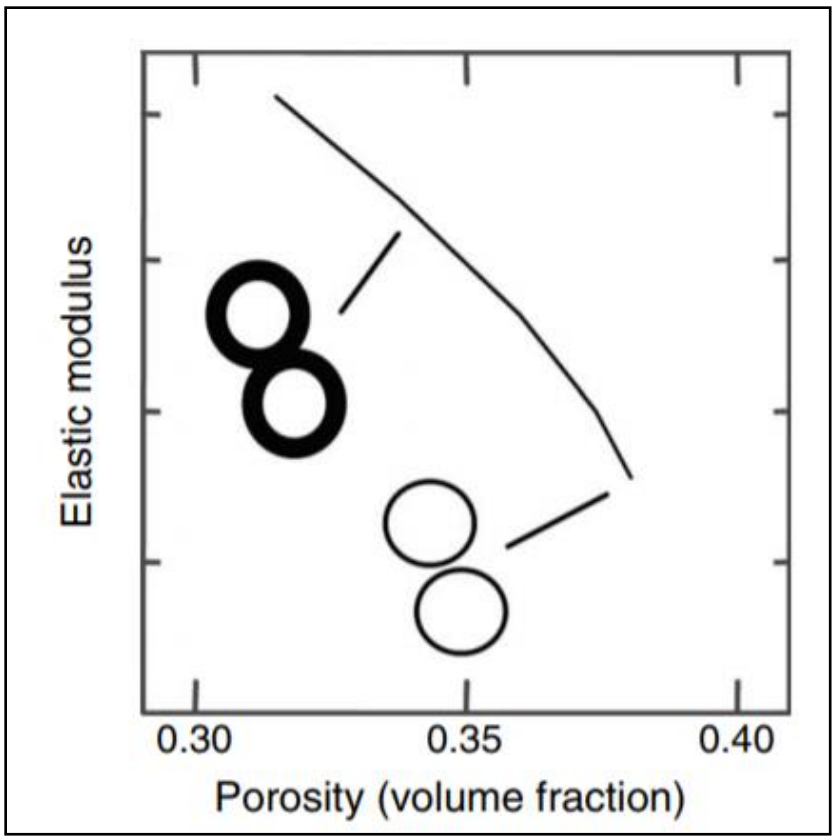

Figure 3.10: Schematic representation of the contact-cement model (Avseth et al., 2010).

3.3.1.3 The Constant-Cement Model

In theory, the constant-cement model is a combination of the two previous models, assuming a decrease of the initial porosity due to the contact cement deposition and deteriorating sorting.

In the constant-cement model, the curves from the data and the theoretical model deviates from the contact cement curve because the grain sorting begins to deteriorate at the cemented porosity point (Avseth et al., 2010).

3.3.2 Vs prediction

The estimation of the shear wave velocity plays an important role in the rock physic analysis for fluid and lithology predictions. In this study, only three wells 7220/7-1 (Havis), 7220/7-3 (Drivis), and 7219/8-2 (Iskrystall) have the S-wave velocity included. For other wells, Vs is estimated employing several empirical equations summarized in Table 3.6.

Table 3.6: Empirical equations to predict Vs (Dvorkin and Nur, 1996).

Authors (year)	Equation
Castagna et al. (1985)	• $V_p = 1.16Vs + 1.36$ (Mudrock line), equal to $V_s = 0.862V_p - 1.172$
Castagna et al., (1993)	• $V_s = 0.804V_p - 0.856$ (clastic rocks)
Han (1986)	• $V_s = 0.794V_p - 0.787$
Mavko et a1. (1998)	• $V_s = 0.754V_p - 0.657$ ($Vsh < 0.25$) • $V_s = 0.842V_p - 1.099$ ($Vsh > 0.25$) • $V_s = 0.853V_p - 1.137$ ($\varphi < 0.15$) • $V_s = 0.756V_p - 0.662$ ($\varphi > 0.15$)
Williams (1990)	• $V_s = 0.846V_p - 1.088$ (water − bearing sands) • $V_s = 0.784V_p - 0.893$ (shales)
Greenberg and Castagna (1992)	• $V_s = 0.8041V_p - 0.85588$ (sandstones) • $V_s = -0.05508V_p^2 + 1.1067V_p$ (limestone) • $V_s = 0.58321V_p - 0.07775$(dolomite) • $V_s = 0.76969V_p - 0.86735$ (shales)
Krief et al. (1990)	• $V_p^2 = 2.213V_s^2 + 3.857$ (water − bearing sandstone) • $V_p^2 = 2.282V_s^2 + 0.902$ (gas − bearing sandstone) • $V_p^2 = 2.033V_s^2 + 4.894$ (shaley sandstone) • $V_p^2 = 2.872V_s^2 + 2.755$ (limestone)

3.3.3 Calculation of Elastic Parameters

Any isotropic and linear elastic material is characterized by a set of elastic parameters establishing a linear relationship between stress and strain. These are Young's Modulus (E), Poisson's ratio (ν) and density (ρ). However, these can also be expressed in terms of Lame's coefficients (λ), shear moduli (μ), and bulk moduli (k) (Gelius, 2017b; Mavko, 2009a).

$$\lambda = \frac{E * \nu}{(\nu + 1)(1 - 2\nu)} \qquad \text{Eq. 3.8}$$

$$\mu = \frac{E}{2(\nu + 1)} \qquad \text{Eq. 3.9}$$

$$k = \lambda + \frac{2\mu}{3}$$ Eq.3.10

$$\nu = \frac{3k - 2\mu}{2(3k + \mu)}$$ Eq. 3.11

Nevertheless, these coefficients can also be related to P-wave and S-wave velocities by the following equations (Mavko, 2009b).

$$V_p = \sqrt{\frac{K + {}^{4\mu}/_{3}}{\rho}}$$ Eq.3.12

$$V_s = \sqrt{\frac{\mu}{\rho}}$$ Eq.3.13

Poisson's ratio can be related to the ratio between the P-wave velocity and the S-wave velocity ($\frac{V_P}{V_S}$) for an elastic material. Equation 3.14 represents the relation between these parameters (Gelius, 2017a). Finally, Table 3.7 summarizes relations between different elastic constants (Mavko, 2009a).

$$\nu = \frac{0.5(\frac{V_P}{V_S})^2 - 1}{(\frac{V_P}{V_S})^2 - 1}$$ Eq. 3.14

Table 3.7: Relations between elastic parameters and velocities (Sheriff, 2002).

	Young's modulus, E	Poisson's ratio, σ	Bulk modulus, k	Shear modulus, μ	Lamé constant, λ	P-wave velocity, α	S-wave velocity, β	Velocity ratio, β/α
(E, σ)			$\frac{E}{3(1-2\sigma)}$	$\frac{E}{2(1+\sigma)}$	$\frac{E\sigma}{(1+\sigma)(1-2\sigma)}$	$\left[\frac{E(1-\sigma)}{(1+\sigma)(1-2\sigma)\rho}\right]^{1/2}$	$\left[\frac{E}{2(1+\sigma)\rho}\right]^{1/2}$	$\left[\frac{(1-2\sigma}{2(1-\sigma)}\right]^{1/2}$
(E, k)		$\frac{3k-E}{6k}$		$\frac{3kE}{9k-E}$	$3k\left(\frac{3k-E}{9k-E}\right)$	$\left[\frac{3k(3k+E)}{\rho(9k-E)}\right]^{1/2}$	$\left[\frac{3kE}{(9k-E)\rho}\right]^{1/2}$	$\left(\frac{E}{3k+E}\right)^{1/2}$
(E, μ)		$\frac{E-2\mu}{2\mu}$	$\frac{\mu E}{3(3\mu-E)}$		$\mu\left(\frac{E-2\mu}{3\mu-E}\right)$	$\left[\frac{\mu(4\mu-E)}{(3\mu-E)\rho}\right]^{1/2}$	$\left(\frac{\mu}{\rho}\right)^{1/2}$	$\left(\frac{3\mu-E}{4\mu-E}\right)^{1/2}$
(σ, k)	$3k(1-2\sigma)$			$\frac{3k}{2}\left(\frac{1-2\sigma}{1+\sigma}\right)$	$3k\left(\frac{\sigma}{1+\sigma}\right)$	$\left[\frac{3k(1-\sigma)}{\rho(1+\sigma)}\right]^{1/2}$	$\left[\frac{3k}{2\rho}\left(\frac{1-2\sigma}{1+\sigma}\right)\right]^{1/2}$	$\left[\frac{1-2\sigma}{2(1-\sigma)}\right]^{1/2}$
(σ, μ)	$2\mu(1+\sigma)$		$\frac{2\mu(1+\sigma)}{3(1-2\sigma)}$		$\mu\left(\frac{2\sigma}{1-2\sigma}\right)$	$\left[\left(\frac{2\mu}{\rho}\right)\left(\frac{1-\sigma}{1-2\sigma}\right)\right]^{1/2}$	$\left(\frac{\mu}{\rho}\right)^{1/2}$	$\left[\frac{1-2\sigma}{2(1-\sigma)}\right]^{1/2}$
(σ, λ)	$\lambda\frac{(1+\sigma)(1-2\sigma)}{\sigma}$		$\lambda\left(\frac{1+\sigma}{3\sigma}\right)$	$\lambda\left(\frac{1-2\sigma}{2\sigma}\right)$		$\left[\left(\frac{\lambda}{\rho\sigma}\right)(1-\sigma)\right]^{1/2}$	$\left[\frac{\lambda}{\rho}\left(\frac{1-2\sigma}{2\sigma}\right)\right]^{1/2}$	$\left[\frac{1-2\sigma}{2(1-\sigma)}\right]^{1/2}$
(k, μ)	$\frac{9k\mu}{3k+\mu}$	$\frac{3k-2\mu}{2(3k+\mu)}$			$k-2\mu/3$	$\left(\frac{k+4\mu/3}{\rho}\right)^{1/2}$	$\left(\frac{\mu}{\rho}\right)^{1/2}$	$\left(\frac{\mu}{k+4\mu/3}\right)^{1/2}$
(k, λ)	$9k\left(\frac{k-\lambda}{3k-\lambda}\right)$	$\frac{\lambda}{3k-\lambda}$		$\frac{3}{2}(k-\lambda)$		$\left(\frac{3k-2\lambda}{\rho}\right)^{1/2}$	$\left[\frac{3(k-\lambda)}{2\rho}\right]^{1/2}$	$\left[\frac{1}{2}\left(\frac{k-\lambda}{k-2\lambda/3}\right)\right]^{1/2}$
(μ, λ)	$\mu\left(\frac{3\lambda+2\mu}{\lambda+\mu}\right)$	$\frac{\lambda}{2(\lambda+\mu)}$	$\lambda+\frac{2}{3}\mu$			$\left(\frac{\lambda+2\mu}{\rho}\right)^{1/2}$	$\left(\frac{\mu}{\rho}\right)^{1/2}$	$\left(\frac{\mu}{\lambda+2\mu}\right)^{1/2}$
(α, β)	$\rho\beta^2\left(\frac{3\alpha^2-4\beta^2}{\alpha^2-\beta^2}\right)$	$\frac{\alpha^2-2\beta^2}{2(\alpha^2-\beta^2)}$	$\rho\left(\alpha^2-\frac{4}{3}\beta^2\right)$	$\rho\beta^2$	$\rho(\alpha^2-2\beta^2)$			

3.3.4 Construction of Rock Physics Templates (RPT)

The rock physics templates analysis introduced by Ødegaard and Avseth (2003) has become a tool for sorting, lithology and fluid prediction (Avseth et al., 2010). The common form of RPT consist of crossplot of Vp/Vs versus acoustic impedance (AI), porosity (φ) versus elastic properties (K, V_P, V_S, μ), and LMR (λρ versus μρ). To generate RPTs it is important to consider geological parameters (e.g. lithology, mineralogy, burial depth, diagenesis, pressure, and temperature) that honor local geological factors for a specific basin (Avseth et al., 2010; Liu et al., 2015).

3.3.4.1 Porosity versus Vp

Plotting porosity values against Vs and/or Vp are normally used to obtain information about microstructures (texture). For years, the time average equation from Wyllie (1956) has been used to establish a relation between porosity and velocity (Eq. 3.2).

This equation works properly for clean sandstones with porosities between 10 up to 25%. However, since the velocities depend on the pore pressure, temperature, pore geometry, and cementation, an improvement of Wyllie's equation was defined by Raymer et al. (1980).

$$V_p = (1-\varphi)^2 V_m + \varphi V_{fl} \qquad \text{Eq. 3.15}$$

Where V_p is the P-wave velocity of the log, V_m is the velocity of the matrix, V_{fl} is the velocity of the fluid, and φ is the porosity.

Neither of these equations can be used in case of shaly sandstones, therefore Han et al. (1986) introduced several empirical equations (Eq. 3.16 and 3.17) that relate ultrasonic velocity to porosity and clay content (C.C). They were defined for shaly sandstones at 40 MPa of confining pressure, 1.0 MPa of pore pressure, and clay content between 0 up to 50% (Fig. 3.11).

$$V_p = 5.59 - 6.393\varphi - 2.18C \qquad \text{Eq. 3.16}$$

$$V_s = 3.52 - 4.91\varphi - 1.89C \qquad \text{Eq. 3.17}$$

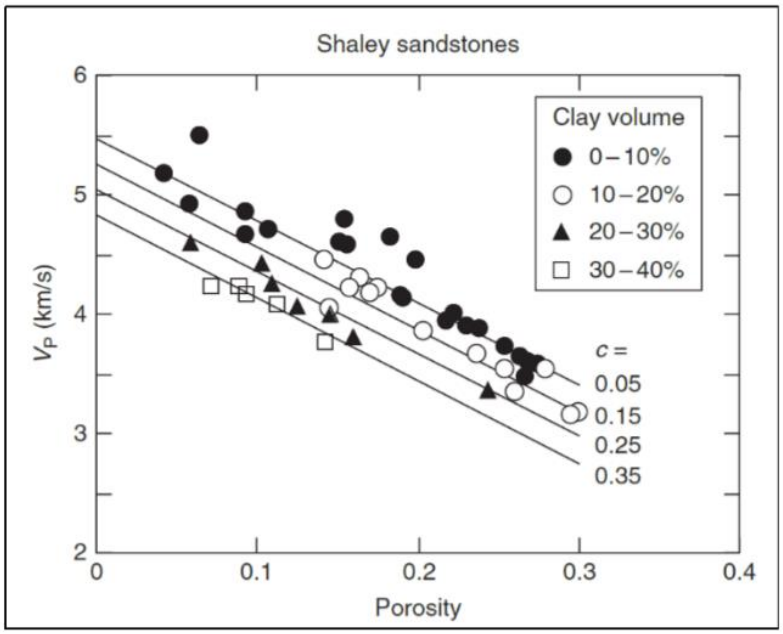

Figure 3.11: Han's water-saturated ultrasonic velocity data at 40 MPa with different empirical relations for the four different clay fractions (Mavko et al., 2009)

3.3.4.2 Vp/Vs versus AI

The Vp/Vs versus AI crossplot (Fig. 3.12) is used for fluid and lithology discrimination in siliciclastic sediments. Mechanical compaction, low clay content, or gas might cause low Vp/Vs ratio; while higher Vp/Vs values are associated with the low net-to-gross ratio. Moreover, porosity losses during mechanical and chemical compaction have higher AI (Ødegaard and Avseth, 2003).

The separation is considerable in unconsolidated, homogeneous sand. However, the presence of quartz cement in a brine-sand would reduce the fluid sensitivity. As a result, the brine saturated-sand will have lower Vp/Vs ratio, similar to the oil saturated sand (Avseth et al., 2010).

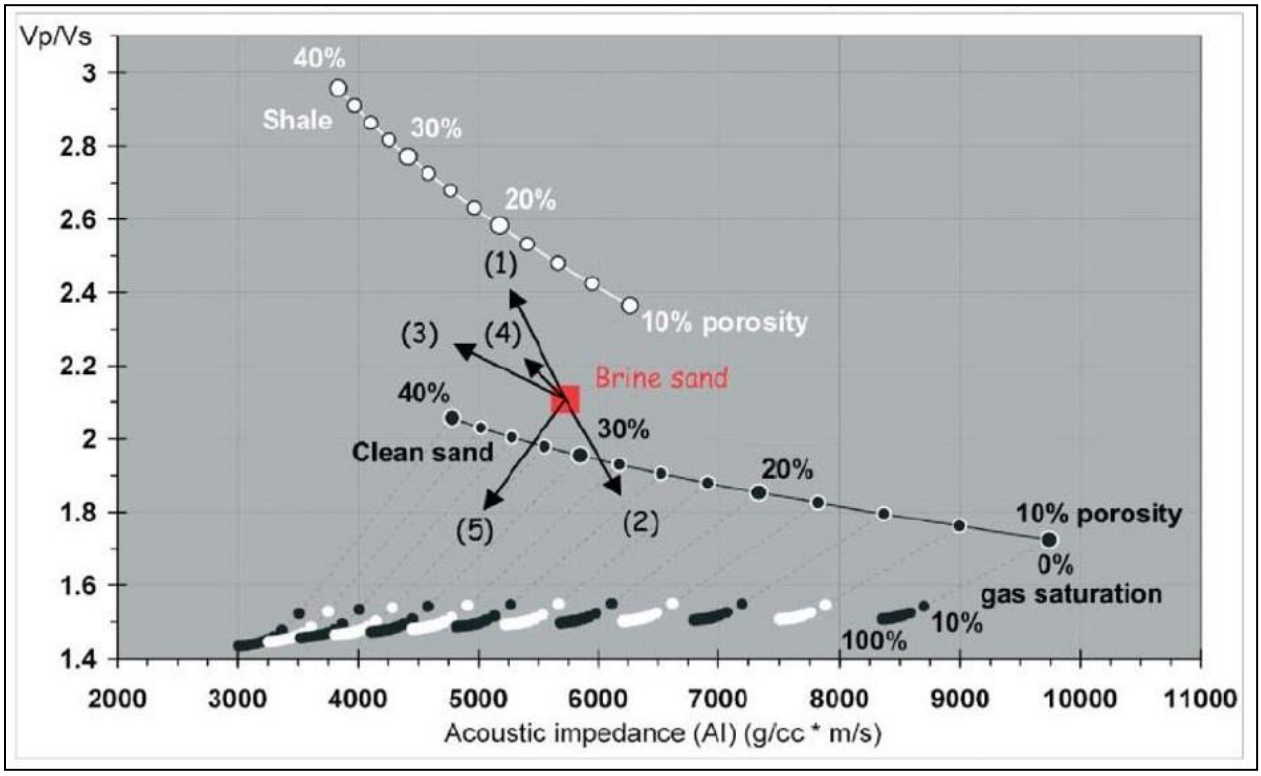

Figure 3.12: Standard rock physics template of Vp/Vs versus AI. Black arrows are indicating: (1): Increasing shaliness, (2): Increasing cement volume, (3): Increasing porosity, (4): Decreasing effective pressure and (5): Increasing gas saturation (Ødegaard and Avseth, 2003).

In Figure 3.13 the data points associated to clean sandstone from the Stø Formation plotted on top of the model water sand and gas sand lines, while the Fuglen Formation (cap rock) clustered along the shale line. The RPT shows a good lithology and fluid discrimination.

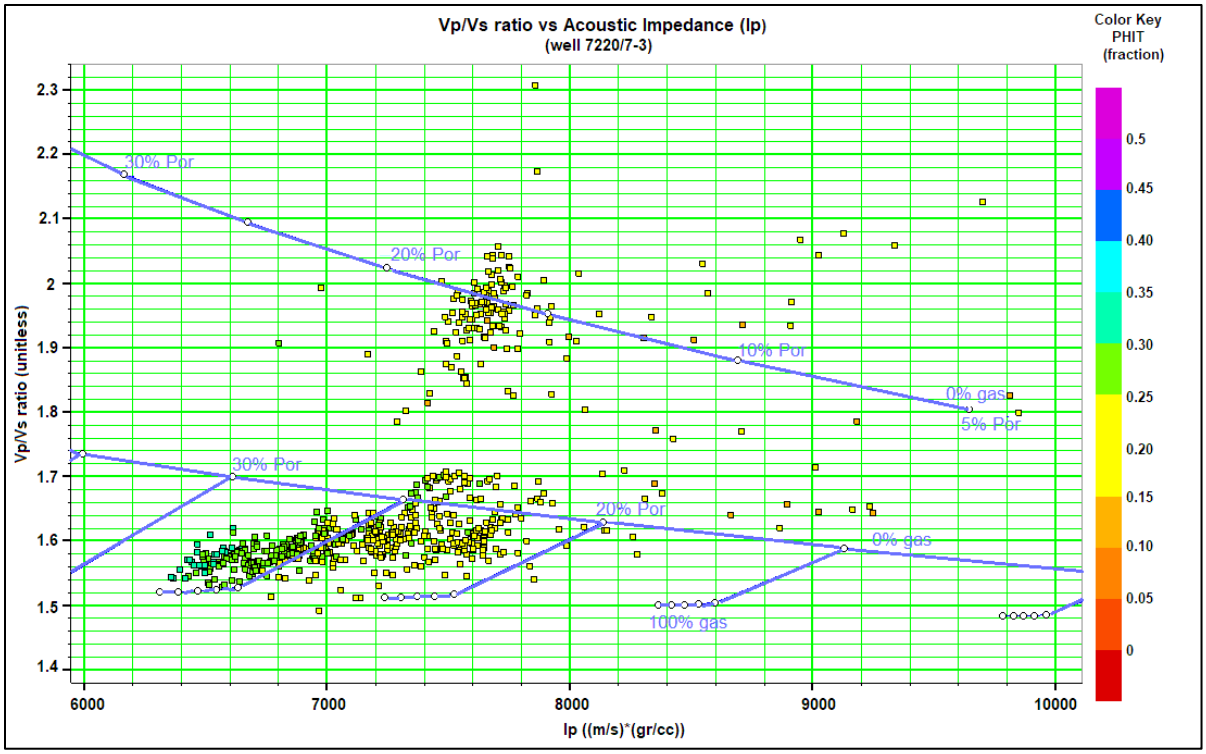

Figure 3.13: Standard RPT for Vp/Vs versus AI for the Stø and Fuglen Formations from well 7220/7-3 (Drivis).

3.3.4.3 LMR (Lambda-Mu-Rho)

Lambda-Rho versus Mu-Rho crossplot is based on Lamé's parameters, rigidity (μ) and pure incompressibility (λ). Along with density, they are considered good lithology and fluid indicator (Fig. 3.14). Their relationship with velocities (Vp, Vs) is established through the acoustic impedance (Ip, Is) by employing the following equations (Goodway et al., 1997):

$$\lambda\rho = I_p^2 - 2I_s^2 \qquad \text{Eq. 3.18}$$

$$\mu\rho = I_s^2 \qquad \text{Eq. 3.19}$$

Where $I_p = V_p x\, \rho$ (P-wave impedance), $I_s = V_s x\, \rho$ (S-wave impedance), and ρ= density.

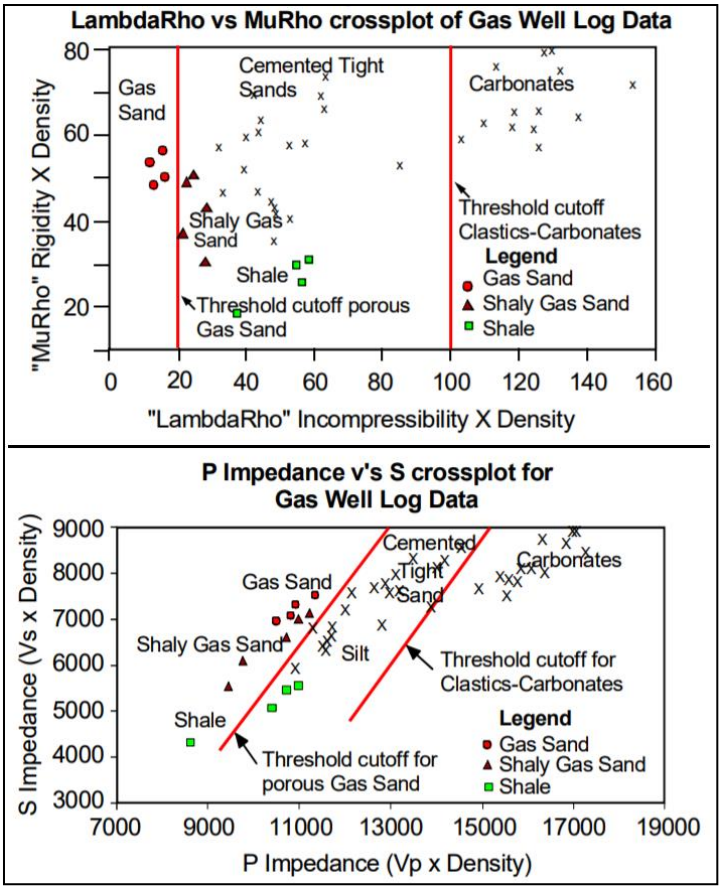

Figure 3.14: RPT of LambdaRho versus MuRho (above), and P-wave impedance versus S-wave impedance (below) (Goodway et al., 1997).

The Lamé parameters are also considered a good indicator of the grains organization, and its effects on the stress distribution. In case of a material with an incompressibility module higher than the rigidity ($\lambda > \mu$), the grains would be deformed in large aspect ratio due to the anisotropic stress distribution. Nevertheless, when the stress is distributed evenly ($\lambda = \mu$), it is assumed that the grains are organized randomly.

In terms of fluid discrimination, the rock properties do not vary but might affect considerably $\lambda\rho$. As a consequence, it is expected lower $\lambda\rho$ values, and high $\mu\rho$ estimations for gas saturated sand (Perez and Tonn, 2003).

3.4 AVO Modeling

AVO modeling is a technique used in pre-stack data analysis, which study changes in the amplitude or "anomalies" that are associated with gas sand. These variations caused by the lower impedance of the gas sand in comparison to the surrounding shales (Avseth et al., 2010). However, AVO is a method that must be used carefully since it has ambiguities and pitfalls related to lithology, overburden effect, tunning effect, data acquisition and processing effects.

3.4.1 Generation of Synthetic Seismogram

The creation of synthetic seismogram would provide a link between rock properties and seismic reflection. A seismic trace X(t) is the result of the convolution of the source wavelet s(t) and the reflectivity series r(t) plus noise (N) (Fig. 3.15) (Mondol, 2015a).

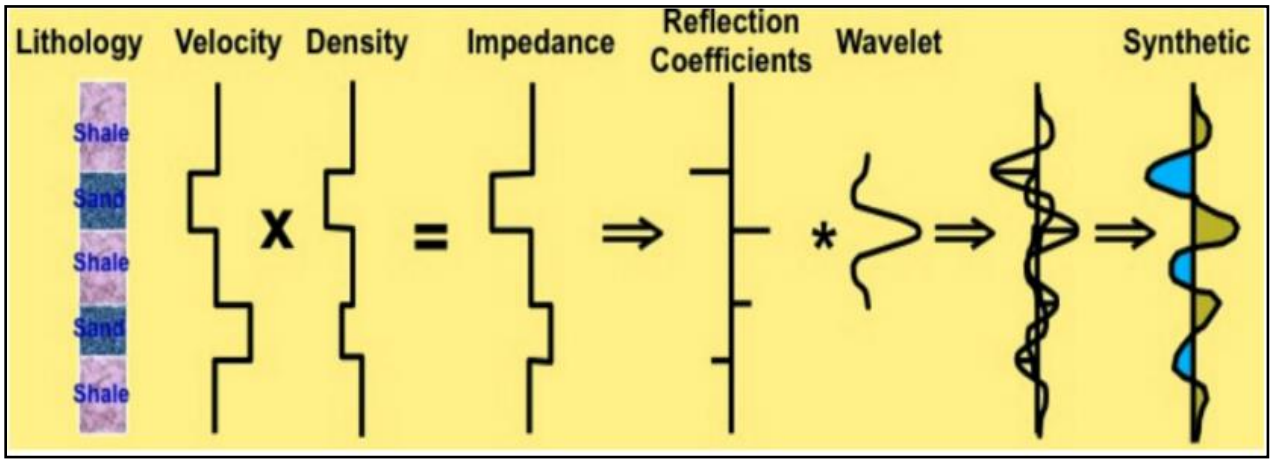

Figure 3.15: Schematic representation of the convolution to generate synthetic seismogram.

$$X(t) = s(t) * r(t) + N \qquad \text{Eq. 3.20}$$

A wavelet is considered a mathematical function, which separates the given function into several frequencies components. Moreover, the combination of density (ρ) and velocity (V_p) would result in the determination of the acoustic impedance (I_p) (Eq. 3.21) (Mondol, 2015a). The impedance contrast across an interface causes the wave reflection phenomena, which is known as the reflection coefficient (Z) (Eq. 3.22).

$$I_p = \rho \cdot V_p \qquad \text{Eq. 3.21}$$

$$Z = \frac{I_{p2} - I_{p1}}{I_{p2} + I_{p1}} \qquad \text{Eq. 3.22}$$

3.4.2 Angle Dependence Reflection Coefficient

When a pulse emitted by a source propagates between two layers with different velocities, an angle of incident will split the wave into reflected and refracted P-and-S waves (Fig. 3.16), following the angular relationship established in Snell's law (Chopra and Castagna, 2014; Mondol, 2015a).

$$\rho = \frac{\sin(\theta_1)}{V_1} = \frac{\sin(\theta_2)}{V_2} \qquad \text{Eq. 3.23}$$

Where θ_1 is the incident angle, θ_2 is the transmitted angle and V_1 and V_2 are the layer velocities (P- or S-wave velocity).

The partition of incident-wave-energy into the different components is a function of the angle of incidence and the physical properties of the media (e.g. density, bulk, and shear moduli) (Chopra and Castagna, 2014).

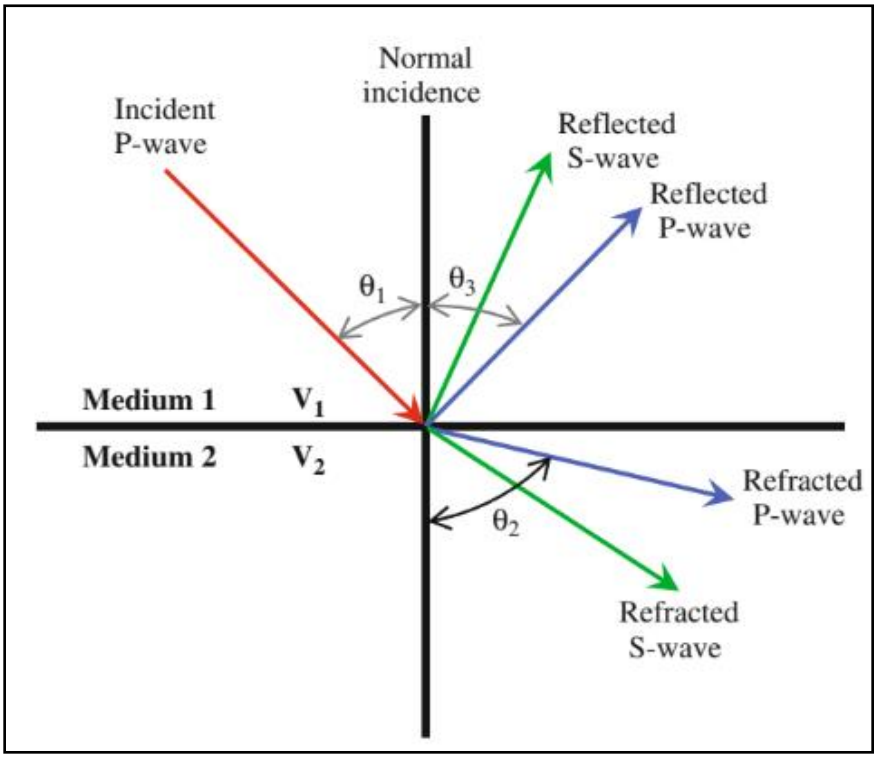

Figure. 3.16: Schematic representation of reflected and refracted waves created at a layer interface (Mondol, 2015a).

At zero-offset reflection, normal incidence, the reflection coefficient (Rp) is expressed in Equation 3.22 between two isotropic and homogeneous layers.

For an angle of incidence, the reflection and transmission coefficient varies as a function of the angle (θ), and of the three independent elastic parameters on each side of the interface. These coefficients are described in Zoeppritz equations. However, simplified versions of these complex equations have been introduced by Aki and Richard (1980) for the P-wave reflection ($R(\theta)_{pp}$)) (Gelius et al, 2017a).

$$R(\theta)_{pp} = \frac{1}{2}\left[\frac{\Delta V_p}{V_p} + \frac{\Delta \rho}{\rho}\right] - 2\left(\frac{V_p}{V_s}\right)^2 \left[2\frac{\Delta V_s}{V_s} + \frac{\Delta \rho}{\rho}\right] \sin(\theta)^2 + \frac{1}{2}\frac{\Delta V_p}{V_p}\tan(\theta)^2 \qquad \text{Eq. 3.24}$$

Where $\Delta V_p = V_{p2} - V_{p1}$, $\Delta \rho = \rho_2 - \rho_1$, $V_p = \frac{V_{p2}+V_{p1}}{2}$, $\rho = \frac{\rho_2+\rho_1}{2}$, and the same for the Vs equivalents.

Moreover, Wiggens or Gelfand's (1986) approximation is applied in for small angles assuming that $\frac{V_p}{V_s} = 2$, and $\mathrm{tg}(\theta) = \sin(\theta)$.

$$R(\theta)_{pp} = R_p - G\sin(\theta) \qquad \text{Eq. 3.25}$$

Where $G = R_p - 2R_s$, G is the gradient, and R_p and R_s are the zero-offset P- and S-wave reflection coefficients calculated as follows:

$$R_p = \frac{1}{2}\left[\frac{\Delta V_p}{V_p} + \frac{\Delta \rho}{\rho}\right] \qquad \text{Eq. 3.26}$$

$$R_s = \frac{1}{2}\left[\frac{\Delta V_s}{V_s} + \frac{\Delta \rho}{\rho}\right] \qquad \text{Eq. 3.27}$$

The amplitude values change described by the AVO gradient (G) are commonly plotted as a function of angles (offset), and are used to classified gas sand **(**Fig. 3.17) (Chopra and Castagna, 2014). Brine saturated sandstones and shale normally follow a background trend define by a fluid/ shale line known as Mudrock line (Gelius, 2017a). In case of deviation from the background trend, this response may be associated with hydrocarbon or lithologies with anomalous elastic properties.

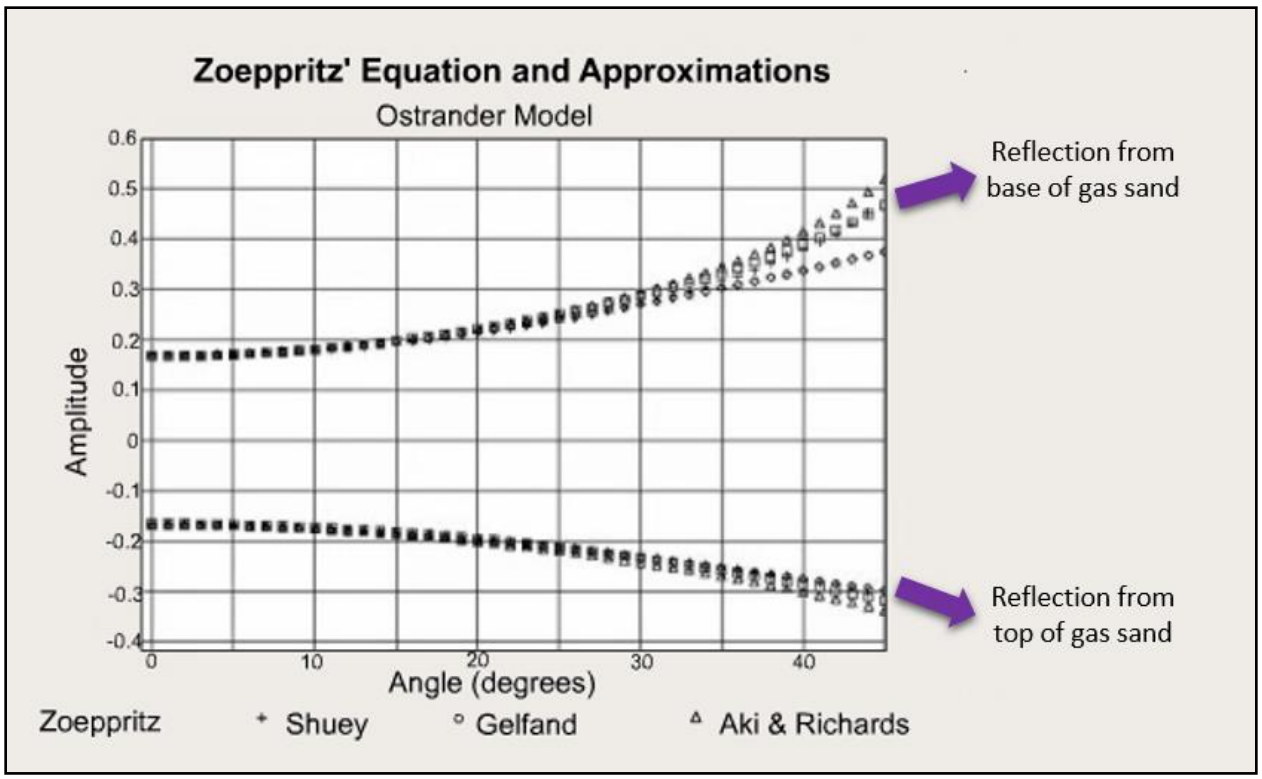

Figure 3.17: Comparison of Shuey, Gelfand, Aki and Richard approximations to original Zoeppritz equation (modified from Gelius, 2017b).

3.4.3 Gassmann Fluid Substitution

The Gassmann model is a method commonly applied to predict the effective elastic properties (bulk moduli) for a rock saturated with a given fluid. This model assumes a homogeneous, isotropic rock, which pores are connected and filled with one fluid (Adam et al., 2006; Gelius, 2017b).

$$K^* = K_d + \frac{\left(1-\frac{K_d}{K_s}\right)^2}{\frac{\varphi}{K_f}+\frac{1-\varphi}{K_s}-\frac{K_d}{{K_s}^2}} \qquad \text{Eq. 3.28}$$

Where K_f is bulk moduli of the pore fluid, K_d is bulk moduli of the frame or dry rock, and K_s is the bulk moduli of the solid material of the rock.

In fluid substitution, Gassmann equation helps to predict variations of seismic velocities in a rock, caused by changes in the pore fluids. Initially the effective bulk moduli of a rock (K_1^*) saturated with a fluid (K_{fl1}) are known. Later after the originally fluid is replaced by a new one (K_{fl2}), the new effective bulk moduli is estimated (K_2^*) by the following equation (Gelius, 2017b; Mavko et al., 1995):

$$\frac{K_1^*}{(K_s - K_1^*)} + \frac{K_{fl1}}{(K_s - K_{fl1})} = \frac{K_2^*}{(K_s - K_2^*)} + \frac{K_{fl2}}{(K_s - K_{fl2})} \quad \text{Eq. 3.29}$$

3.4.4 AVO classification

The modern use of the AVO allows the analysis and identification of gas sand. Based on the qualitative behavior of the PP reflection, from the top of the reservoir, versus the offset, four types of gas could be defined (Fig. 3.18) (Gelius, 2017a).

- Class I sands have higher acoustic impedance than the overlying shales. At zero-offset, the reflection coefficient is positive at the interface and tends to decrease with the offset. This sand is normally associated with onshore areas.

- Class II sands have positive (IIp) or negative intercept and negative gradient. The acoustic impedance is similar to the surrounding shale, indicating a moderate degree of compaction. A polarity change can occur if the reflectivity at zero-offset is positive.

- Class III are considered low impedance gas sand, associated with marine unconsolidated sand. The amplitude tends to increase with the offset.

- Class IV sands have a similar impedance that class III, but with a positive gradient and an amplitude decrease with the offset.

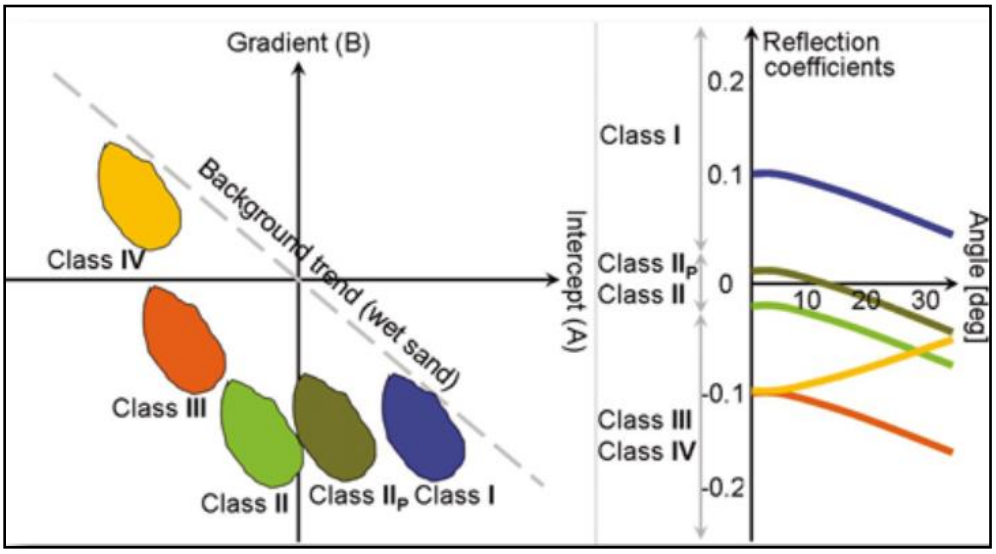

Figure 3.18: AVO gas sand classification (CGG Veritas, 2018).

Chapter 4: Petrophysical Analysis

4.1 Results

In this chapter results from the petrophysical analysis are presented with further discussion and uncertainties. Each formation that describes target reservoir is based on the drilling reports, and interpretation of gamma ray, neutron-density, velocity, and resistivity log responses.

A summary of the thickness and depth location of the target formations identified in six exploration wells is presented in Table 4.1.

Table 4.1: Depth and thickness of target reservoir units in the study area.

Well	Possible target formation	Top (m BSF)	Bottom (m BSF)	Gross Reservoir (m)
72207-1	STØ	1376	1452	76
	NORDMELA	1452	1618	166
72207-2	TUBÅEN	739	810	71
	FRUHOLMEN	810	1042	232
72207-3	STØ	1072	1150	78
	NORDMELA	1150	1334	184
7219/8-1	HEKKINGEN	3079	3935	856
	FUGLEN	3935	4128	193
	STØ	4128	-	-
7219/8-2	STØ	2523	2610	87
	NORDMELA	2610	2796	158
7219/9-1	STØ	1572	1683	111
	NORDMELA	1683	1827	144
	TUBÅEN	1827	1926	99

The Stø and Nordmela Formations are missing in well 7220/7-2 (Iskrystall). The thickness of potential reservoir units increases toward the southwestern. In overall, the Middle Jurassic Stø Formation has best reservoir properties, while reservoir quality deteriorates in the Nordmela Formation. The Tubåen and Fruholmen Formations are present in the majority of the studied wells, except for well 7219/8-1. In general, these two formations do not have good reservoir quality, however, hydrocarbon has been proven in both successions in well 7220/7-2 (Skavl) according to the report of the Norwegian Petroleum Directorate's (NPD).

By applying petrophysical analysis, the shale volume is estimated from the gamma ray and neutron-density log combination and constrained to the selected potential reservoir areas. Both

total (φ_{Total}) and effective (φ_{Ef}) porosities are estimated by using the neutron-density combination and the shale volume; while the water saturation is computed using Archie's equation assuming an apparent formation water resistivity value, which is obtained using the resistivity log information and considering a clean brine saturated sandstone zone.

Finally, the net gross fraction of net sand, the net pay, and the net reservoir values are estimated. The selected cutoff range for the porosity, shale volume and water saturation are displayed in Table 3.4 in chapter 3. However, the utilized values are Vsh <= 0.5, ϕ >= 0.06, and Sw <= 0.6 suggested by Kenedy (2015) for well comparison and to define good reservoir properties.

4.1.1 Stø Formation

The studied formation is present in five of the six given wells except in well 7220/7-2 (Skavl). Most of the wells have penetrated the entire formation with the exception of the well 7219/8-1 that does not reach the base. The formation thickness varies from northeast to southwest, becoming thicker towards the southwest (Fig. 4.1). Considering the information from the wells, the thickest section (110 m) is found in well 7219/9-1, while thickness varies in rest of the wells between 75 m and 96 m.

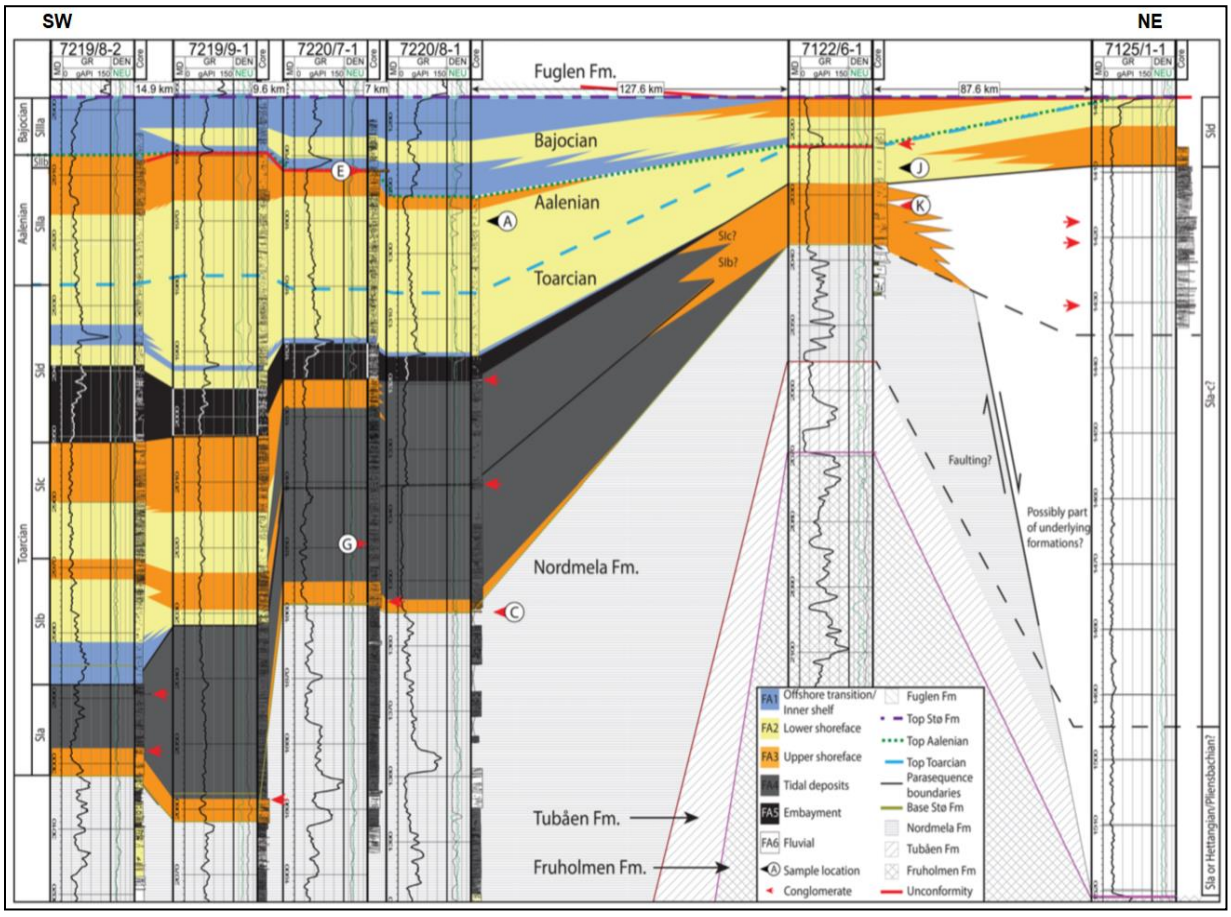

Figure 4.1: Spatial correlation of the Stø Formation, indicating the thickness variation along the area. (modified from Klausen et al., 2017)

As mentioned earlier, the Stø Formation has good reservoir properties. Overall, the average shale volume is 0.16 %, average porosity is 0.20%, and water saturation within the pay zone is 0.3%. The well 7220/7-3 (Drivis) has proven the best reservoir properties (Table 4.2) with a Vsh ≤ 0.16%, φ_{Ef}: 0.24%, Sw ≤ 0.06%, and a net pay of 74.55 m within the 78.05 m of gross interval (Fig. 4.2).

Table 4.2**:** Petrophysical analysis of the Stø Formation. Gross interval, Vsh – shale volume, φ_e – effective porosity, N/G – net over gross in the reservoir, Net. Reser.– net reservoir thickness, Sw – water saturation within the pay zone.

STØ FORMATION										
Well	**Reservoir Depth (m BSF)**	**Gross Interval (m)**	**GR min (API)**	**GR max (API)**	**Vsh (%)**	**φ_e (%)**	**N/G reser.**	**Net reser. (m)**	**Sw in pay (%)**	**Net pay (m)**
7220_7_1	1376	75.89	15	171.23	0.16	0.207	0.832	63.17	0.208	63.1
7220_7_3	1072	78.05	27.41	125.9	0.16	0.237	0.969	75.61	0.06	74.8
7219_8_1	4128	96.13	23	90	-	-	0	0	-	-
7219_8_2	2523	87.17	20.38	143.72	0.08	0.103	0.827	71.86	0.331	71.7
7219_9_1	1572	110	41.39	105.46	0.41	0.160	0.006	0.76	0.56	0.76

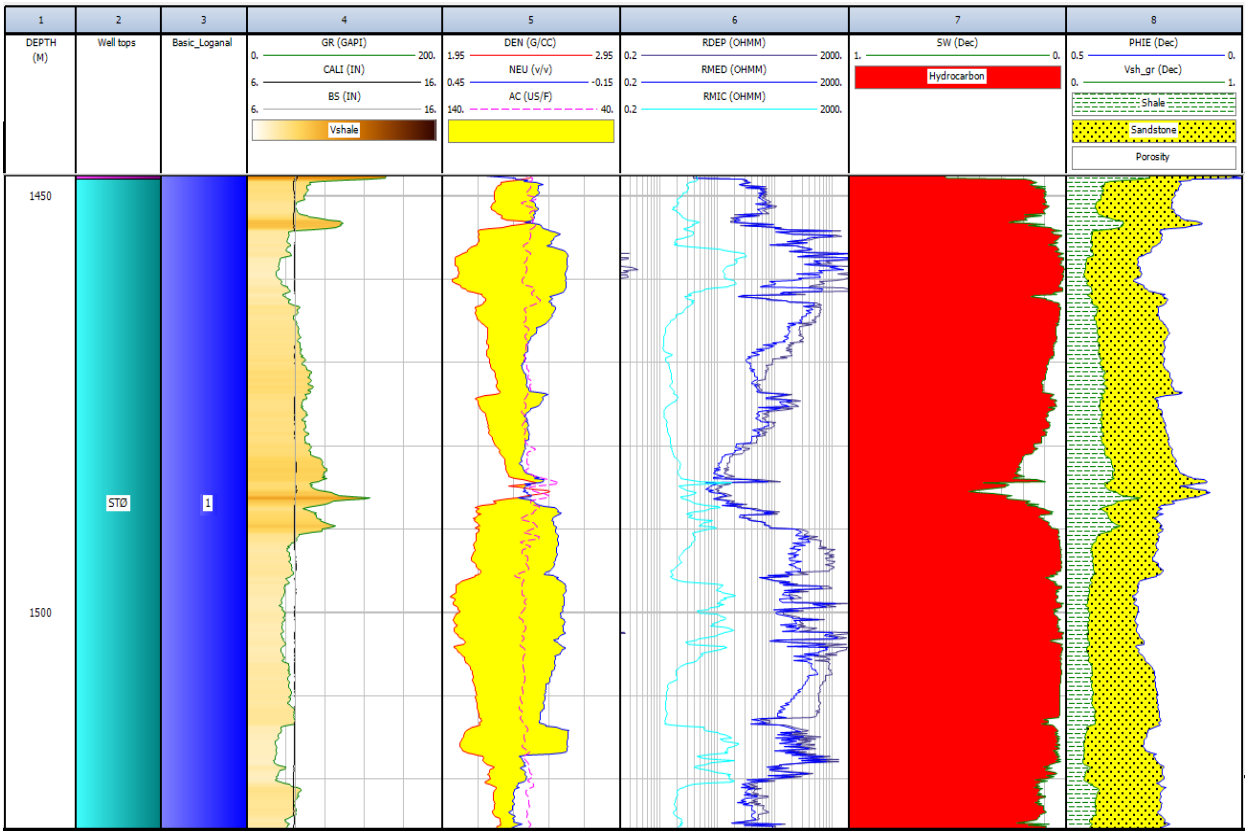

Figure 4.2: Composite log display of the Stø Formation of well 7220/7-3 (Drivis).

Nevertheless, Stø Formation in wells 7219/8-1 and 7219/9-1 have poor reservoir quality. According to NPD´s report, the formation in well 7219-8-1 the formation consists of tight water-bearing sandstones, with porosities of 5 to 8%; while the well 7219/9-1 has relative higher shale content of 43% to 50%. As a consequence, these wells are assumed dry due to the insignificant net pay thickness.

The Stø Formation exhibits several intervals with good reservoir qualities (Table 4.3). The presence of hydrocarbon has been proven in three of the five wells (NPD,2017b), with a maximum cumulative pay zone in the well 7220/7-3 (Drivis) of 74.85 m, followed by the well 7219/8-2 (Iskrystall) with two net pay zones, one located on the upper part of 33.6m and the lower of 33.07 m. In the well 7220/7-1 (Havis), the Stø Formation has also two potential intervals, being the upper one with less net pay due to a relative high shale volume of 21% and water saturation of 32%, while the lower interval has 34.14 m of net pay with better properties.

Table 4.3: Petrophysical analysis of the reservoir intervals of the Stø Formation. Gross interval – total thickness in meters, Vsh – shale volume; φe –effective porosity, N/G – net to gross fraction in the reservoir, Net. Reser.– net reservoir thickness, and Sw – water saturation within the pay zone.

STØ FORMATION								
Well	**Reservoir Depth (m BSF)**	**Gross Interval (m)**	**Vsh (%)**	**φ_e (%)**	**N/G reservoir**	**Net reser. (m)**	**Sw in pay (%)**	**Net pay (m)**
7220_7_1	1375 – 1413.49	31.85	0.219	0.189	0.832	26.59	0.325	26.59
	1413,49 – 1416,69	3.2	0.246	0.19	0.595	1.91	0.219	1.91
	1416,69 – 1451.89	35.2	0.106	0.222	0.97	34.14	0.126	34.14
7220_7_3	1072 – 1109,95	37.65	0.186	0.220	0.949	35.74	0.078	35.28
	1109,95 - 1150	40.40	0.151	0.253	0.987	39.87	0.056	39.57
7219_8_1	4128	96.13	-	-	0	0	-	-
7219_8_2	2523 – 2557.16	33.9	0.102	0.079	0.989	33.6	0.274	33.6
	2560,9 – 2575,16	14.17	0.118	0.072	0.328	4.65	0.531	4.65
	2575.16 – 2610.06	34.9	0.066	0.131	0.948	33.07	0.349	33.07
7219_9_1	1572	119.33	0.413	0.160	0.006	0.76	0.566	0.76

On the three other wells the neutron-density negative crossover caused by low porosity and density values, and high resistivity values on the deep resistivity log are indicative of gas bearing zones. Composite well log plots represent the reservoirs zones are shown in Figure 4.2, 4.3, and 4.4.

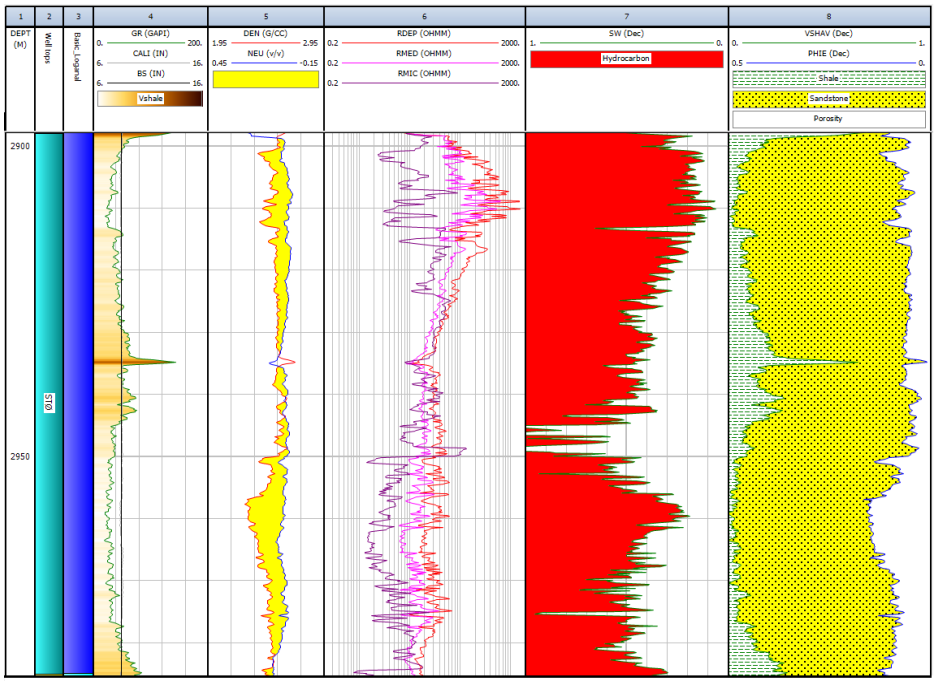

Figure 4.3: Composite log display of the Stø Formation of well 7219/8-2 (Iskrystall).

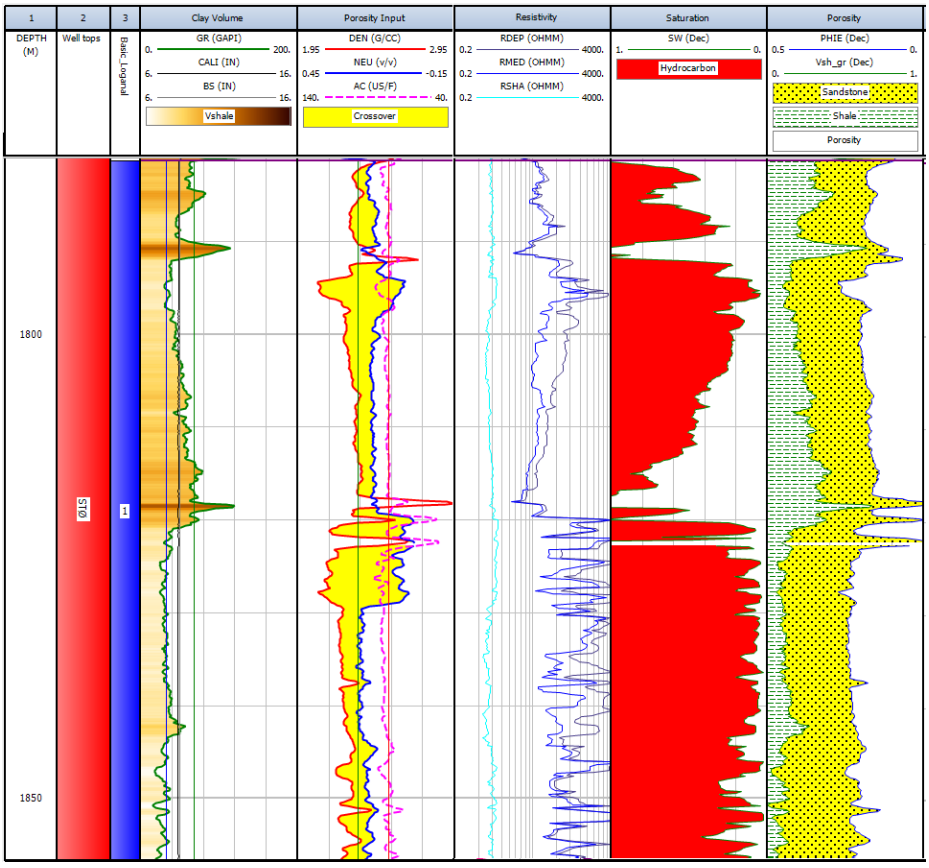

Figure 4.4: Composite log display of the Stø Formation of well 7220/7-1 (Havis).

4.1.2 Nordmela Formation

Results from the petrophysical analysis of the Nordmela Formation are summarized in Table 4.4. This formation is only present in four wells, taking into account that the well 7219/9-1 has not reached the base. Well 7220/7-3 (184.23 m) constitutes the maximum thickness among the four wells. Generally, the formation thickness increases towards southwest while it thins eastward.

Table 4.4: Petrophysical analysis of the Nordmela Formation. Gross interval – total thickness in meters; Vsh – shale volume, φ_e –effective porosity, N/G – net to gross fraction in the reservoir, Net. Reser.– net reservoir thickness, and Sw – water saturation within the pay zone.

NORDMELA FORMATION										
Well	**Reservoir Depth (m BSF)**	**Gross Interval (m)**	**GR min (API)**	**GR max (API)**	**Vsh (%)**	**φ_E (%)**	**N/G reser.**	**Net reser. (m)**	**Sw in pay (%)**	**Net pay (m)**
7220_7_1	1451	166.57	19	180.2	0.14	0.22	0.199	33.15	0.30	33.15
7220_7_3	1150	184.23	31.73	175.0	0.20	0.23	0.494	91.04	0.16	48.06
7219_8_2	2610	157.73	20.32	177.3	0.15	0.09	0.304	47.93	0.41	47.93
7219_9_1	1683	136.66	41.07	122.1	0.25	0.16	0	0	-	-

In addition of Figures 4.5 and 4.6 is indicated the location of the wells used for the petrophysical analysis of the Nordmela Formation and the spatial correlation.

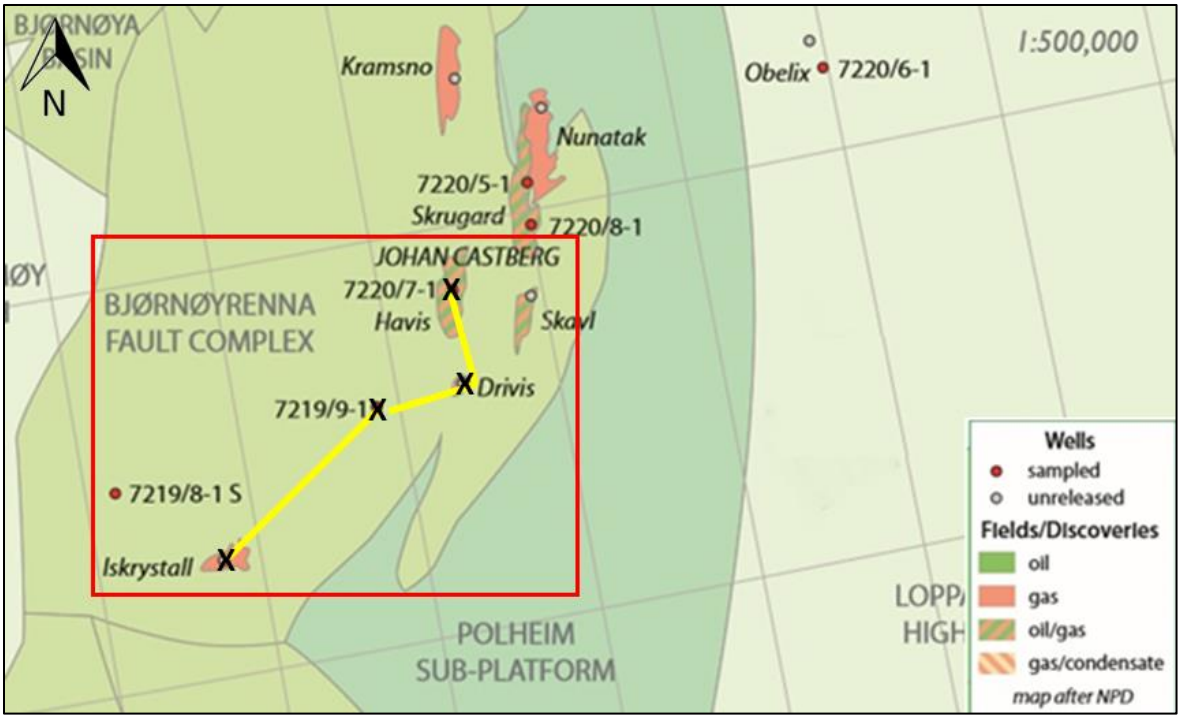

Figure 4.5: Location of the selected within the study area for the petrophysical analysis of Nordmela Formation (modified from APT, 2016).

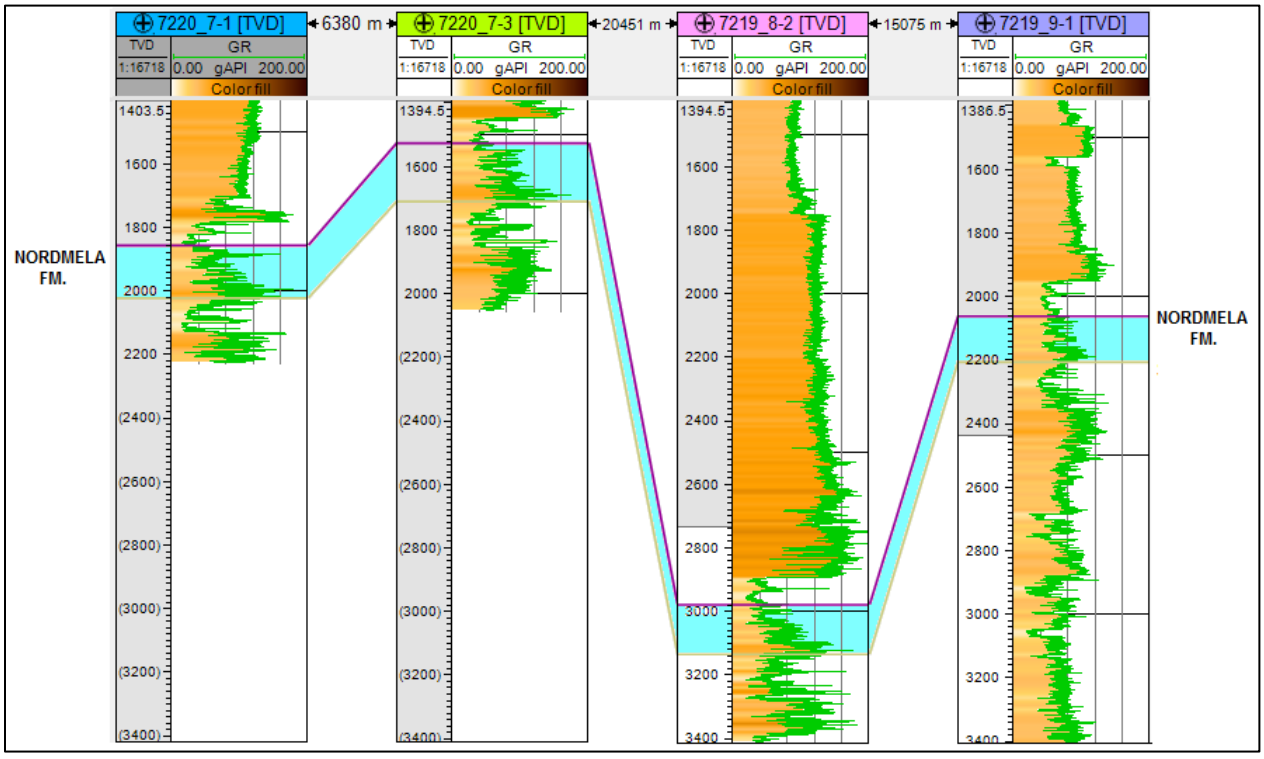

Figure 4.6: Spatial correlation of the Nordmela Formation, indicating the thickness variation along the wells where the formation is present.

Considering the entire formation, the reservoir quality deteriorates compare to Stø Formation due to the presence of mudstone interbedded with silty sandstones. The average effective porosity varies from 0.103 to 0.230%, and the shale volume values vary from 0.135 to 0.202%. Moreover, the water saturation within the pay zone ranges from 0.16 – 0.37%.

The well with the best quality reservoir properties is the 7220/7-3 (Drivis), exhibiting an Sw of 0.16%, φ_E of 0.230%, Vsh of 0.20%, and a net pay of 48.06 m within 184.23m of the gross interval. In contrast with the well 7220/8-2 (Skavl), the reservoir intervals are thin and have fair reservoir quality properties of Vsh= 0.15, φ_E = 0.09, and Sw of 0.41%.

A comparison of the Stø and Nordmela Formations shale volume is shown in Figure 4.7. In wells 7220/7-3 (Drivis) and 7219/8-2 (Iskrystall), the Nordmela Formation shows an increase of the shale content in comparison to the Stø Formation and an increase of the sand content in the upper section.

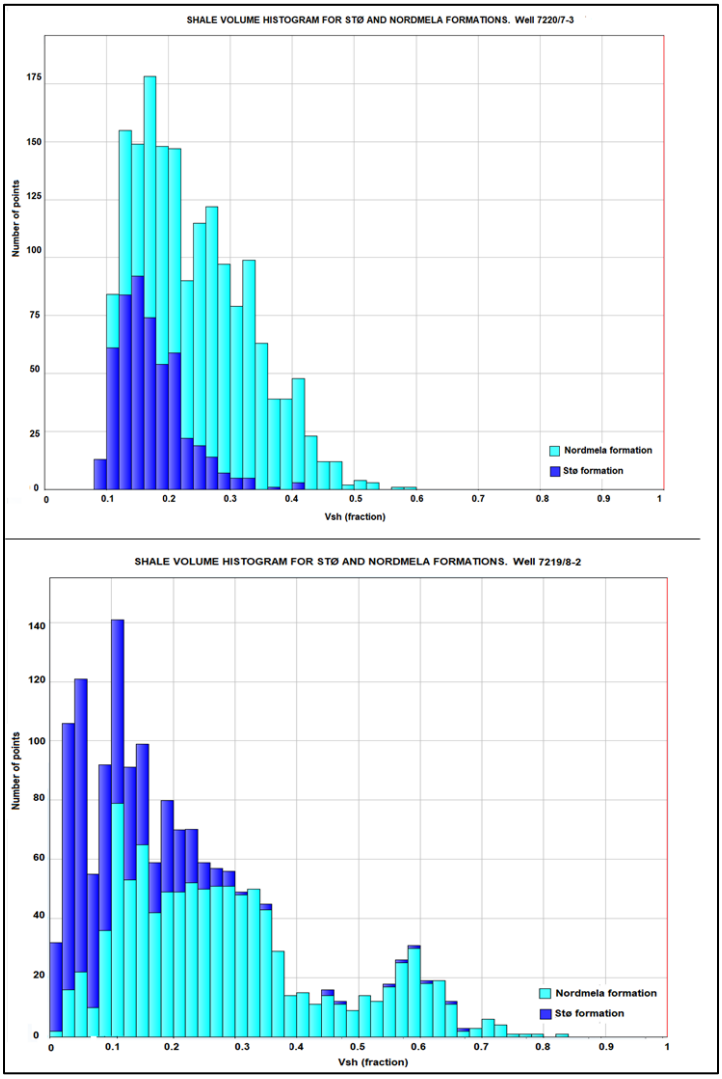

Figure 4.7: Comparison of the shale volume between the Stø and Nordmela Formations for wells 7220/7-3 (top) and 7219/8-2 (bottom).

Gas bearing intervals have been proven in the well 7220/7-1 (Havis), well 7220/7-3 (Drivis), and well 7219/8-2 (Iskrystall). Weak hydrocarbon shows are found in well 7219/9-1. The maximum pay zones are located in the upper unit of 21.09m to 27.13m, and the minor pay zone in well 7220/7-1 of 33.15 m (Table 4.5).

Table 4.5: Petrophysical analysis of the reservoir intervals of the Nordmela formation. Gross interval – total thickness in meters; Vsh – shale volume, φ_e –effective porosity, N/G – net to gross fraction in the reservoir, Net. Reser.– net reservoir thickness, and Sw – water saturation within the pay zone.

NORDMELA FORMATION								
Well	**Reservoir Depth Interval (m BSF)**	**Gross Interval (m)**	**Vsh (%)**	**φ_E (%)**	**N/G reservoir**	**Net reser. (m)**	**Sw in pay (%)**	**Net pay (m)**
7220_7_1	1451 – 1471.65	19.66	0.123	0.214	0.554	10.9	0.38	10.9
	1482.52 – 1618.21	135.48	0.151	0.236	0.164	22.25	0.276	22.25
7220_7_3	1150 – 1171.32	21.32	0.147	0.245	1	21.32	0.117	21.09
	1185.34 – 1334.23	148.89	0.219	0.226	0.468	69.95	0.191	27.13
7219_8_2	2610 – 2627.13	17.07	0.123	0.99	0.513	8.76	0.456	8.76
	2627.13 – 2632.95	5.79	0.219	0.89	0.671	3.89	0.508	3.89
	2665.51 – 2647.4	11.89	0.143	0.099	0.821	9.75	0.415	9.75
	2647.4 – 2655.93	8.53	0.131	0.089	0.911	7.77	0.453	7.77
	2655.93 – 2680.16	24.23	0.112	0.1	0.252	6.1	0.364	6.1
	2680.16 – 2767.79	87.63	0.202	0.09	0.132	11.58	0.356	11.58
7219_9_1	1683	136.66	0.25	0.16	0	0	-	-

Composite well logs are shown in Figures 4.8, 4.9 and 4.10. High resistivity readings and negative crossover of neutron – density logs are observed in the upper part of the formation.

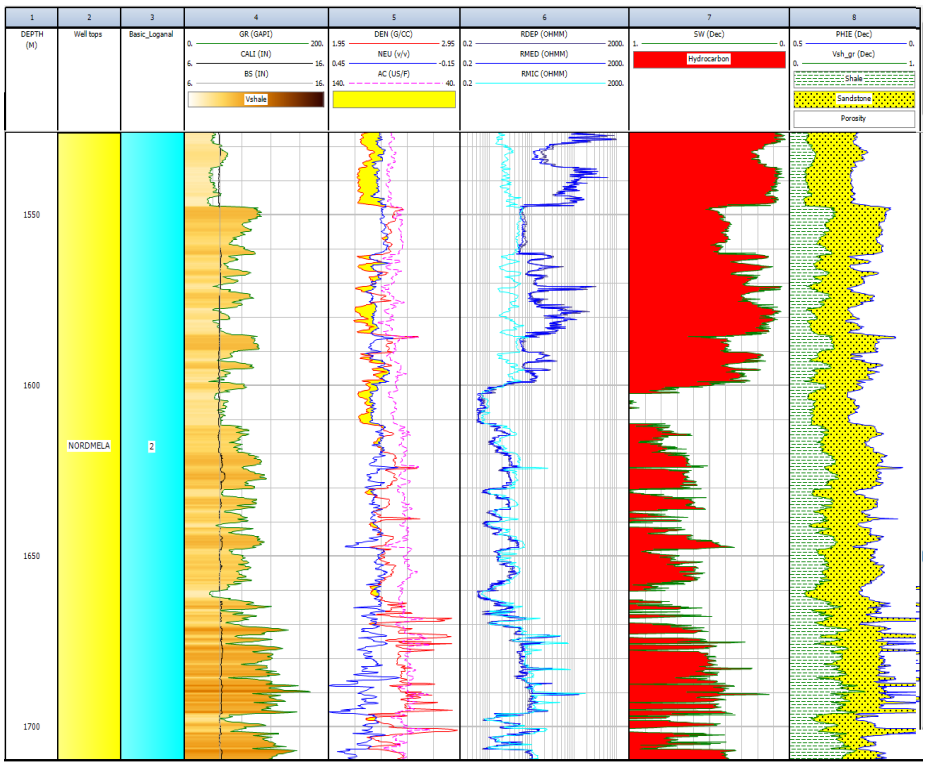

Figure 4.8: Composite logs display of the Nordmela Formation of the well 7220/7-3 (Drivis)

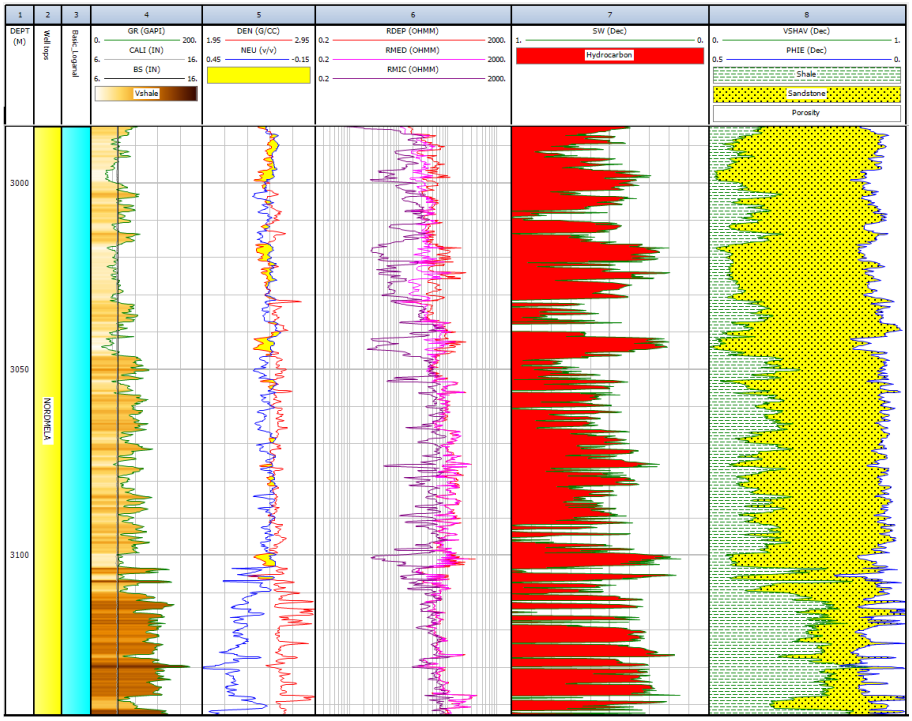

Figure 4.9: Composite logs display of the Nordmela Formation of the well 7219/8-2 (Iskrystall)

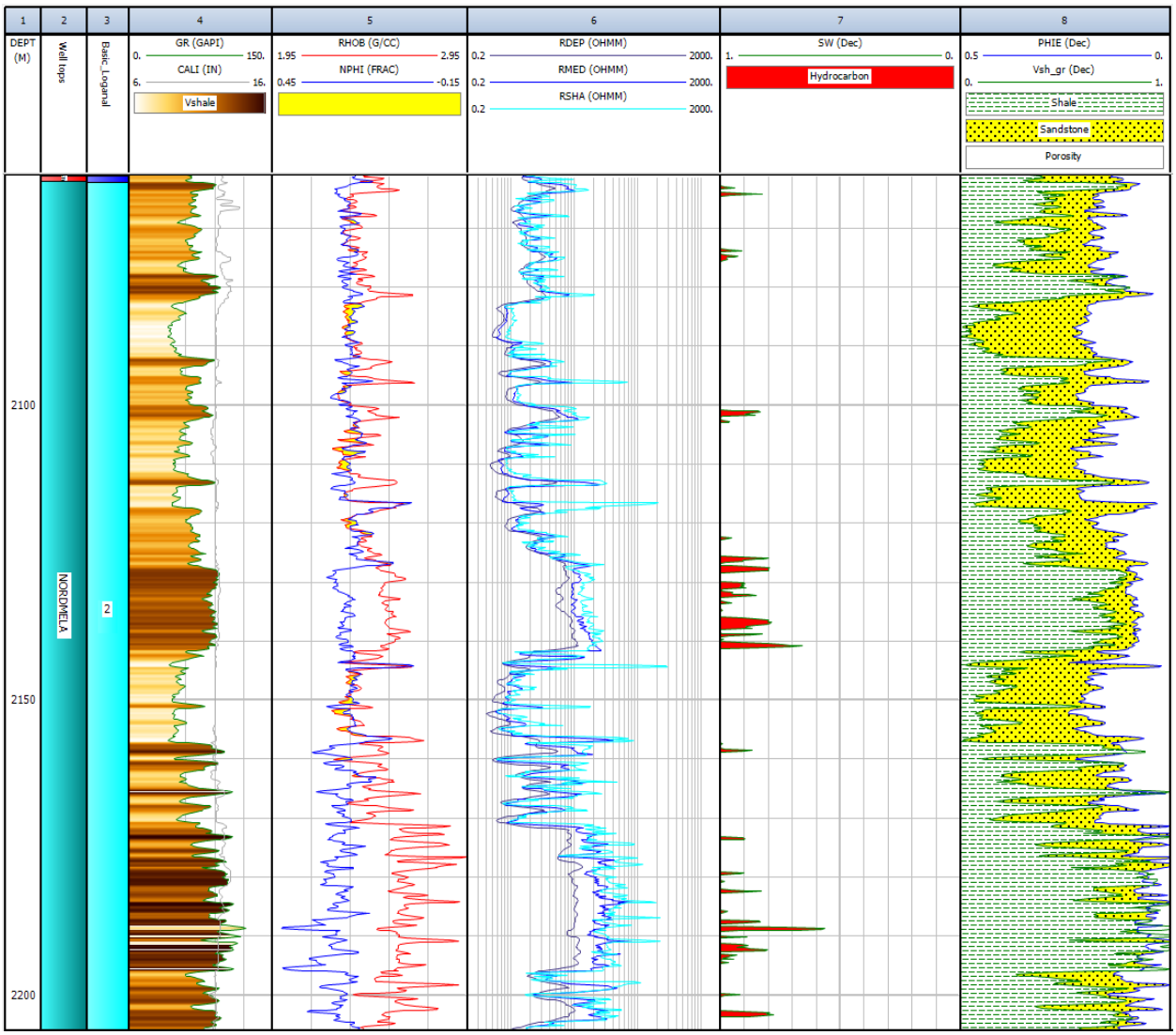

Figure 4.10: Composite log of the Nordmela formation of the well 7219/9-1.

4.1.3 Tubåen Formation

The Tubåen Formation is present in two of the six studied wells. The estimated shale volume in the formation is 0.16% in well 7220/7-2 (Skavl) and 0.21% in well 7219/9-1. Overall, the formation thickness increase towards the southwest (Fig. 4.11), reaching the maximum thickness of 97 m in well 7219/9-1 (NPD, 2017b).

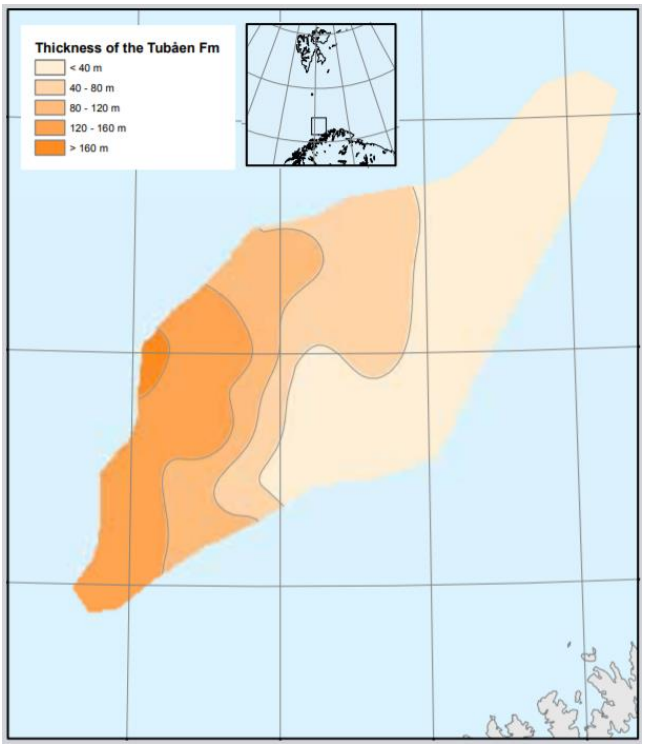

Figure 4.11: Thickness map of the Tubåen Formation (Halland et. al, 2014)

Results of the petrophysical analysis of Tubåen Formation are presented in Table 4.6 with the well locations and spatial distribution in Figures 4.12 and 4.13. The Tubåen Formation has good reservoir properties compared to the Stø Formation. The shale volume is estimated to be around 0.16 to 0.21%, the average effective porosity between 0.17 and 0.22%, and the water saturation is 0.15%, as a consequence, the resulting net-to-gross ratio is high 0.98.

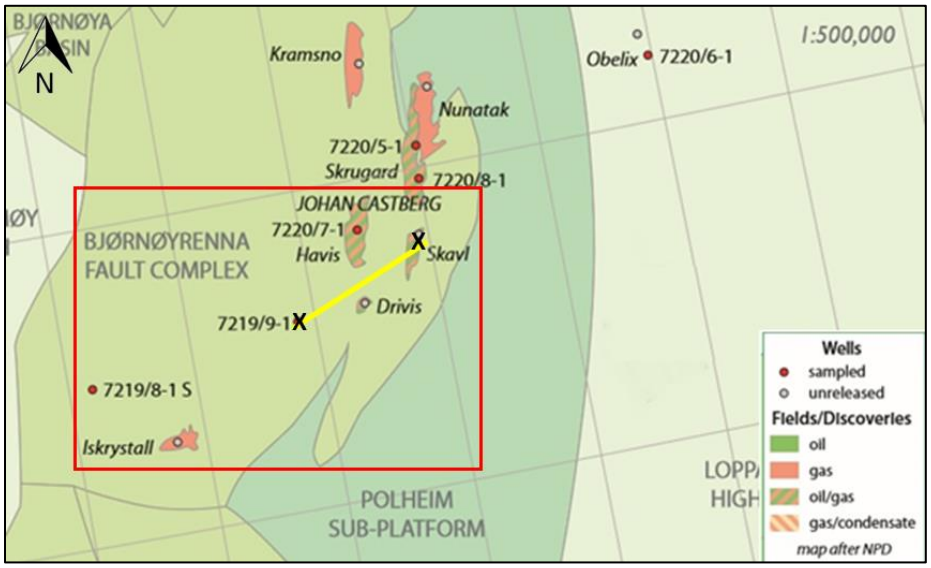

Figure 4.12: Location of the selected within the study area for the petrophysical analysis of Tubåen Formation (modified from APT, 2016).

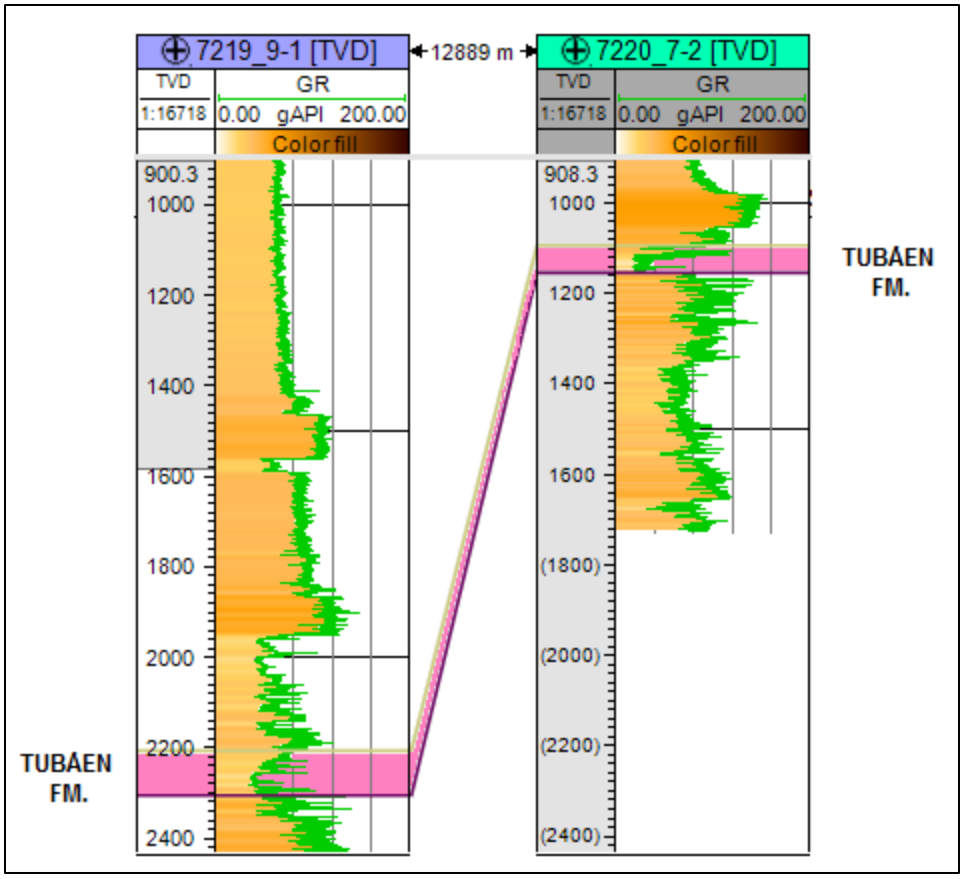

Figure 4.13: Spatial correlation of the Tubåen Formation, indicating the thickness variation along the wells where the formation is present.

Table 4.6: Petrophysical analysis of the Tubåen Formation. Gross interval – total thickness in meters; Vsh – shale volume, φ_e –effective porosity, N/G – net to gross fraction in the reservoir, Net. Reser.– net reservoir thickness, and Sw – water saturation within the pay zone.

TUBÅEN FORMATION										
Well	**Reservoir Depth (m BSF)**	**Gross Interval (m)**	**GR min (API)**	**GR max (API)**	**Vsh (%)**	**φ_E (%)**	**N/G reser.**	**Net reser (m)**	**Sw in pay (%)**	**Net pay (m)**
7220_7_2	739	71.63	19.27	121.36	0.16	0.28	0.987	70.71	0.15	35.5
7219_9_1	1826	97.42	35.22	103.49	0.21	0.17	0	0	-	-

The presence of hydrocarbon has been proven on the well 7220/7-2 (Skavl). The maximum pay zone (28.04 m) is located in the upper part of the formation within the 71.63 m of the gross interval. However, in the well 7219/9-1, the net pay is minimum, this might because of the high-water saturation and the presence of residual oil (NPD, 2017b) (Table 4.7).

Table 4.7: Petrophysical analysis of the Tubåen Formation. Gross interval – total thickness in meters; Vsh – shale volume, φ_e –effective porosity, N/G – net to gross fraction in the reservoir, Net. Reser.– net reservoir thickness, and Sw – water saturation within the pay zone.

TUBÅEN FORMATION								
Well	**Reservoir Depth (m BSF)**	**Gross Interval (m)**	**Vsh (%)**	**φ_E (%)**	**N/G reservoir**	**Net reservoir (m)**	**Sw in pay (%)**	**Net pay (m)**
7220_7_2	739 – 758.43	19.66	0.225	0.252	0.992	19.51	0.141	7.01
	795.06 – 809.9	45.57	0.112	0.310	1	45.57	0.155	28.04
7219_9_1	1826	97.42	0.21	0.17	0	0	-	-

Composite logs display of the formation are shown in Figures 4.14 and 4.15. In the well 7220/7-2 (Skavl), high resistivity values with a simultaneous negative crossover of the neutron-density log suggest the presence of hydrocarbon. Nevertheless, in the well 7219/9-1 the resistivity log display low resistivity values and in overall a positive crossover of the neutron-density log associated with the high shale content.

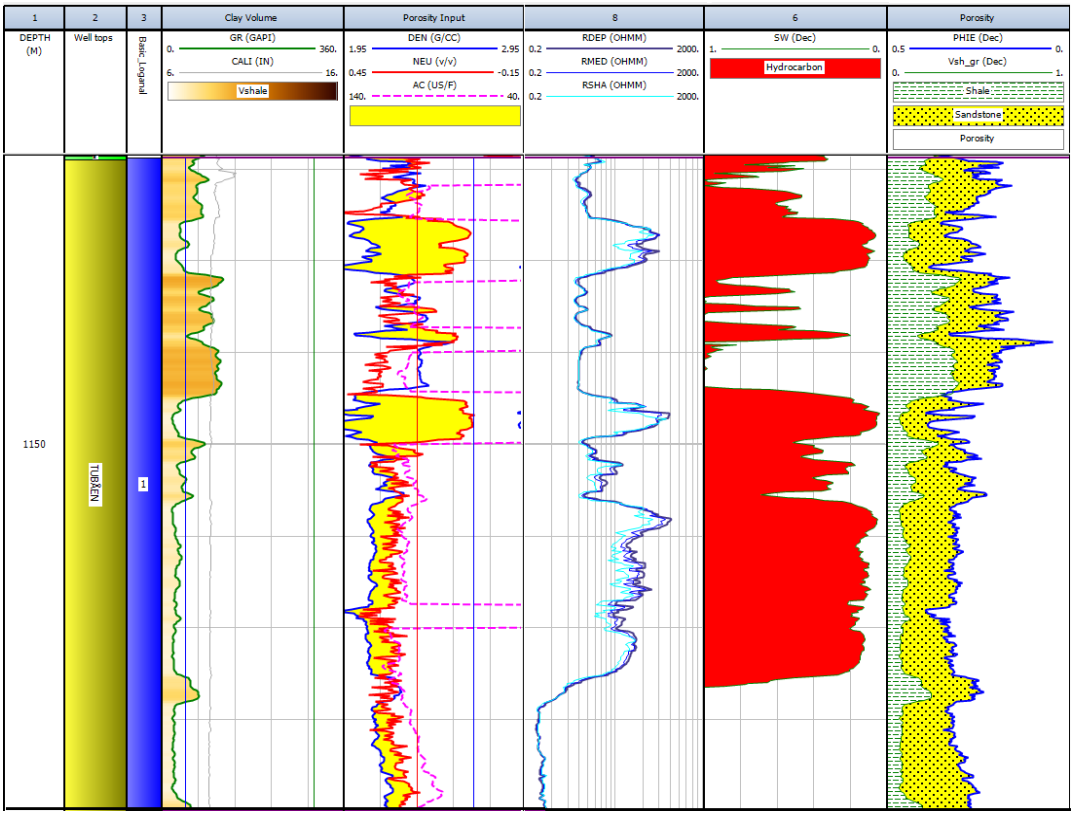

Figure 4.14: Composite logs display of the Tubåen formation of well 7220/7-2 (Skavl).

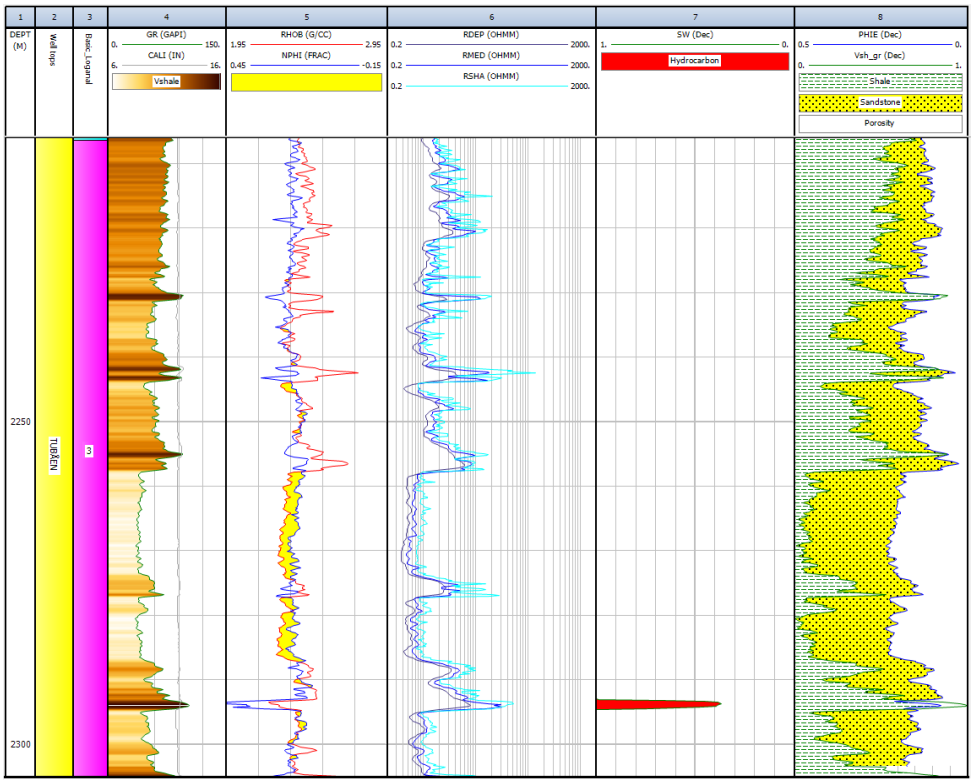

Figure 4.15: Composite logs display of the Tubåen formation of well 7219/9-1.

4.1.4 Fruholmen Formation

The Fruholmen Formation is only present in one (7220/7-2) of the six wells. The reservoir quality is poor compared to Tubåen Formation. A comparison of the shale volume between two formations is shown in Figure 4.16. Shale volume range from 0.14 to 0.5% with an average of 0.298%. The results of the petrophysical analysis are summarized in Table 4.8, the average porosity is 0.28%, water saturation is 0.293%, and a minimum net pay zone is 16m.

The presence of hydrocarbon has been proven in the Krabbe member. In the composite log display this is confirmed by the resistivity log (Fig. 4.17), and the negative crossover of the neutron-density logs.

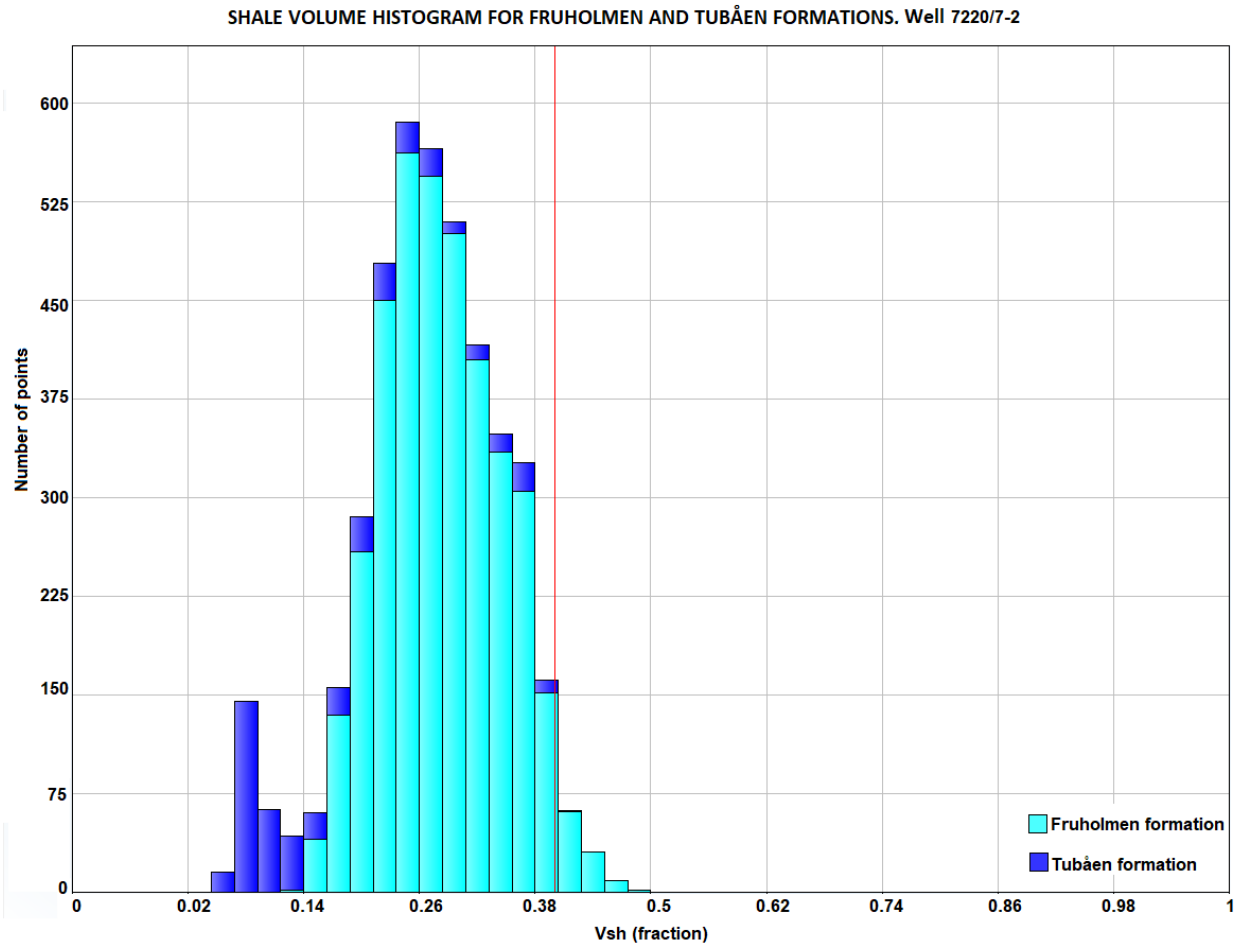

Figure 4.16: Shale volume histogram of the well 7220/7-2 (Skavl).

Table 4.8: Results of petrophysical analysis of the Fruholmen Formation. Gross interval – total thickness in meters, Vsh – shale volume, φ_e –effective porosity, N/G – net to gross fraction in the reservoir, Net. Reser.– net reservoir thickness, and Sw – water saturation within the pay zone.

FRUHOLMEN FORMATION										
Well	**Reservoir Depth (m BSF)**	**Gross Interval (m)**	**GR min (API)**	**GR max (API)**	**Vsh (%)**	**φ_E (%)**	**N/G reser.**	**Net reser (m)**	**Sw in pay (%)**	**Net pay (m)**
7220_7_2	810 – 948,38	107.75	45.96	146.44	0.293	0.222	0.675	72.69	0.294	5.33
	948,38 – 961.79	13.41			0.266	0.253	0.915	12.27	0.274	7.62
	961.79 - 1042	110.90			0.308	0.224	0.771	85.53	0.345	3.05

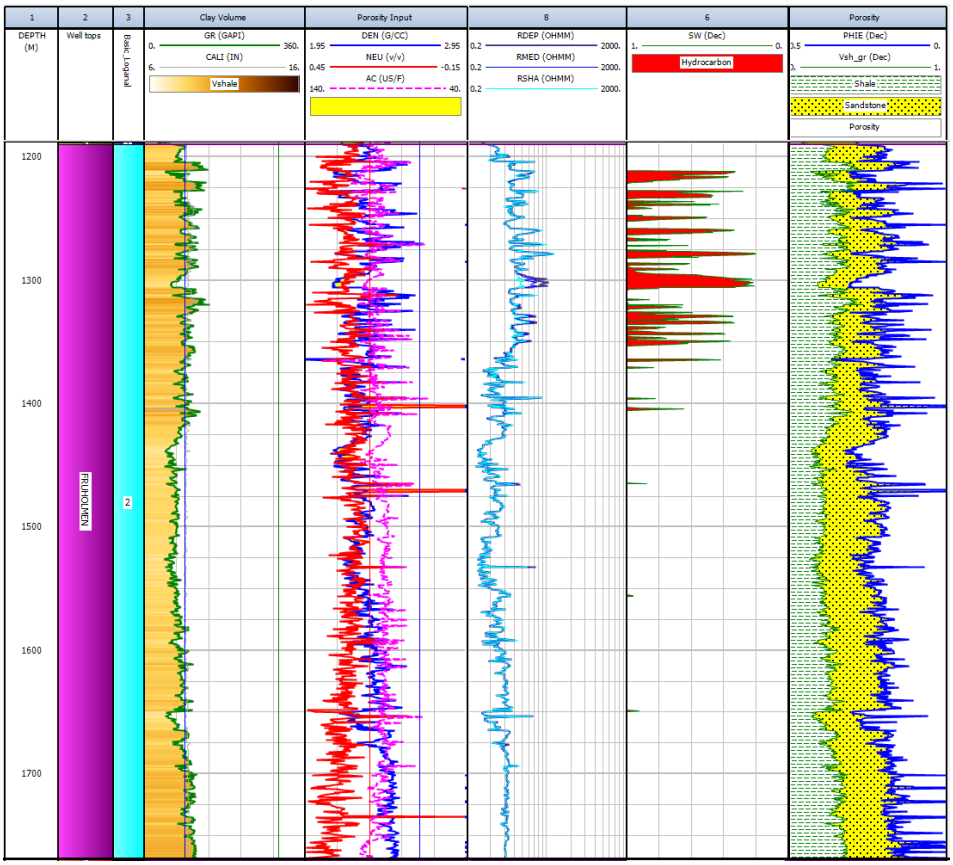

Figure 4.17: Composite log display of the Tubåen Formation of well 7220/7-2 (Skavl).

4.1.5 Hekkingen Formation

Petrophysical analysis results for the Hekkingen Formation are shown in Table 4.9. Considering the entire formation, the reservoir properties are fair, the average porosity is 0.1%, shale volume is 0.47 %, and water saturation is 0.52%. Due to high shaliness, the net-to-gross and the net pay are very low (1m). Therefore, the formation is no longer considered a potential target.

Table 4.9: Petrophysical analysis of the Hekkingen Formation. Gross interval – total thickness in meters; Vsh – shale volume, φ_e –effective porosity, N/G – net to gross fraction in the reservoir, Net. Reser.– net reservoir thickness, and Sw – water saturation within the pay zone.

HEKKINGEN FORMATION										
Well	**Reservoir Depth (mRKB)**	**Gross Interval (m)**	**GR min (API)**	**GR max (API)**	**Vsh (%)**	**φ_E (%)**	**N/G reser.**	**Net reser. (m)**	**Sw in pay (%)**	**Net pay (m)**
7219_8_1	3079	857.38	37	192	0.475	0.138	0.001	1	0.520	1

Furthermore, the composite log display of the formation is shown in Figure 4.18. The positive crossover of the neutron-density and the simultaneous low readings of the resistivity log suggest no hydrocarbon in the formation and high shale content.

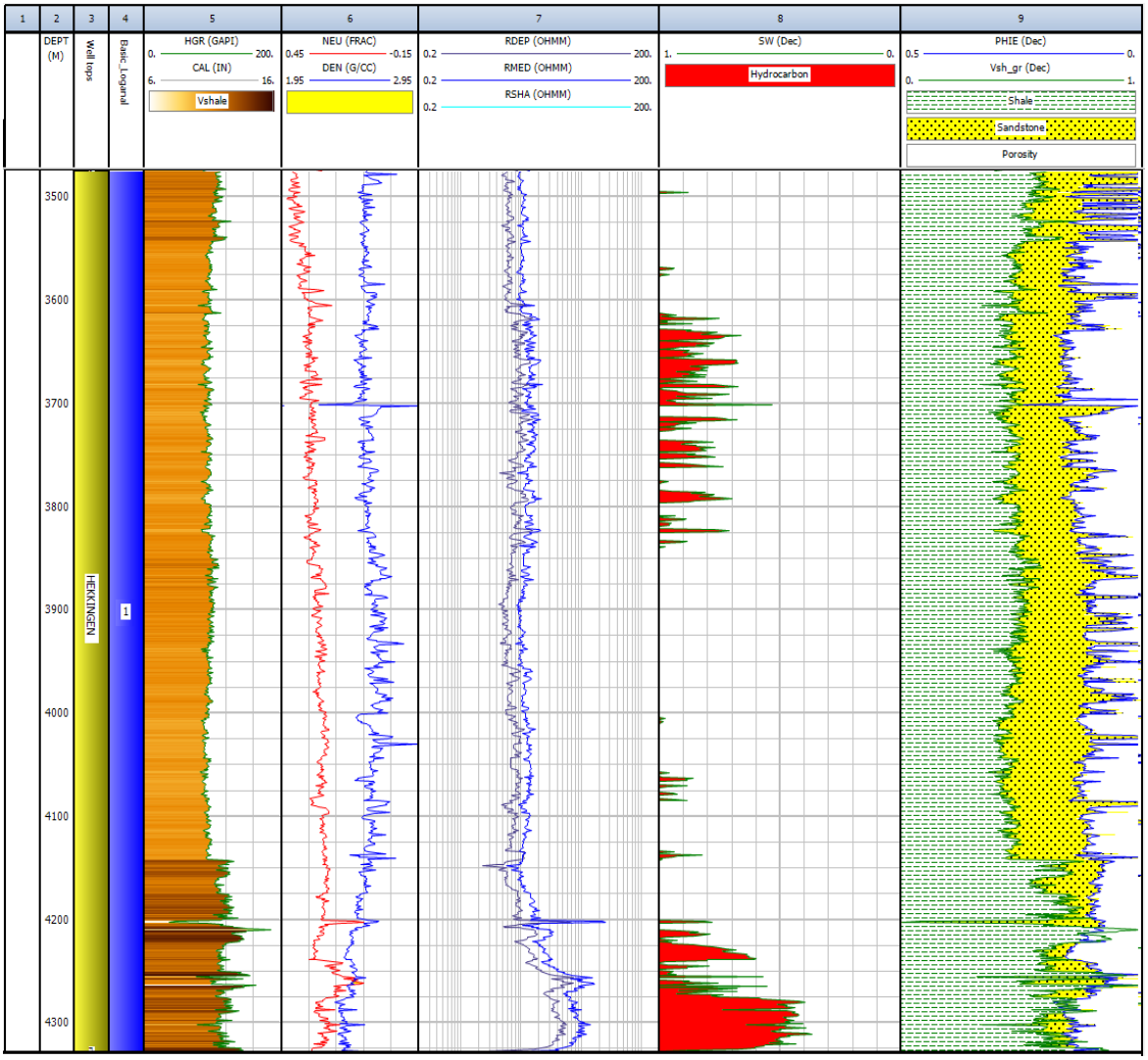

Figure 4.18: Composite log display of the Hekkingen Formation of well 7220/8-2 (Iskrystall).

4.1.6 The Fuglen formation

The Fuglen Formation petrophysical analysis results are shown in Table 4.10. The entire formation has poor reservoir quality, even though it is considered for a possible prospect in well 7219/8-1. The average shale volume is 0.54%, and average effective porosity is 0.14%. Composite well log of the formation is displayed in Figure 4.19, high reading of the gamma ray, positive crossover of the neutron-density, and simultaneous low resistivity readings confirmed high shale content and absence of hydrocarbons.

Table 4.10: Petrophysical analysis of the Fuglen Formation. Gross interval – total thickness in meters; Vsh – shale volume, φe –effective porosity, N/G – net to gross fraction in the reservoir, Net. Reser.– net reservoir thickness, and Sw – water saturation within the pay zone.

FUGLEN FORMATION										
Well	**Reservoir Depth (mRKB)**	**Gross Interval (m)**	**GR min (API)**	**GR max (API)**	**Vsh (%)**	**φ_E (%)**	**N/G reser.**	**Net reser. (m)**	**Sw in pay (%)**	**Net pay (m)**
7219_8_1	3935	193.13	63	156	0.54	0.14	0	0	-	-

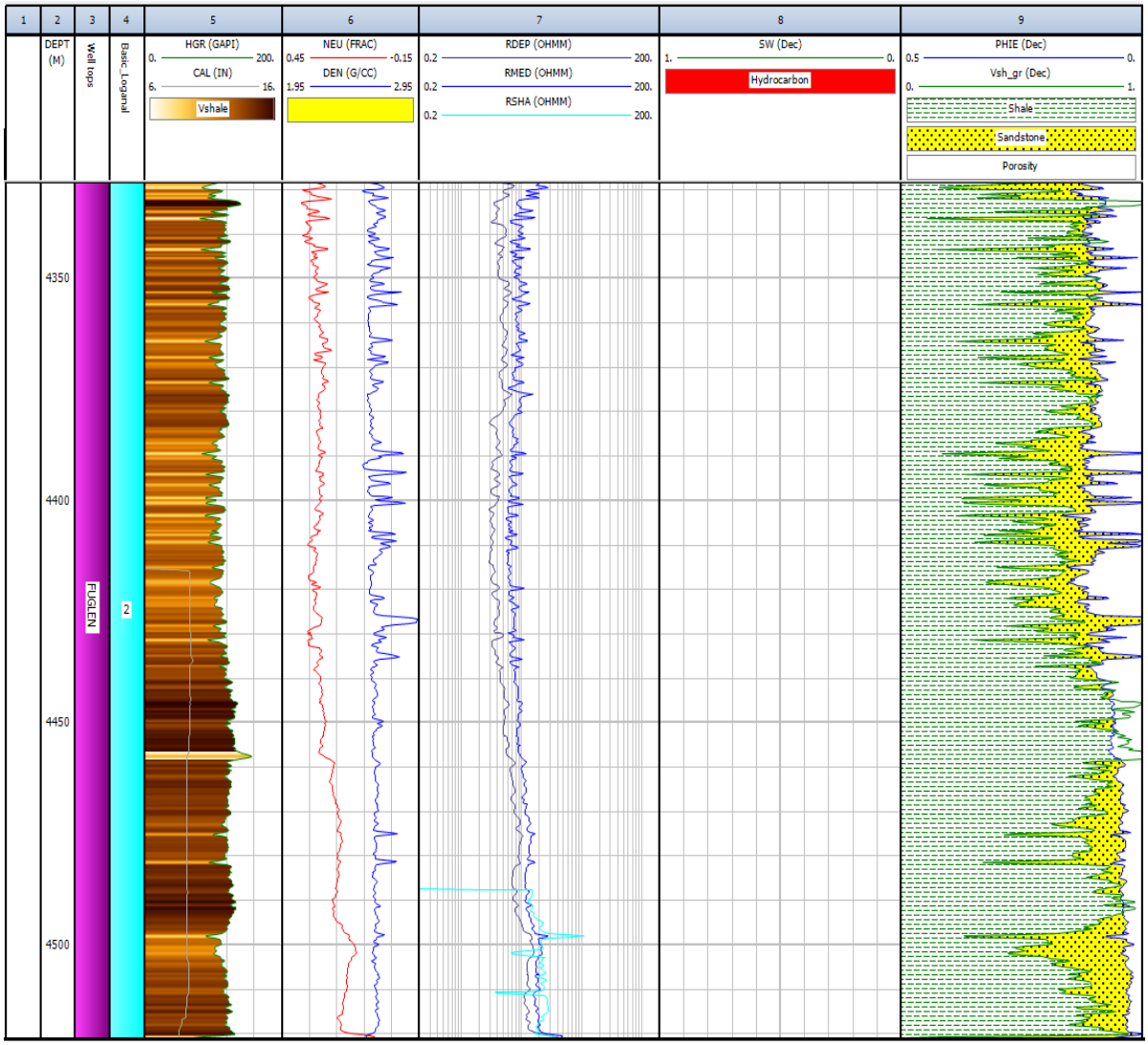

Figure 4.19: Composite log display of the Fuglen Formation of well 7220/7-2 (Skavl).

4.1.7 Analysis and Interpretation of Spectral Gamma Ray (SGR)

Results from the analysis of the spectral gamma ray based on the thorium/potassium ratio for the Stø formation are shown in figure 4.20 and 4.21 for from well 7220/7-1 (Havis), 72207/-3 (Drivis) and 7219/8-2 (Iskrystall). Overall, as it is displayed on the histogram, the dominant clays in the studied formation are smectite and illite (Fig. 4.22). In case of well 7220/7-1(Havis), the cluster points suggest that the 20% of the estimated shale is composed by 37% smectite, 35% illite, 26% mica and 2% kaolinite. Furthermore, the shale content on well 7220/7-3 (Drivis) mainly consists of 66% smectite with an even distribution of 17% for illite and kaolinite. For the same formation in well 7219/8-2 (Iskrystall), illite is dominant clay of 54 %, followed by mica 40% and smectite 6%.

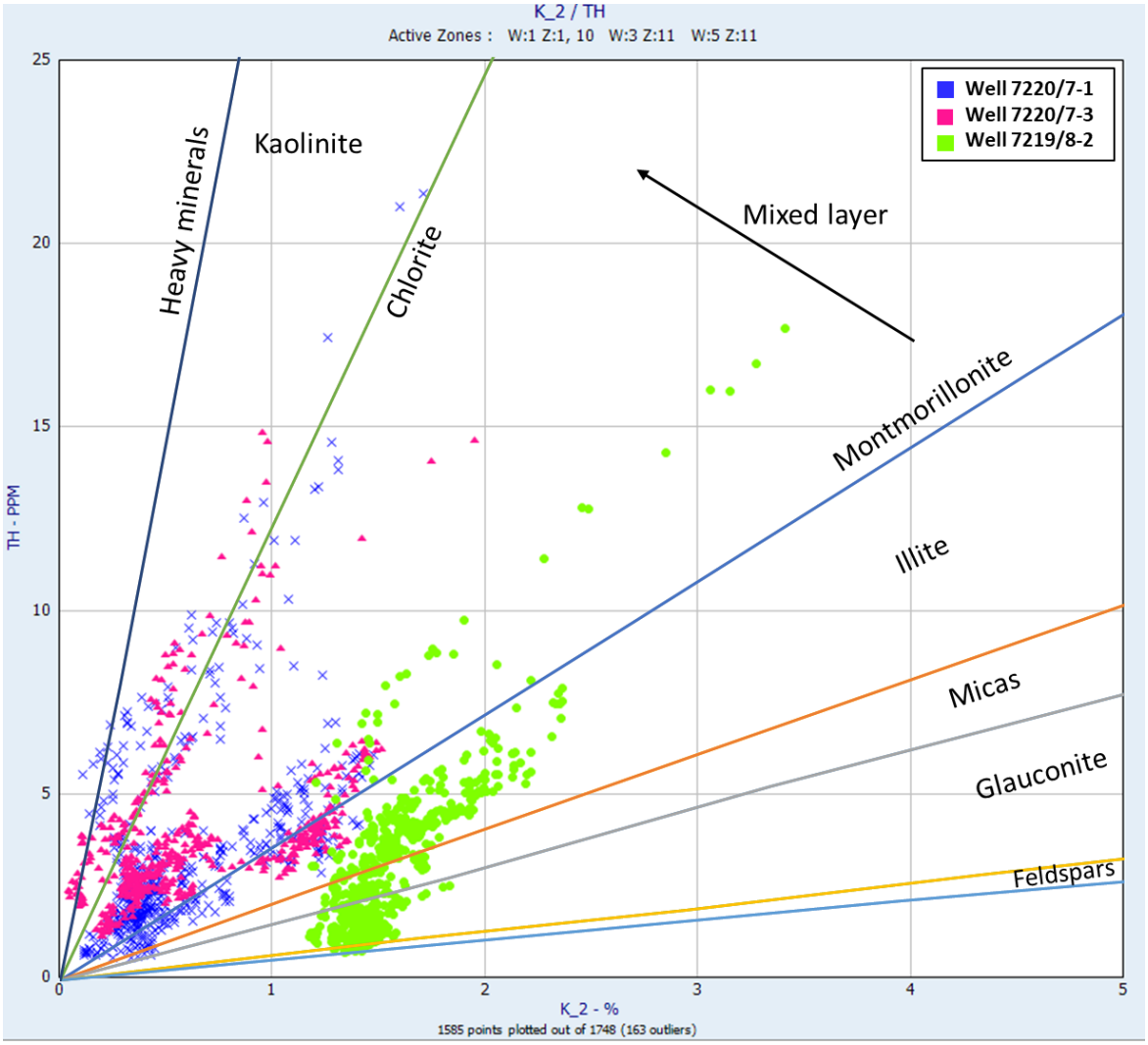

Figure 4.20: Determination of the clay mineral types based on the Th/K ratio for Stø Formation based on the information from well 7220/7-1 (Havis), 7220/7-3 (Drivis) and 7219/8-2 (Iskrystall). The data is color-coded according to the respective well, 7220/7-1 (blue), 7220/7-3 (fucsia), and 7219/8-2 (green).

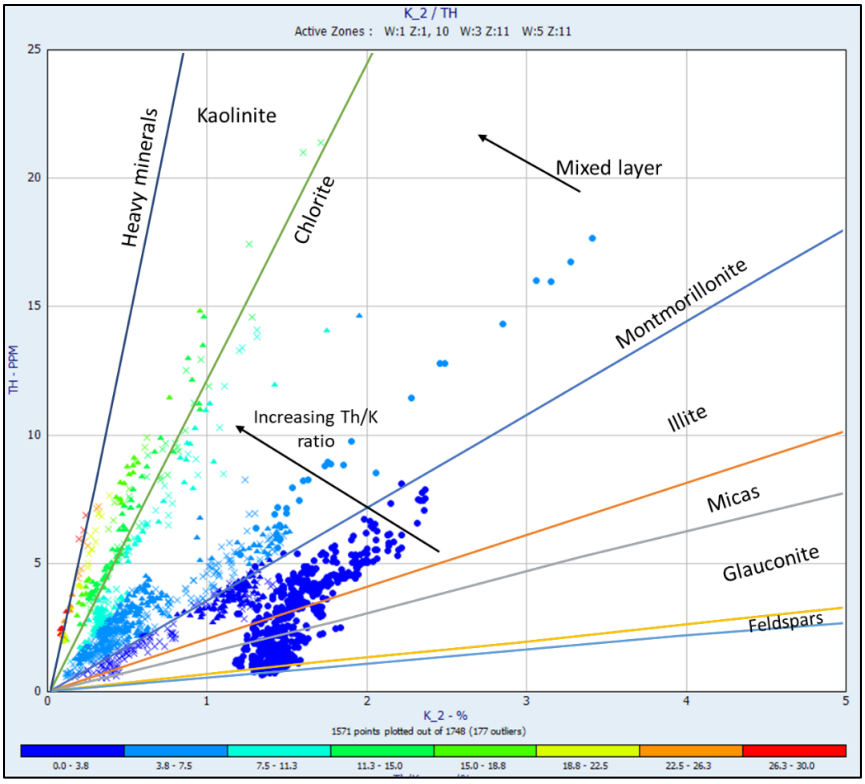

Figure 4.21**:** Determination of the clay mineral types based on the Th/K ratio for Stø Formation of wells 7220/7-1, 7220/7-3 and 7219/8-2, the data is color-coded based on the Th/K ratio.

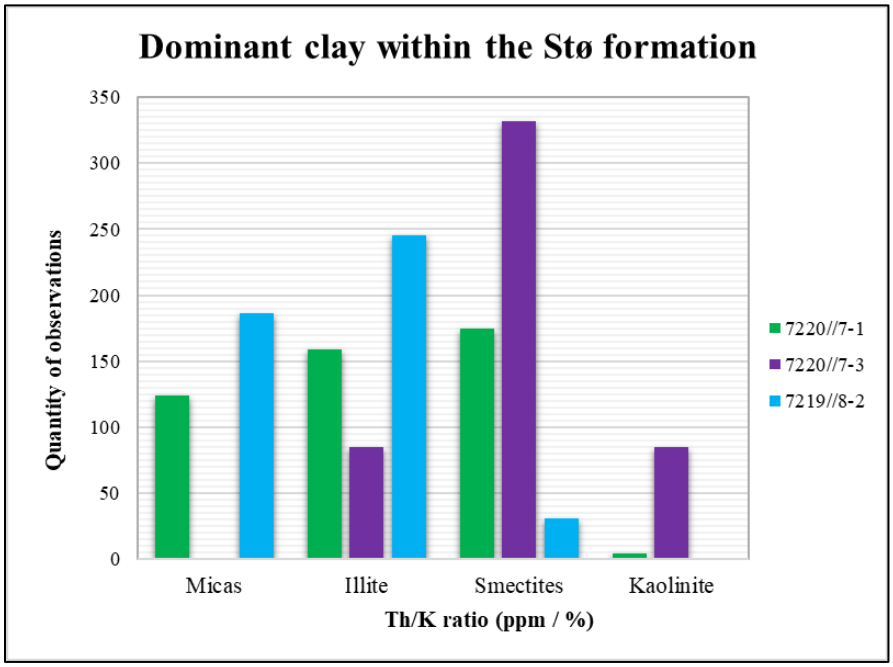

Figure 4.22: Determination of the dominating clay minerals based on histograms of the Th/K ratio for the Stø Formation.

In addition, results from the Nordmela Formation shows that is composed by the following clay minerals: smectite, illite, mica, and kaolinite (Figs. 4.23 and 4.24). Histogram of the Th/K shows, in general, the dominant clay is smectite followed by illite (Fig. 4.25). On one hand, in well 7220/7-1 (Havis) the estimated shale volume of 14% is composed by 75% smectite, 19% illite, 4.7% mica and 1.1% kaolinite. On the other side, well 7220/7-3 (Drivis) consists of 94% smectite, 5% illite and 1% kaolinite in total clays. The shale volume in the well 7219/8-2 (Iskrystall) is characterized by 54% smectite, 42% illite and 4% mica.

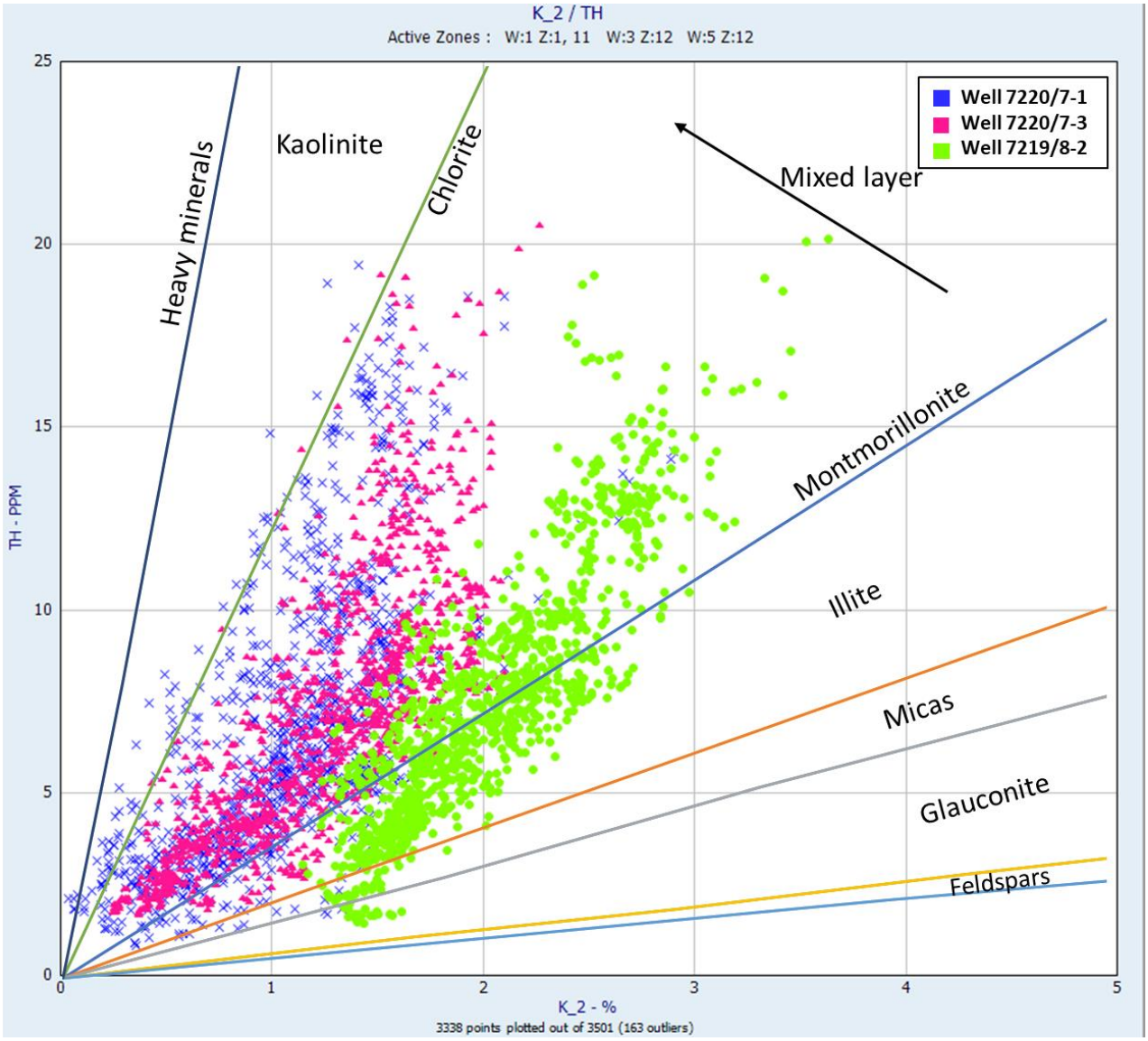

Figure 4.23: Determination of the clay mineral types based on the Th/K ratio for Nordmela Formation based on the information from well 7220/7-1 (Havis), 7220/7-3 (Drivis) and 7219/8-2 (Iskrystall).

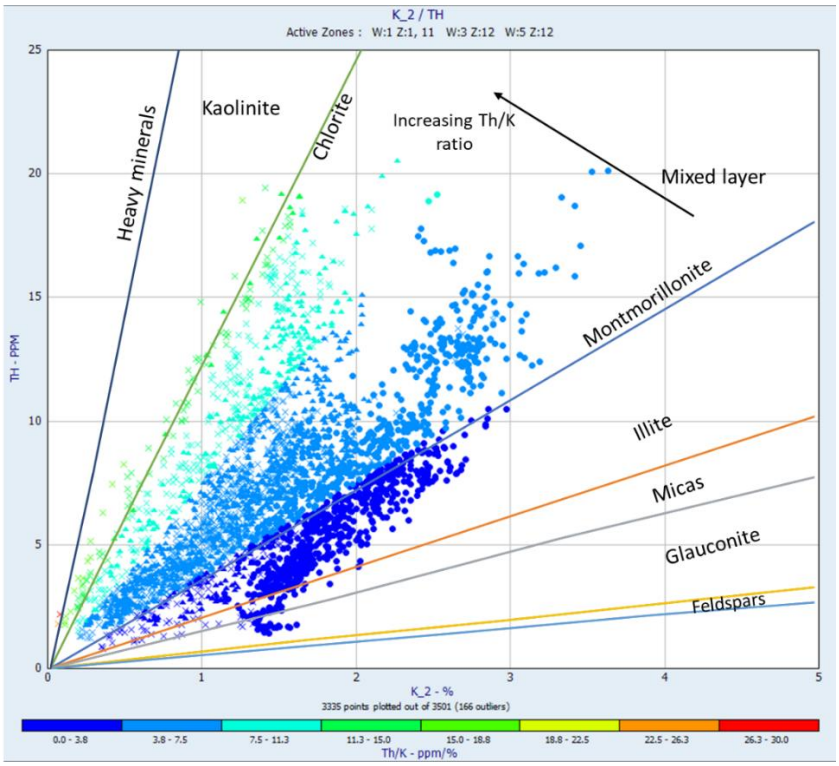

Figure 4.24: Determination of the clay mineral types based on the ThF/K ratio for Nordmela Formation based on the information from wells 7220/7-1 (Havis), 7220/7-3 (Drivis) and 7219/8-2 (Iskrystall), the data is color-coded by Th/K ratio.

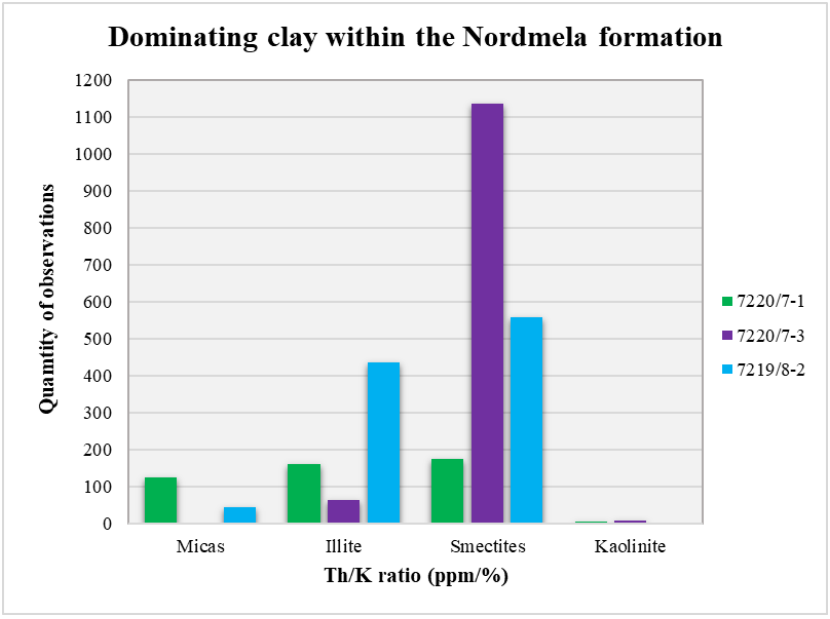

Figure 4.25: Determination of the dominant clay minerals based on histograms of the Th/K ratio for the Nordmela Formation.

4.2 Discussion

4.2.1 Stø Formation

In wells where the Stø Formation is present, it appears that the formation has good reservoir properties due to the depositional condition (dominated by wave and tidal energy that reworked the sediments, Olaussen et al., 1984). Well 7220/7-3 (Drivis) has the highest porosity of 0.237%, low shale volume of 0.16%, and 74.85 m of net pay, followed by the well 7219/8-2 (Iskrystall) with 0.16% of shale volume and 0.24% effective porosity.

The gamma ray log is characterized by low values displaying blocky-to-cylindrical shapes. The formation is delimited by the Nordmela Formation below and by the clay-rich Fuglen Formation on the top. The transition between the Stø and the overlain formations is characterized by a sudden and sharp increase in gamma ray values. In the wells 7220/7-1, 7220/7-3, 7219/8-2, and 7219/9-1 the formation can be subdivided into two sequences separated by a sudden increase in the gamma ray response. The upper section consists of clay base that is coarsening (cleaning) upwards, while the bottom section is represented by cleaner sand.

The Stø Formation represents inner shelf and lower shoreface deposits. The origin began during Late Toarcian when it was deposited during a transgressive event, which led to a change in the depositional environment from flood-plain to prograding coastal. Nevertheless, shallow marine depositional environments were later established over most of the basins over the Barents Sea (Fig. 4.26). Therefore, the lower section of the gamma ray response might be associated with shoreline sediments, influenced by mainly wave processes whereas some intervals might have been tidal dominate (Olaussen et al., 1984). Additionally, the cleaning upward trends observed on the wells suggest a progradational system, response that corresponds to the prograding coastal regimes on which the formation was deposited (Dalland et al., 1988), while the thinner changes that interrupt both sequences could be interpreted as minor transgressive episodes.

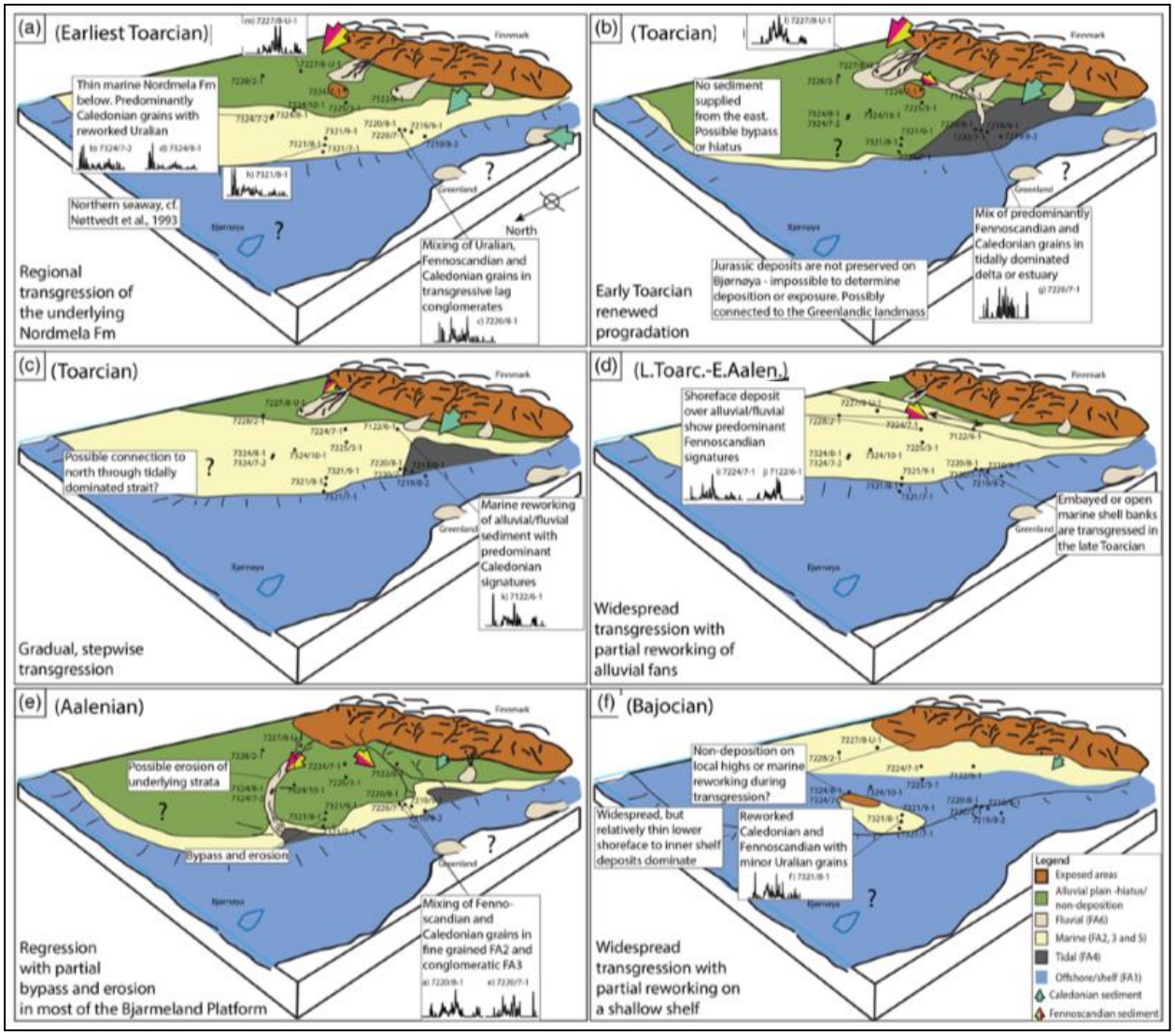

Figure 4.26: Development of the depositional environments and structures for the Stø Formation from earliest Toarcian (A) to Bajocian (F) (Klaussen et al., 2017).

The main target within the Stø Formation is located in the rotated fault blocks, structural trap, such as the Havis discovery of well 7220/7-1 (Fig. 4.27). The reservoirs consist of gas saturated sand in wells 7220/7-1 (Havis), 7220/7-3 (Drivis), and 7219/8-2 (Iskrystall) (NPD,2017b). It is confirmed by the response of the well log in the entire section. However, the sands in well 7219/9-1 are fully water saturated.

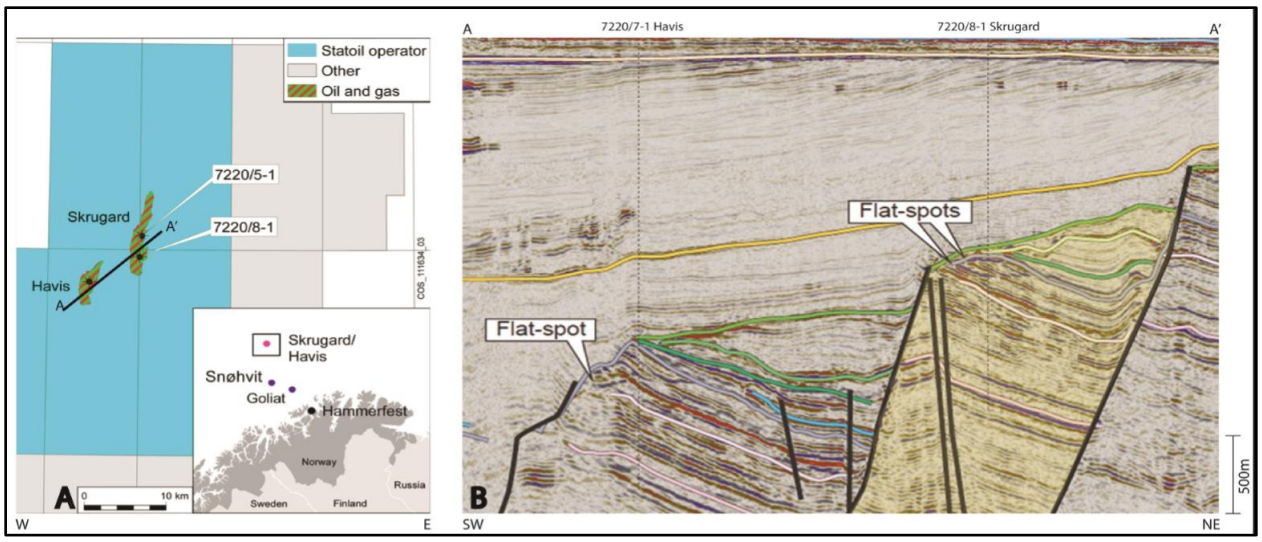

Figure 4.27: Representation of the Stø Formation in the rotated fault block within the Havis discovery. a) Map showing the Skrugard and Havis discoveries, and b) The seismic section of the profile A-A' in Figure A. The interpreted "Flat-spots" indicate fluid contacts (Kristensson, 2016).

4.2.2 Nordmela formation

On the four wells where the Nordmela formation is present, the well has the best reservoir properties is 7220/7-3 (Drivis). The effective porosity is 0.230%, shale volume is 0.202%, and net pay is 48.06m, followed by the well 7220/7-1 (Havis) that also has good reservoir qualities.

Compared with the Stø, the Nordmela Formation has an increase in the shale content affecting the reservoir quality. The gamma ray log over the interval is defined by a coarsing upward and a blocky pattern in wells 7220/7-1 (Havis), 7220/7-3 (Drivis), 7219/8-2 (Iskrystall), and 7219/9-1. The Stø Formation is overlain, while the Tubåen Formation is underlain the Nordmela Formation. The transition between the underlain formation, the Nordmela Formation is marked by a sudden high gamma ray reading due to a change in lithology.

The Nordmela Formation was deposited during Early Jurassic in a paralic system where the environment was low to medium energy, tidal to floodplain, with individual sandstone bodies from an estuarine and tidal channel environment (Fig. 4.28).

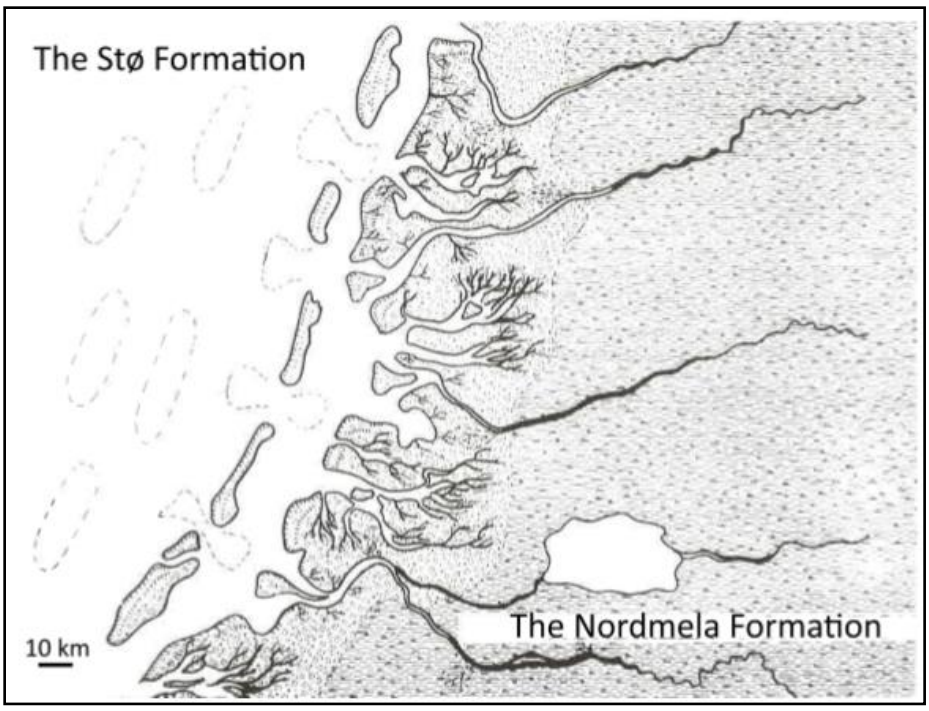

Figure 4.28: Representation of the depositional environment of the Stø and Nordmela Formations (Olaussen et al., 1984).

The coarsening upward section located on the bottom part might be fine to very fine sand interbedded with mudstone layer and poor reservoir qualities; while the upper section might consist of fine to medium grain sand from tidal channels, that possess good reservoir properties (Olaussen et al., 1984).

The presence of hydrocarbon has been proven in wells 7220/7-1 (Havis), 7220/7-3 (Drivis), and 7219/8-2 (Iskrystall) confirmed by the petrophysical analysis. The reservoir consists of gas and oil-bearing zones in the upper part of the formation; this is because the reservoir quality improves upward due to the increase of channel sandstone. However, the reservoir is water-bearing in well 7219/9-1 (Saadullah, 2015).

4.2.3 Tubåen Formation

The Tubåen Formation is mainly sandstones with subordinate shales; that exhibits relative good reservoir properties. The thickest potential sands are located in the lower section in well 7220/7-2, containing low shale volume of 0.11%, high effective porosity of 0.310%, and 28.04 m of hydrocarbon filled sandy zone.

The gamma ray is characterized by low values displaying blocky to bell-shaped. The formation is bounded by the Nordmela Formation at the top and the Fruholmen Formation at the bottom. In wells 7220/7-2 and 7219/9-1, the formation can be subdivided into two sequences, the lower boundary is marked by an increase in the sandstone content, whereas the upper contact marked by a transition into finer grained sandstones and siltstones.

The Tubåen Formation represents a significant change in the fluvial style in the Barents Sea with stacked sandstone bodies and less interbedded fine-grained deposits. The sandstone bodies are the result of high energy and distributary channels with good reservoir quality (Fig. 4.29).

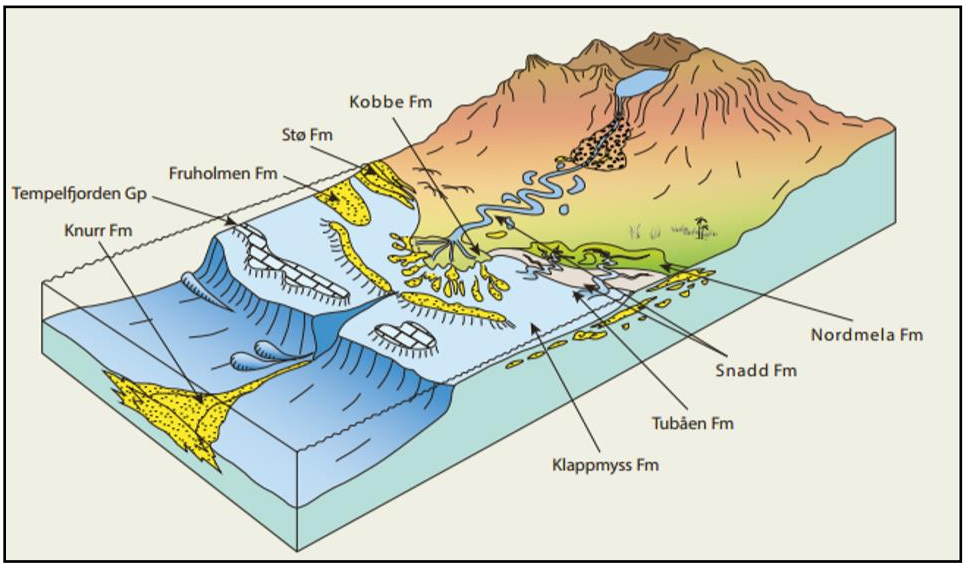

Figure 4.29: Depositional environments for the major reservoir formations (NPD, 2014).

The reservoirs are located in rotated fault blocks as it shows on a seismic section (Fig. 4.30. In case, of well 7220/7-2, the Skavl discovery, the sandstones are filled with oil and gas. Nevertheless, the sandstones in well 7219/9-1 are water bearing.

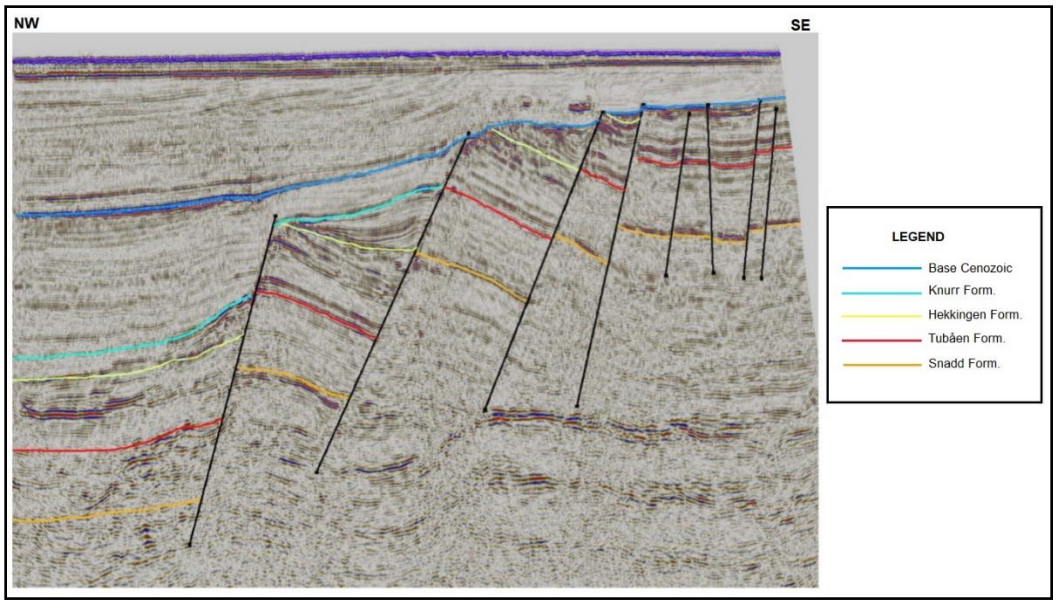

Figure 4.30: 2D Seismic section (F-86-205) of the southwestern Barents sea, where the red horizon is the interpretation of the Tubåen Formation (Zhaolong, 2013)

4.2.4 Fruholmen Formation

Compared with Tubåen, the Fruholmen Formation is less clean in terms of the shale volume affecting the net-to-gross ratio and the net pay thickness. The formation is present in four of the six wells, 7220/7-2, 7220/7-3, 7219/8-2, and 7219/9-1. However, only well (7220/7-2) is taking into consideration for the petrophysical analysis. The well 7220/8-2 has a thin reservoir, while the wells 7220/7-3 and 7219/9-1 are water bearing (NPD, 2017b).

The gamma ray log response can be subdivided into a coarsening upward and blocky-cylindrical patterns. The Fruholmen Formation is limited by the Snadd Formation at the bottom, and by the Tubåen formation in the upper part. The lower boundary is marked by a sudden increase in the gamma ray reading associated with shale deposits. This change is interpreted as the transgressive event that occurred during Early Norian (Ryseth, 2014).

The Fruholmen Formation represents a transition from open marine to coastal and fluvial sandstones with a fluvial-deltaic progradation. Therefore, the coarsening upward sequence in the lower part is interpreted as a delta progradation, that was followed by the Early Norian transgression; meanwhile, the middle and upper part might be related to deposition in a variety of subenvironments of delta-plain, such as mouth bar and distributary channels (Fig. 4.31). The reservoirs are generally located in the middle sequence (the Rekke member). Nevertheless, in this study in the well 722/7-2 (Iskrystall) oil saturated sandstones have been proven within the upper sequence, the Krabbe member.

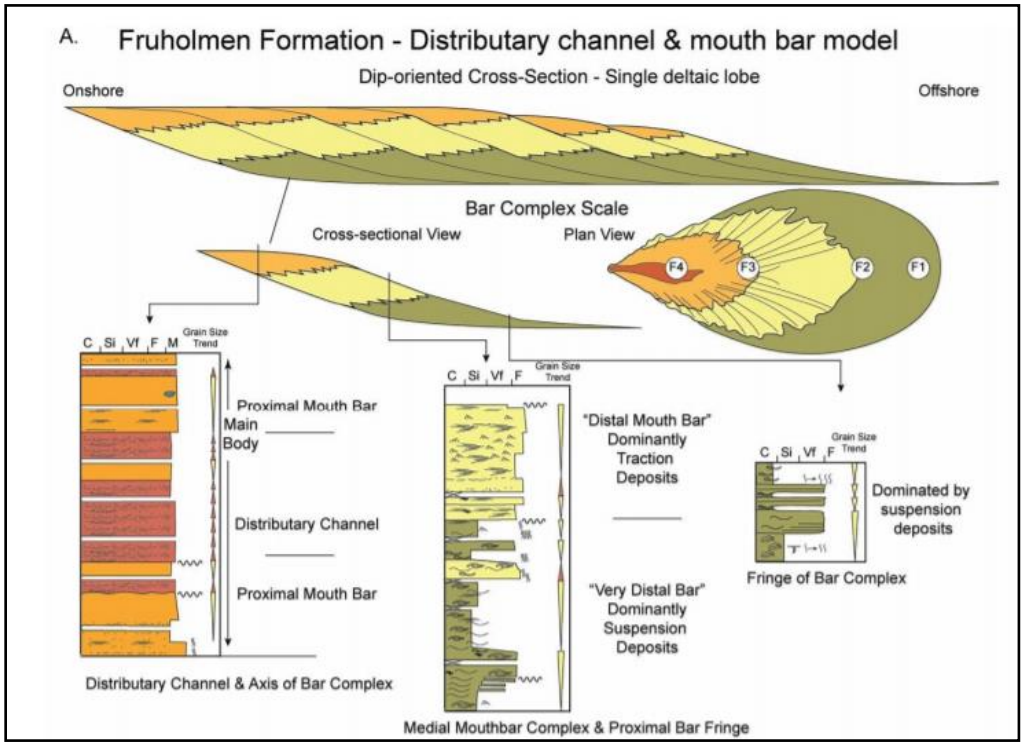

Figure 4.31: Conceptual models applied to the Fruholmen Formation. Grain size trends and sedimentary structures for the proximal, medial and distal portions of a channel and mouth bar complex (Clark, 2017).

4.2.5 Hekkingen and Fuglen Formations

Compared with the previous formations, the Hekkingen and the Fuglen Formations are clay-rich, with a shale volume over 0.46%, have low porosity, and high-water saturation. These conditions affect directly the net-to-gross and the net pay thickness. In case of well 7219/8-1, the net pay and N/G ratio are very low (1m) and (0.001) respectively.

For both formations, the gamma ray is characterized by high readings. The transition from Fuglen to Hekkingen Formation is not abrupt. According to Dalland et al. (1988) and NDP (2017b), the transition is defined by a change from carbonate cemented mudstone to poorly consolidated shale. Furthermore, there is a contrast with a sharp transition between Stø and Fuglen Formations due to a change in the lithology from sandstones to mudstones.

The Hekkingen Formation is assumed to be deposited during a transgression process, under anoxic deep marine conditions. The shales and claystones have good porosity in the upper part, however, it decreases considerably due to extensive quartz cementation. Moreover, the Fuglen Formation is associated with a highstand shelf with low sedimentation rate. In this case, the decrease in the porosity is due to the presence of fine-grained texture (Javid, 2013).

As reservoir potential, both formations are considered to have poor quality. Nevertheless, the high TOC content makes them good source rock. As we know the Hekkingen Formation is the most prolific and widespread source rock in the Barents Sea.

4.3 Uncertainties

The petrophysical analysis is considered an important method that provides a link between reservoir properties and rock physics trends. However, these reservoir variables (porosity, water saturation, and shale volume) are not directly measured instead, they are derived to follow several steps. Each step involves the use of equations, selection of parameters, assumptions that could carry uncertainties in the results. These uncertainties are the following:

- Overall, the accuracy of the geophysical tools could carry uncertainties during the acquisition. The log measurements could be affected by total or partial tool failure, due to mechanical problems, and/or by borehole conditions (Moore et al, 2011).

  The borehole condition plays an important role. If the borehole is uneven the tool might not be in contact with the formation. As consequence, the readings might be due to the drilling mud and may not be given actual information of the formation.

- The gamma ray readings are affected by the borehole conditions and the radioactive elements.

The presence of radioactive elements provides anomalous gamma ray readings. These high values of GRmax affected directly the shale volume estimation by reducing its value.

- The selection and interpretation of the sand and shale baseline could also influence the shale volume calculation.

- Bias is a factor in the selection of the fluid and matrix parameters for the porosity estimation (see chapter 3, section 3.2.4). The choice varies for each well according to the available data as well as the analyst preference (Moore et al., 2011).

- The accuracy of porosity estimation by using a single well log will carry more uncertainties than applying the differentt well log combinations.

- The water saturation is calculated using Archie's equation. This estimation is not precise since it depends on a number of uncertain factors such as the formation water resistivity and apparent mud filtrate resistivity. In addition, typical values for the cementation exponent (m), saturation exponent (n), and tortuosity factor are assumed based on previous publications.

4.3.1. Specific uncertainties

All studied wells show porosity values higher than 0.47%, which is the maximum values for a cubic packed rock made of spherical grains of a uniform size.

After verifying the data, all the higher values are located in the upper section, however, these values represent less than 10% of the entire sampling. Therefore, it is assumed that the values located in the shallower part might be due to unconsolidated sediments and since they are not included in the interval of interest they are not corrected.

However, the anomalous values located in the target zones are quantified and analyzed in order to discriminate between a possible tool failure and actual data from the formation. In case of the well 7220/7-2, only nine anomalous values are identified, followed by the wells 7220/7-1,7220/7-3 and 7219/9-1 with three anomalous values each. Since these values are spotted randomly along the intervals, it is assumed that this response might be a tool failure, thus they are corrected based on the surrounding readings.

Chapter 5: Rock Physics Diagnostics.

In this section, the results of the rock physics diagnostic are presented and discussed. The purpose of this analysis is to improve the understanding of rock properties by linking them with elastic properties such as Vp, Vs and Acoustic Impedance (AI). The theoretical models and backgrounds trends related to rock physics diagnostics are described in Chapter 3. Furthermore, several crossplots are generated in order to study the effect of lithology and pore fluid. That standard Vp versus Vs, Vp/Vs versus AI, and Lamda-Mu-Rho templates are used to distinguish lithology and fluid saturation. However, it is important to keep in mind that direct measurement of Vs data is only available on half of the wells (7220/7-1, 7220/7-3, and 7219/8-2). The Vs is predicted from the Vp for the rest of the wells (7220/7-2, 7219/8-1S, and 7219/9-1).

Moreover, depositional and diagenetic trends in the reservoir zones are analyzed by using the "Vp versus porosity and Vs versus porosity crossplots with the help of the effective medium models (Avseth et al., 2005). The results from rock physics diagnostics are compared with the results presented in Chapter 4 (Petrophysical Analysis). Uncertainties associated with the rock physics diagnostic and to constrauct rock physics are discussed in this chapter.

5.1 Results

5.1.1 Shear Wave Velocity (Vs) Estimation

Shear wave velocity usually is not available in old well logs database. Therefore, the estimation of Vs is based on published relations suggested by many authors (e.g. Castagna et al., 1985 and Krief et al., 1990).

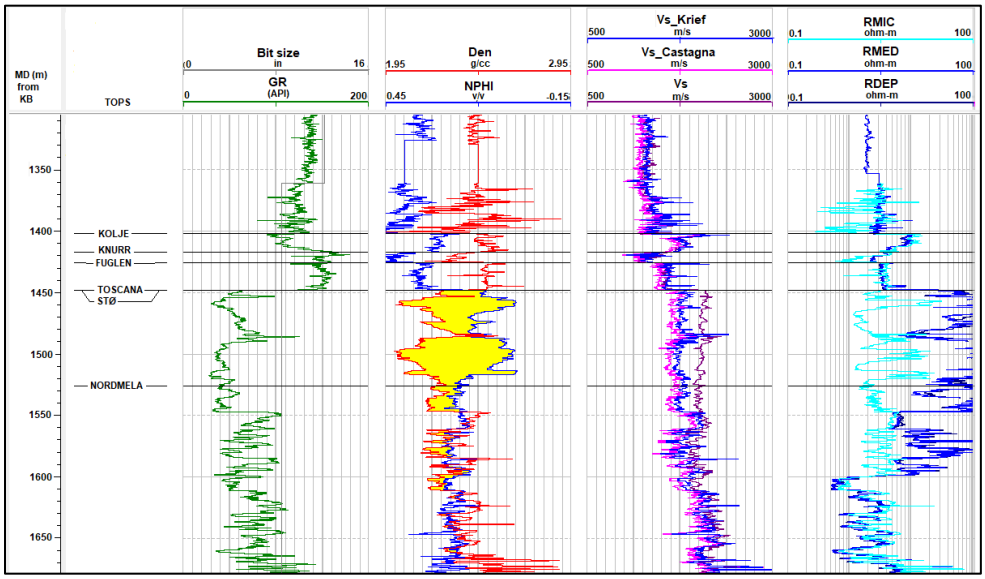

Figure 5.1: Comparison between the estimated and measured Vs in the well 7220/7-3 (Drivis). The Vs relation derived from the data in this study suited to predict Vs in the shaley and sandy intervals, except in the hydrocarbon reservoir.

Figure 5. 1, shows both velocities, measured and estimated Vs, for well 7220/7-3 (Drivis). The measured and estimated Vs follow more or less the same trends in the shaley and brine saturated sandy intervals, suggesting a good fit between measured and predicted Vs in these intervals. The estimated Vs (Krief et al., 1990: blue line and Castagna et al., 1985: purple line in Fig. 5.1) differed from the measured Vs in the hydrocarbon zones, showing an underestimation of Vs.

As a consequence, the estimated Vs in hydrocarbon saturated zone is not accurate (due to fluid effect on Vp) and so did not use in rock physics diagnostics.

5.1.2 Velocity versus porosity relationship based on the clay effect.

5.1.2.1 Marion's (Marion et al.,1992) velocity- porosity relationship in sand-clay mixtures

It has been proven that in consolidated rock the large part of the scatters in the velocity-porosity relationship can be attributed to lithology, more specifically, the clay content. Moreover, for unconsolidated sediments, not only the lithology but also the compaction and porosity have a big influence on the velocity (Marion et al., 1992).

In case of a shaly sand model, Marion et al. (1992) assumed that clay particles are filling the sand pore space without disturbing the sand pack but affecting the porosity. Thus, the porosity of the rock will decrease linearly as the clay content increase, making the rock stiffer which directly increases the velocity. However, when the pores are full-filled, the addition of clay will become part of the rock matrix making it softer than the sand; therefore, the velocity will decrease as the volume of clay increases.

To study the clay effect on the porosity and velocity, Vp versus Vsh, and porosity versus Vsh crossplots are generated using data points of the Stø, Nordmela and Fruholmen Formations that are color-coded by estimated shale volume. As expected, an inverted V-shape trend is observed in the Vp versus Vsh plot for the Nordmela Formation of well 7219/8-2 (Iskrystall). The velocity reaches its maximum value around 4.8 km/s when the shale volume is estimated to be from 30 to 50% (Fig. 5.2a). On the other hand, the V-shape behavior is observed in the porosity versus Vsh crossplot, on which the porosity began to decrease reaching its minimum around 8% when the shale volume range between 30 to 50% (Fig.5.2b). In well 7220/7-3 (Drivis), the formation reaches a maximum velocity of 4 km/s when the shale volume ranges from 30 to 34% (Fig. 5.2c). The behavior that correlates properly with the decrease of the porosity up to 16 to 20% within the same shale volume (Fig. 5.2d).

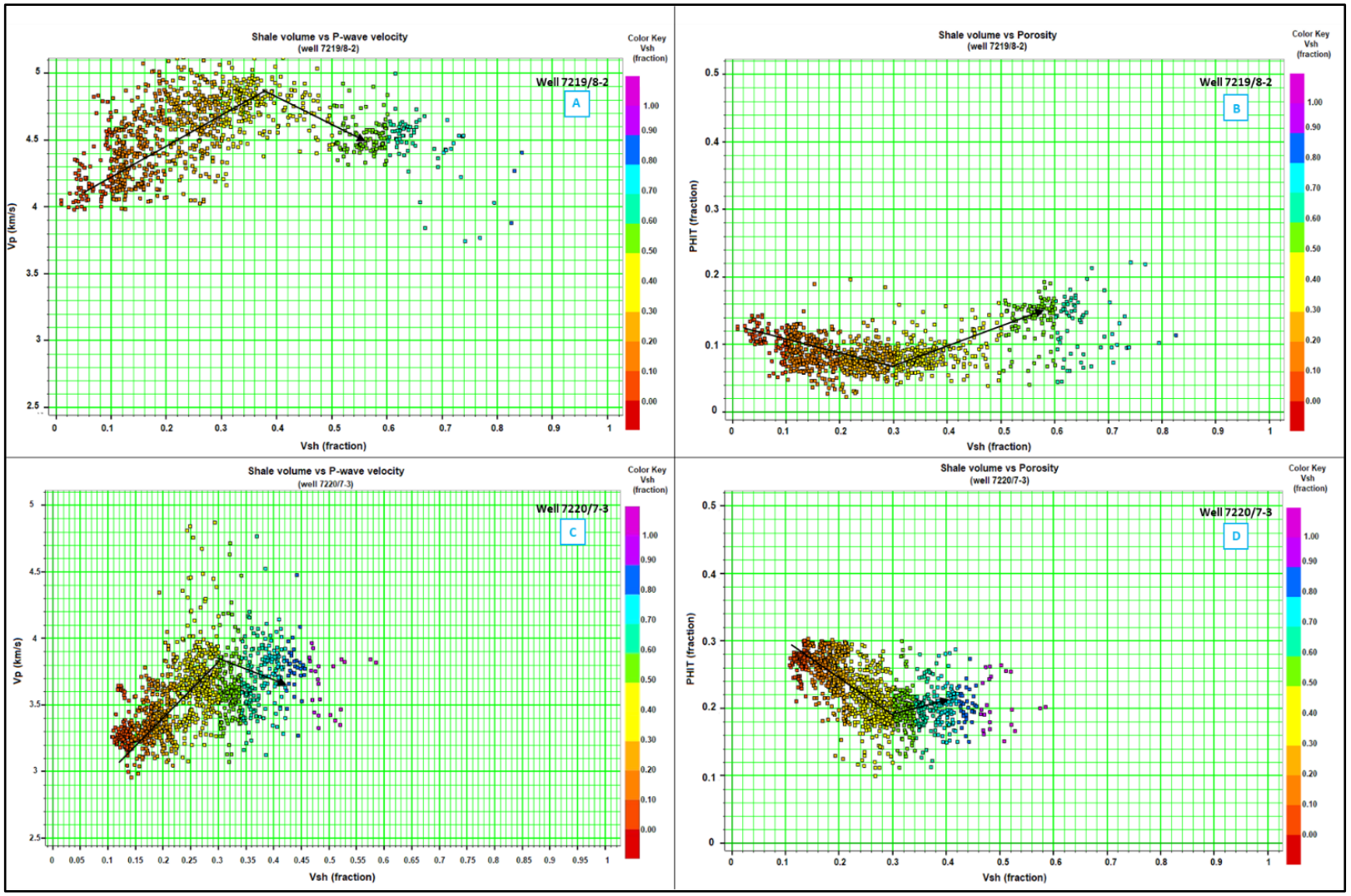

Figure 5.2: Comparison between velocity and porosity data of the Nordmela Formation. Upper part represents well 7219/8-2 (a) Vp versus Vsh and (b) PHIT versus Vsh. Bottom plot represents well 7220/7-3 (c) Vp versus Vsh and (d) PHIT versus Vsh.

Furthermore, for the Stø formation, the expected V-trends are not fully identified (Fig. 5.3) since this formation is considered a clean sandstone with no or very low clay content. Nevertheless, the formation reached its minimum porosity of 20% and maximum Vp velocity of 3.5 km/s when the shale volume is around 28 to 30%.

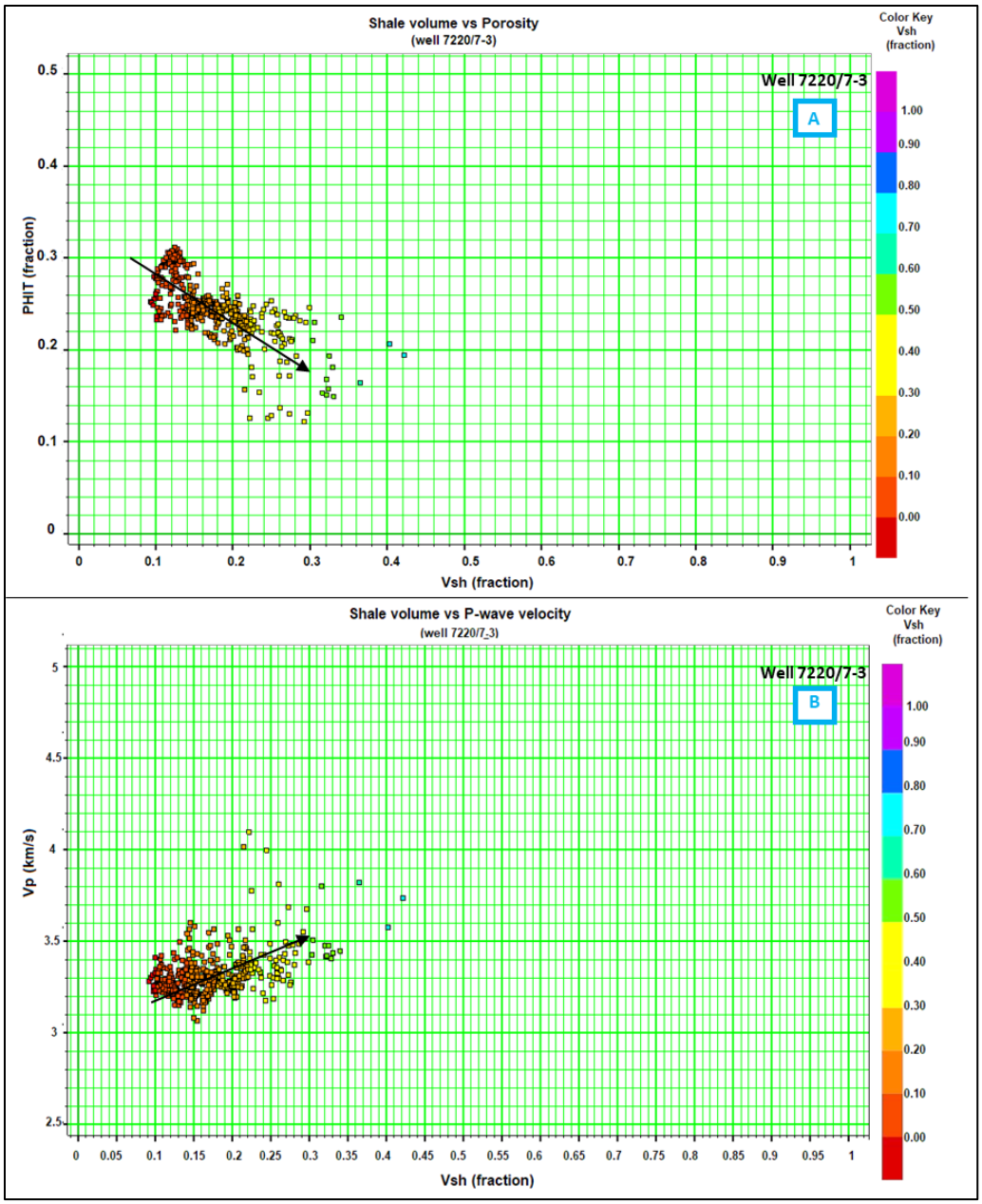

Figure 5.3: Comparison between velocity and porosity data of the Stø Formation from the well 7220/7-3 (Drivis). a) Upper part represents total porosity versus Vsh, b) Bottom plot represents Vp versus Vsh.

Moreover, a characteristic inverted V-shape trend, probably associated with sorting effects, is identified in the Vp versus porosity crossplot for the Fruholmen Formation. An increasing shale volume from 0 to 40% causes the velocity to increase, reaching a maximum velocity of 3.6 km/s while simultaneously the porosity decreases up to 22% (Fig.5.4). Additional porosity versus Vsh and Vp versus Vsh crossplots of the Fruholmen Formation of well 7220/7-2 (Skavl) are plotted (Appendix B, Figure B.1, and B.2) showing the V-shape and inverted V-shape trends from Marion et al. (1992).

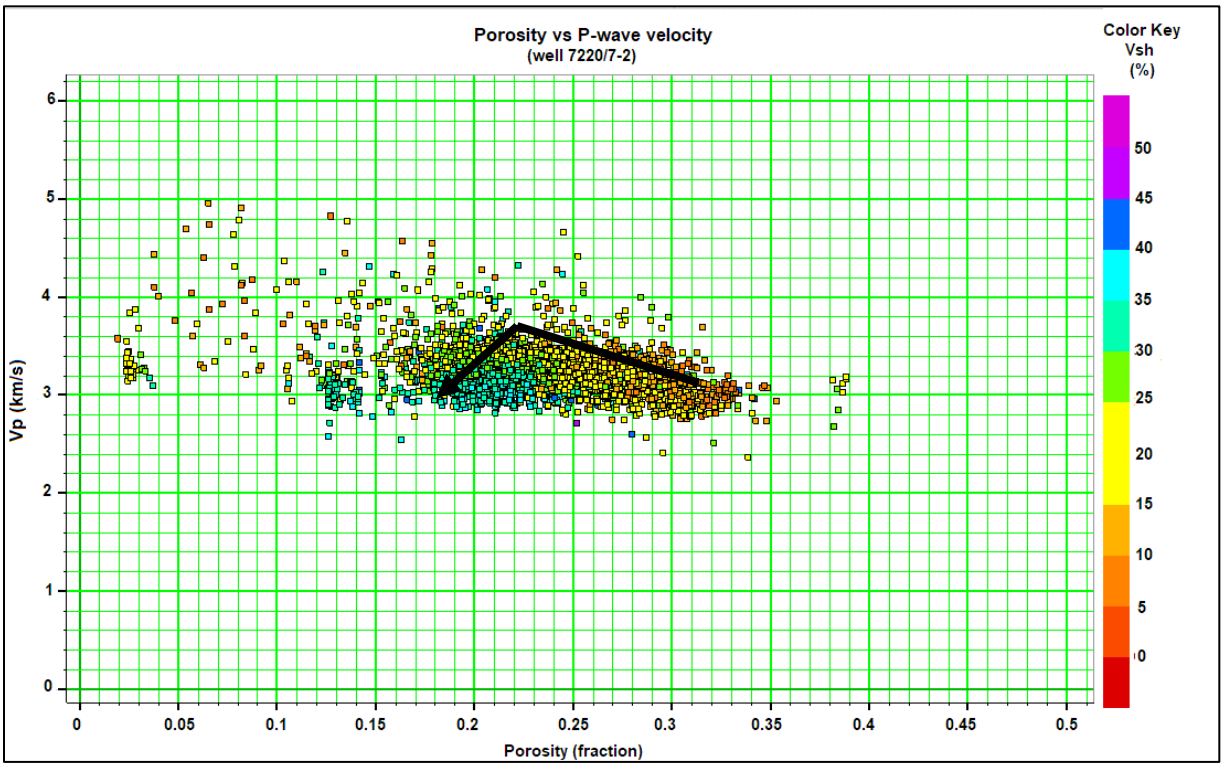

Figure 5.4: Crossplot of Vp versus total porosity of Fruholmen Formation of well 7220/7-2 (Skavl).

5.1.2.2 Han's (Hans et al., 1986) empirical relation for Vp - porosity for shaly sandstones

Another attempt to study the clay effect is based on Han et al. (1986) equations in order to estimate the clay volume on the reservoir and see the effect on the velocity and elastic modulus. The presence of a large amount of clay in the sandstone tends to soften the grain contact, while the decrease of the porosity makes the rock stiffer increasing the shear and bulk modulus.

Empirical constant clay for lines from Han et al. (1986) for 20 MPa of effective pressure are used to construct the Vp-porosity relation considering variable clay volume in the target areas such as Nordmela, Stø, and Fruholmen Formations. Overall, all data points from Stø and Nordmela Formations are observed to plot within the lines according to the estimated shale volume (Fig.5.5 and 5.6), displaying an increase of the Vp and porosity decreases when the shale volume goes from lower to higher.

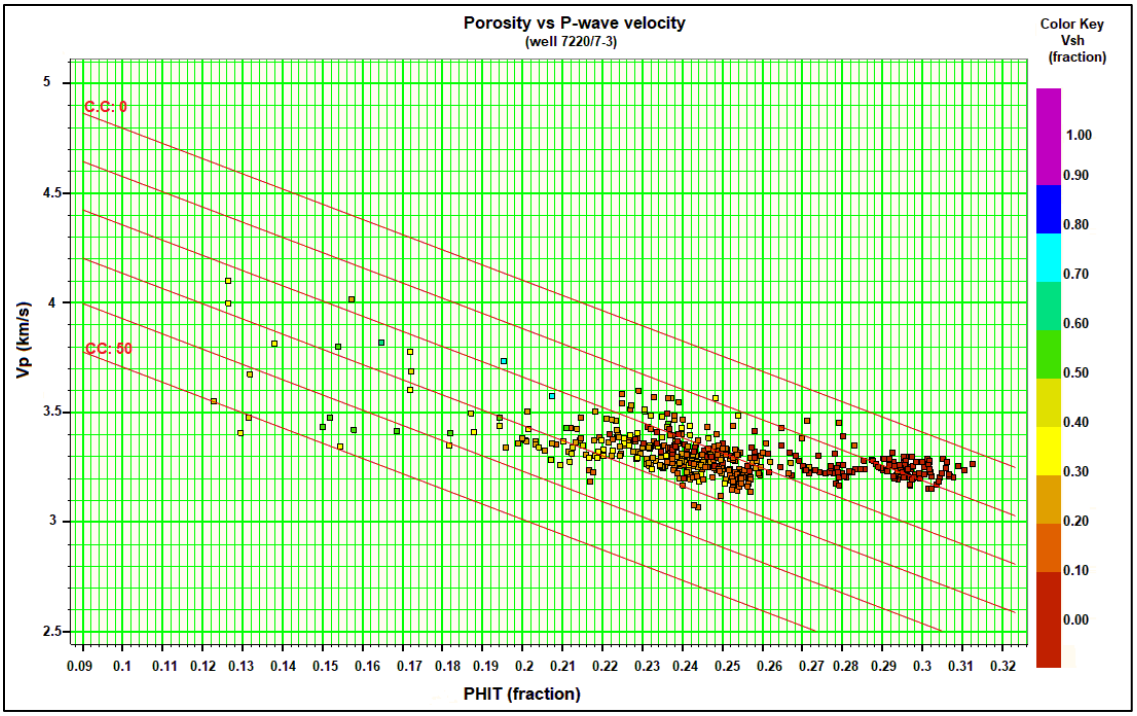

Figure 5.5: Clay volume prediction using Vp versus total porosity (PHIT) for the Stø Formation from well 7220/7_3. The lines represent constant clay lines from Han et al. (1986) for 20 MPa confining pressure. CC: clay content.

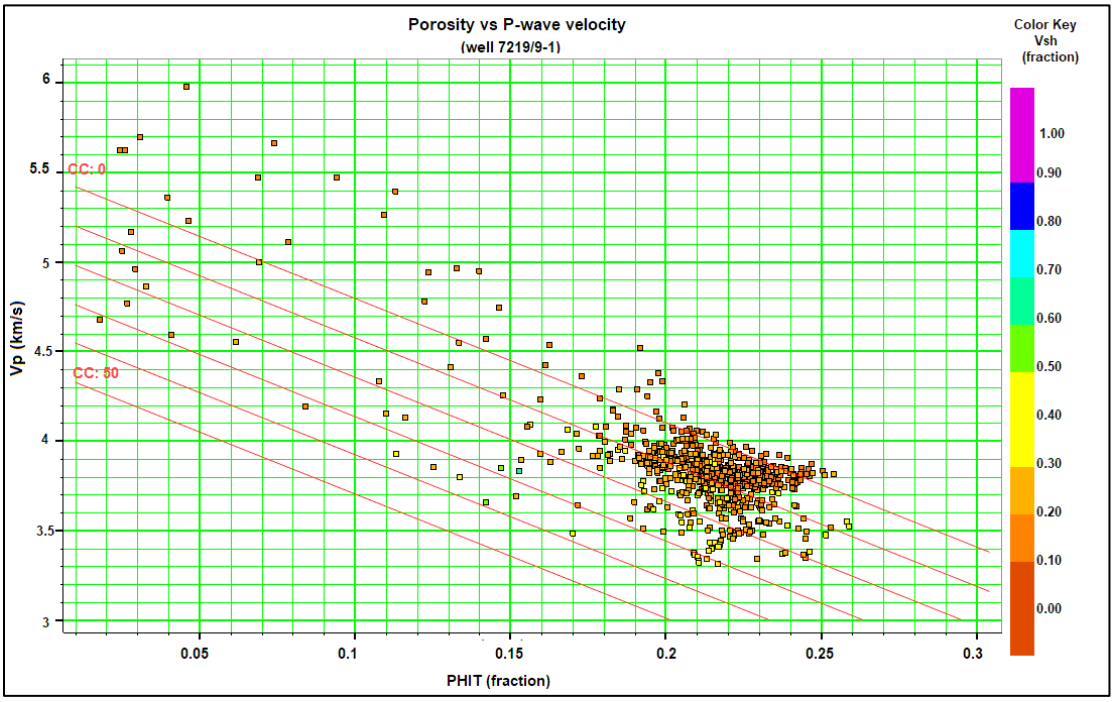

Figure 5.6: Clay volume prediction using Vp versus total porosity (PHIT) for the Nordmela Formation from well 7219/9-1. The lines represent constant clay lines from Han et al. (1986) for 20 MPa confining pressure. CC: clay content.

In case of the Fruholmen Formation (Fig. 5.7) a good discrimination between the data points is observed within the lines of lower clay content, but as the shale content increases distinguishing the data became more difficult. Although a slight trend displays an increasing Vp and decreasing porosity as the shale content goes higher, the lack of differentiation can be associated to a misleading shale content estimation during the petrophysical analysis. Moreover, variation in the mineralogy, pore geometry, cementation, confining pressure and pore fluid might also generate different results than the one observed in earlier studies, since Han's empirical relationship provides a good fit with data that is similar to the one originally used.

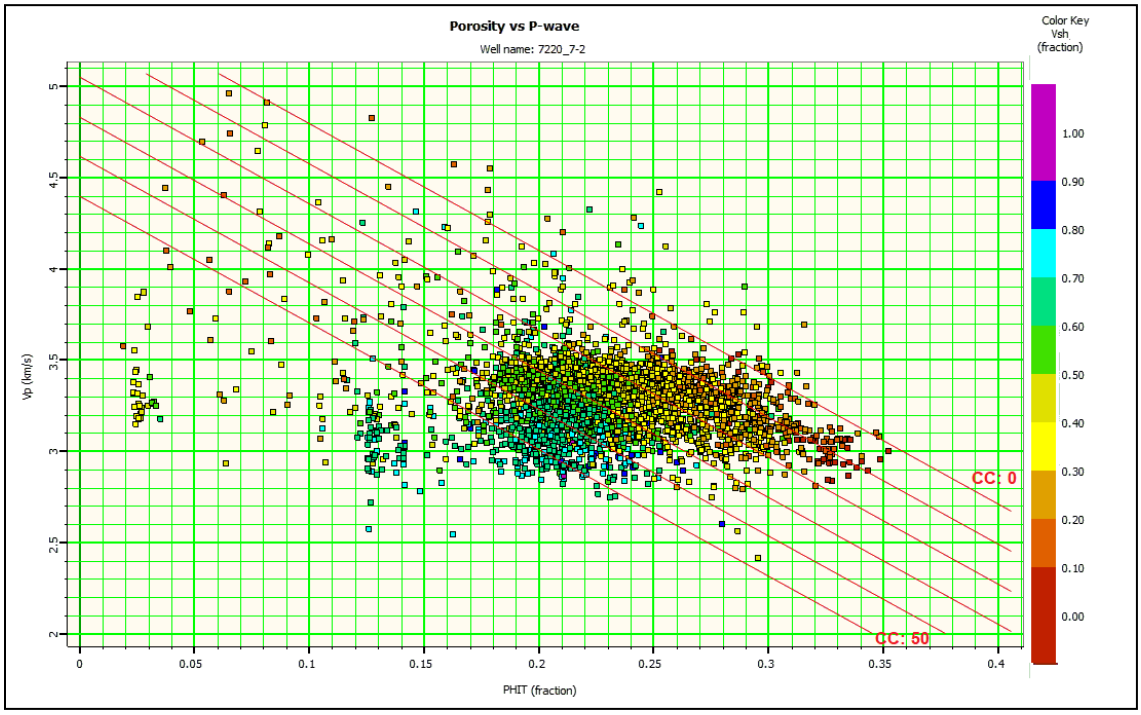

Figure 5.7: Clay volume prediction using Vp versus total porosity (PHIT) for the Fruholmen formation from well 7220/7-2. The lines represent constant clay lines from Han et al. (1986) for 20 MPa confining pressure. CC: clay content.

5.1.3 Vp versus Vs relationship

The Vp versus Vs crossplot remains tightly clustered and shows a linear trend despite variation in porosity, effective pressure and clay content for brine saturated sand (Fig. 5.8a). Nevertheless, changes in the fluid saturation will cause the gas and water saturated data move towards two well-separated trends (Avseth et al., 2005) (Fig. 5.8b). However, this plot is not useable in wells where Vs is estimated from Vp since it would plot in a linear trend (Fig. B.2).

Examples of this analysis are represented in Figure 5.8 and 5.9 for the Stø and Nordmela Formations respectively. In case of the Drivis (well 7220/7-3) and Iskrystall discoveries (well 7219/8-2), the presence of gas has been proven in the petrophysical analysis for the Stø Formation. The gas effect is confirmed on the Vp-Vs crossplot since the sands saturated with hydrocarbon plot over the gas sand trend, however, a poor discrimination is shown in well 7219/8-2 since the gas saturation is less in comparison with the other well.

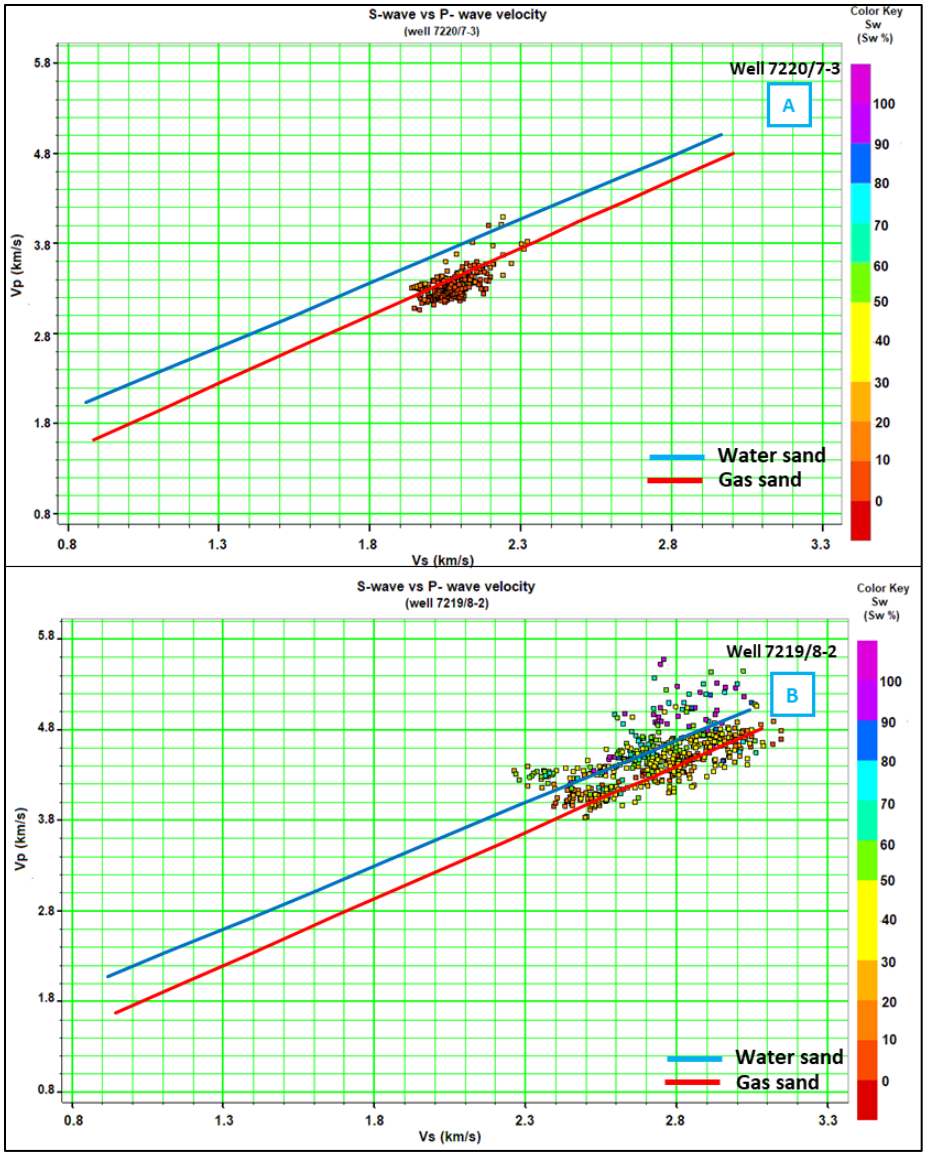

Figure 5.8: Gas effect on Vp vs Vs relation for the Stø Formation. a) Well 7220/7-3 (Drivis), b) Well 7219/8-2 (Iskrystall).

The Vp-Vs relation for the Nordmela Formation reflects a poor discrimination between fluids even though it has been confirmed the presence of gas. This response can be associated with the increase of the clay content proven by petrophysical analysis (Chapter 4). Thus, the increase of clay helps to increase the rock matrix stiffness affecting the elastic waves.

Finally, in Figure B.3 it can be seen a good discrimination between the different fluids from Stø to Nordmela Formations. The oil and gas zones plot practically on top of each other, while the brine saturated points plotted on top of the water sand line. The discrimination in color is based on a report of the gas-oil contact from the drilling company

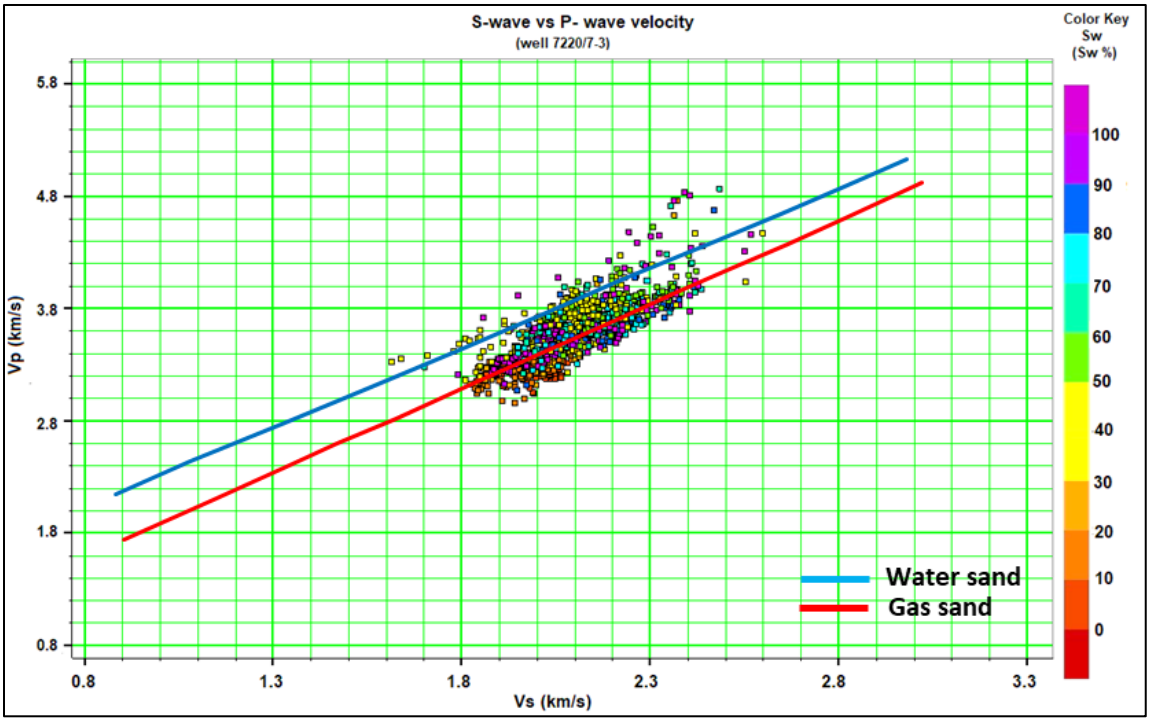

Figure 5.9: Gas effect on Vp versus Vs relation of Nordmela Formation of well 7220/7-3 (Drivis).

5.1.4 Rock Physics Cement Models

Rock physics cement models have become a well-known technique for inferring rock type and microstructure from the velocity- porosity relation. The amount of contact cement and non-cement pore-filling material can be also determined using rock physics cement model. The pore filling cement has a complex effect on rock properties and is recognizable in the velocity-porosity plane (Avseth, 2000). In the following section, the degree of cementation and sorting in the reservoir intervals of the Stø, Nordmela, and Fruholmen Formations are described.

For a first look analysis, all reservoirs intervals from the Stø Formation have been plotted in the Vp versus total porosity together with an overlay of the cement models (Fig.5.10). The data has been limited to a sand lithology (Vsh ≤ 50%) since the models proposed by Avseth et al. (2005) are applicable to a certain sandstone trend. In general, the data plot from the diagenetic trends to the contact cement line, where the majority of the data points are distributed.

A continuous and drastic increase in the velocity from 2.2 km/s to 5.5 km/s is defined as the porosity decreases from 32% to 4%. This response might be associated with an increase of cement on the grain surface due to an increase of burial depth affecting the rock stiffness.

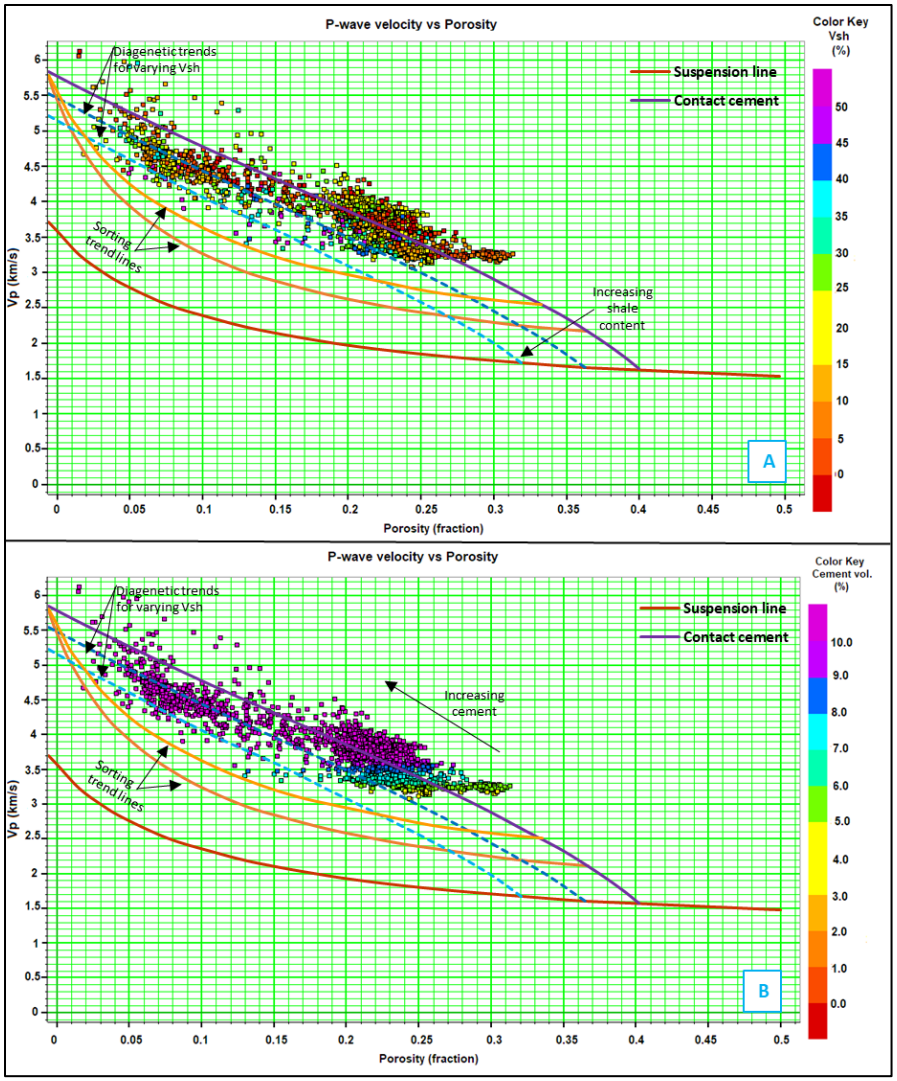

Figure 5.10: Overlaying from the reservoir intervals of Stø Formation on rock physics cement models. a) the data are color-coded by shale volume lower than 50%, and b) the data are color-coded by the cement volume estimated by Marcussen et al. (2010).

Looking more closely to the Stø Formation in well 7220/7-1 (Havis) on the Vp versus total porosity (Fig. 5.11a and 5.11c), all data points are plotted on the contact cement as expected since on this well the gamma ray response confirmed a clean sand interval (Fig. 4.4). The sharp increase of the velocity within a short range of porosity decrease might suggest that the formation is under the effect of diagenetic processes such as compaction and cementation. The cement volume is limited below 10% to create additional crossplot (Fig. 511b and 5.11d) to verify if the data show a similar percentage of the quartz cement defined by each cement line. In this case, the amount of cement is relatively high, therefore the points plotted correctly on the trends with quartz cement percentage higher than 5%.

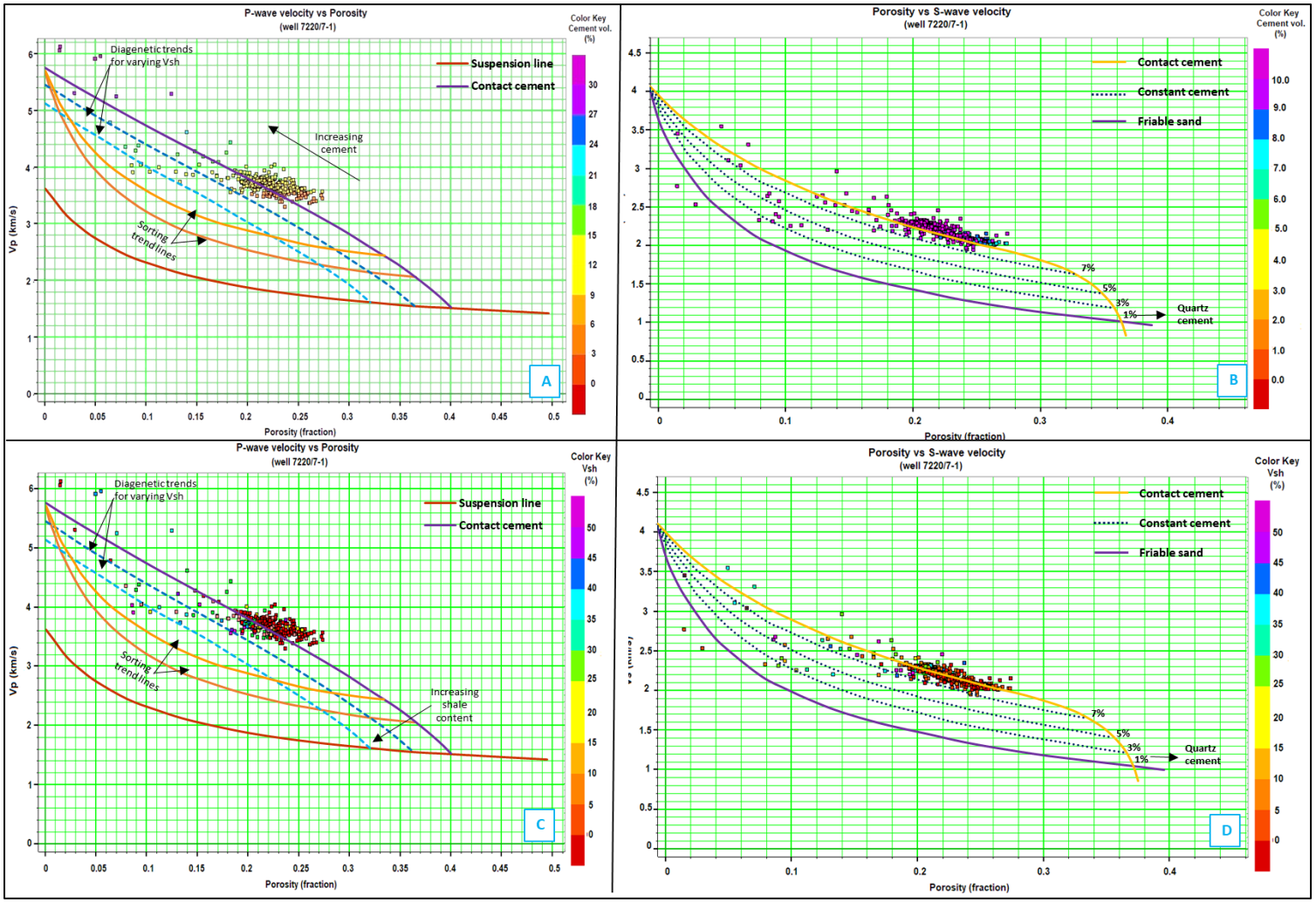

Figure 5.11: Diagnostic rock physics models overlaying the data points from the Stø Formation from well 7220/7-1 (Havis).Only the measured Vp and Vs are used. a) Vp versus porosity color-coded by cement volume, b) Vs versus porosity color-coded by cement volume (≤10% cement), c) Vp versus porosity color-coded by shale volume, and d) Vs versus porosity color-coded by shale volume.

Moreover, in well 7220/7-3 (Drivis), the sandstone points from the Stø Formation follow the diagenetic trends, however, the velocity has a steady response in comparison to well 7220/7-1 (Fig. 5.12). This response might be due to a low cementation rate since the formation is located a shallow depth and has not suffered a significant burial. In Figure 5.12c, the cement volume estimation from Marcussen et al. (2010) indicated values lower than 9%, which are plotted on the contact cement line. Furthermore, in the Vs versus total porosity plot (Fig. 5.12b and Fig. 5.12d) the data points preserved the same behavior as the previous plot on which the low cement percentage is plotted on the constant cement trend of 7% quartz and higher.

Even though in this well the Stø Formation is located at shallow depth (1072 m BSF), it has buried below the transition zone or in the chemical compaction domain. The maximum burial of the Stø Formation might be in the initial stage of quartz cementation and therefore a small amount of cement is developed.

Further search for the transition zone between the mechanical and chemical compaction domain in the well 7220/7-3 is executed through the shear modulus vs density crossplot (Fig. 5.13). Even though the data are not continuous due to lack of density values in several intervals a change in the spatial distribution of the data is identified, indicated with the stippled line, around 1263m – 1400 m MDKB ≈ 887 m- 1024m BSF, coinciding with the estimated depth of the transition zone. In addition, an increase of the shear modulus in the direction of the black arrow suggest that on this part of the well, the rock has higher rigidity probably due to an increase of burial depth and diagenetic cementation.

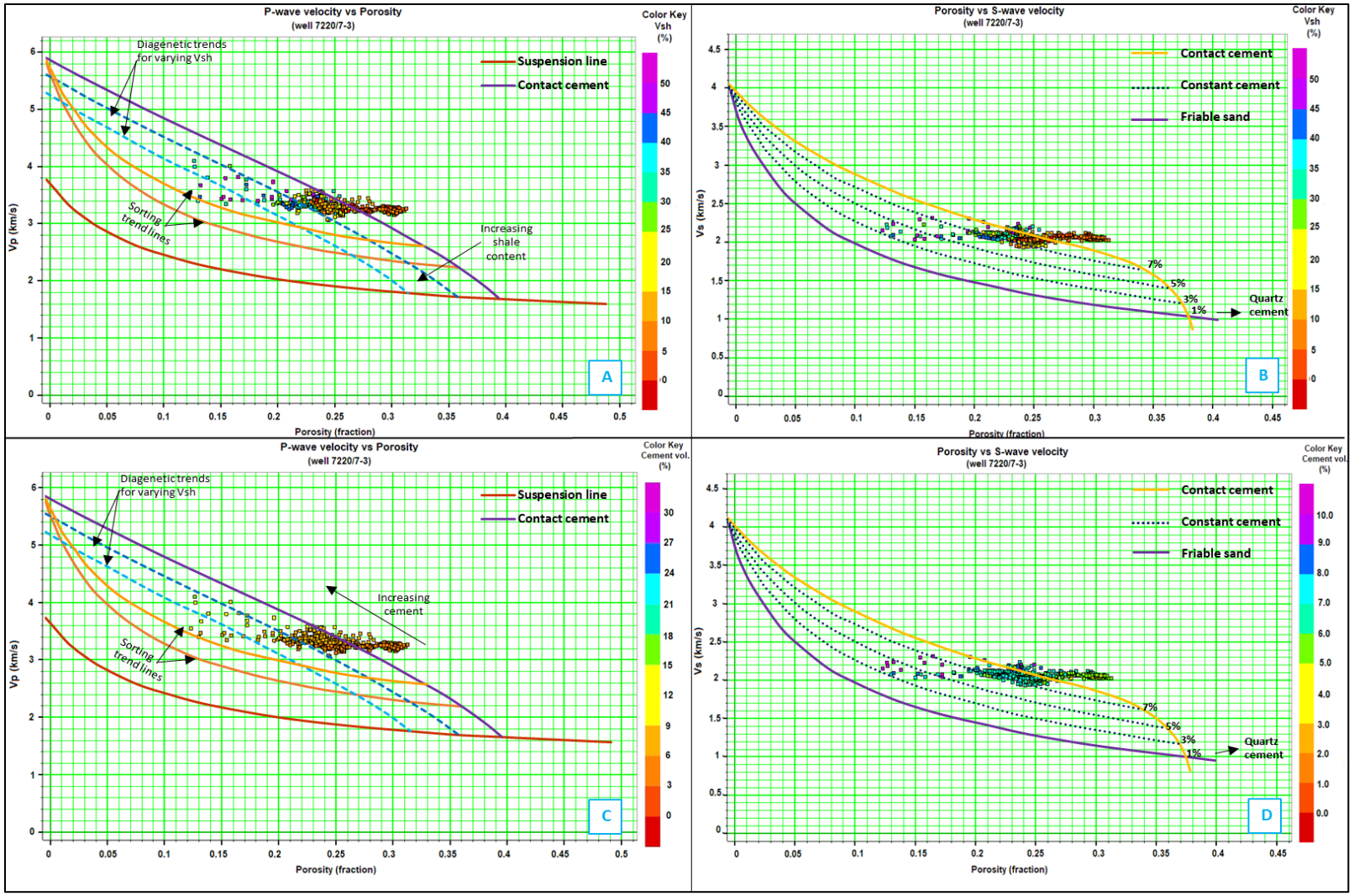

Figure 5.12: Diagnostic rock physics overlaying the data points from the Stø Formation in well 7220/7-3. Only the measured Vp and Vs are used. a) Vp versus porosity color-coded by shale volume, b) Vs versus porosity color-coded by shale volume, c) Vp versus porosity color-coded by cement volume, and d) Vs versus porosity color-coded by cement volume (≤10% cement).

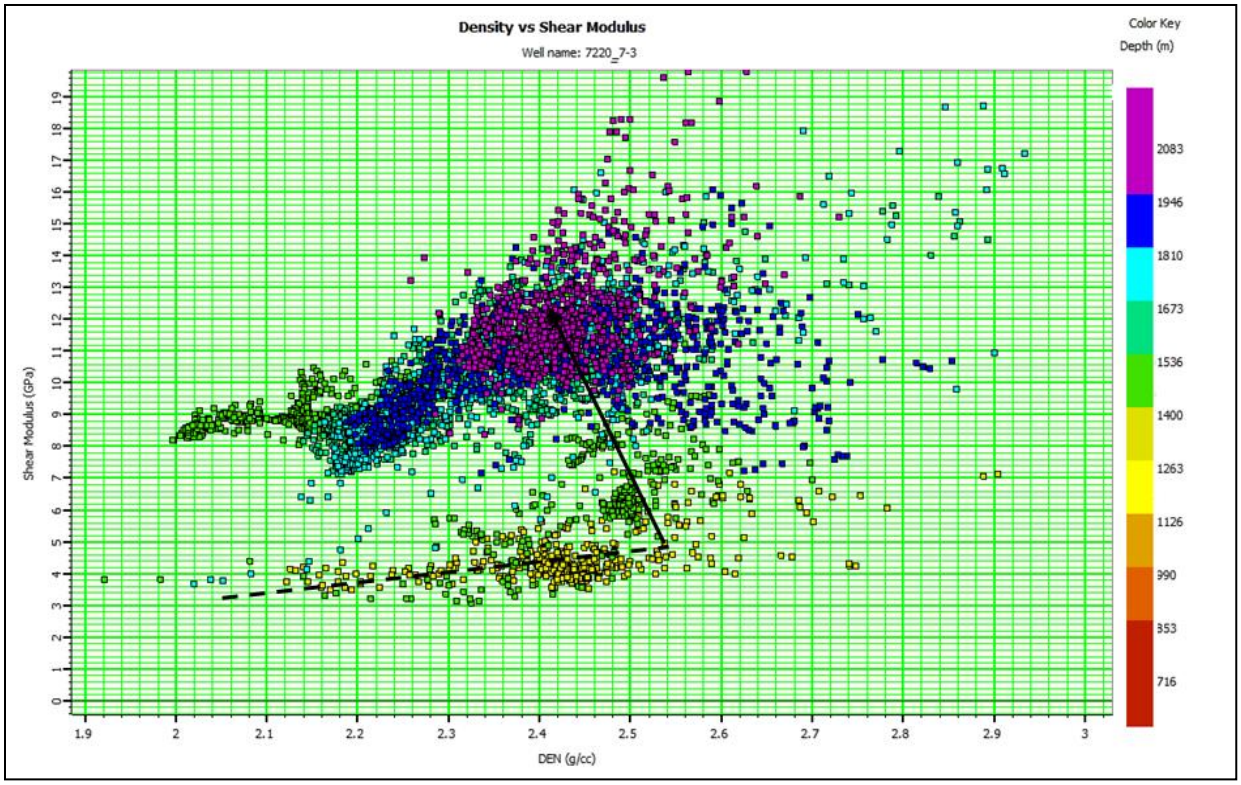

Figure 5.13: Crossplot of shear modulus versus density of entire data of well 7220/7-3 (Drivis). The data is color-coded by depth (in meters).

The results of rock physics cement models of all the reservoir intervals within the Nordmela Formation are displayed in Figure 5.14. Since this formation is less clean than the Stø Formation, the data points plotted not only on the contact cement line but also in the diagenetic trends with more clay content. It is also noticed that the cement volume increases with increasing burial (towards the upper left).

A closer look at the Nordmela Formation in well 7220/7-1 (Havis) is presented in Figure 5.15. A sudden change of velocity from 3.2 km/s to 4.2 km/s in a short range of porosity from 28 to 14% suggests that the formation is influenced by diagenetic processes like pressure solution, cementation or compaction. Furthermore, on the same well the Vs versus porosity crossplot is also generated. In general, most of the data from the reservoirs intervals are clustered around the 7% constant cement and above the contact cement line, showing also the same behavior on the velocity.

Since the Nordmela Formation is also considered a target in the well 7219/8-2 (Iskrystall), two crossplots of Vp and porosity are generated (Figure 5.16a and 5.16b). The Vp shows a sharp increase within the diagenetic lines from 4 km/s to 5.4 km/s as the porosity decreases. In terms of the cement volume estimated by Marcussen et al. (2010) a high quartz cementation above 15% is defined. As previously mentioned the Nordmela Formation is located at greater depth (2610m BSF after uplift) compared to the rest of the studied wells, and almost 600m below the transition zone (2000m BSF). Therefore, it is inferred that the formation experiences a deep burial; and so higher amount of quartz cement.

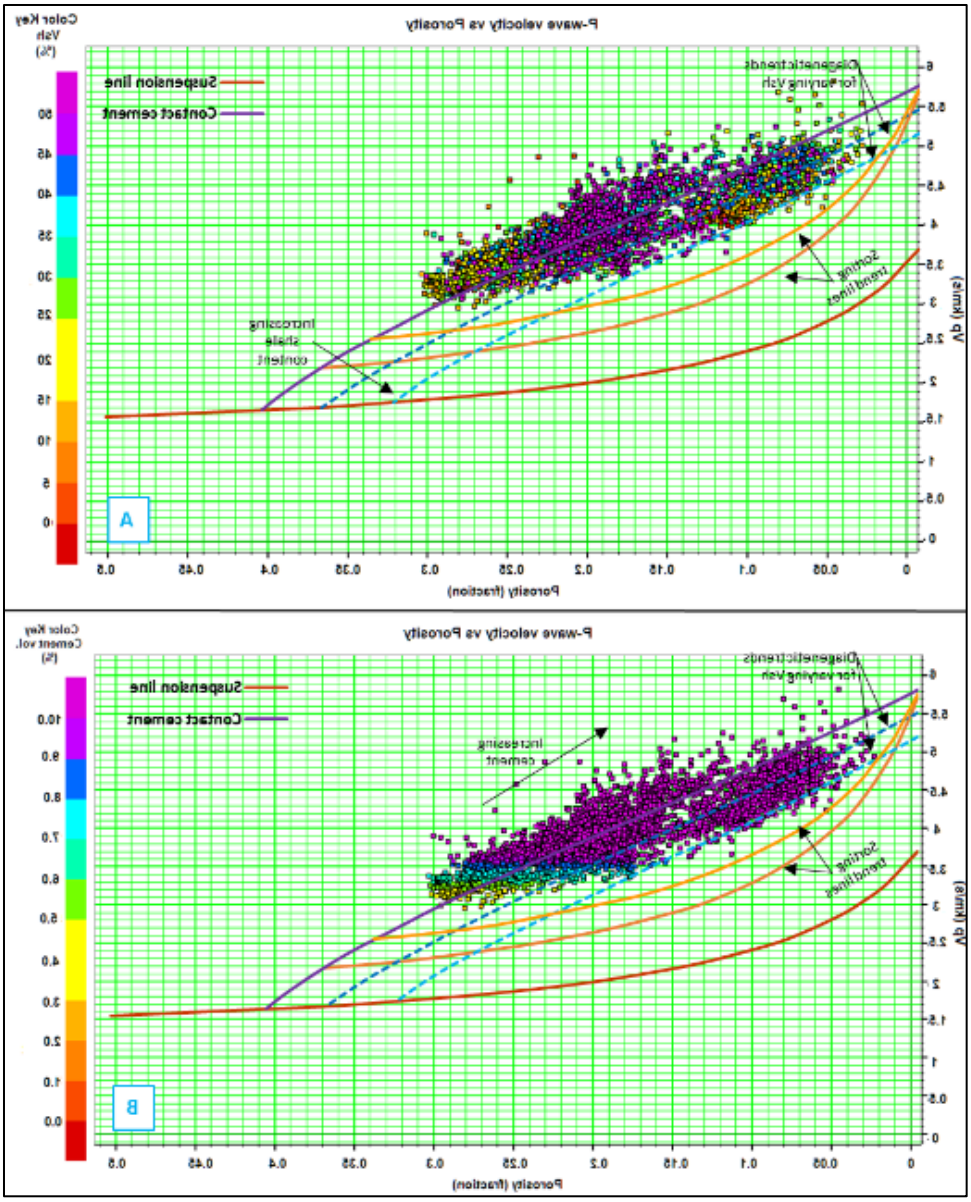

Figure 5.14: Diagnostic rock physics models overlaying all the reservoir intervals from the Nordmela Formation. a) The data is color-coded by shale volume lower than 50%, and b) The data is color-coded by cement volume estimated by Marcussen et al. (2010).

Finally, on well 7220/7-2 (Skavl), the rock cement models based on the data from the Fruholmen formation are created (Fig. 5.17). In Figure 5.17, it can be noticed that the data points are plotted on the sorting trends towards the contact cement line as the formation reduces the shale content. This behavior is expected since this formation consists of interbedded shales and sandstones. In addition, the velocity of the plot does not change drastically and has low values of quartz cement. In this well the formation is located above the transition zone, 810m, therefore it has not been influenced by quartz cementation.

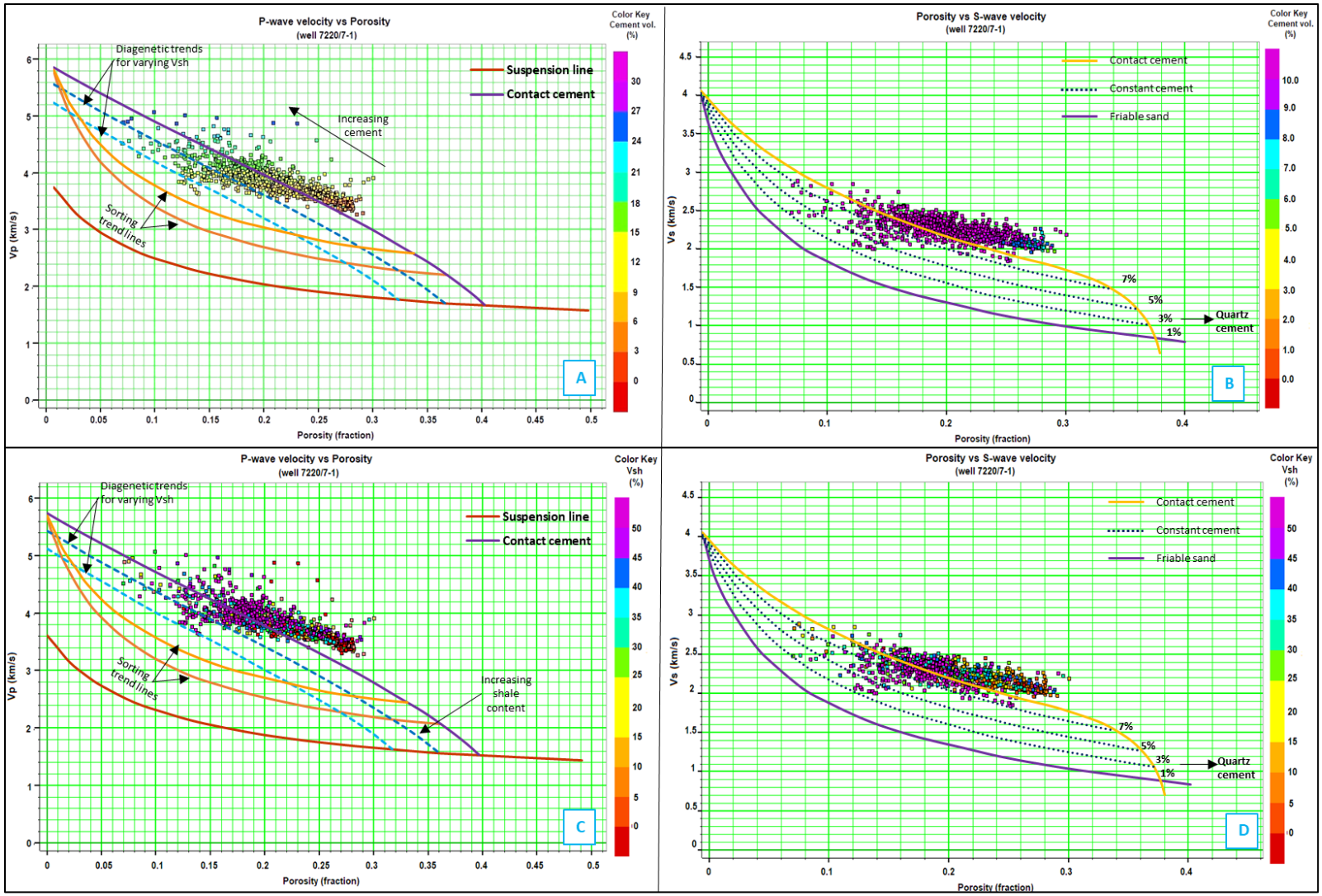

Figure 5.15: Diagnostic rock physics overlaying the data points from the Nordmela Formation from well 7220/7-1 (Havis). Insitu Vp and Vs were used. a) Vp versus PHIT color-coded by cement volume, b) Vs versus PHIT color-coded by shale volume, c) Vp versus PHIT color-coded by cement, and d) Vs versus PHIT color-coded by shale volume.

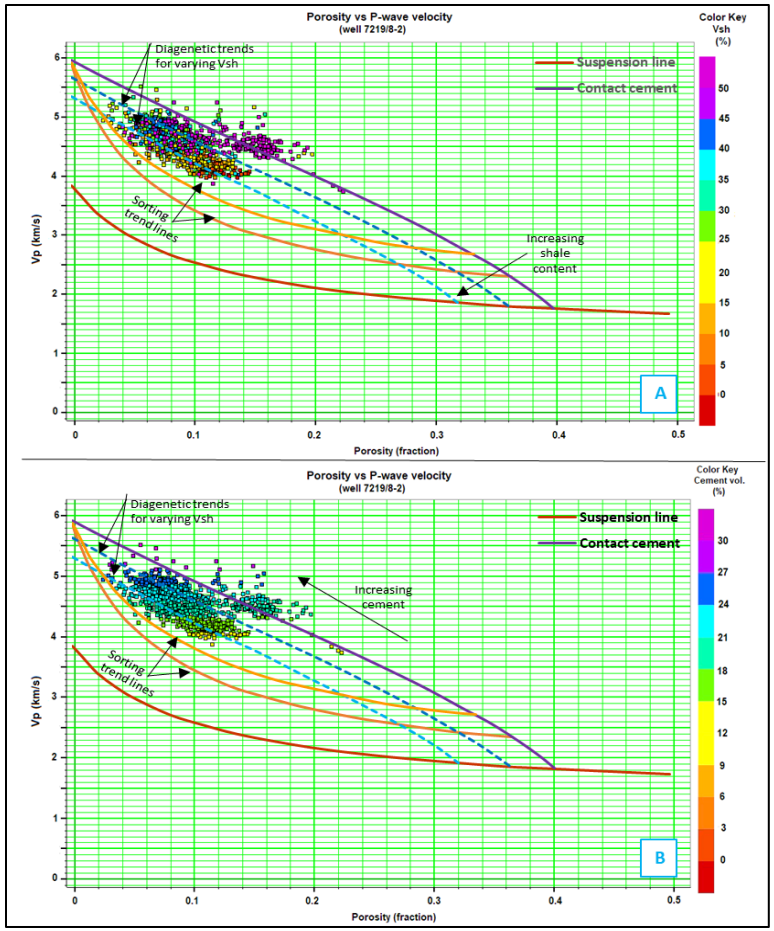

Figure 5.16: Diagnostic rock physics models overlaying the reservoir intervals of the Nordmela Formation from well 7219/8-2 (Iskrystall). Only the measured Vp is used. a) The data are color-coded by shale volume lower than 50%, and b) The data are color-coded by cement volume estimated from Marcussen et al. (2010)

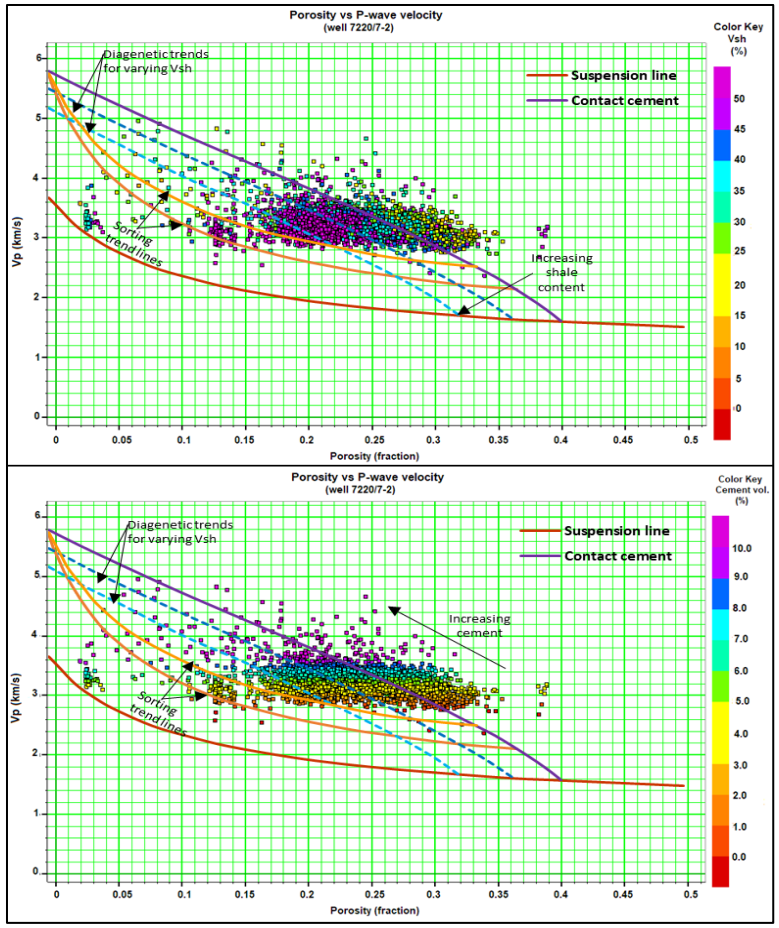

Figure 5.17: Diagnostic rock physics models overlaying all the reservoir intervals of the Fruholmen Formation from well 7220/7-2 (Skavl). Only the measured Vp is used. a) The data are color-coded based on the shale volume lower than 50%, and b) The data are color-coded by cement volume estimated from Marcussen et al. (2010)

5.1.5 LamdaRho-Mu-Rho (LMR) relationship

The transformation of velocity measurement into Lame's parameters of rigidity (μ) and incompressibility (λ) provides a general guideline for lithology and fluid discriminations. An improved identification of the reservoir zones is possible by the enhanced sensitivity to pore fluids from the incompressibility moduli and by the lithological changes represented by variations in the rigidity values (Goodway et al., 1997).

In case of a gas sand low incompressibility (< 20 GPa) and high rigidity (> 20 Gpa) are expected. It is important to remember that the rigidity parameter is insensitive to fluid changes, therefore this would help to discriminate between lithologies, while the incompressibility response would provide information about fluid content.

LMR crossplot of data from the target reservoir zones of well 7220/7-1 (Havis) shows a slight distinction between shaly and sandy intervals with an overlap of the data (Fig. 5.18). The zones that are estimated to contain hydrocarbon from the petrophysical analysis plot in the porous sand region with an incompressibility lower than 20 GPa* g/cm^3 and a rigidity from 20 GPa* g/cm^3 and higher. Nevertheless, in this analysis only results from the wells with measured Vs are included. This is because the estimated data points clustered in almost a linear trend, affecting directly the S-wave impedance. As a consequence, the results (using estimated Vs) do not provide enough information and fail to discriminate lithology or fluids.

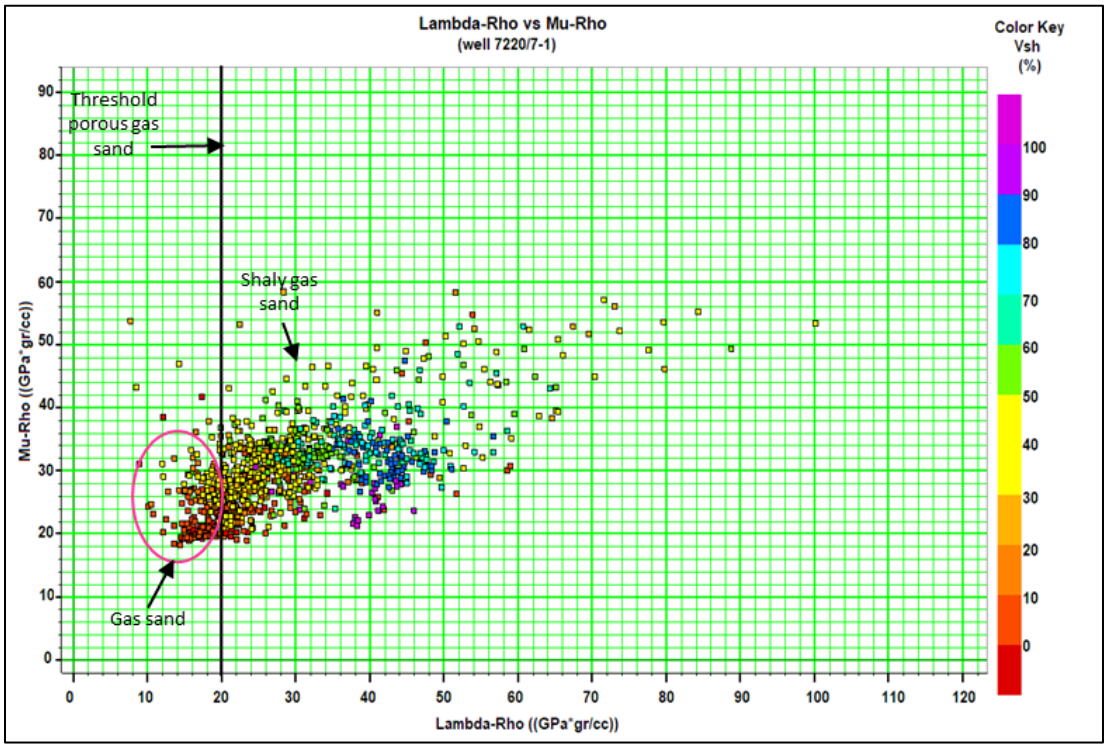

Figure 5.18: LMR crossplot of the Nordmela Formation from the well 7220/7-1 (Havis). Data is color-coded by shale volume.

The LMR results from the Stø Formation from wells 7220/7-1 (Havis) and 7220/7-3 (Drivis) are presented in Figure 5.19. This template color-coded by the cement volume is generated to investigate the response of the elastic properties with the increase of cement. More cemented sandstones are expected to plot higher in the plot with a high Mu-Rho since the rock has become stiffer. Based on the results by Marcussen et al. (2010), it can be seen that the amount of cement increases from lower left to upper right reaching a maximum of 12% of cement with a Mu-Rho between 20 – 30 GPa* g/cm^3.

In addition, the LMR results in well 7220/7-1 indicates the presence of clean sand (Fig. 5.20a and 5.20c) which correlates with the formation description on chapter 4, while the well 7220/7-3 shows a better discrimination between sand and shaly sand (Fig. 5.20b and 5.20d). In overall, for both wells, the data plots within the porous gas sand interval from Goodway et al. (1997), the average gas saturation estimated from the petrophysical analysis indicates up to 20% in well 7220/7-1 and 6% for well 77220/7-3.

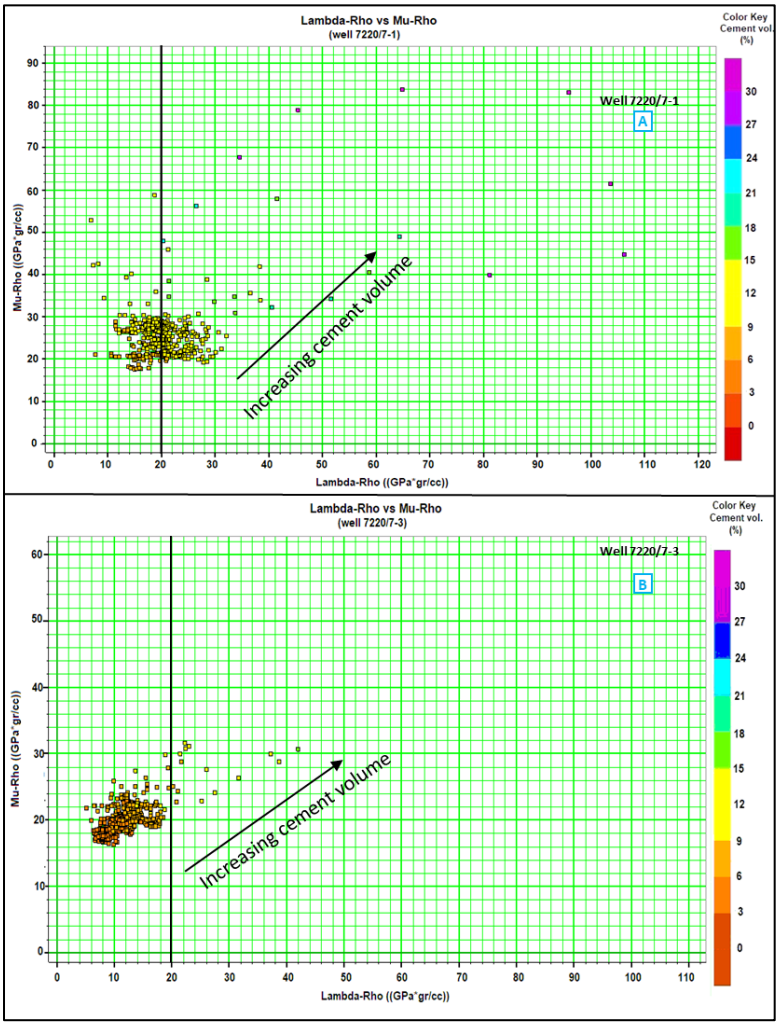

Figure 5.19**:** LMR crossplot of the Stø Formation of wells 7220/7-1 (Havis) (a) and 7220/7-3 (Drivis), (b) using measured Vs and color-coded by cement volume estimated by Marcussen et al. (2010).

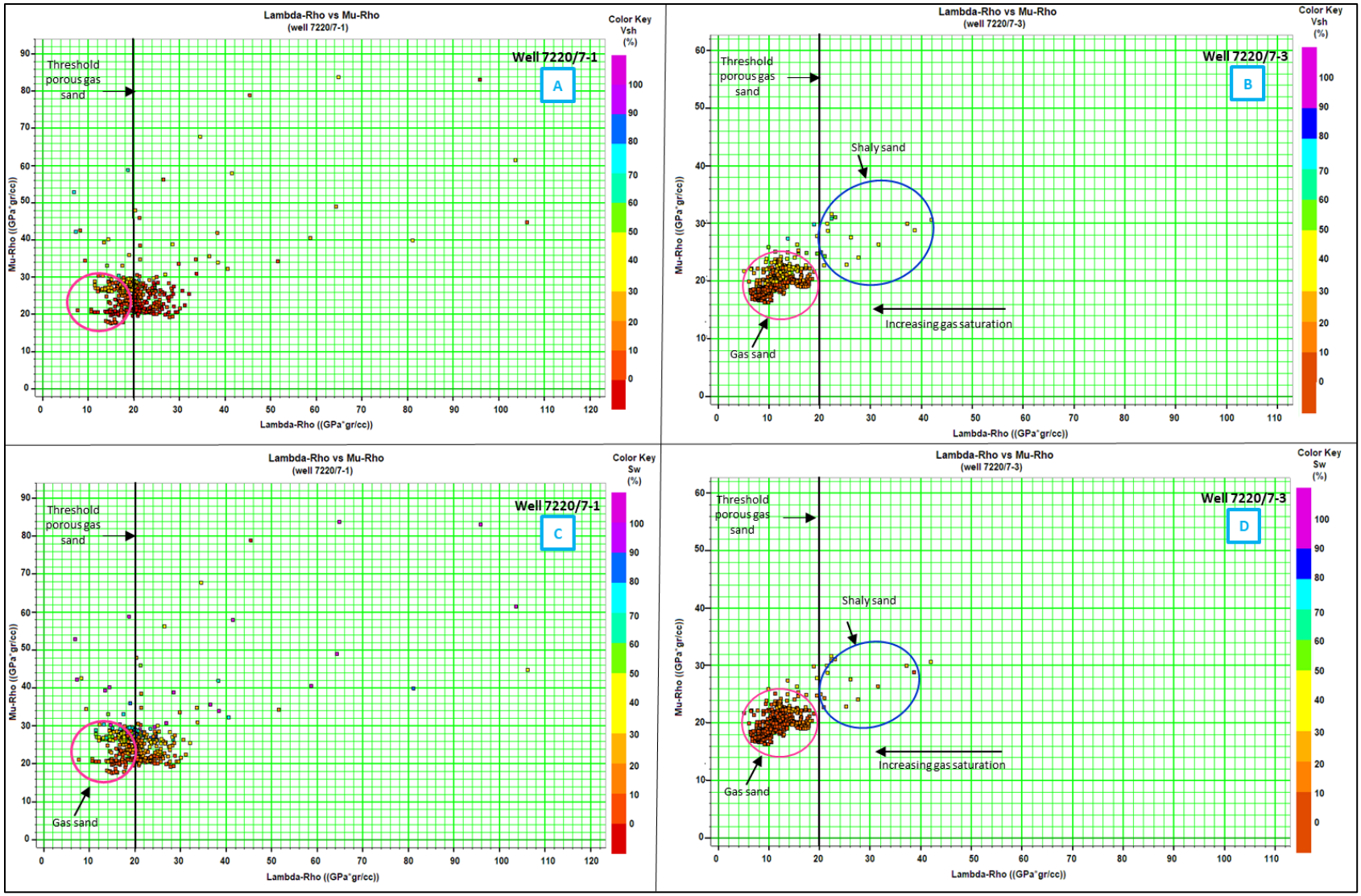

Figure 5.20: LMR crossplot of the Stø Formation for wells 7220/7-1 and 7220/7-3. Data points color coded by shale volume on top (a,b); and Data points color coded by water saturation at the bottom (c,d).

In Figure 5.21 the LMR crossplot associated with the amount of cement of the Normela Formation is presented. It can be seen how the cement volume increases from lower left to upper right. As a consequence, the Mu-Rho and Lamda-Rho values increase with the cement amount, reaching a value of 32 GPa* g/cm^3 and 44 GPa* g/cm^3 respectively. As the amount of cement increase, the rock becomes stiffer affecting the sensitivity of the elastic parameter to fluids.

Finally, the LMR crossplot of Nordmela Formation LMR is shown in Figure 5.22 for wells 7220/7-3 (Drivis) and 7219/8-2 (Iskrystall). In both cases, the gas sand can be found in the gas sand interval, however, the well 7219/8-2 has higher Mu-Rho values up to 56 GPa* g/cm^3 and low Lamda-Rho. Additionally, the shaly sands saturated with water and shales plotted on the left side of the threshold suggesting an accurate lithology and fluid discrimination. From the petrophysical analysis presented in Chapter 4, the saturation of gas in Nordmela Formation is estimated 16% in well 7220/7-3 (Drivis) and 37% in well 7219/8-2 (Iskrystall).

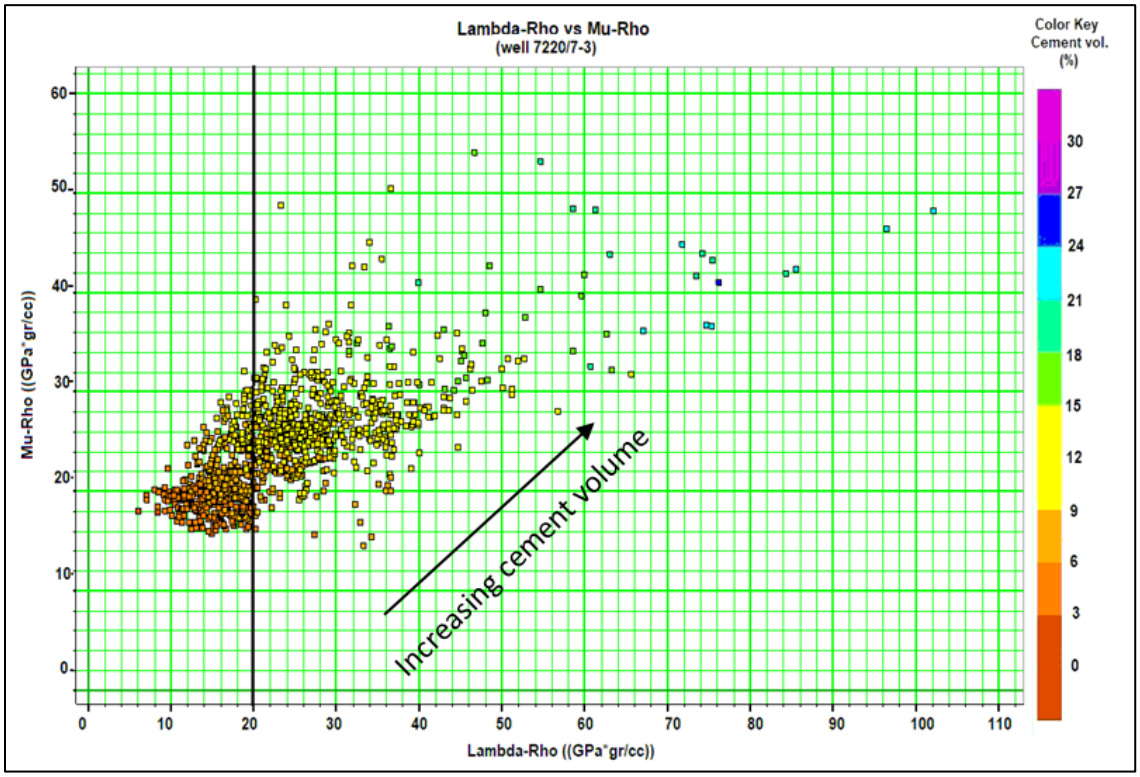

Figure 5.21: LMR crossplot of the Nordmela Formation of well 7220/7-3, with measured shear velocity and color-coded by cement volume estimated by Marcussen et al. (2010).

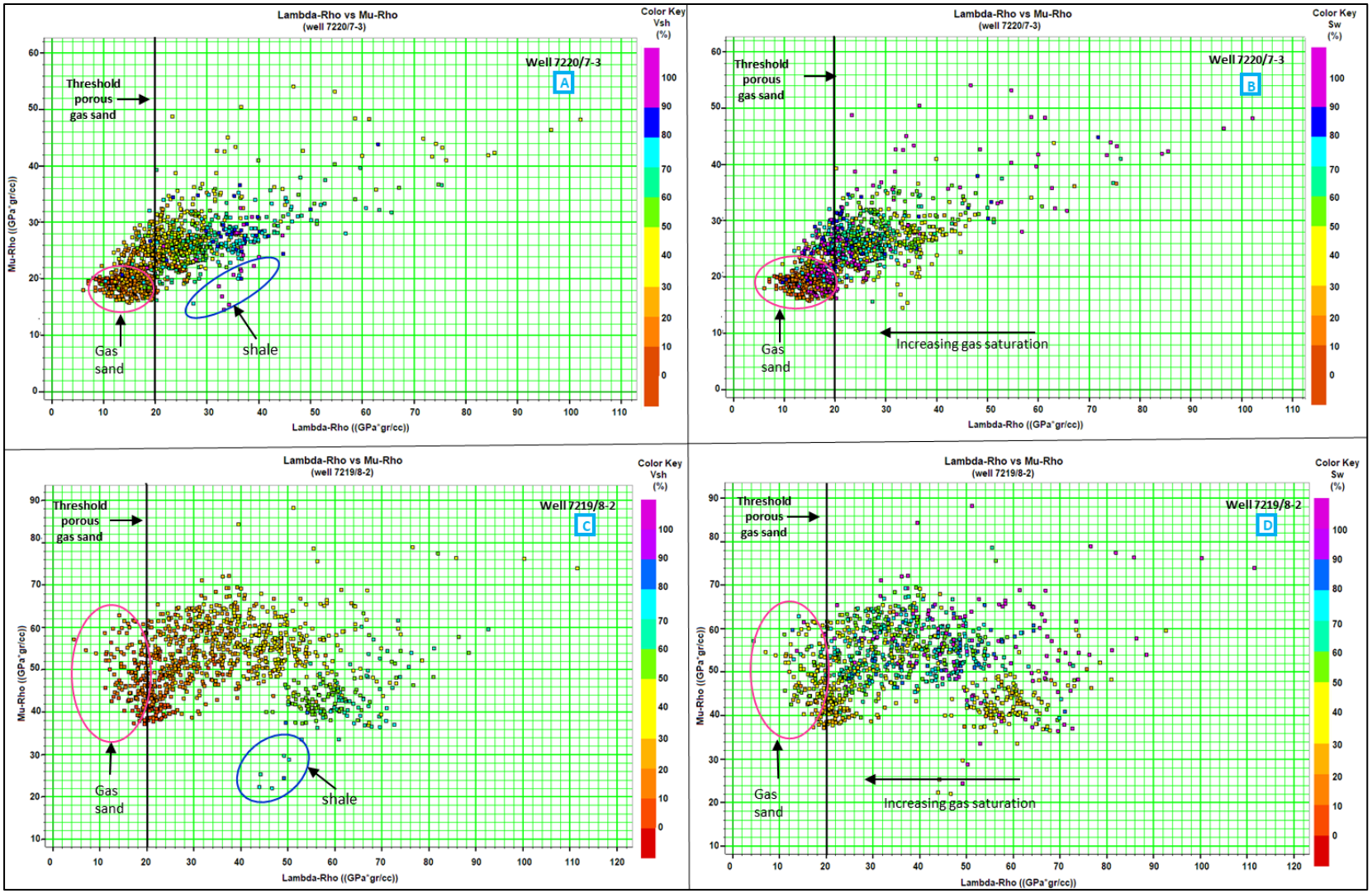

Figure 5.22: LMR crossplot of the Nordmela Formation for wells 7220/7-3 and 7219/8-2. Data points color-coded by shale volume on the left side (a,c); and Data points color-coded by water saturation on the right side (b,d).

5.1.6 Vp/Vs versus Acoustic Impedance (AI)

As discussed earlier, rock physics templates provide links between the elastic parameters and the reservoir properties, which helps to estimate the lithology and fluid content within the area of interest. The Vp/Vs versus AI template helps to differentiate the data points to certain trend based on porosity, lithology and saturation values. Therefore Vp/Vs vs AI template plays an important role to discriminate lithology and fluid in the reservoir.

In this study, a rock physic template is created in the Hampson and Russell software, on which the input parameters are assumed 4GPa and 4.4 GPa for the dry bulk and shear modulus respectively, an effective pressure of 20 MPa, critical porosity of 40%, and density of the matrix of 2.65 g/cm^3.

In Figure 5.23 reservoirs from Stø Formation from well 7220/7-1 (Havis) is presented. Even though this well contains the less thick net pay section (67.13 m), it is observed that most of the data is plotted on the gas sand trend and has low Vp/Vs values, since the Stø Formation is considered a clean sand with less than 20% of clay content according to the petrophysical results (Chapter 4).

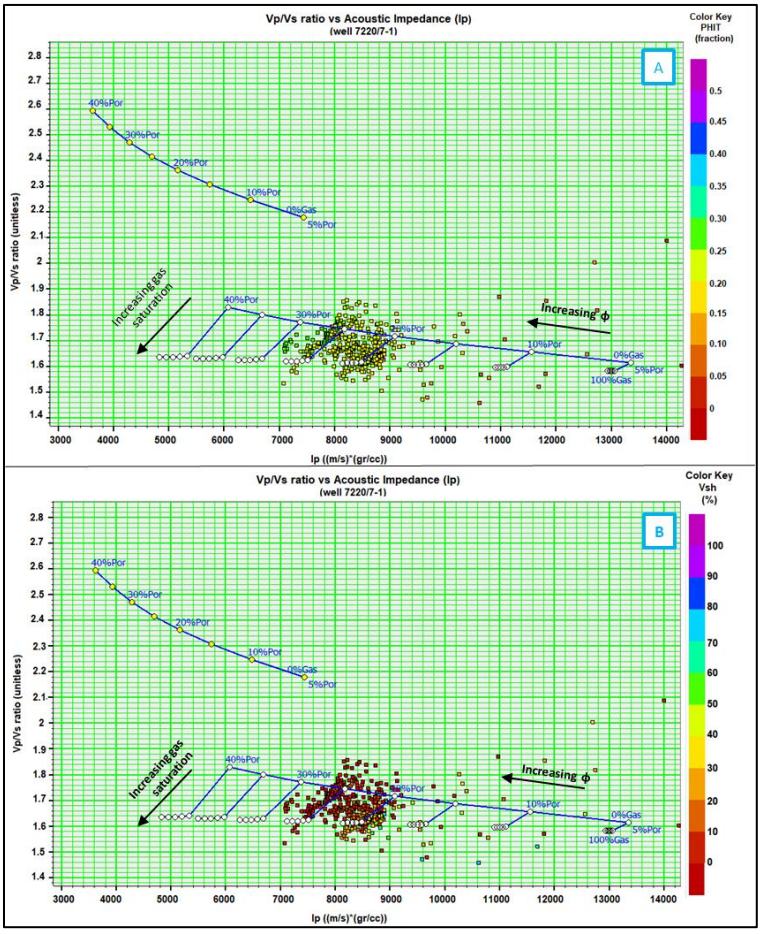

Figure 5.23: Vp/Vs versus AI crossplot of data from the Stø Formation from well 7220/7-1 (Havis). a) The data is color-coded based on the total porosity, and b) The data is color-coded based on the shale volume.

In Figure 5.24, additional to the Stø Formation, the Fuglen Formation data are added. A good discrimination between clean sand and shale data is detected, with shale from the Fuglen Formation plotting in a different trend compared to the Stø Formation sands.

The cleanest sands with hydrocarbon are plotted on the gas sand lines with low Vp/Vs of 1.6 – 1.7 and AI ranging from 6300 – 7800 (m/s)*(g/cm^3) for the well 7220/7-3 (Drivis); while for the well 7219/8-2 (Iskrystall) the Vp/Vs ranges from 1.5 – 1.7 and the AI from 9000 – 12000 (m/s)*(g/cm^3). The increment in the AI response between wells might be due to the fact that the Stø Formation is deeper in the well 7219/8-2 and looking more closely to the petrophysical analysis the porosity has also decreased in this zone, been 8% the average porosity. Therefore, the increase of the burial depth might cause a decrease of the porosity making the rock denser increasing the velocity.

The Fuglen cap rock plots in the vicinity of the shale model fitting properly between the porosity range estimated during the petrophysical analysis.

An example of the Nordmela Formation in wells 7220/7-3 and 7220/7-1 is shown in Figure 5.25. In overall, a good discrimination between lithologies can be identified. The sands with less than 20% of shale volume plot on the gas sand lines, while the shaly sand (Vsh > 40%) and shale plotted towards the shale line.

The clean sand points are interpreted in the petrophysical analysis as hydrocarbon-bearing plot under low Vp/Vs values (1.6- 1. 8) in both wells, and acoustic impedance ranging from 6500 – 9500 (m/s)*(g/cm^3), and 7000 -10000 (m/s)*(g/cm^3) for wells 7220/7-3 (Drivis) and 7220/7-1 (Havis) respectively. In this case, the variation between AI is not that remarkable since both wells are relatively close to each other, therefore the depth difference is not that significant (1376m BSF in well 7220/7-1 and 1072m BSF in well 7220/7-3), compared to the previous example from the Stø Formation where the distance between studied wells is quite large (Figure 1.2).

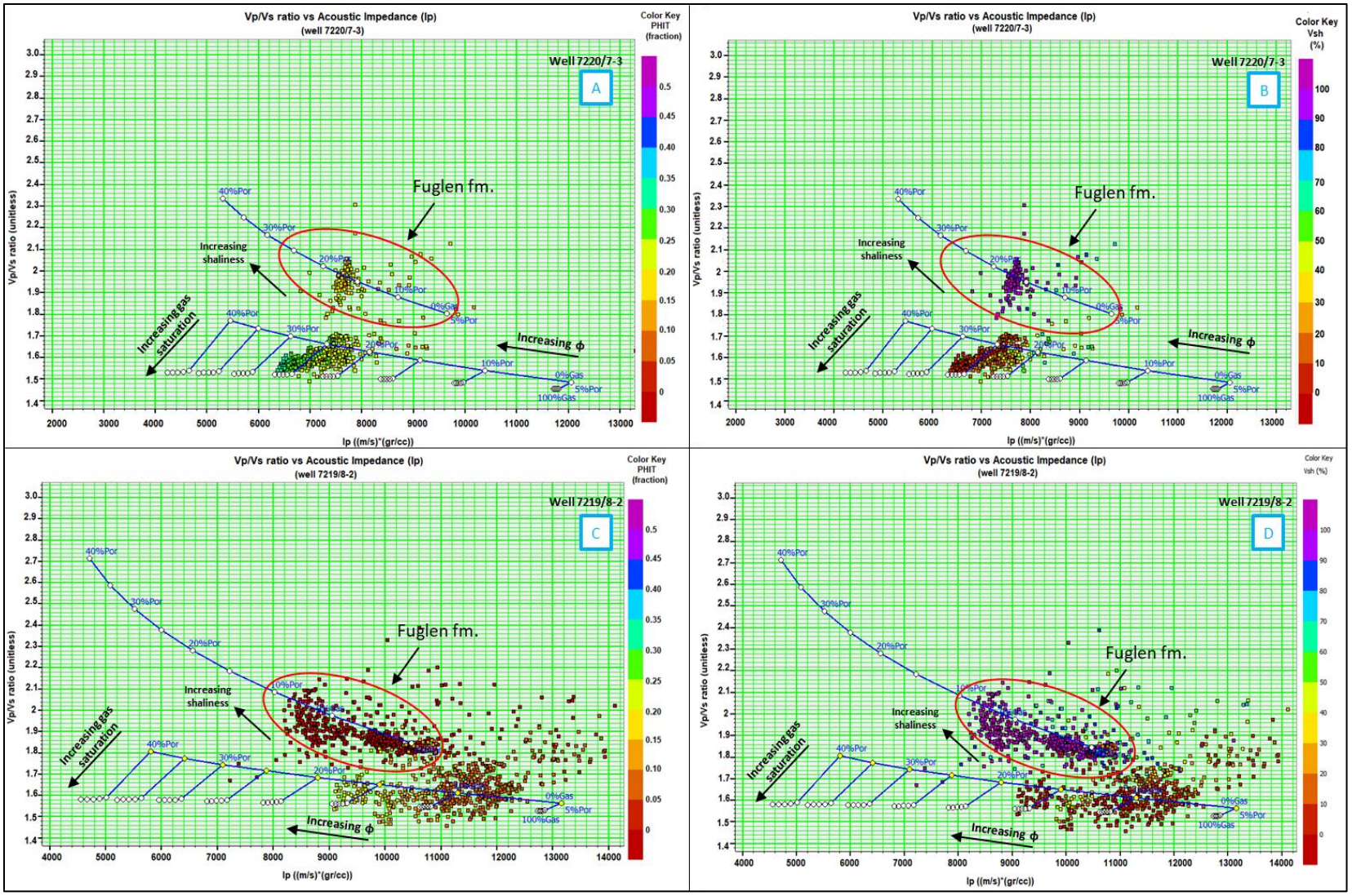

Figure 5.24: Vp/Vs versus AI plot from the Stø and Fuglen Formations in wells 7220/7-3 (Drivis) and 7219/8-2 (Iskrystall). The arrows indicate the direction towards the property is increasing. The data is color-coded based on the total porosity (a, c), and color-coded based on the shale volume (b,d).

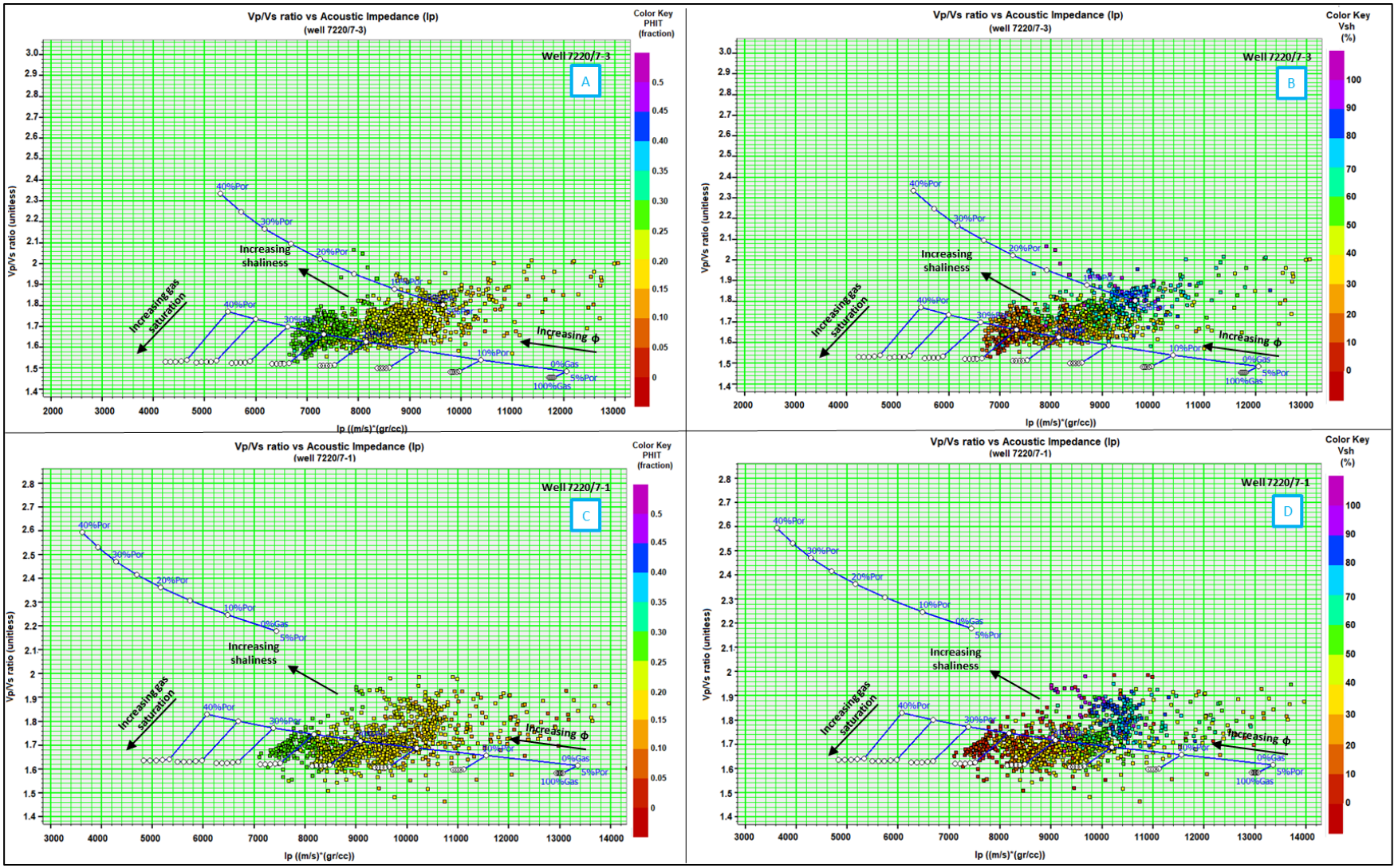

Figure 5.25: Vp/Vs versus AI plots for the Nordmela Formation from wells 7220/7-3 (Drivis) and 7220/7-1 (Havis). The arrows indicate the direction towards the property is increased. On the left side the data is color-coded by total porosity (a, c), and by on the shale volume (b,d).

If the template is investigated more closely for well 7220/7-3 (Havis) where the Stø Formation has the thickest net pay (74.85 m), a good correlation between the porosity estimated by petrophysical analysis (Chapter 4) and the one inferred from the template can be seen. The water saturation calculated around 6% in the petrophysical analysis plotted in the expected water saturation range of the template from 0 to 10% (Fig. 5.26).

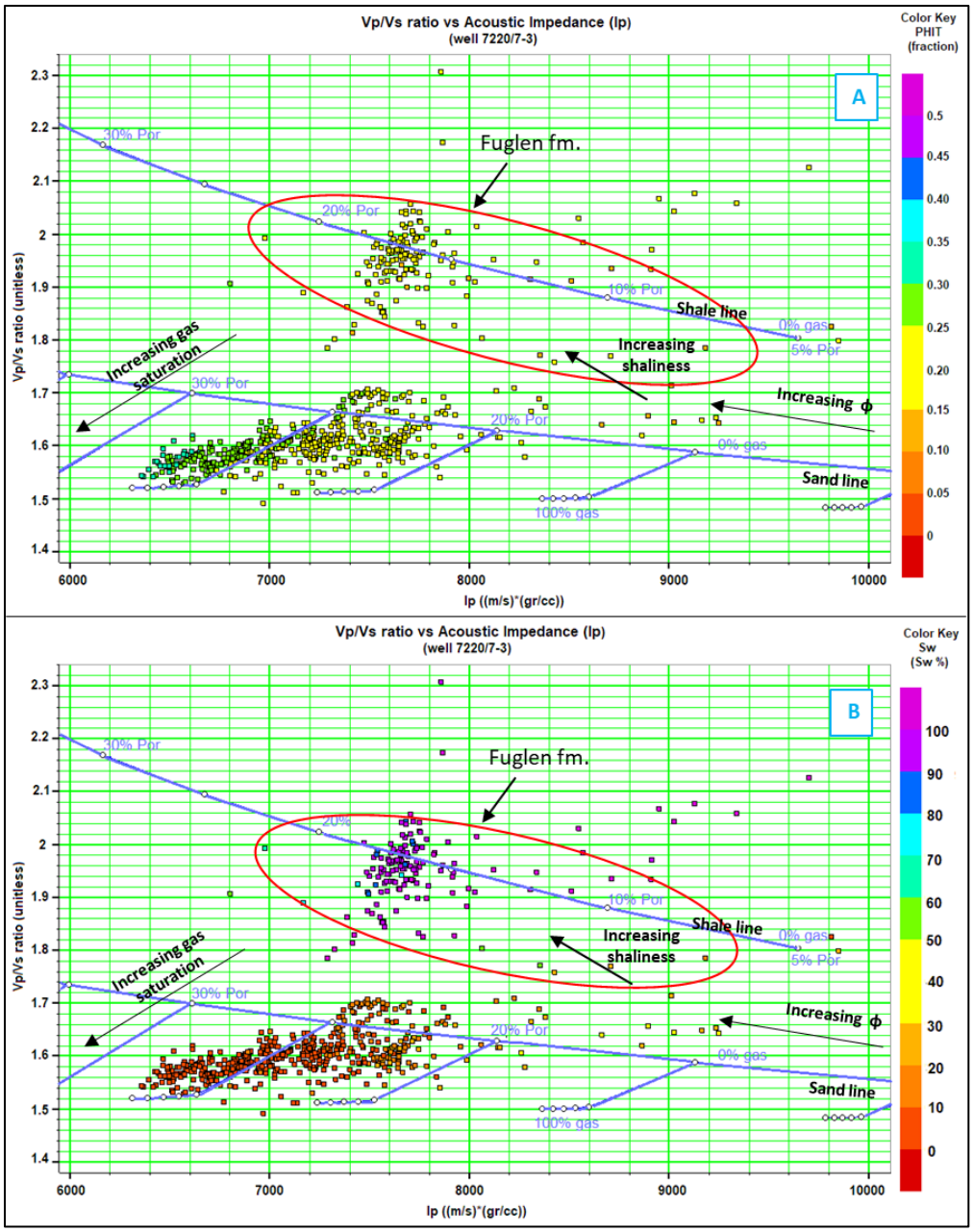

Figure 5.26: Vp/Vs versus AI crossplot with data from the Stø Formation sandstones reservoir and the Fuglen Formation cap rock for the well 7220/7-3 (Drivis). The data is color-coded by total porosity (a) and water saturation (b).

Finally, in Figures B.5 and B.6, a general overview of Vp/Vs versus AI relations of the Stø and Nordmela Formations are presented. In both Figures, it is also confirmed a better fitting between the petrophysical analysis and the rock physics diagnostics.

5.2 Discussion

5.2.1 Effect of clay

The effect of the clay content within a consolidated rock has been analyzed using porosity vs Vsh, Vp versus Vsh crossplots, and Han's (Han et al., 1986) and Marion (Marion et al., 1992) models.

Overall, most of the results from this study match nicely with Marion's model (Marion et al., 1992). The results show a similar inverted V-trend in the Vp versus Vsh plots, and V-behavior on the porosity versus Vsh plots. The trends are more evident on those formations with a shale volume above 50% such as Nordmela and Fruholmen Formations (Fig. 5.2 and 5.4).

According to the model proposed by Marion et al. (1992) the zone that reaches the maximum velocity or minimum porosity, define the transition zone between grain supported to clay supported matrix (Fig. 5.27). On this plot is proven how the variation of the clay content within the sand can influence the seismic properties, velocity, especially when the composite began to be clay supported.

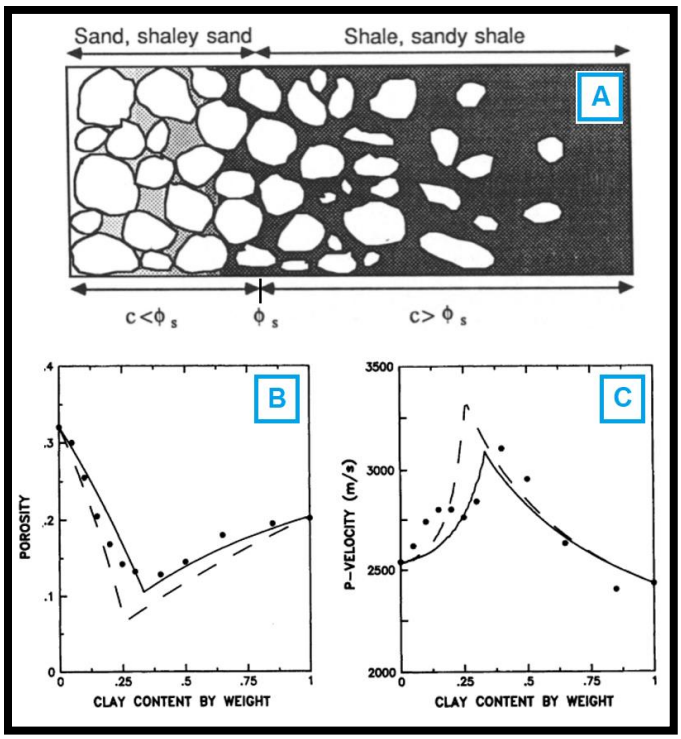

Figure 5.27**:** Shale effect in a sand-clay mixture. a) representation of the shaly sand model that shows increasing shale content towards the right, b) porosity versus Clay content, and c) P wave velocity versus clay content (modified from Marion et al. 1992).

In both cases, an increase of the velocity and porosity reduction is observed as the shale volume reaches 28 to 30%. Once this point is reached, both properties changed their response in the opposite direction since it defines the shift from a grain supported to clay supported sediments. In case of a clean sand formation (Vsh ≤ 50% in Stø Formation), those trends are not found in this study since the shale volume is very low and is gas saturated.

If the results are compared with Han's (1986) models, a certain trend is identified for an increasing shale volume (towards the lower left) while the porosity is reduced and the velocity increase. These behaviors are distinct not only on the Nordmela and Fruholmen Formations but also in the Stø Formation. However, the data points have shown certain misfit between the lines and the clay content, this might be due to a misleading shale volume estimation during the petrophysical analysis, or probably because the shale proportion is not necessarily in consonance with the variable clay volume used by Han's models. An example is shown in the Stø Formation from well 7220/7-3 (Fig. 5.5), where the formation is identified as clean sandstone with less than 40% shale volume. Even though the data points fit between the 0% and 40% clay lines, the estimated shale volume does not match with the percentage defined on Han's models.

Nevertheless, in Nordmela and Fruholmen Formation, the estimated shale volume provides a good fitting with the models. The Nordmela Formation plots between 0%-20% clay with a few points on the 30% (Figure 5.6); while the Fruholmen Formation points plotted on 0%-50% clay, a response that is in agreement with the lithology and shale volume estimated in the petrophysical analysis in chapter 5 (Fig. 5.7).

5.2.2 Chemical Compaction and Cementation

Prediction of the cement amount based on Marcussen et al. (2010) using Vp measurements are discussed. However, the accuracy of the results would be higher if they are compared with thin section studies. Due to short time frame, thin-section studies are not included in the study; instead results from previous study Saadullah (2015) are utilized. A comparison between Saadullah's analysis and the cement model (Fig. 5.11) from Stø Formation is carried out. The study found that the sandstones are quartz arenite with more than 95% of quartz and are affected by quartz and carbonate cement (siderite) during early diagenesis. In Figure 5.27, a thin section of a sample located at depth 1829m in well 7220/7-1 (Havis) shows quartz overgrowth on the grain and illite.

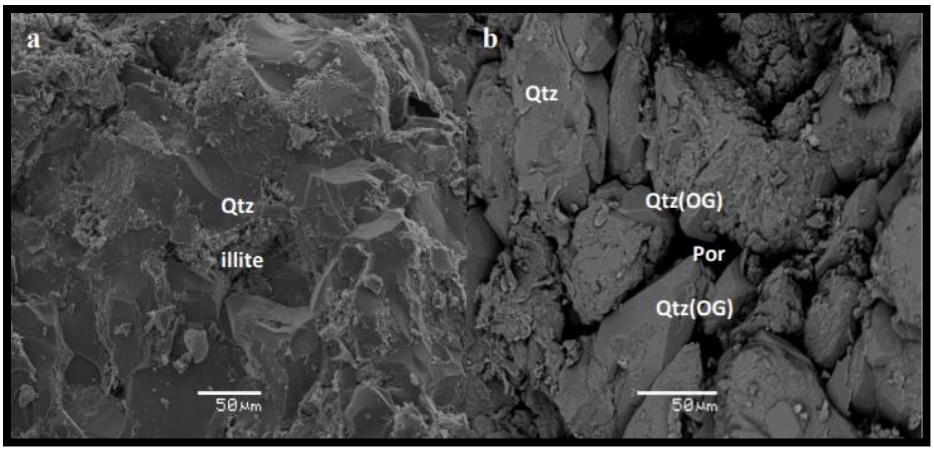

Figure 5.27**:** XRD results from the well 7220/7-1 (Havis), show quartz overgrowth, K-feldspar, and illite (modified from Saadullah, 2015).

Moreover, in this study the data points from the Stø Formation plot on top of the contact cement model showing a drastic change in the velocity within a small range of decreasing porosity, a response that may be attributed to cementation (Fig. 5.11). This is confirmed in Saadullah's study (2015) and in the compaction and uplift analysis.

The uplift is estimated to be 1100m; therefore maximum burial of the formation is estimated about ~2476m BSF(above ~80˚C) that represents a depth of early phase of quartz cementation before they uplift (Fig. 5.28).

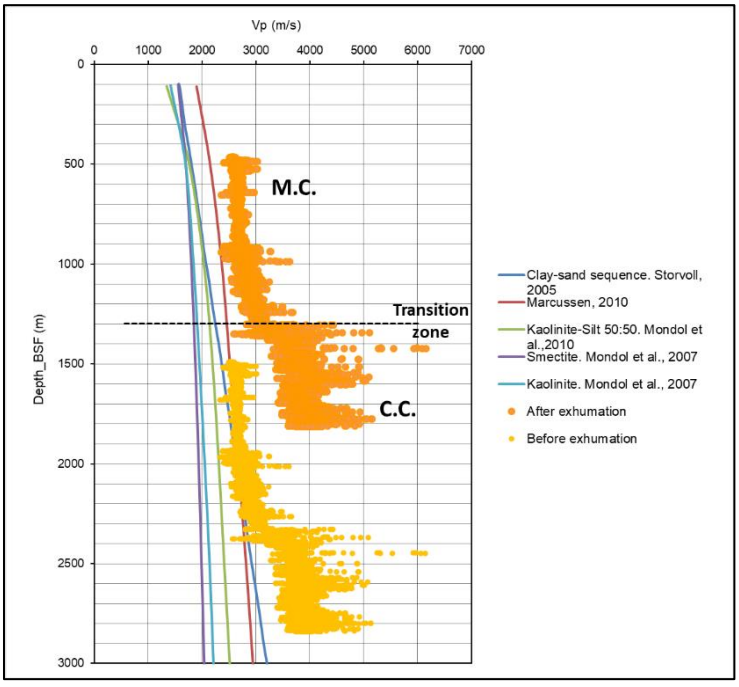

Figure 5.28: Crossplot of Vp versus depth, of the published trend (Marcussen et al., 2010; Mondol et al., 2007; Storvoll et al., 2005) and the data from well 7220/7-1 (Havis).

However, in wells where the formation is located at shallow depth (e.g.7220/7-3), the response in the velocity versus porosity varies significantly (Fig. 5.13). This behavior is attributed to a low cementation rate, which points towards some influence of chemical compaction. Before exhumation correction, the Stø Formation is located at 1072 m BSF below the transition zone (Fig. 5.29). Considering a thermal gradient of 36 ˚C, a total depth of 2095m, water depth of 345m, and 1050 of uplift, then the reservoir was located at the starting point of the quartz cement generation (~ 2 km) before the uplift, and has therefore been less involved in the cementation process.

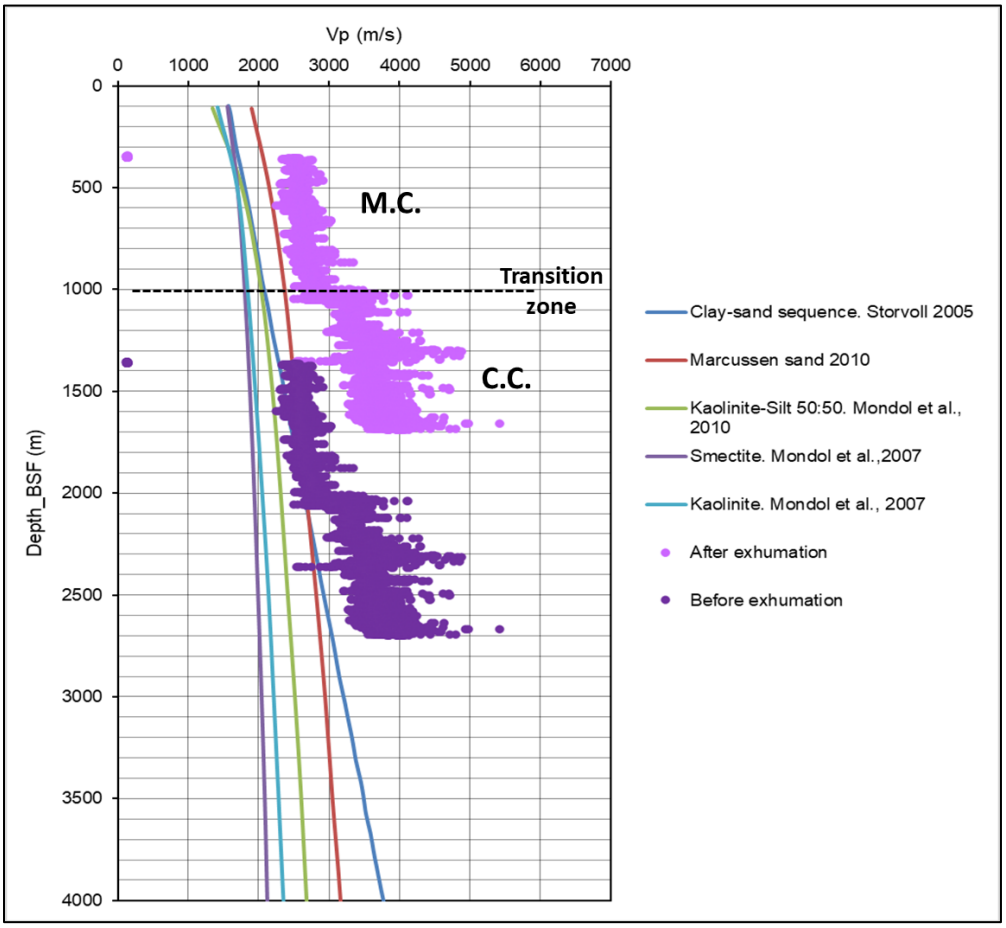

Figure 5.29: Crossplot of Vp vs depth, of published trend (Marcussen et al., 2010; Mondol et al., 2007; Storvoll et al., 2005) and the data from the well 7220/7-3.

The thin sections from the Nordmela Formation (Saadullah, 2015) are also used during correlation (Fig. 5.30) for well 7220/7-1 (Havis). In this study, the formation is described as well to moderately sorted sand, with a porosity decrease caused by carbonate (siderite) and quartz cement, with a minimal proportion of kaolinite and illite filling the pores. Comparing these observations with the cement model templates in Figure 5.15, it is noticed that most of the data points are scattered from the constant cement line of 7% to the contact cement line, with a sharp increase in the velocity in a comparison to the porosity. A considerable increase in velocity and porosity reduction is remarkable on well 7219/8-2 (Iskrystall) where the formation is located at greater burial depth.

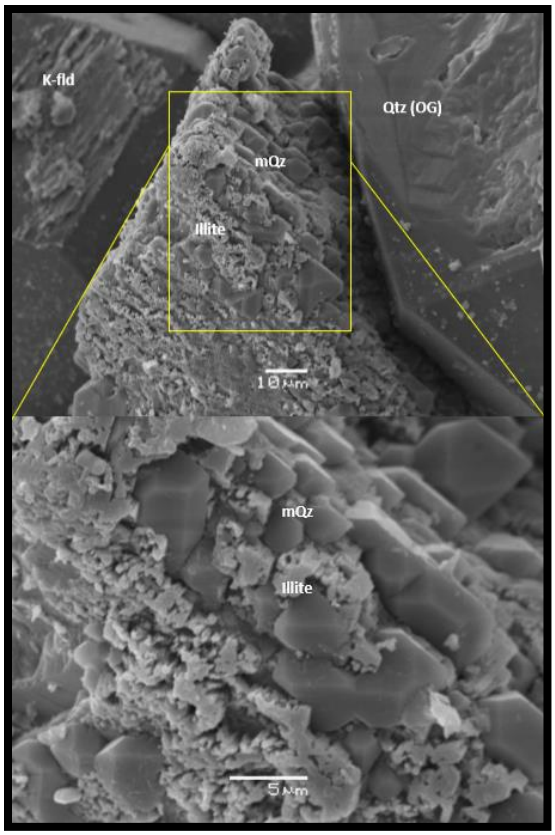

Figure 5.30: XRD results from the Nordmela Formation of well 7220/7-1 (Havis) at 1922m depth, showing micro quartz coating. (modified from Saadullah, 2015).

From a closer look in the uplift and compaction analysis, the depth of the formation is defined, in both wells, below the transition zone in the chemical compaction domain 1452m BSF in well 7220/7-1 and 2610m BSF in well 7219/8-2 (Fig. 5.28 and 5.31). However, the original depth before the uplift is 2552m BSF and 3560m BSF in well 7220/7-1 and 7219/8-2 respectively. From these observations, a good correlation is established between the cement models and the compaction study. The deeper well 7219/8-2 of the formation is above 100 ˚C, and therefore a high cementation is identified making the rock stiffer due to significant porosity reduction.

Finally, in case of the Fruholmen Formation the cement model templates (see Fig. 5.17) has indicated an equitable distribution of the data points from the sorting trend to the contact cement line due to the higher shale content. In addition, a steady velocity response suggested a low cementation rate at this depth, which is confirmed in the uplift and compaction analysis (Fig. 5.32). Based on the last analysis and considering an uplift of 1200m, a water depth of 349m, and a thermal gradient of 36 ˚C/km, the reservoir is estimated to be at 2010m before the uplift having some influence from the chemical compaction but not enough to generate a considerable amount of cement.

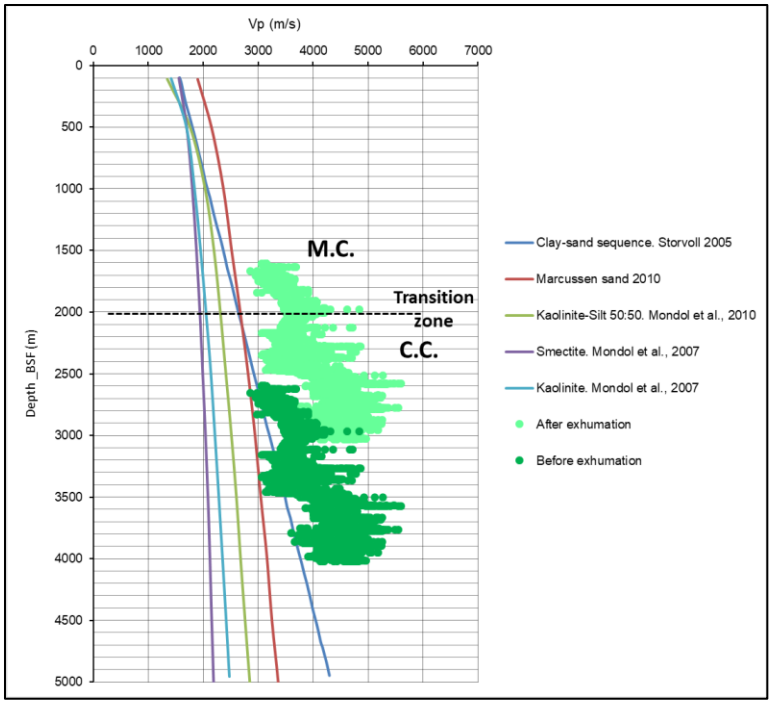

Figure 5.31: Crossplot of Vp versus depth, of published trends (Marcussen et al., 2010; Mondol et al., 2007; Storvoll et al., 2005) and the data from well 7219/8-2 (Iskrystall).

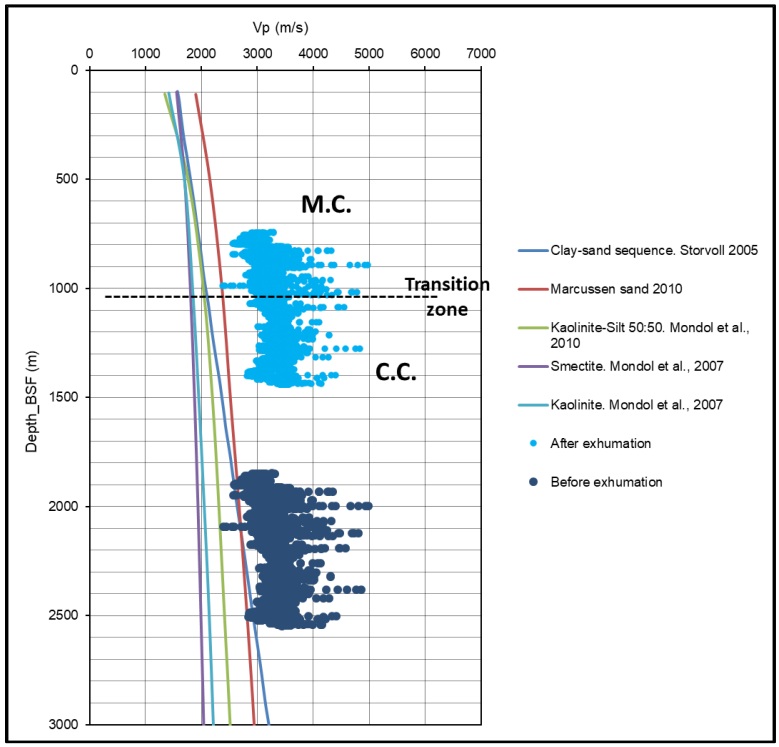

Figure 5.32: Crossplot of Vp vs depth, of published trends (Marcussen et al., 2010; Mondol et al., 2007; Storvoll et al., 2005) and the data from well 7220/7-2 (Skavl).

5.2.3 Fluid and Lithology Discrimination

By employing Vp/Vs versus AI and LMR crossplots lithology and fluid discrimination could be done in the target formations. Shale volume, porosity, water saturation and cement volume are taken from the petrophysical analysis and used as the properties during the litho-fluid discrimination process.

In general, in the Vp/Vs versus AI crossplot, the gas-saturated intervals from the Stø Formation plot on the model sand line in a porosity range of 15% - 25% and water saturation above 10% that correlates reasonably well with porosity and saturation values estimated through the petrophysical analysis. In case of well 7220/7-1 (Havis) the values are φ= 20% and Sw= 20%; whereas in well 7220/7-3 (Drivis) φ=23% and Sw= 6% (Fig. 5.23, 5.24 and 5.26). Moreover, in Figure 5.24 the cap rock (Fuglen Formation) is included along with Stø Formation just to check the accuracy of the method. At first, a good discrimination between shales and sandstones is noticeable. The data points from the Fuglen Formation plotted along the shale trend while the Stø Formation plotted along the sand line.

A small amount of cement has been proven to exist within the Stø Formation in well 7220/7-1 (Havis), having a stiffening effect on the rock but it did not affect the AI response. Further, on the LMR plots, both wells displayed an increase in the shear response not only because of the fluid content but also for the cement (Fig. 5.20). The data are plotted below the cutoff value of $\lambda\rho$: 20 GPa*g/cm^3, which defines the threshold for the gas bearing sand (Fig. 5.19).

Furthermore, the Vp/Vs versus AI crossplot of Nordmela Formation shows a good lithology discrimination (Fig. 5.27). The clean sandstones (Vsh $\leq$ 25%) are distributed along the sand model lines, but as the Vsh increases the data starts to plot in the direction marked by the black arrow (Fig. 5.25). The points located on the sand line are distributed properly between the porosity range of 15% - 30% and correlates with the estimated porosity of the upper reservoirs, φ= 22% in well 7220/7-1 (Havis) and φ=23% in well 72207-3 (Drivis). Comparing that observation with the LMR results the gas-saturated sands are plotted on the porous gas sand interval, showing a decrease on the incomprehensibility and an increase of the rigidity caused also by the increase of cement.

5.3 Uncertainties

- Since only half of the wells contained direct Vs measurement, the rock physics diagnostic are limited to wells 7220/7-1 (Havis), 7220/7-3 (Drivis) and 7219/8-2 (Iskrystall). The estimated Vs data are not able to discriminate between lithology and fluid saturation.

- The rock physics models of Marion (1992) is developed based on unconsolidated, brine saturated shaly sand. While Han et al., (1986) models assumed well sorted shaly sandstones saturated with brine. Changes in the fluid type, geological scenario, sorting, burial depth and pressure would generate results with a different response than the expected. Thus those variables must be considered during the creation of the rock physics templates.

The pre-existing RPT which describes the cement models using velocity versus porosity are based on a dry rock with a specific effective pressure, dry shear and bulk modulus adjusted for a given case.

- The effective pressure is computed assuming a constant pressure gradient of 10 kPa/m, and it is used as an input on the rock physic model. Nevertheless, several geological variables might cause changes in the effective pressure.

- Due to restricted time frame, a proper compaction study and thin section analysis is not performed in this study. The validation of the results lies mainly in previous publications that considered in the study.

- The cement volume estimated using Marcussen et al. (2010) equation is accurate on lithologies that are similar to the Etive sandstones in the North Sea, while the current data has been developed on a different geological setting with variations on the sediment composition.

Chapter 6: AVO Modeling

The AVO modeling is considered an effective technique for reservoir characterization. Through this method, it is possible to understand the seismic response when lithology and/or fluids changes within a reservoir. In this chapter results from AVO modeling applied for few wells are discussed. This includes the sensitivity analysis caused by the parameter selection for the creation of synthetic seismogram and the changes in the AVO signature when fluid substitution is performed.

The reservoir used for modeling are located at different depths and have different properties. The location of the wells used in AVO modeling is shown in Figure 6.1 and a general overview of the Stø and Fuglen Formations distribution along the studied wells Figure 6.2. The information related to AVO modeling is summarized in Table 6.1. The reason for this selection is to detect possible variation on the AVO modeling when variations in depth, thickness, and shaliness are involved.

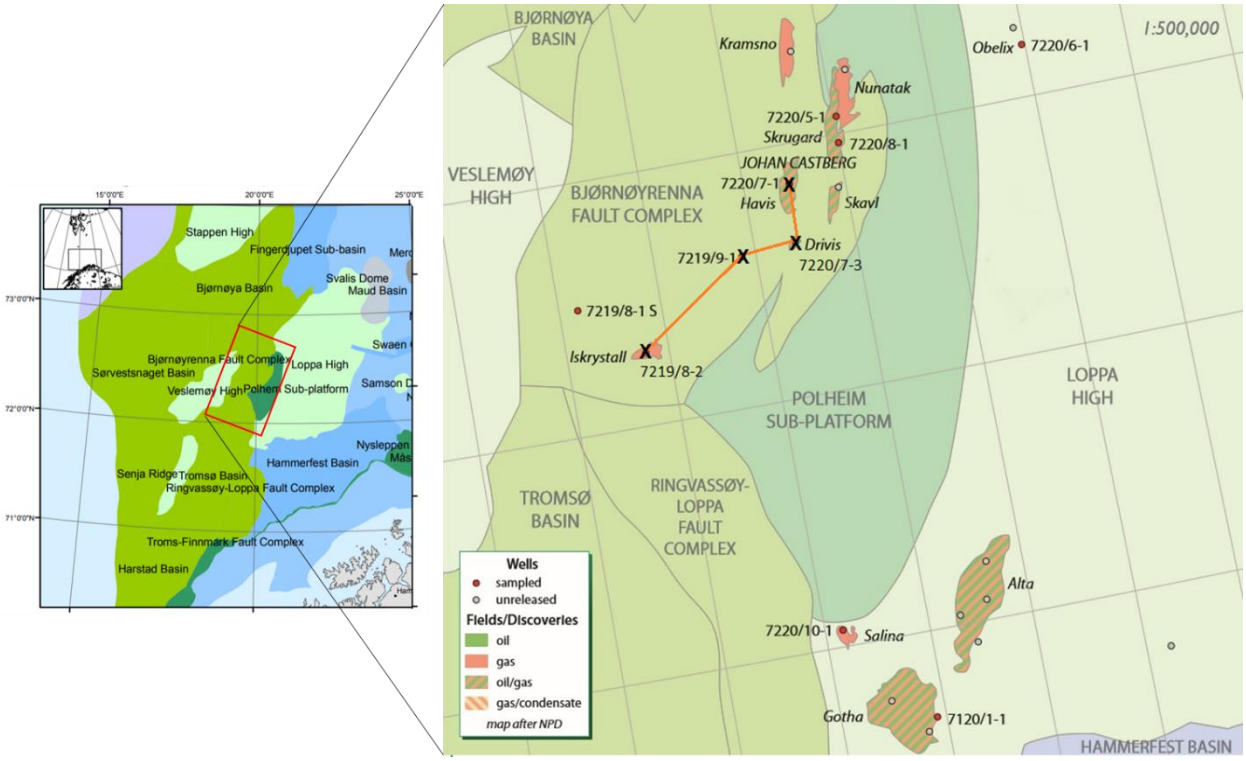

Figure 6.1: Location of the study area. In the right map, the selected wells for the AVO modeling are marked by crosses. (modified from APT, 2016; NPD, 2014)

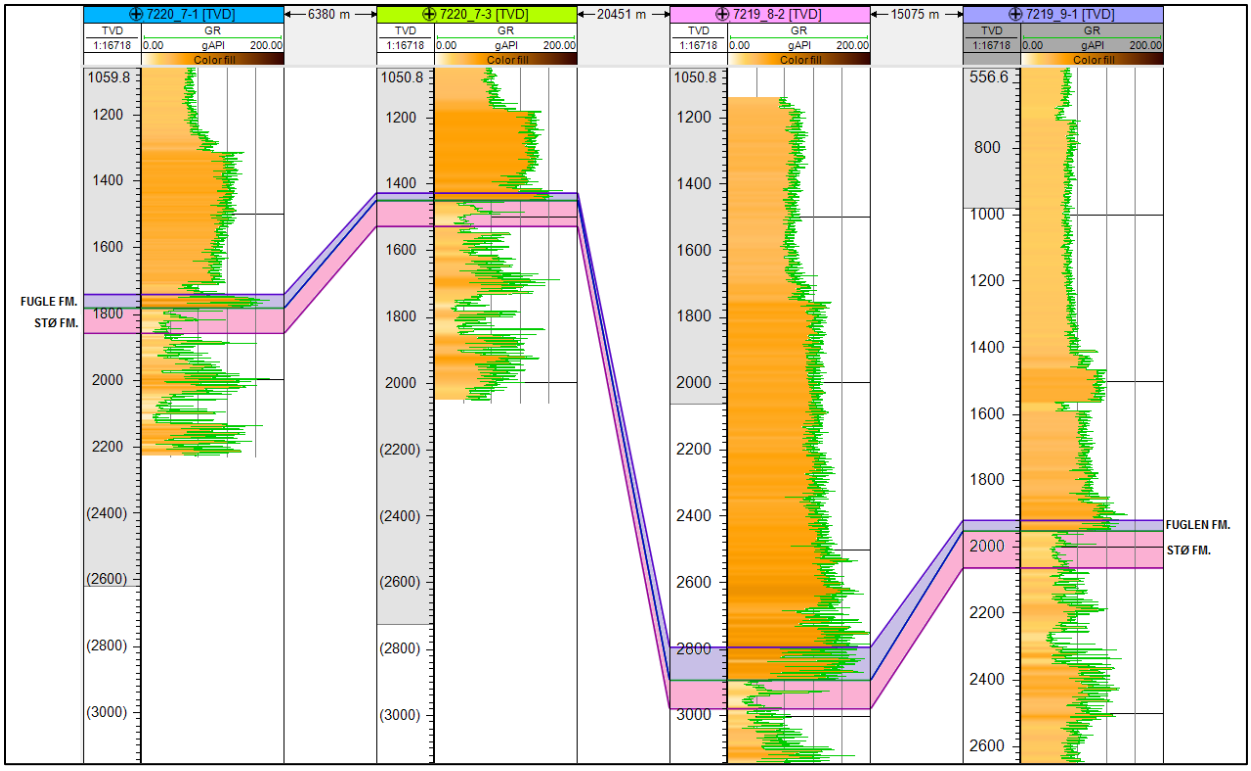

Figure 6.2: Distribution of the Stø and Fuglen Formations along the four wells use during the analysis.

Table 6.1: An overview of the reservoir interval from Stø Formation and cap rock shales (Fuglen Formation) used in the AVO modeling.

Well	Cap Rock (Fuglen Formation)			Reservoir (Stø Formation)			Vsh Average (%)	Insitu fluid
	Top (m MD_KB)	Bottom (m MD_KB)	Thickness (m MD_KB)	Top (m MD_KB)	Bottom (m MD_KB)	Thickness (m MD_KB)		
7220/7-1	1740	1781	41	1781	1857	76	16	~62% gas 38% oil
7220/7-3	1426	1448	22	1448	1526	78	16.6	~87% gas 13% oil
7219/8-2	2798	2898	100	2898	2985	87	9	~70% gas
7219/9-1	1919	1951	32	1951	2062	111	41	brine

6.1 Results

6.1.1 Blocking/ Upscaling of Well Log Data

Upscaling is an important and necessary method that is used to fit all the information from the well logs and the seismic data at the same scale since the well logs contain higher frequency information than the seismic. This process also helps to reduce the computing time in case of a large dataset.

The proper selection of the blocking and averaging method play an important role in the appearance of the resulting synthetic seismogram. Normally there is a relation between the resolution and the block size, the larger is the blocking the less frequency and resolution. In this section, blocking size of 3m, 5m, and 10m are applied on the density and velocity logs for uniform, non-uniform and Backus average (Fig.6.3, C.1, C.2, C.3, C.4, C.5, and C.6). The resultant curves are used for constructing a reflectivity model, which combined with a Ricker wavelet will be used to create the synthetic seismogram.

The blocking method is applied before the generation of the synthetic, and the Backus average algorithm is the one selected for simplicity since it considers an effective, homogenous and anisotropic medium. Moreover, the selection of the block thickness depends on the shear wave velocity and the dominant frequency; therefore based on the data in Table 6.2, a dominant frequency of 30 Hz and the Equation 6.1. from Liner and Fei (2006), the window length would need to be 21m or less in order to preserve the accuracy. A 3m block size is the one selected as the window length since it provides a precise capture of the important interface contrast (Fig.6.4).

$$L = \frac{Vs_{min}}{3f} \qquad \text{Eq. 6.1}$$

Where L is the window length in meters, Vs_{min} is the minimum shear velocity in the interval, and f is the dominant frequency.

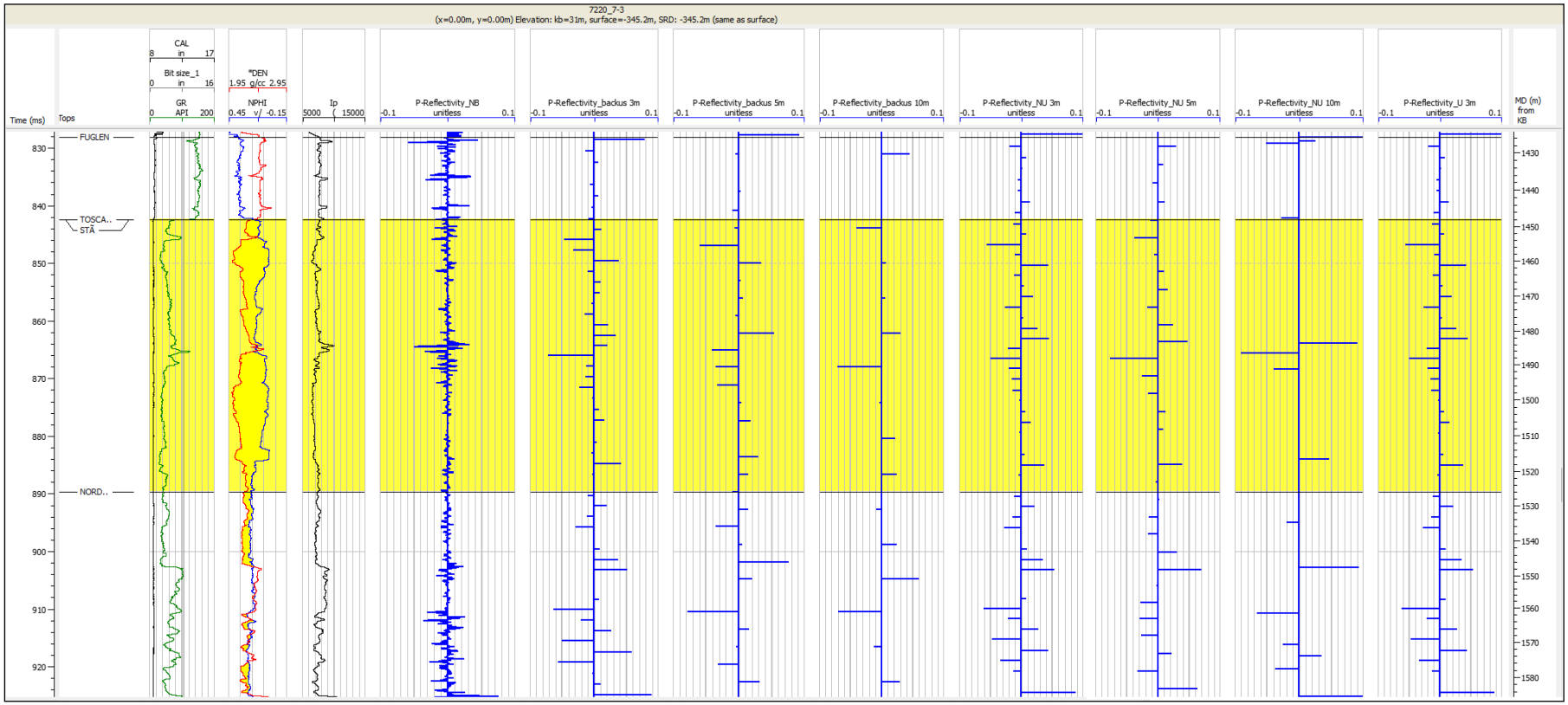

Figure 6.3: Comparison of all the P wave reflectivity series using for different block sizes. The area highlighted in yellow represents the area of the study that is hydrocarbon saturated in well 7220/7-3. (NB: non- blocking, Backus: Backus average, NU: non-uniform, and U: uniform).

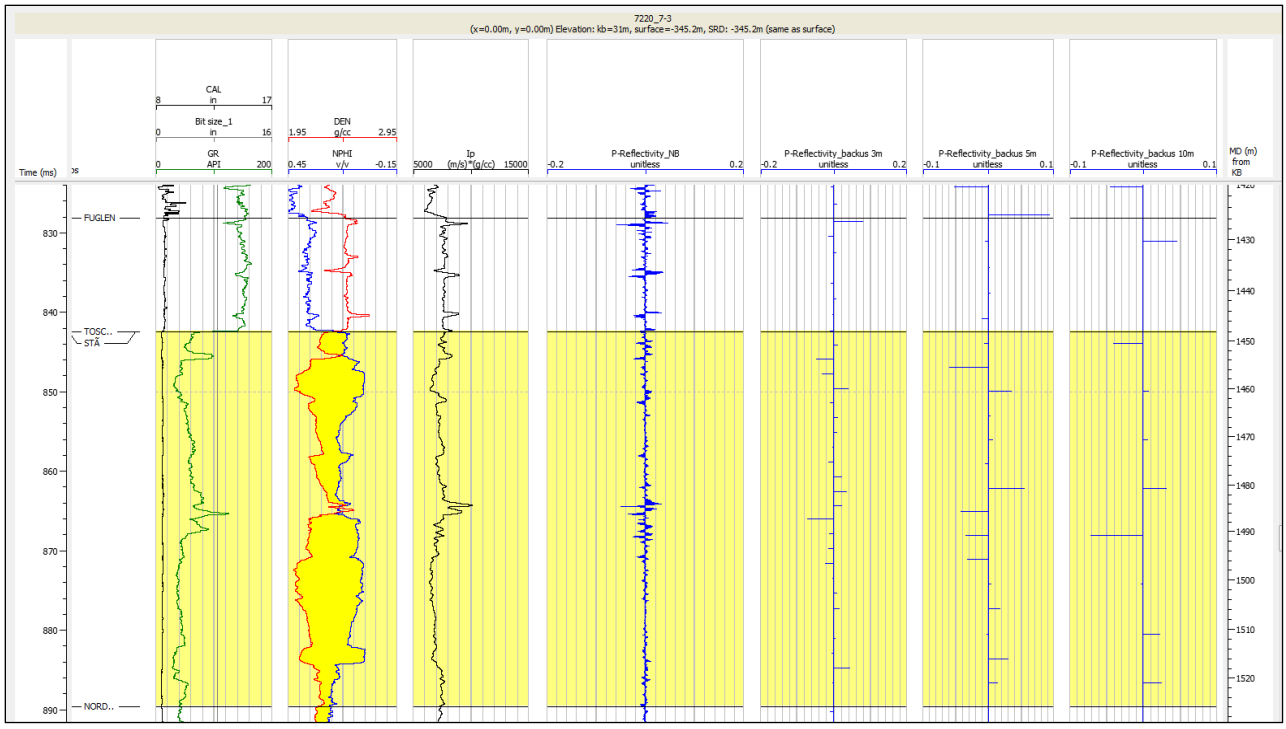

Figure 6.4: P-wave reflectivity series for well 7220/7-3 using Backus average with 3m, 5m and 10m block sizes. The highlighted yellow zone corresponds to the hydrocarbon saturated interval.

Synthetic seismograms are also generated using the resulting Backus logs and later plotted on the Gradient versus Intercept crossplot and on the Reflectivity versus Angle to compare AVO responses as the window length varies (Fig. 6.6 and 6.7). From both Figures, it is observed that except for the 3m blocking, the other two window lengths are not able to detect changes in terms of the amplitude for a near, middle and far angle stacks. This is because on the synthetic seismograms that do not show changes in the amplitude (Fig. 6.5).

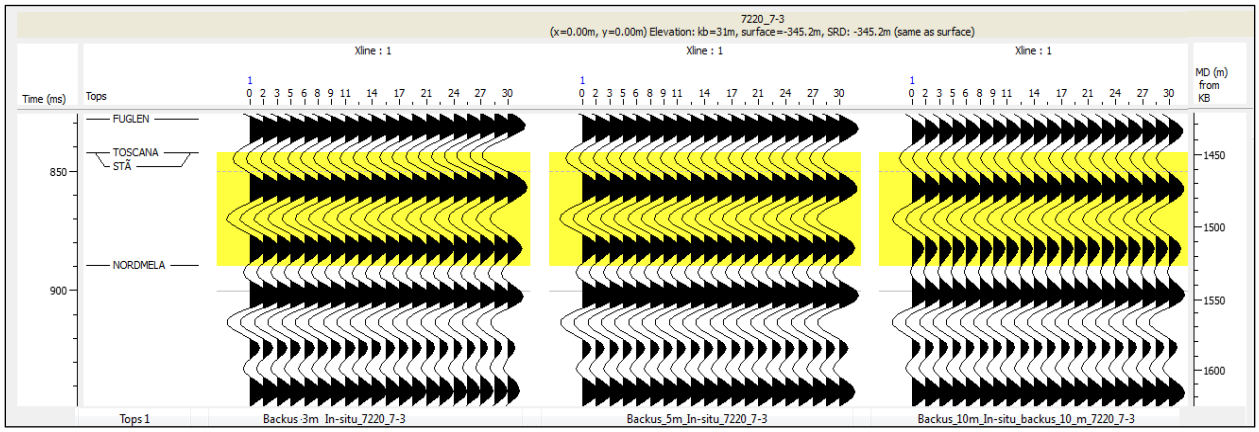

Figure 6.5: Comparison of the resulting synthetic seismogram for 3m, 5m and 10m blocking using Backus average method for well 7220/7-3 (Drivis).

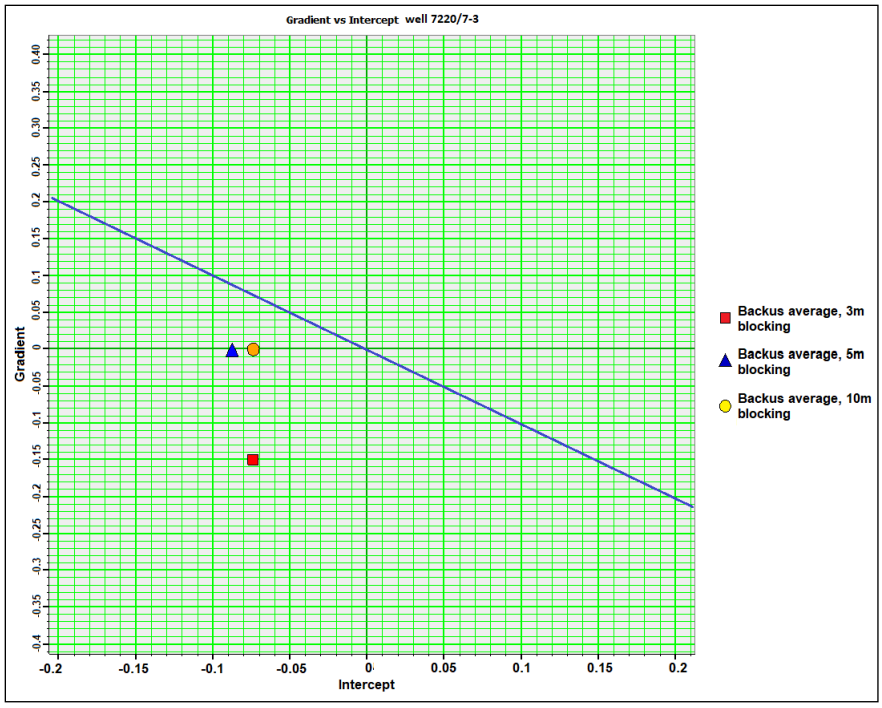

Figure 6.6: Gradient versus Intercept crossplot for the 3m, 5m, and 10m blocking based on Backus average on Top Stø in well 7220/7-3 (Drivis). The blue line represents the background trend of Vp/Vs=2.

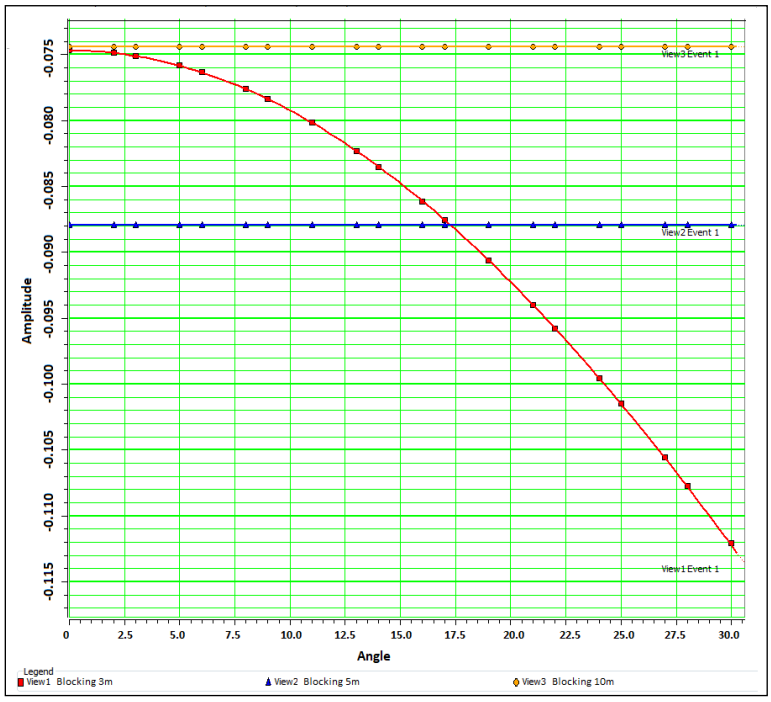

Figure 6.7: Reflectivity Rpp (θ) versus Incidence Angle for the 3m, 5m, and 10m blocking based on Backus average on Top Stø Formation in the well 7220/7-3 (Drivis).

6.1.2 Generation of the synthetic seismogram

In order to generate a synthetic seismogram, it is important to create a seismic wavelet. The selection of the proper wavelet will provide good vertical resolution and less noise influence. In this study, a linear Ricker wavelet with a dominant frequency of 30 Hz, 200 ms wavelength, and 2 ms sample rate is used. The frequency range is obtained from the spectral analysis of the "West Loppa 2008" seismic data (Larsen, 2011).

The Zoeppritz equation is later used to generate the synthetic, which is presented as angle-domain gathers. Moreover, the classification plot is analyzed using the simplified Aki-Richard two-term equation, and presented with variable incidence angles rather than offset for a more intuitive comprehension.

6.1.3 Effects of the Mixed Fluid Phases

The analysis of the effect of the fluid on the AVO response is performed through fluid substitution using Gassman's equation. In this method, the fluid inside the pores is replaced with another fluid causing changes in the P-wave and S-wave velocity due to variation in the rock compressibility and bulk density. The spatial distribution of the phases within the rock also influence the velocities responses, thus it is important to study this variable and see the effect as the hydrocarbon saturation increases.

In Figure 6.8, a comparison of the Vp response in case of a uniform and patchy saturation is presented. A homogeneous saturation assumed that both phases are distributed uniformly and have the same wave induced pore-pressure; therefore the pore-pressure is able to diffuse and equilibrated during a seismic period. In the case where a small amount of a strongly compressible fluid is introduced into the system, a noticeable drop in the Vp is expected because of the dramatic change in the bulk modulus. As the gas amount increase, slight changes in the bulk modulus and rapidly density decrease occurs, causing a slight increase in the velocity.

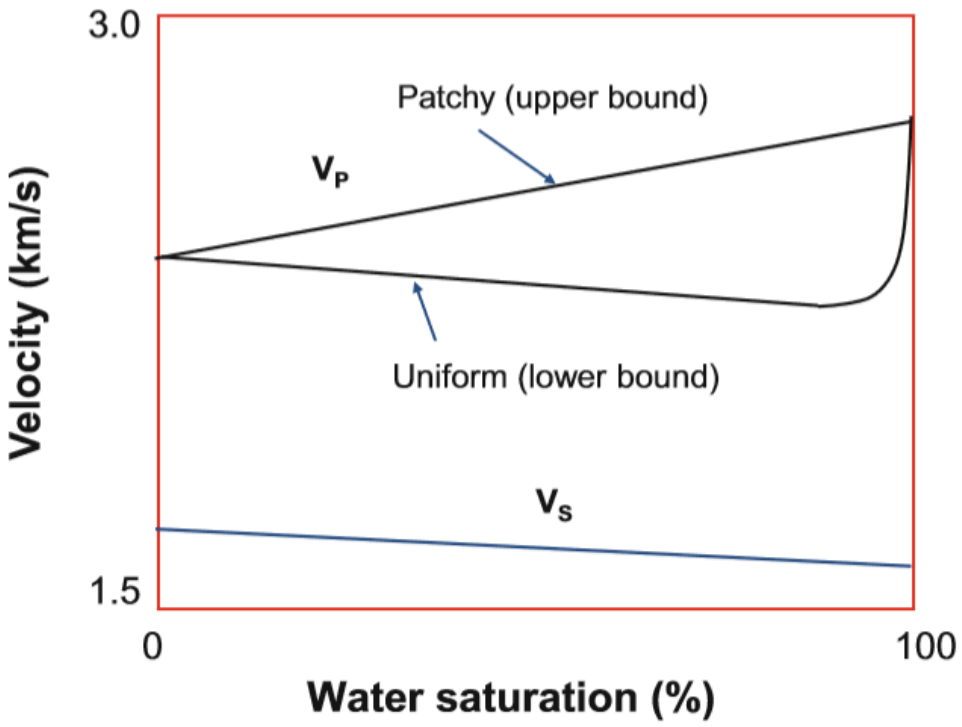

Figure 6.8: Representation of patchy versus uniform saturations for a gas and brine saturated sandstones (Avseth et al., 2005).

For a patchy saturation, the wave-induced period is too short to allow pressure equilibration between the two fluids, causing higher P-wave velocity, impedance and Poisson ratio values in comparison to the homogenous distribution. As the hydrocarbon replaces the brine, Vp decreases linearly (Avseth et al., 2015; Nisar et al., 2016).

In this study it is necessary to assume one option between the uniform and the patchy saturation. Therefore, the uniform, homogenous saturation is considered due to the assumption that strong AVO signature could appear at low gas saturation.

6.1.4 Gassmann fluid substitution

The Gassman fluid substitution method has the potential to provide information about in-situ fluid and show variations on the AVO signatures as the saturations within the pores is varied, due to changes on the elastic properties such as Vp, Vs, and ρ. In this study the fluid substitution is carried out through the Fluid Replacement Modeling (FRM) using Hampson and Russell software, to investigate different scenarios with variable saturation and fluid types. These include 100% brine, 100% oil, 10% gas, 50% gas and 100% gas. The quantitative changes in the elastic properties at top of the Stø Formation of wells 7220/7-1 (Havis), 7220/7-3 (Drivis), and 7219/8-2 (Iskrystall) are described in Table 6.2.

Table 6.2: Resulting P-wave velocity, S-wave velocity, density and Poisson's ratio values at different saturation levels of oil, gas and water at top of the Stø Formation in wells 7220/7-1, 7220/7-3 and 7219/8-2.

Well	Pore Fluid	CAP ROCK (FUGLEN FM.)				INTERFACE BETWEEN STØ AND FUGLEN			
		Vp (m/s)	Vs (m/s)	Density (g/cm3)	Poisson ratio	Vp (m/s)	Vs (m/s)	Density (g/cm3)	Poisson ratio
7220/7-1	Insitu	3307.61	1678.00	2.55	0.32	3658.79	2292.86	2.38	0.1766
	100% gas					3711.00	2333.52	2.30	0.1731
	100% oil					3787.65	2289.95	2.39	0.2110
	100% brine					3812.41	2268.11	2.43	0.2400
7220/7-3	Insitu	3064	1609.21	2.52	0.3	3352.57	2100.92	2.27	0.1766
	100% gas					3361.7	2107.04	2.25	0.1764
	100% oil					3415.95	2061.3	2.35	0.22
	100% brine					3621.81	2038.52	2.41	0.26
	10%gas					3296.89	2045.08	2.39	0.187
	50% gas					3309.86	2071.93	2.33	0.1778
7219/8-2	Insitu	3999.48	2186.8	2.655	0.28	4199.21	2578.15	2.45	0.1974
	100% gas					4224.13	2594.22	2.42	0.1972
	100% oil					4275.37	2568.46	2.48	0.21
	100% brine					4360.46	2547.8	2.51	0.2408
	10%gas					4176.82	2552.97	2.5	0.2
	50% gas					4188.53	2570.88	2.46	0.1977

Figures 6.9 and 6.10 show the changes in the elastic parameters and in the synthetic seismogram, when the saturations are changed from in-situ to 100% brine, 100% oil and 100% gas in the Stø Formation in well 7220/7-3 (For other wells, the modeling results are given in Appendix C).

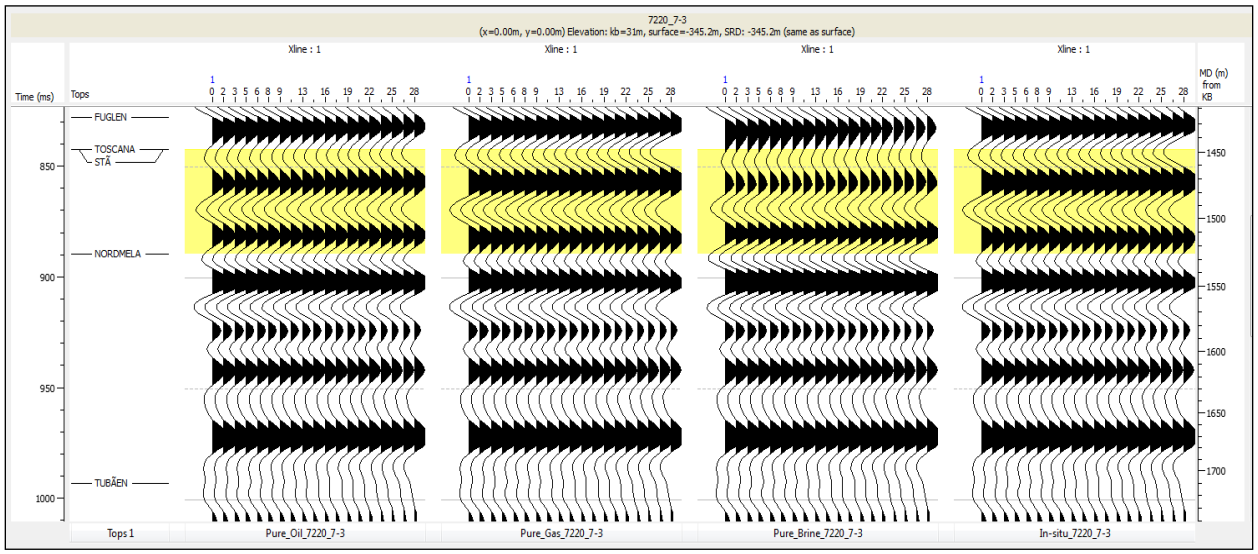

Figure 6.9: Synthetic seismogram for scenarios of 100% oil, brine and gas in well 7220/7-3(Drivis).

.

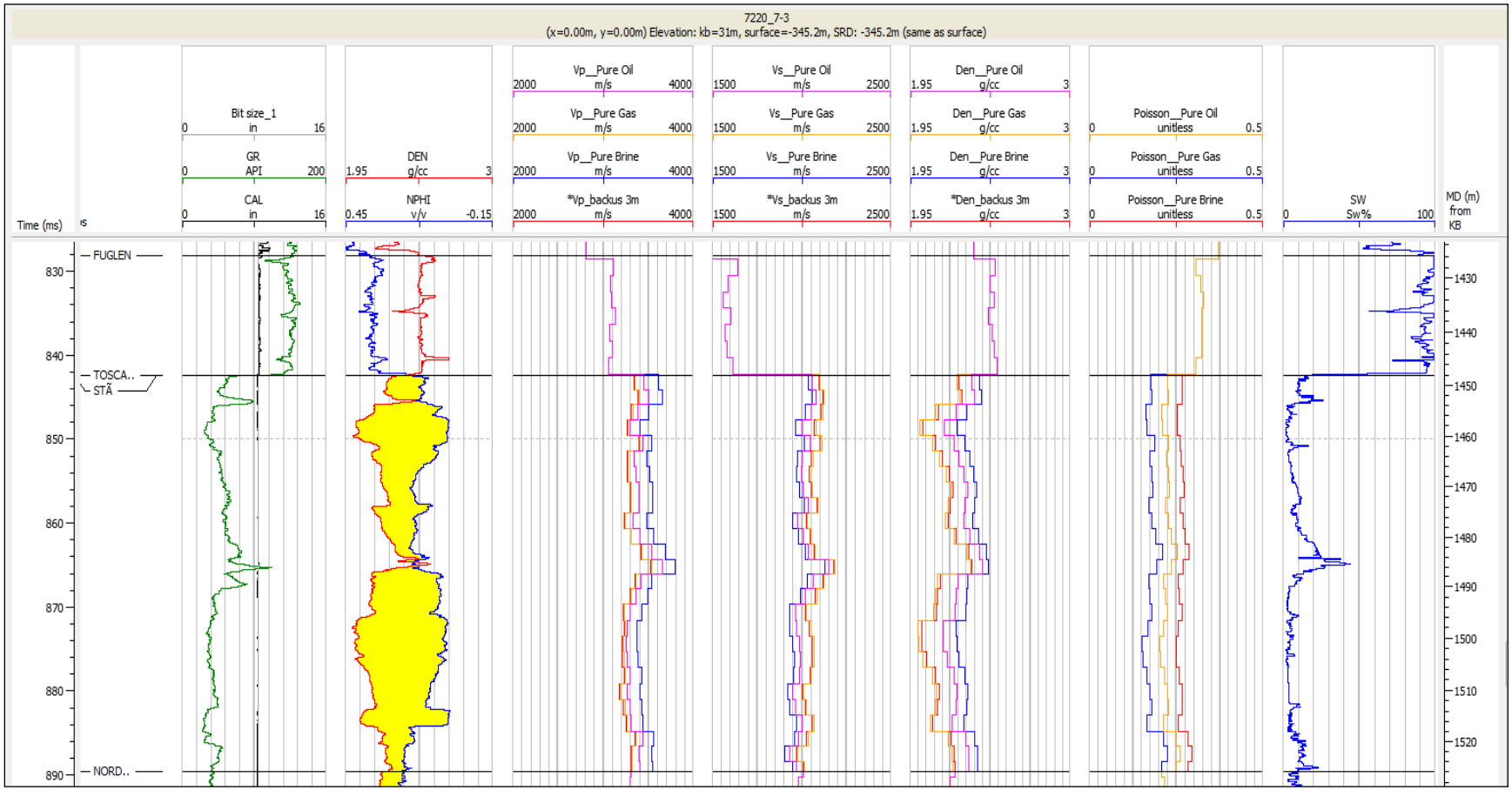

Figure 6.10: Relevant logs within the reservoir interval, showing variation according to the level of saturation in well 7220/7-3 (Drivis).

6.1.5 Variations in the AVO response using estimated Vs.

In order to perform AVO modeling, several parameters are needed as an input such as Vp, Vs and bulk density. In some cases, if all the logs are available they might be in poor conditions due to borehole instabilities; while there might be other scenarios where part of the data is not included. That is the case of the shear wave log, which is not common in some wells, and even in the new discoveries, it is not usually present in the whole section. As a result, estimation of Vs from measured Vp log is executed using the mudrock equation from Castagna et al.,(1985). (See Table 3.4 in Chapter 3).

In this part of the study, a comparison of the AVO response using measured and estimated Vs in the well is performed to verify variations on the AVO gradient and intercept. In Figure 6.11, it is shown that the resulting AVO gradient curves from both velocities have the same initial reflection coefficient at zero offsets, as expected. However, as the angle increases more contribution of the Vs and density are recorded providing most likely the same geometry. Nevertheless, the curve obtained using Vs from Castagna et al., (1985) has a lower gradient in comparison to the one with direct measurement. Result that is confirmed on the gradient versus intercept crossplot (Fig. 6.12), where the intercept remains the same in both scenarios while the AVO gradient from the measured Vs is larger (-0.25) in comparison to the other gradient (-0.17).

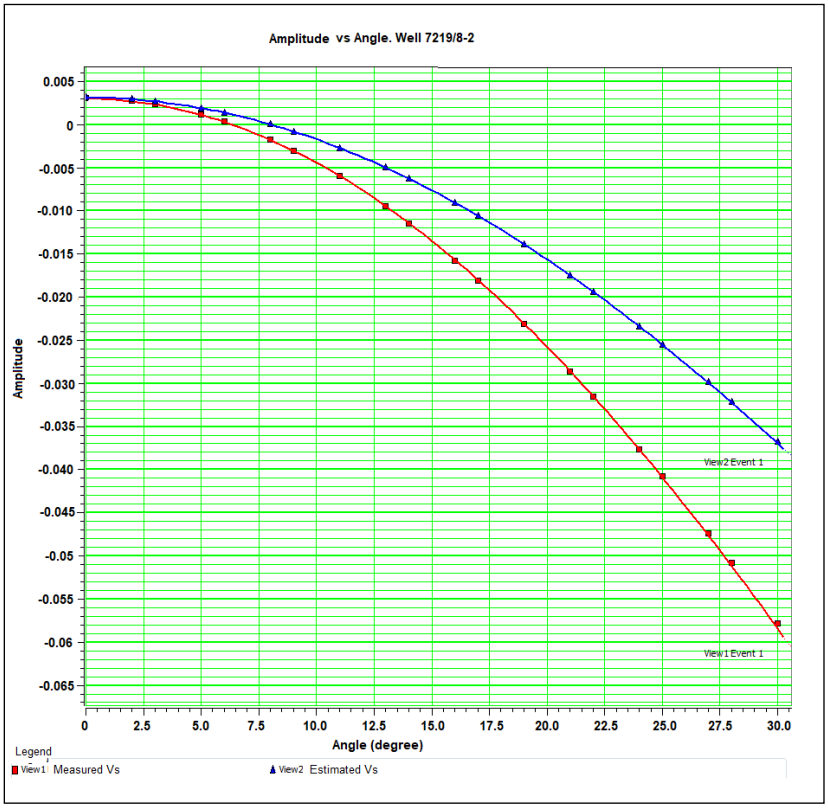

Figure 6.11: Comparison between the AVO gradient curves using estimated and measured Vs on the Amplitude versus Angle plot of well 7219/8-2 (Iskrystall).

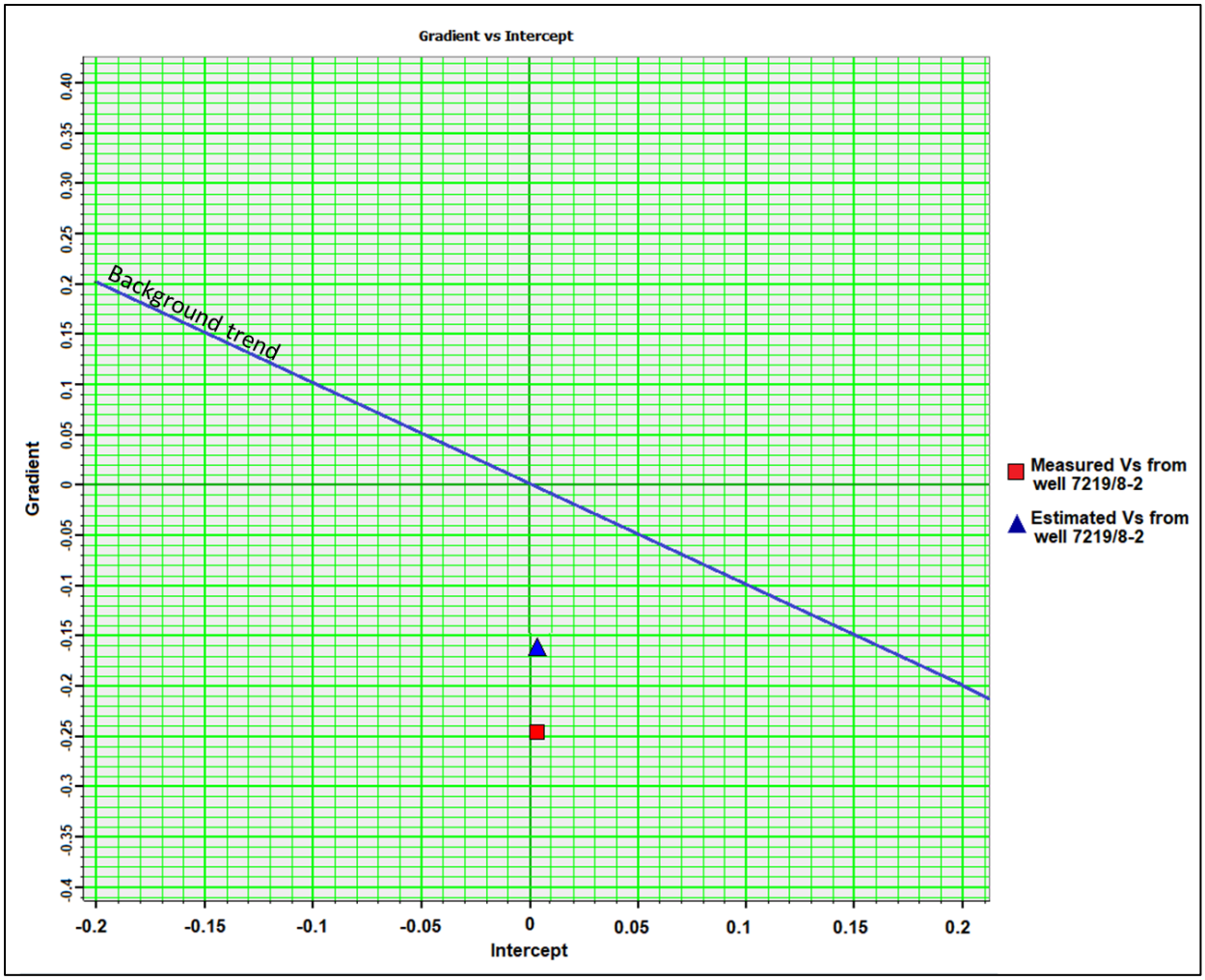

Figure 6.12: Gradient versus intercept crossplot for comparison of AVO responses using the measured and the estimated Vs for well 7219/8-2 (Iskrystall). The blue line (background trend) is Vp/Vs ratio=2.

This response can be attributed to an underestimation of the Vs inside the reservoir when Castagna 's equation is used since this method is based on brine saturated sand and the study area is filled with hydrocarbon. Therefore, the decrease in the estimated Vs is translated to an increase of the Vp/Vs ratio and Poisson's ratio, that play an important role on the gradient. Additionally, a decrease in the Poisson's ratio contrast at the interface will produce a low gradient (Rutherford and Williams 1989; Simm et al., 2000).

6.1.6 AVO Classification

In the AVO modeling using AVO gas sand classification (the Aki Richard two terms method) is considered. The incident angle is limited to 0˚ - 30˚ since angles above 30˚ do not allow a proper comparison between Aki Richard and Zoeppritz equation (Gelius, 2017b).

A standard background trend of Vp/Vs= 2 from Castagna et al. (1998) is also added on the crossplot as an overlay in order to see the deviation from the trend caused by hydrocarbon or replacement of the pore fluid. The different AVO responses from the in-situ and the different fluid substitution scenarios in the wells 7220/7-3 (Drivis) and 7219/8-2 (Iskrystall) for the gradient versus intercept crossplot and the reflectivity versus angle are discussed below.

First, it is noticed in Figure 6.13 from well 7220/7-3 that the in-situ points and 100% gas are plotted very close to each other, with a small variation in the gradient and intercept. Originally the formation has a gas saturation of ~80%, therefore an increment of 20% of gas will not cause a remarkable change, a decrease on the intercept (get more negative) from -0.0746 to -0.0766 and a change of the gradient from -0.15 to -0.14 is identified. However, for a small amount of gas (10%) the points moved closer to the background trend with an increase in the intercept to -0.05 and a small gradient of -0.1.

When the fluid is replaced by 100% oil and brine it is also seen a considerable change; both points move towards the center of the plot and closer to the theoretical trend. The intercept increases in both scenarios (less negative) to -0.401 and – 0.008 for the oil and brine case. What is more, the gradient reduces ~ -0.02 for oil and ~-0.03 for 100% brine. In overall, the AVO response is interpreted as class II when the gas saturation is very low, and a weak class III when the gas saturation is above 50%.

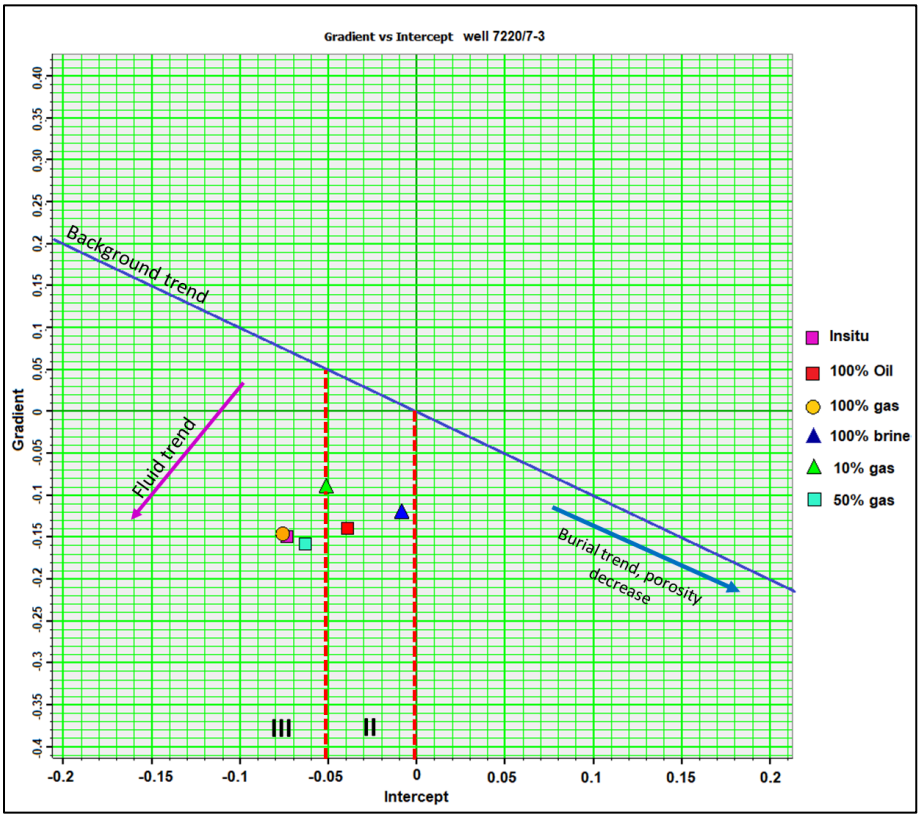

Figure 6.13: Gradient versus Intercept crossplot for all the fluid substitution scenarios on Top of the Stø Formation in well 7220/7-3 (Drivis). The dashed lines represent the limit for a type II and III gas sands.

In Figure 6.14 is represented the amplitude variation as the offset increases. It is noticed a gradient increment as the gas saturation increases from 10% to 100%, while in case of the 100% brine and 100% oil the gradient values drop.

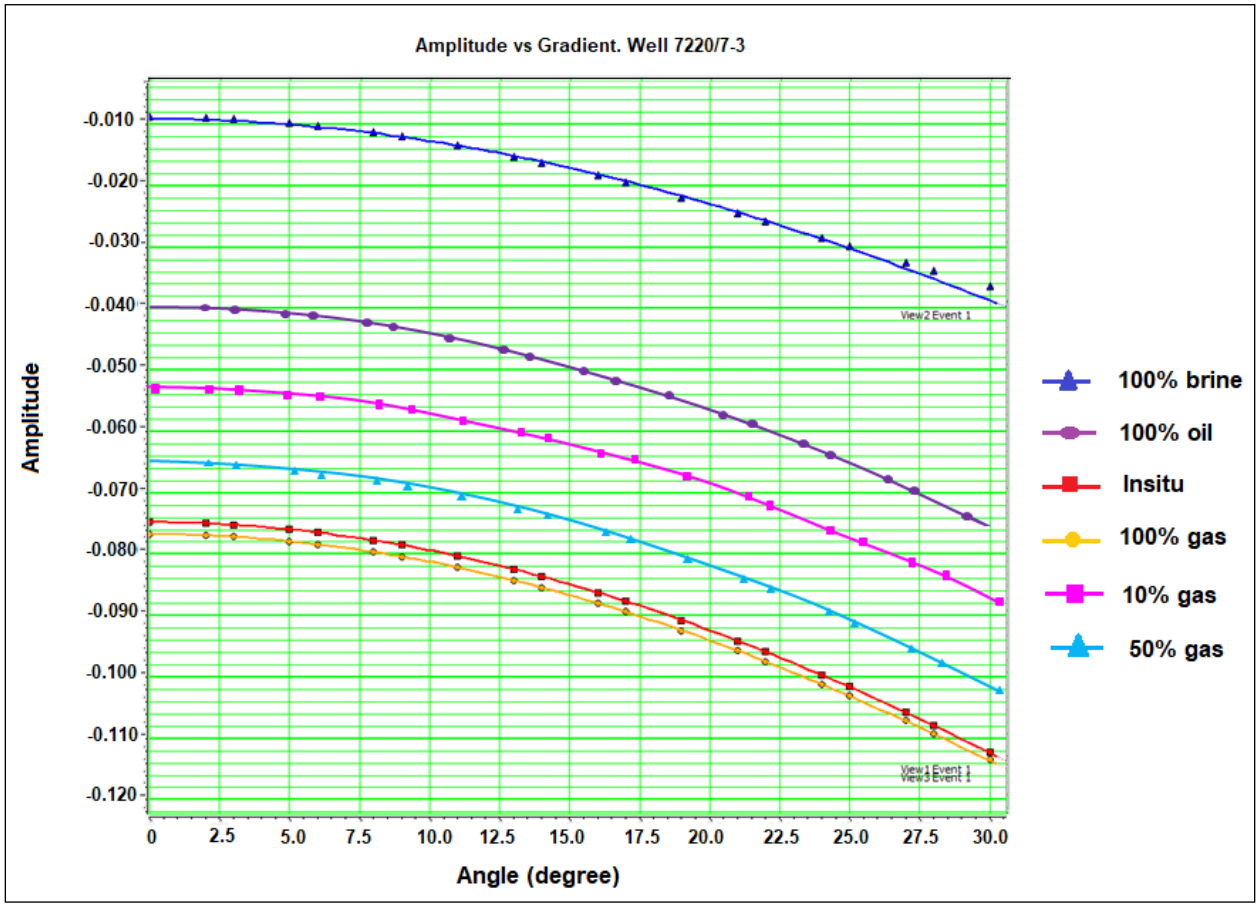

Figure 6.14: AVO gradient curves from all the fluid substitution scenarios for well 7220/7-3 (Drivis).

In well 7219/8-2 the Stø Formation has less gas saturation (60%), however, a similar response in the AVO modeling is observed for the same variable saturation. The intercept and the gradient show little variation as the gas saturation changed from 100% to 10%; the intercept varies linearly from 0.005 to 0.009 while the gradient magnitude also increases from -0.243 to -0.248. Nevertheless, at 100% brine saturation, the top reservoir has a significantly larger intercept and small gradient. Based on the AVO signature from all the cases, this response is interpreted as class II P, since it has an intercept lower than 0.05 (Fig.6.15).

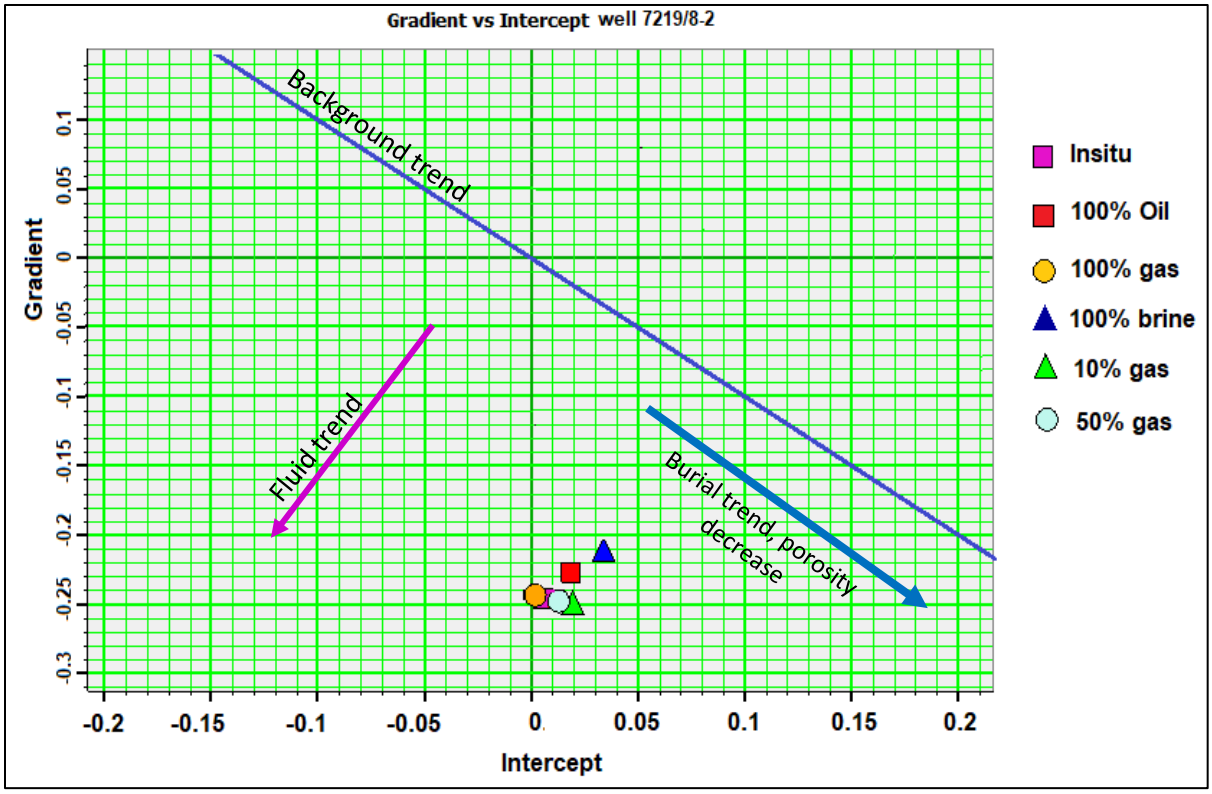

Figure 6.15: Gradient versus Intercept for all the fluid substitution cases for well 7219/8-2 (Iskrystall).

6.2 Discussion

6.2.1 AVO classification

An initial examination of Figure 6.16 allows the proper classification of the reservoir sands according to the different AVO classes mentioned in Chapter 3. Overall, two of the wells exhibited a class II anomaly (well 7220/7-1 (Havis) and 7219/8-2 (Iskrystall)), while wells 7219/9-1 and 7220/7-3 (Drivis) have a different classification (Table 6.3).

Table 6.3: AVO sand classification, AVO parameters, depth, and shale volume for the top Stø Formation in four studied wells.

Well	Stø Formation				
	AVO class	Gradient	Intercept	Depth (m MD_KB)	Vsh Average (%)
7220/7-1	II	-0.16	-0.046	1781	16
7220/7-3	II/weak III	-0.15	-0.074	1448	16.6
7219/8-2	II P	-0.24	-0.003	2898	9
7219/9-1	I	-0.07	0.06	1951	41

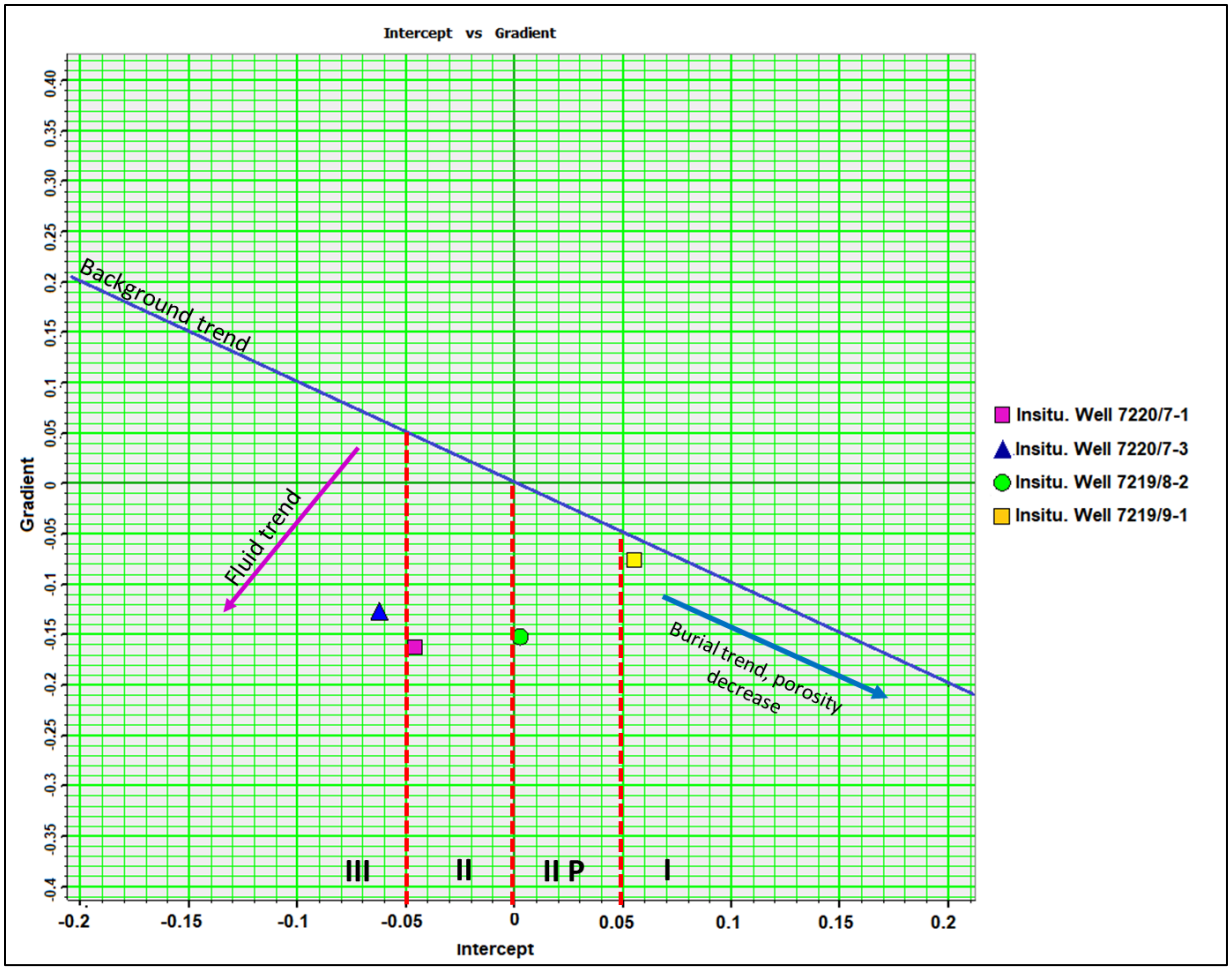

Figure 6.16: Classification of the gas sand on the different wells, according to their location in the Gradient versus Intercept crossplot.

Analyzing closely each of the gas sand classifications, on one side the AVO anomaly on well 7220/7-1 (Havis) is classified as class II. The Class II sands is typically associated with moderately compacted and consolidated sands, that has nearly the same impedance as the overlying cap rock (Rutherford and Williams, 1989), which coincides with the lithological description of the Stø Formation on chapter 2 and the results from the petrophysical analysis on chapter 4.

On the other hand, in well 7220/7-3 (Drivis) the anomaly falls within the class III (very close to the limit of class II), thus to the fitting, it is perhaps a weak class III. A class III anomaly corresponds to unconsolidated sediment and may be thought of as unexpected for this reservoir interval, due to their maximum burial depth before uplift (chapter 3 uplift estimation). However, in comparison to the well 7220/7-1 (Havis), the Stø Formation is located at shallower depth and has been exposed to less cementation, thus the reservoir might be less compacted and consolidated, being more sensitive to fluids.

The results from wells 7219/8-2 (Iskrystall), the anomaly is also identified as class II P since it has a positive reflectivity at near offset (Rutherford and Williams, 1989). Meanwhile, the top Stø anomaly in well 7219/9-1 is classified as a weak class I. This class is typically related to sands that have been exposed to moderate – high compaction and has higher impedance than the overlying shale. In this case, the sand is brine saturated with a shale content higher than 40% according to the petrophysical analysis (Chapter 4), thus the increment of the clay plus the brine within the pore produced an increment on the intercept.

One of the other factors that also influence the AVO classification is the shale content, according to Simm et al. (2000), the increment of clay in the sands causes a decrease on the intercept and gradient. The well that has the lower shale volume (~4%) is the well 7219/8-2, here it is confirmed that both AVO parameters increase. On the wells 7220/7-1 and 7220/7-3, the shale content is estimated ~16% a decrease in the gradient and intercept occurs.

Finally, the compactional difference between the sands based on their burial and exhumation history also helps separate this reservoir. The class II is normally associated to sands that had an intermediate level of mechanical compaction and chemical compaction, which correlates with the location at which the formation was expected to be before the uplift.

6.2.2 Deviation from the background trend

A key issue for AVO interpretation is the magnitude of the deviation of the scatter from the background trend in the intercept gradient domain caused by fluid alteration. This movement can be described by fluid vectors. A fluid vector is commonly displayed when the brine is replaced by gas, showing, as a result, the movement of the AVO reflection coefficient from the given background trend (Castagna, 1998). In Figure 6.17 a general view of the sensitivity effect is shown when the initial gas is replaced by brine; in general, it could be seen that the gas sand does tend to plot to the lower left of the brine sand decreasing the intercept. Closer examination of the point-to-point fluid vector from well 7220/7-3 is represented in Figure 6.18. The direction of movement at top of the formation can be seen, the gas scatters tend to plot towards the lower left position and away from the background trend.

In general terms, it is expected that the scatters from the 100% brine case behaves as a background. However, certain deviation is noticed, thus could be related to the fact that the used background trend is not constant in all depths being valid only a certain depth window, as a consequence, some errors in the positioning can occur (Castagna et al., 1998).

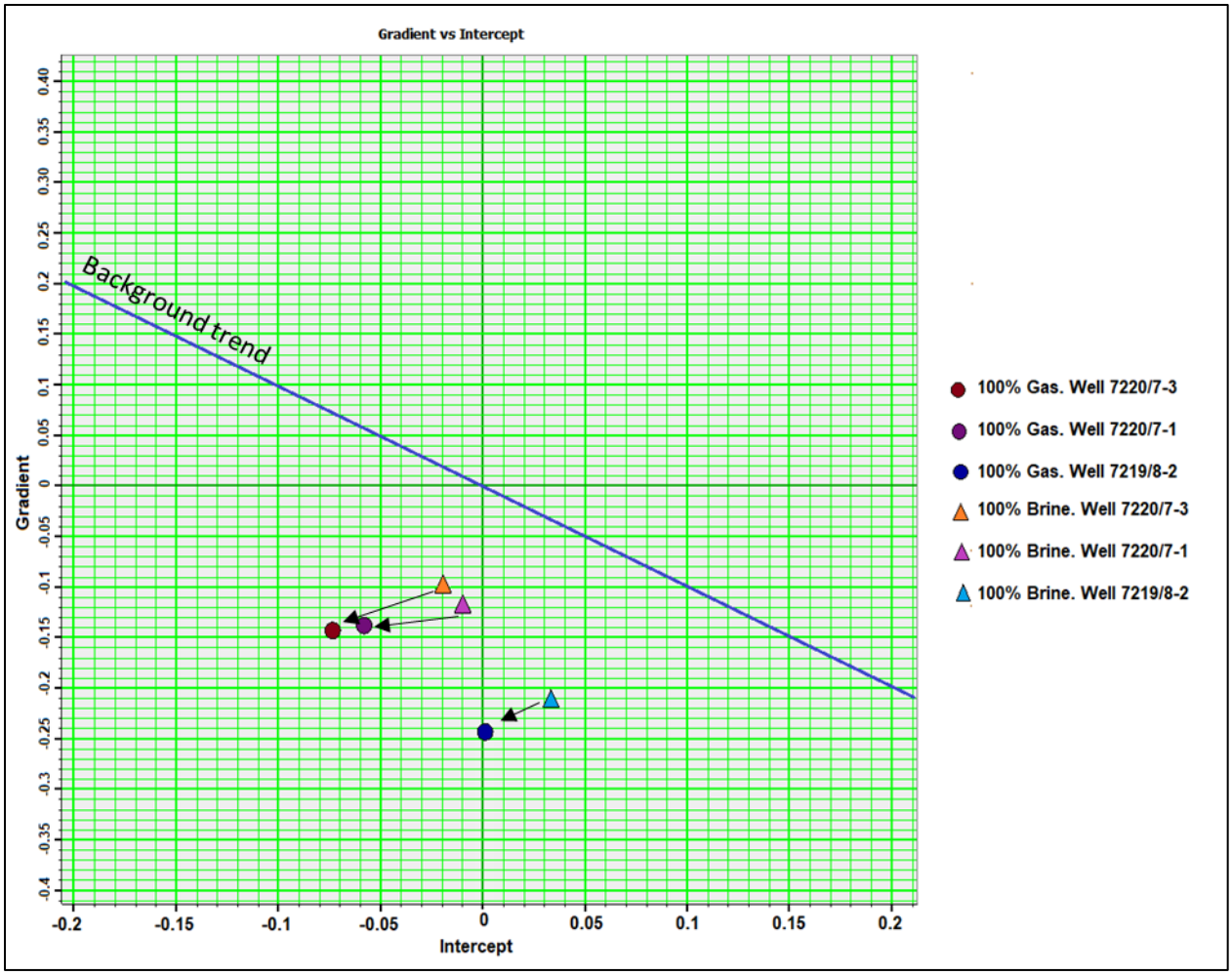

Figure 6.17: A general overview of the fluid vector in the study wells when brine is replaced by gas. The blue line represents the Vp/Vs ratio=2 (the background trend).

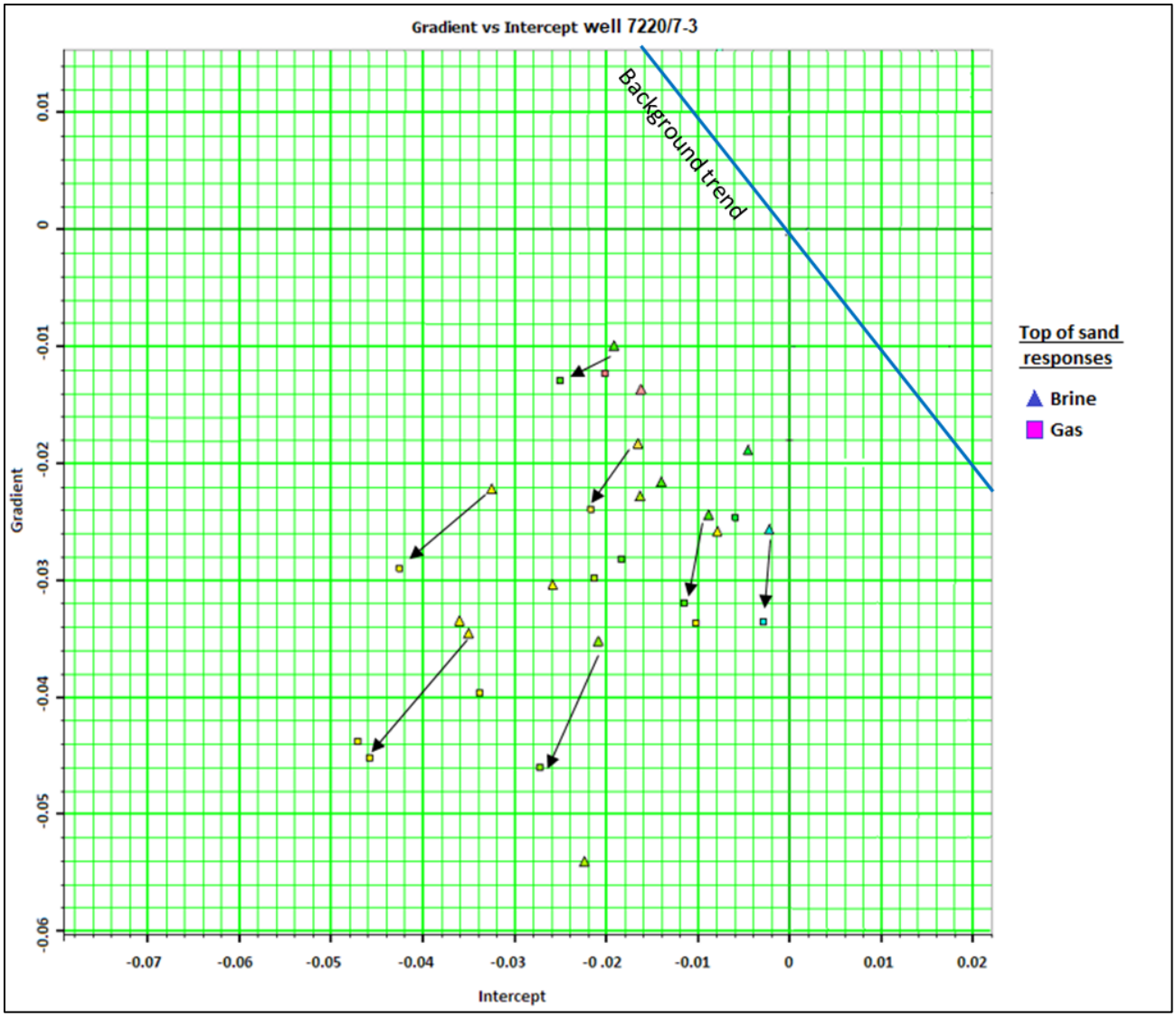

Figure 6.18: Representation of the fluid vector of top Stø Formation in well 7220/7-3 (Drivis) when brine is replaced by gas.

Additional observations can be made from the gradient vs intercept plot from well 7220/7-1 (Havis). The scatter points seem to follow a different orientation which appears to be lower than 2, suggest the Vp/Vs ratio is lower. This can be related to uplift and compaction, according to Pelletier (2008) as more tight and compacted the rock the lower Vp/Vs ratio, leading to a steep background trend. In Figure 6.19, the background trend is shown in blue, whereas the apparent trend followed by the data points is indicated in red. It is observed that the scatters points from the brine gas has a better approximation to the new trend.

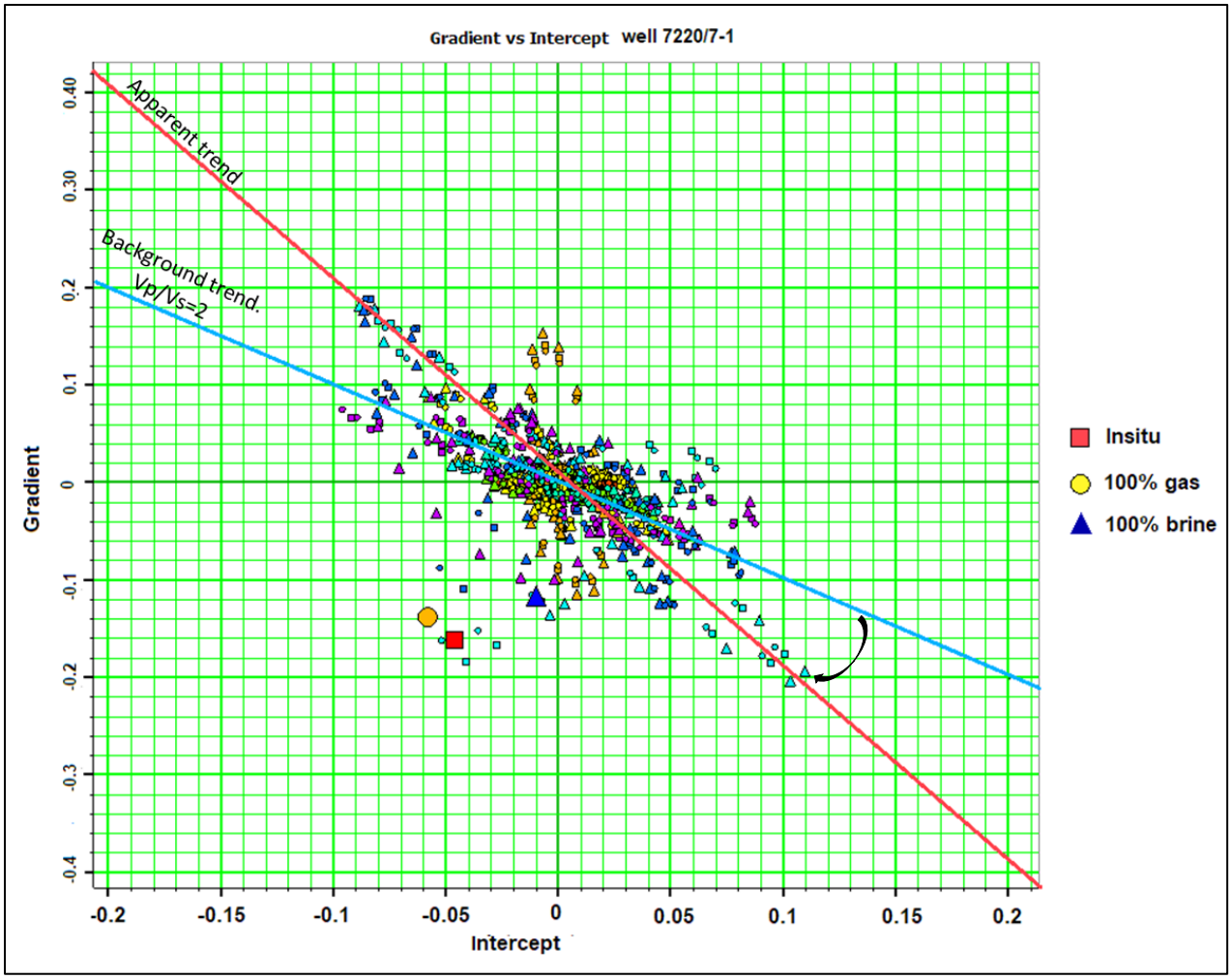

Figure 6.19: Intercept versus gradient crossplot of the top Stø formation in well 7220/7-1. The blue line represents the background trend of Vp/Vs= 2, while the red line indicates the apparent trend of the scatters points.

6.3.3 Effect of blocking size

As it is mentioned at the beginning of this chapter, the proper selection of the blocking size would affect AVO modeling results.

In Figure 6.5 and 6.6, it is observed that using a window length higher than 3m would not show any changes on the AVO signatures. The bigger the block size, information from a higher number of smaller scale reflections would be included in each block, as a consequence, the seismogram will display fewer visible events. In the given data set, the events do not show a high dominant reflectivity, therefore the synthetic seismogram with a block size above 3m has neglected those reflections.

6.3.4 Variation in the half-space models

The replacement of the given pore fluid for another one produced a considerable change in the AVO intercept and AVO gradient. The quantitative changes in the rock parameters when the in-situ fluid is fully replaced by 100% oil, brine or gas are summarized in table 6.4.

Table 6.4: Variation in Vp, Vs, density and Poisson's ratio with changing the saturation to 100% brine, oil or gas.

Well	Pore Fluid	∆Vp (%)	∆Vs (%)	∆Density (%)	∆v (%)
7220/7-1	100% brine	7.05	-1.93	4.22	47.06
	100% oil	3.15	-0.94	2.50	23.53
	100% gas	0.70	1.04	-1.81	-5.88
7220/7-3	100% brine	8.03	-2.97	6.22	47.23
	100% oil	1.89	-1.89	3.18	3.88
	100% gas	0.27	0.29	-0.71	-0.11
7219/8-2	100% brine	3.84	-1.18	2.41	21.99
	100% oil	1.81	-0.38	1.18	6.38
	100% gas	0.59	0.62	-1.22	-0.10

For the Stø Formation, the replacement of the in-situ fluid by another fluid that is less compressible and dense, as brine or oil, produced an increment on the compressional velocity and bulk density, affecting directly the Poisson's ratio and intercept; while the shear-velocity tends to reduce, being more significant in case of 100% brine saturation. Moreover, the opposite effect is expected when the pore fluid is replaced by gas. The shear-wave velocity tends to increase as the P-wave velocity and density decrease since the gas is considered a less dense and more compressible fluid.

Overall, the major change occurs in the 100% brine replacement, the Vp, density and Poisson's ratio increases 8.03%, 6.22%, and 47.23% respectively as the Vs reduces 2.97%. The less noticeable change is observed in the 100% gas case (Fig. 6.20 and C.9). In in-situ scenario, all the reservoirs are gas saturated (~ Sw > 60%) and the increment of gas to 100% implied a small variation (Fig. 6.2,1 C.7 and C.8).

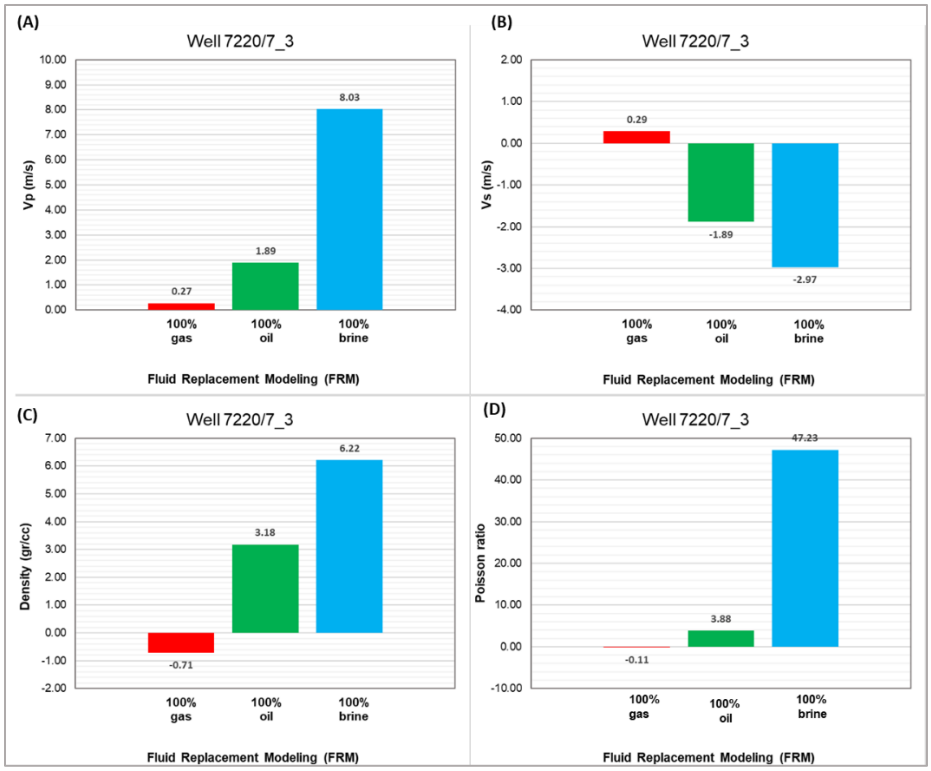

Figure 6.20: Effect of replacing the in-situ fluid for 100% brine, oil and gas on the Vp (a), Vs (b), density (c) and Poisson's ratio (d) of well 7220/7-3 (Drivis).

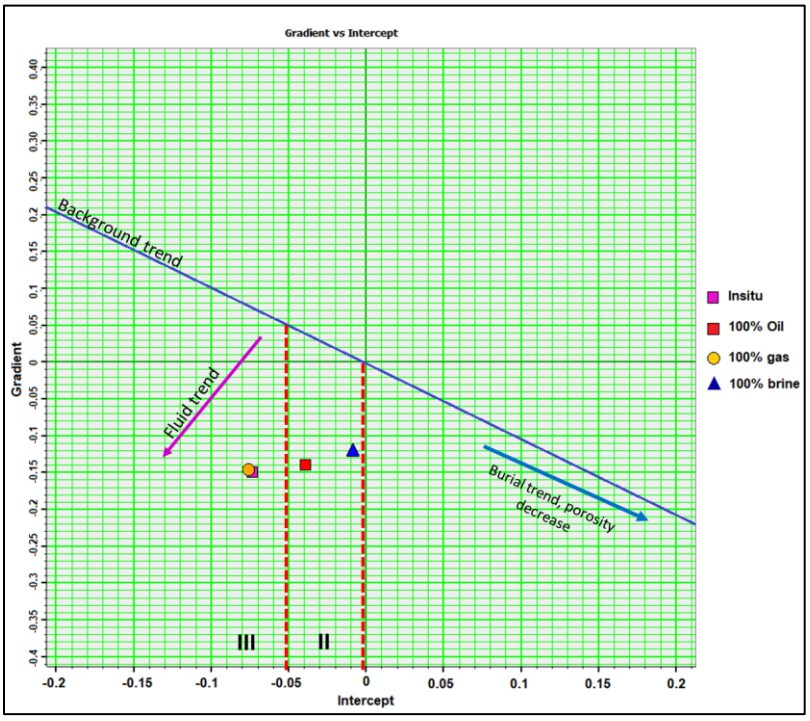

Figure 6.21: Gradient versus intercept crossplot for all the fluid replacement scenarios in well 7220/7-3 (Drivis).

After evaluating the effect of replacing the pore fluid by only one type of fluid (100% oil, brine or gas); another type of analysis is done. During this evaluation, the gas content is increased gradually in order to detect how sensitive is the AVO signature as the fluid varies its concentration. An increase from 0% to 10% on the gas saturation caused a significant change in the AVO interface (Fig. 6.13 and 6.1)7. As the amount of gas approaches 100% the points tend to increase the gradient (less negative).

In Table 6.5, the measured variations in the elastic parameters at the interface between Fuglen and Stø Formations are summarized. The changes consider the case of replacing brine with gas, therefore values are shown relative to the 100% brine case. The in-situ scenario is estimated to be ~80% and ~60% gas saturation in wells 7220/7-3 and 7219/8-2 respectively.

Table 6.5: Change in rock parameters due to fluid substitution, from pure brine to pure gas along the Stø Formation.

Well	Pore Fluid	ΔVp (%)	ΔVs (%)	ΔDensity (%)	Δv (%)
7220/7-3	10% gas	-8.97	0.32	-0.71	-28.08
	50% gas	-8.61	1.63	-3.20	-31.62
	100% gas	-7.18	3.36	-6.52	-32.15
7219/8-2	10% gas	-4.21	0.20	-0.20	-16.53
	50% gas	-3.94	0.91	-1.71	-18.19
	100% gas	-3.13	1.82	-3.55	-18.11

After introducing 10% gas into the pore system, there is a significant drop in the Poisson's ratio and Vp of -28.08% and -8.97%, respectively, as shown in Figure 6.22. In addition, for the same amount of gas (10%), the density decreases -0.71% and the shear velocity had an increment of 0.32 %. Increasing the gas saturation above 10% results in small changes in the rock parameters in comparison with the variations during the introduction of gas.

These estimations later compare with the response on the gradient versus intercept crossplot, show a proper correlation. The gradient and intercept move around the plot as the gas saturation varies, behavior that is also linked to the acoustic impedance and Poisson's ratio.

The presence of less gas reduces the impedance in the reservoir increasing the acoustic impedance contrast across the interface. Since the P-wave velocity depends on the bulk modulus, the Poisson's ratio also drops its value in presence of gas.

In Figure C.10, the variations in the rock parameters from well 7219/8-2 (Iskrystall) are shown. The same behavior observed in well 7220/7-3 (Drivis) when a small amount of gas (10%) is introduced into the system the Vp and Poisson's ratio have a considerable drop of -4.21% and -16.53% respectively; while the Vs has a small increment of 0.20%.

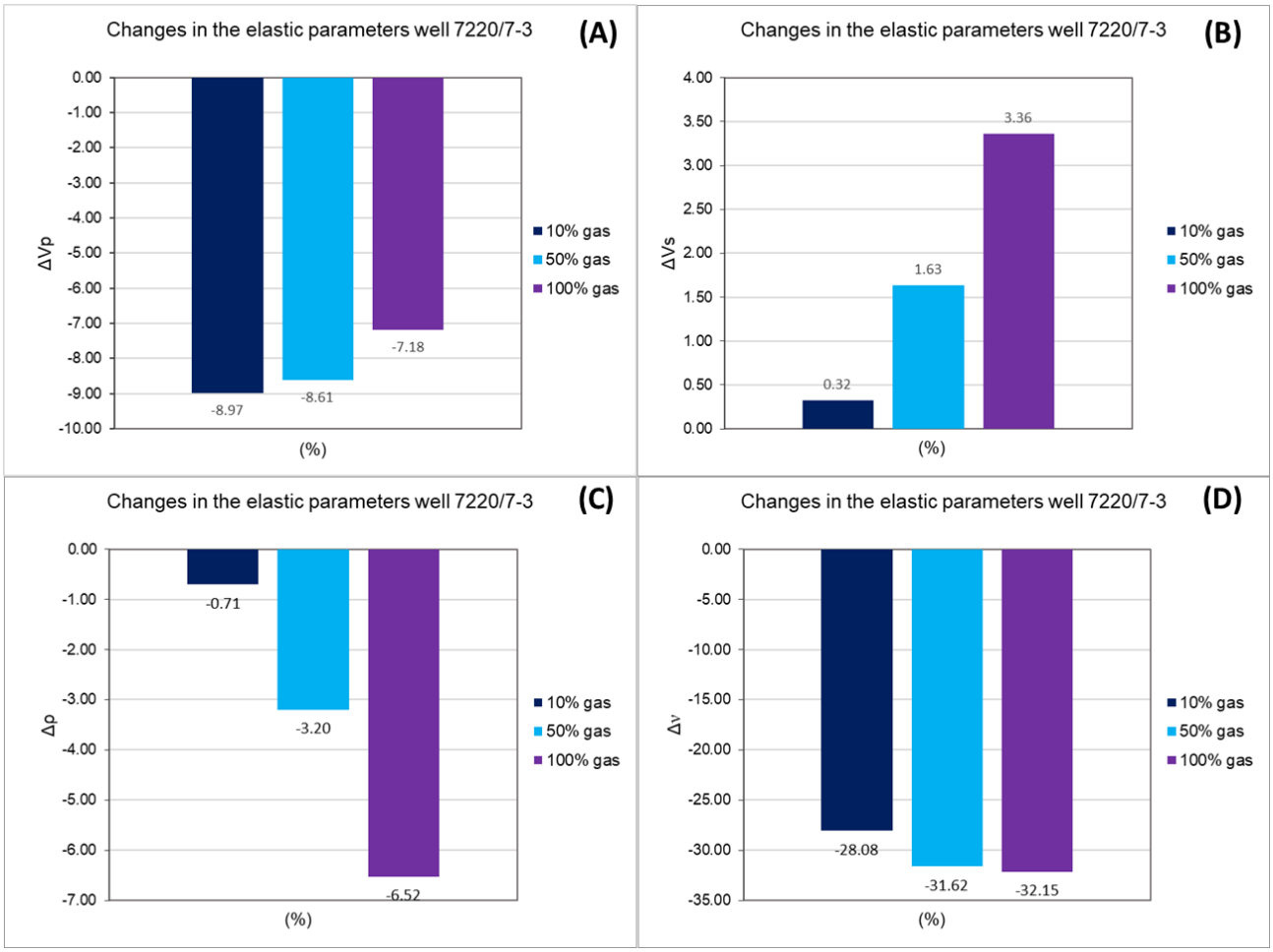

Figure 6.22: Effect of changing gas saturation on Vp (a), Vs (b), density (c) and Poisson's ration (d) of well 7220/7-3 (Drivis).

6.3.5 Implication Using Measured versus Estimated Vs

The implication of using estimated Vs from Castagna et al. (1985) instead of direct measurement has shown no influence on the AVO intercept. In Figure 6.12, it is observed that this parameter remained the same in both cases. This response is because the conversion of Vp into Vs only occurs for incidence angle greater than zero, which implies that ΔVs has not affected the reflection coefficient at zero-offset, influencing the PP reflection coefficient with increasing offset (see eq. 3.25 in chapter 3).

Nevertheless, a considerable change is observed in the AVO gradient. This value seems to decrease when the estimated Vs is used. The reasoning behind this behavior is attributed to an underestimation of Vs using Castagna's equation since it considers a brine saturated rock being unable to show a proper response due to hydrocarbon presence. From Equations 6.2 and 6.3, it is evident the direct relation among Vs, Poisson's ratio, and gradient. For a low Vs values an increase of the Poisson's ratio is expected, which might generate a small contrast at the interface and by a direct relation, the gradient would be small.

$$\nu = \frac{V_p^2 - 2V_s^2}{2(V_p^2 - V_s^2)} \quad \text{Eq. 6.2}$$

$$\Delta\nu = \frac{4}{9}(R_p + G) \quad \text{Eq. 6.3}$$

Where, ν is the Poisson's ratio, Δν the Poisson's ratio contrast, G for the gradient, and Rp the intercept.

In Table 6.6 and Figure 6.23, it is shown the Poisson's ratio estimation and contrast in case of using measured or estimated Vs. Overall, the resulting ν (Poisson's ratio) using S-wave from Castagna et al., (1985) is relatively high in comparison with the one from direct measurement. Therefore, Δν between the cap and the reservoir rocks would be smaller, as a consequence, the gradient reduces its value (Eq. 6.3). Finally, the AVO gas classification does not change despite the selection of the velocity.

Table 6.6: Poisson's ratio and contrast values at the interface using the estimated (Castagna et al., 1985) and measured Vs.

Well	**INSITU CONDITIONS**		**CONTRAST AT THE INTERFACE**	
	Poisson's ratio		**Measured**	**Castagna**
	Measured	**Castagna**	**Δν**	**Δν**
7220/7-1	0.17	0.264	-0.15	-0.06
7220/7-3	0.1766	0.255	-0.12	-0.05
7219/8-2	0.197	0.24	-0.08	-0.04

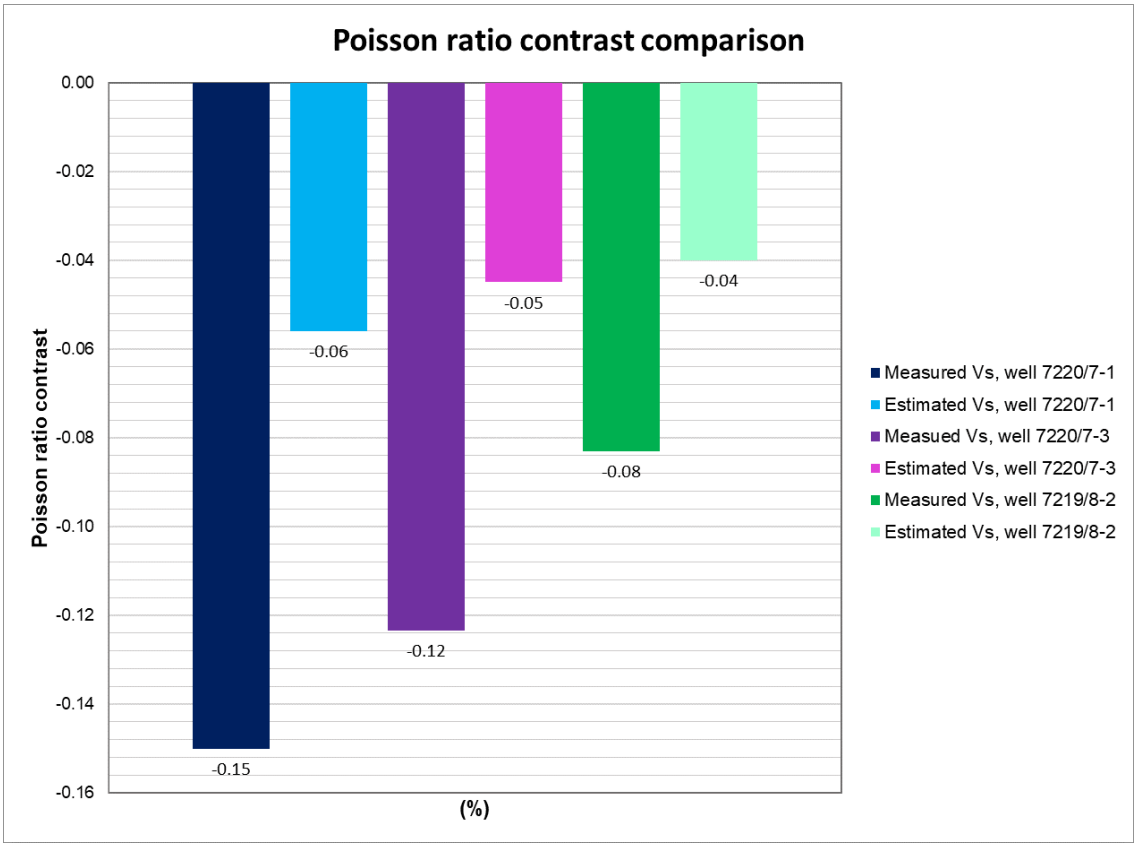

Figure 6.23: Estimation of the magnitude of the Poisson's ratio contrast across the interface on the studied wells using estimated and direct Vs values.

6.4 Uncertainties

- Several uncertainties involved in the AVO modeling are related to the fluid substitution. First, the uncertainties, carried from chapter 4, about the accuracy of the log measurement would also be involved during the creation of predicted logs for the brine, oil and gas saturated scenarios; therefore, it is important to know if the log data is providing true information about the formation.

- The absence of core data do not allow the proper mineralogy control and calibration between the porosity estimated in the petrophysical analysis and the core porosity. This correction might significantly alter the results during the fluid substitution since the Gassmann equation considers an effective medium, where low porosity and complex lithology changes are neglected. Furthermore, the violation of the other Gassmann's assumptions like low permeability, heterogenous fluid distribution would also limit the use of Gassman's equation as a direct method for AVO modeling.

- Finally, during the analysis, it is assumed a half-space model, however when multiples layers are included in the model factors that can affect the

amplitude like multiples, converted waves, attenuation must be taken into account. The presence of noise is also not considered, nevertheless random noise tends to affect the gradient and intercept (Cambois, 1998).

Chapter 7: Summary and Conclusions

The Norwegian Barents Sea has recorded a higher success rate than the North Sea and the Norwegian Sea, however, the area is considered a prospective but very challenging to find commercial quantities of hydrocarbon due to the complexity associated with regional tectonic, depositional environment, and significant uplift and erosion during Cenozoic time. Despite the effect of those factors several fields and discoveries have been made (e.g. Goliat, Snøhvit, Wisting and Johan Castberg) in the Norwegian Barents Sea.

The study area is located in the Norwegian Barents Sea within the Bjørnøyerenna Fault Complex (BFC), bounded by the Polheim Sub-Platform and Loppa High to the east, the Ringvassøy – Loppa Fault Complex and Trømso Basin to the south, and the Bjørnoya Basin in the northwest. The Jurassic successions are considered the most important reservoirs in the study area.Therefore, this work lays emphasis on the Jurassic Stø and Nordmela Formations including their cap rock shale (Fuglen Formation). The main objective is to characterize the quality of two Jurassic reservoirs that penetrated by six exploration and appraisal wells. The four wells 7220/7-1 (Havis), 7220/7-2 (Skalv), 7220/7-3 (Drivis) and 7219/8-2 (Iskrystall) included in this study have documented hydrocarbon discoveries, while the wells 7219/8-1 and 7219/9-1 are described as dry.

Petrophysical analysis, Rock Physics diagnostics and AVO forward modeling are the methods applied for this study. By combining and comparing the results and discussion, it can be stated that each method has contributed significantly to a better understanding of the target reservoirs intervals. Uncertainties and limitations associated with data and methods are included in the respective chapters.

The petrophysical analysis is carried out in all six wells where net-to-gross, shale volume, porosity, and water saturation are calculated. The results suggest that the Jurassic reservoirs units have better reservoir qualities compared to the Triassic units. The good quality reservoir of the Stø Formation has been related to the tidal and strong wave energy environments, with an average porosity of 16% and shale volume below 20%. The Nordmela Formation is more shaley than the Stø Formation. Only the upper section of the formation is interpreted as tidal channel deposits and is considered good reservoir (φ: 20%, Vsh: ~14%, and Sw: 20%). The pay zones are estimated by establishing cut-offs on the porosity, shale volume and water saturation on each of the wells. The Stø and Nordmela Formations have proven hydrocarbon and proper reservoir quality in wells 7220/7-1 (Havis), 7220/7-3 (Drivis) and 7219/8-2 (Iskrystall).

Rock physic diagnostic is carried out by using data from well 7220/7-1, 7220/7-3 and 7219/8-2 since the wells have measured Vs and proven to contain hydrocarbons. The rock physics models are utilized to obtain information about compaction, sorting, cementation, hydrocarbon content and lithological effects. Crossplots with relevant templates such as “Vp versus Porosity”, “Vp versus Vs”, “Vp/Vs versus AI” and “LMR” are used to analyze the data. The cement model (“Vp versus porosity”) is especially used for evaluating cementation effect on the reservoir rocks and the influence toward fluid sensitivity. The “Vp versus depth” trend is used to estimate the amount of uplift in the study area. The results compare with other crossplots (e.g. “Vp/Vs versus AI and LMR”), provide reasonable correlation among the amount of cement, burial depth, the level of exposure in the mechanical and chemical compaction domains and evolution of their elastic

properties. Finally, a clear separation of the data due to hydrocarbon and lithology changes has been clearly documented in the "Vp versus Vs", "Vp/Vs versus AI" and LMR crossplots.

The final method consider is the AVO modeling. This process involves generation of synthetic seismograms using information from the P-wave, S-wave and density logs, and considering a Ricker wavelet with a dominant frequency of 30 Hz. Finally, using the Gassmann's equation, fluid substitution is performed to study the fluid sensitivity and variation of the AVO signatures when one pore fluid is replaced by other fluid. Results show clear AVO signatures for target – reservoirs despite the limitation of Gassmann's equations.

To consider limitations (e.g. very short timeframe, many simplistic assumptions in models and unavailability of real seismic and cores/cuttings) to validate the results that are described in the thesis, the following conclusions are made:

- Potential Jurassic reservoir intervals are identified in the Stø and Nordmela Formations in four of the six studied wells. In general, these intervals are considered to have good reservoir qualities, however, it tends to vary from well to well due to changes in the shale content, porosity, burial depth, and burial depth. On one hand, the shallow well 7220/7-3 (Drivis) has proven to have the best reservoir qualities because it is less affected by chemical diagenesis and cementation. On the other hand, the deepest well, 7219/8-2 (Iskrystall) has the lowest reservoir qualities in comparison to the other wells where the porosity has been reduced as a consequence of significant chemical compaction and high quartz cementation.

- Reservoirs intervals of the Stø Formation are found to vary its thickness from NE to SW, becoming thicker towards SW. The effective porosity in the Stø Formation is estimated to be ~ 20%, the average shale volume is 16% and the water saturation is less than 3%. The well that has the best reservoir quality and the thickest net pay (74.8m), corresponds to well 7220/7-3 (Drivis discovery).

- The Nordmela Formation is found to have good reservoir quality only on the upper part of the succession. This formation is the thickest compared to other potential reservoirs recorded among the wells in the study area. Reservoir quality of the Nordmela Formation is not as good as the Stø Formation due to high shale/clay content. Nevertheless, the estimated porosity is between 10% - 20%, the water saturation is 16% to 37% and the shale volume is 13% - 20%. The Nordmela Formation in well 7220/7-3 (Drivis discovery) has the best reservoir quality and thickest net pay of 48.06m compared to other wells.

- Even though both Stø and Nordmela Formations are found in well 7219/9-1 and their quality is adequate in terms of thickness, porosity (16%) and shale volume (25%), it is water-bearing and classified as a dry well. The reason for dry or only having residual oil/gas is leakage and reactivation of the faults or failure of the cap rock due to Cenozoic uplift and erosion (Ofstad et al. , 2000).

- Extensive uplift and erosion have been evidenced through the entire Barents Sea area. Based on compaction trend of Storvoll et al. (2005), the exhumation is assessed to be in the range of ~870m – 1100 m, that affecting the reservoir quality in the study area.

- Compaction and cementation analysis shows that the reservoir from well 7219/8-2 is highly affected by quartz cementation. This is because Stø and Nordmela Formations were located below ~2.5km and at 100 ºC at their maximum burial, been more exposed to diagenetic processes such as cementation. However, in the shallower wells, 7220/7-1 and 7220/7-3, the Stø and Nordmela Formations have been less affected by quartz and carbonate (siderite) cement.

- The "Vp/Vs versus AI" rock physics templates work as a good fluid and lithology discriminating tool. The gas sands in the deep and shallow wells are plotted along the gas saturated line in the expected porosity range of 15% - 25% and water sand above 10%, which match reasonably well with porosity and saturation values from the petrophysical analysis. In addition, it also providess a good lithology discrimination of cap rock, since the data points from the Fuglen Formation plotted on the shale line.

- In general, LMR template works as a good fluid discriminator. The sandstones fully saturated with gas plot below the cut-off $\lambda\rho$: 20 GPa*gr/cm^3 with a high Mu-Rho response. Moreover, in wells 7220/7-1 and 7219/8-2, an increase in the shear response is attributed not only to reflect fluids in the pores but also to the increment of cement.

- The AVO modeling of the top Stø Formations at different depth across the wells results in different AVO gas sand classes. In case of wells 7220/7-1 and 7219/8-2, the anomalies are classified as class II and II P respectively. A weak class II anomaly is defined in well 72207/-3 since the formation is located at shallow depth and the sediments might be less affected by cementation. Finally, the anomaly from well 7219/9-1 is classified as class I gas sand.

- A small increase on the gas saturation (10%) creates a considerable change in the Vp and Poisson's ratio, while the relative variation in the Vs and density indicated their slight insensibility to saturation. However, for saturations above 10%, the sensitivity of all the parameters are not significant.

Reference List

Adam, L., Batzle, M. and Brevik, I. (2006). Gassmann's fluid substitution and shear modulus variability in carbonates at laboratory seismic and ultrasonic frequencies. *Geophysics*, *71*(6), 173–183.

Adams, J. A. and Weaver, C. E. (1958). Thorium-to-Uranium Ratios as Indicators of Sedimentary Processes: Example of Concept of Geochemical Facies. *AAPG Bulletin*, *42*(2), 387–430. https://doi.org/10.1306/0BDA5A89-16BD-11D7-8645000102C1865D

American Association of Petroleum Geologists (AAPG). (1994). The Photoelectric Index. *The Society for Sedimentary Geology (SEPM)*, 91–114.

Applied Petroleum Technology (APT). (2016). Petroleum Systems of the Western Margin of the Loppa High, Norwegian Barents Sea. Retrieved December 19, 2017, from http://www.aptec.no/~/media/images/23r/4069_w loppa high.ashx

Asquith, G. and Krygowski, D. A. (2004). Porosity logs. In *Basic well log analysis* (AAPG Sp., pp. 37–76). Tulsa, Oklahoma: AAPG.

Avseth, P. (2000). *Combining Rock Physics and Sedimentology for Seismic Reservoir Characterization of North Sea Turbidite Systems*. Stanford University.

Avseth, P., Mukerji, T., Mavko, G. and Dvorkin, J. (2010). Rock-physics diagnostics of depositional texture, diagenetic alterations, and reservoir heterogeneity in high-porosity siliciclastic sediments and rocks — A review of selected models and suggested work flows. *Geophysics*, *75*(5), 7531–7547.

Avseth, P., Mukerji, T. and Mavko, G. (2005). *Quantitative Seismic Interpretation. Applying Rock Physics Tools to Reduce Interpretation Risk*. Cambridge University Press.

Baig, I., Faleide, J.I., Jahren, J. and Mondol, N. H. (2016). Cenozoic exhumation on the southwestern Barents Shelf: Estimates and uncertainties constrained from compaction and thermal maturity analyses. *Marine and Petroleum Geology*, *73*, 105–130. Retrieved from http://dx.doi.org/10.1016/j.marpetgeo.2016.02.024

Cambois, G. (1998). AVO attributes and noise: Pitfalls of crossplotting. *SEG Technical Program Expanded Abstracts 1998*, 244–247. Retrieved from https://library.seg.org/doi/abs/10.1190/1.1820390

Castagna, J., Batzle, M. L. and Eastwood, R. (1985). Relationships between compressional-wave in elastic silicate. *Geophysics*, *50*(4), 571–581.

Castagna, J., Swan, Herbert, W. and Foster, D. (1998). Framework for AVO gradient and intercept interpretation. *Geophysics*, *63*(3), 948–956. Retrieved from https://library.seg.org/doi/10.1190/1.1444406

Castagna, J.P., Batzle, M.L., Kan, T. K. (1993). Rock physics. The link between rock properties and AVO response. In astagna, J.P. and Backus, M. (Ed.), *Offset-dependent reflectivity-Theory and practice of AVO analysis: Investigations in Geophysics* (Vol. 8, pp. 135–171).

CGG Veritas. (2018). AVO Attribute extraction. Retrieved January 24, 2018, from https://www.cgg.com/en/What-We-Do/GeoSoftware/Platform-Environment/AVO-Attribute-Extraction

Chopra, S. and Castagna, J. P. (2014). AVO, 1–283.

Clark, S. A., Glorstad-Clark, E., Faleide, J. I., Schmid, D., Hartz, E. H. and Fjeldskaar, W. (2014). Southwest Barents Sea rift basin evolution: Comparing results from backstripping and time-forward modelling. *Basin Research*, *26*(4), 550–566.

Clark, A. (2017). *Reservoir characterization of the Fruholmen and Stø Formations in the Hoop Fault Complex , SW Barents Sea Reservoir quality as a function of provenance*. University of Oslo.

Dalland, A., Worsley, D. and Ofstad, K. (1988). A lithostratigraphic scheme for the Mesozoic and Cenozoic succession offshore mid- and northern Norway. *NPD Bulletin 4*, *4*, 1–65.

Davies, S. J. and Elliott, T. (1996). Spectral gamma ray characterization of high resolution sequence stratigraphy: examples from Upper Carboniferous fluvio-deltaic systems, County Clare, Ireland. *The Geological Society*, *104*, 25–35.

Doré, A.G. and Jensen, L. N. (1996). The impact of late Cenozoic uplift and erosion on hydrocarbon exploration: offshore Norway and some other uplifted basins. *Global and Planetary Change*, *12*(1–4), 415–436.

Doré, A. G. (1995). Barents Sea Geology, Petroleum Resources and Commercial Potential. *Arctic*, *48*(3), 207–221. Retrieved from http://www.jstor.org/stable/10.2307/40511656

Doveton, J. (1994). The Spectral Gamma-Ray Log. In Doveton, J. (Ed.), *Geological Log Interpretation*. SEPM Society for Sedimentary Geology.

Dvorkin, J. and Nur, A. (1996). Elasticity of high-porosity sandstones: Theory for two North Sea data sets. *Geophysics*, *61*, 1363–1370.

Ellis, D. V. and Singer, J. M. (2008). *Well Logging for Earth Scientists* (Second). Springer.

Faleide, J. I., Vågnes, E. and Gudlaugsson, S. T. (1993). Late Mesozoic-Cenozoic evolution of the south-western Barents Sea in a regional rift-shear tectonic setting. *Marine and Petroleum Geology*, *10*(3), 186–214.

Faleide, J.I., Bjørlykke, K. and and Gabrielsen, R. (2010). Geology of the Norwegian Continental Shelf. In *Petroleum Geoscience. From sedimentary environments to rock physics* (pp. 467–499). Springer-Verlag Berlin Heidelberg. https://doi.org/10.1007/978-3-642-02332-3

Fanavoll, S., Gabrielsen, P. T. and Ellingsrud, S. (2014). Special section : Interpretation and integration of CSEM data CSEM as a tool for better exploration decisions : Case studies from the Barents Sea , Norwegian Continental Shelf. *Interpretation*, *2*(3).

Gabrielsen, R. H., Færseth, R. B., Jensen, L. N., Kalheim, J. E. and Riis, F. (1990). Structural elements of the Norwegian continental shelf. Part 1: The Barents Sea Region. *Norwegian Petroleum Directorate Bulletin*, *6*, 1–47.

Gabrielsen, R. H., Grunnaleite, I. and Rasmussen, E. (1997). Cretaceous and tertiary inversion in the Bjørnøyrenna Fault Complex, south-western Barents Sea. *Marine and Petroleum Geology*, *14*(2), 165–178.

Gautier, D., Bird, K., Charpentier, R., Grantz, A., Houseknecht, D., Klett, T., Moore, T., Pitman, J., Schenk, C., Schuenemeyer, J., Sørensen, K., Tennyson, M., Valin, Z. and Wandrey, C. (2009). Assessment of Undiscovered Oil and Gas in the Arctic. *Science Mag*, *324*(5931), 1175–1179. Retrieved from http://science.sciencemag.org/content/324/5931/1175.long

Gelius, L. J. (2017a). Elastic waves. Retrieved January 20, 2018, from https://geoclass.no/node/720

Gelius, L. J. (2017b). Seismic Attributes. Retrieved January 20, 2018, from https://geoclass.no/node/970

Gernigon, L., Brönner, M., Roberts, D., Olesen, O., Nasuti, A. and Yamasaki, T. (2014). Crustal and basin evolution of the southwestern Barents Sea: From Caledonian orogeny to continental breakup. *Tectonics Journal*, *33*(4), 347–373.

Glørstad-Clark, E., Birkeland, E. P., Nystuen, J. P., Faleide, J. I. and Midtkandal, I. (2011). Triassic platform-margin deltas in the western Barents Sea. Marine and Petroleum Geology. *Marine and Petroleum Geology*, *28*, 1294–1314.

Glover, P. (2013). The Spectral Gamma Ray Log. Retrieved August 20, 2005, from http://homepages.see.leeds.ac.uk/~earpwjg/PG_EN/CD Contents/GGL-66565 Petrophysics English/Chapter 12.PDF

Goodway, B., Taiwen, C. and Downton, J. (1997). Improved AVO fluid detection and lithology discrimination using Lamé petrophysical parameters; "λρ","μρ",&"λ/μ fluid stack", from P and S inversions. *Society of Exploration Geophysicists*, 183–186. Retrieved from https://csegrecorder.com/articles/view/improved-avo-fluid-detection-and-lithology-discrimination-using-lame-petrop

Greenberg, M. L. and Castagna, J. P. (1992). Shear-Wave Velocity Estimation in porous rocks: Theoretical Formulation, Preliminary Verification, and Applications. *Geophysical Prospecting*, (2), 195–209.

Gudlaugsson, S. T., Faleide, J.I., Johansen, S.E. and Breivik, A. J. (1998). Late Palaeozoic structural development of the South-western Barents Sea. *Marine and Petroleum Geology*, *15*(1), 73–102.

Hall, M. (2013). Interpreting Spectral Gamma-Ray logs. Retrieved from https://agilescientific.com/blog/2013/2/26/interpreting-spectral-gamma-ray-logs.html

Halland, E., Bjørnestad, A., Gjeldvik I., Bjørheim, M., Magnus, C., Meling, I., Mujezinović, J., Riis, F., Rød, R., Pham, V. and Tappel, I. (2014). Chapter-6: Barents Sea. Retrieved May 18, 2018, from http://www.npd.no/Global/Norsk/3-Publikasjoner/Rapporter/CO2-samleatlas/Chapter-6.pdf

Han, D., Nur, A. and Dale, M. (1986). Effects of porosity and clay content on wave velocities in sandstones. *Geophysics*, *51*(11), 2093–2107. Retrieved from http://library.seg.org/doi/abs/10.1190/1.1442062

Heafford, A. P. (1988). Carboniferous through Triassic stratigraphy of the Barent Shelf. *W.B. Harland and EK. Dowsdeswell (Eds). Geological Evolution of the Barents Shelf Region. Graham and Trotman, Alden Press. Oxford*, 89–108.

Henriksen, E., Ryseth, A. E., Larssen, G. B., Heide, T., Ronning, K., Sollid, K. and Stoupakova, A. V. (2011). Chapter 10: Tectonostratigraphy of the greater Barents Sea: implications for petroleum systems. *Geological Society, London, Memoirs*, *35*(1), 163–195. Retrieved from http://mem.lyellcollection.org/cgi/doi/10.1144/M35.10

Indrevær, K., Gabrielsen, R., and Faleide, J.I. (2016). Early Cretaceous synrift uplift and tectonic inversion in the Loppa High area, southwestern Barents Sea, Norwegian shelf. *Journal of the Geological Society*, *174*, 242–254.

Javid, S. (2013). *Petrography and petrophysical well log interpretation for evaluation of sandstone reservoir quality in the Skalle well (Barents Sea) Sanaz Javid*. University of Trondheim.

Kenedy, M. (2015). *Practical Petrophysics*. (H. Cubitt, J. and Wales, Ed.) (62nd ed.). Elsevier Ltd.

Klaja, J. and Dudek, L. (2016). Geological interpretation of spectral gamma ray (SGR) logging in selected boreholes. *Nafta-Gaz*, *72*(1), 3–14. https://doi.org/10.18668/NG2016.01.01

Klausen, T. G., Müller, R.,Sláma, J., Olaussen, S., Rismyhr, B. and Helland-Hansen, W. (2017). Depositional history of a condensed shallow marine reservoir succession: stratigraphy and detrital zircon geochronology of the Jurassic Stø Formation, Barents Sea. *Journal of the Geological Society*, 1–16.

Klausen, T. G., Ryseth, A. E., Helland-Hansen, W., Gawthorpe, R. and Laursen, I. (2015). *Regional development and sequence stratigraphy of the Middle to Late Triassic Snadd Formation, Norwegian Barents Sea*. *Marine and Petroleum Geology* (Vol. 62). Elsevier Ltd. Retrieved from http://dx.doi.org/10.1016/j.marpetgeo.2015.02.004

Krief, M., Garar, J., Stellingwerff, J. and Ventre, J. (1990). A petrophysical interpretation using the velocities of P and S waves (full-waveform sonic). *The Log Analyst*, *31*, 355–369.

Kristensson, J. (2016). *Formation evaluation of the Jurassic Stø and Nordmela formations in exploration well 7220/8 - 1, Barents Sea, Norway*. University of Lund.

Larsen, D. (2011). *Fluid flow features along the Bjørnøyrenna Fault Complex west of West Loppa High, SW Barents Sea*. University of Tromsø.

Liner, C. L. and Fei, T. W. (2006). Layer-induced seismic anisotropy from full-wave sonic logs: Theory, application, and validation. *Geophysics*, *71*(6), D183–D190.

Liu, Q., Yin, X. and Li, C. (2015). Fluid discrimination based on rock physics templates. *Journal of Geophysics and Engineering*, *12*(5), 830–838.

Lundschien, B., Høy, T. and Mørk, A. (2014). Triassic hydrocarbon potential in the northern Barents Sea; integrating Svalbard and stratigraphic core data. *Norwegian Petroleum Directorate Bulletin*, *11*(11), 3–20.

Magoon, L. B. and Dow, W. G. (1994). The Petroleum System - from source to trap. *AAPG Memoir*, *60*, 3–24.

Manger, E. G. (1963). Porosity and Bulk Density of Sedimentary Rocks. *Geological Survery Bulletin 1144-E*, 62.

Marcussen, Ø., Maast, T. E., Mondol, N. H., Jahren, J. and, & Bjørlykke, K. (2010). Changes in physical properties of a reservoir sandstone as a function of burial depth - The Etive Formation, northern North Sea. *Marine and Petroleum Geology*, *27*(8), 1725–1735. Retrieved from http://dx.doi.org/10.1016/j.marpetgeo.2009.11.007

Marion, D., Nur, A., Yin, H. and, & Han, D. (1992). Compressional velocity and porosity in sand-clay mixtures. *Geophysics*, *57*(4), 554–563. Retrieved from http://library.seg.org/doi/10.1190/1.1443269

Mavko, G., Chan, C. and Mukerji, T. (1995). Fluid substitution: Estimating changes in V[sub P] without knowing V[sub S]. *Geophysics*, *60*(6), 1750–1755. https://doi.org/10.1190/1.1443908

Mavko, G., Mukerji, T.,and Dvorkin, J. (1998). *The Rock Physics Handbook*. Cambridge University Press.

Mavko, G. (2009a). Elasticity and Hooke's law. In *Geophysics The Rock Physics Handbook: Tools for Seismic Analysis of Porous Media* (Second, pp. 21–76). Cambridge University Press.

Mavko, G. (2009b). Seismic wave propagation. In *Geophysics The Rock Physics Handbook: Tools for Seismic Analysis of Porous Media* (Second, Vol. 15, pp. 81–160). California: Cambridge University Press.

Mondol, N. H. (2015). Seismic exploration. In K. Bjørlykke (Ed.), *Petroleum Geoscience. From sedimentary environments to rock physics* (Second Ed, pp. 375–402). Springer-Verlag Berlin Heidelberg.

Mondol, N.H., Bjørlykke, K., Jahren, J. and Høeg, K. (2007). Experimental mechanical compaction of clay mineral aggregates-Changes in physical properties of mudstones during

burial. *Marine and Petroleum Geology*, *24*(5), 289–311.

Mondol, N. H. (2015). Well logging: Principles, Applications and Uncertainties. In K. Bjørlykke (Ed.), *Petroleum Geoscience. From sedimentary environments to rock physics* (Second Ed, pp. 385–425). Springer-Verlag Berlin Heidelberg.

Moore, W. R., Ma, Y. Z., Urdea, J., Bratton, T. and Al, M. E. (2011). Uncertainty Analysis in Well-Log and Petrophysical Interpretations. *Uncertainty Analysis and Reservoir Modeling: AAPG Memoir 96*, 17–28.

Nisar, A., Perveiz, K. and Abdul, W. (2016). Rock physics modeling to assess the impact of spatial distribution pattern of pore fluid and clay contents on acoustic signatures of partially-saturated reservoirs. *Acta Geodaetica et Geophysica*, *51*, 1–13.

Norwegian Petroleum Directorate (NPD). (2014). 6.1 - Geology of the Barents Sea. Retrieved November 1, 2017, from http://www.npd.no/en/Publications/Reports/Compiled-CO2-atlas/6-The-Barents-Sea/61-Geology-of-the-Barents-Sea/

Norwegian Petroleum Directorate (NPD). (2017a). Expecting exploration record in the Barents Sea. Retrieved December 1, 2017, from http://www.npd.no/en/news/News/2017/Expecting-exploration-record-in-the-Barents-Sea/

Norwegian Petroleum Directorate (NPD). (2017b). Fact Pages. Retrieved January 12, 2018, from http://factpages.npd.no/factpages/Default.aspx?culture=en

Norwegian Petroleum Directorate (NPD). (2017c). Plays. Retrieved January 10, 2018, from http://www.npd.no/en/Publications/Reports/Geological-assessment-of-petroleum-resources---Barents-Sea-north-2017/Plays/

Norwegian Petroleum Directorate (NPD). (2018). Fact Maps. Retrieved May 16, 2018, from http://gis.npd.no/factmaps/html_21/

Nyland, B., Jensen, L. N., Skagen, J., Skarpnes, O., Vorren, T. (1992). Tertiary Uplift and Erosion in the Barents Sea: Magnitude, Timing and Consequences. *Structural and Tectonic Modelling and Its Application to Petroleum Geology. NPF, Special Publication No. 1*, 153–162.

Ødegaard, E. and Avseth, P. (2003). Interpretation of elastic inversion results using rock physics templates. In *the 65th EAGE Conference & Exhibition*.

Ofstad, K., Kittilsen, E. J. and Alexander-Marrack, P. (2000). *Improving the Exploration Process by Learning from the Past*. Amsterdam: Elsevier Ltd. Retrieved from https://books.google.no/books?id=_5JatlCpxsAC&pg=PA102&lpg=PA102&dq=well+7219/9-1&source=bl&ots=tmR0L6X7JK&sig=m5KiNSdjkKbkbFckCs_gujNyNuQ&hl=es&sa=X&ved=0ahUKEwj66aXi_eHaAhVBhqQKHS3bCXoQ6AEIZzAO#v=onepage&q=well 7219%2F9-1&f=false

Ohm, S., Karlsen, D. A. and Austin, T. J. F. (2008). Geochemically driven exploration models in

uplifted areas: Example from the Norwegian Barents Sea. *AAPG Bulletin*, *92*(9), 1191–1223.

Olaussen, S., Dalland, A., Gloppen, T. and Johannessen, E. (1984). Depositional environment and diagenesis of Jurassic reservoir sandstones in the eastern part of Troms I area. *Petroleum Geology of the North European Margin. Springer*, 61–79. Retrieved from https://link.springer.com/chapter/10.1007/978-94-009-5626-1_6#citeas

Pelletier, H. (2008). AVO Crossplotting Revisited: A Practitioner's Perspective. *CSEG Recorder*, (December), 41–47.

Perez, M. A. and Tonn, R. (2003). Reservoir Modelling and Interpretation with Lamé ' s Parameters : A Grand Banks Case Study, 1–11.

Petrowiki. (2015). Porosity evaluation with acoustic logging. Retrieved November 1, 2017, from http://petrowiki.org/Porosity_evaluation_with_acoustic_logging

Raymer, L.L., Hunt, E.R. and Gardner, J. S. (1980). An improved sonic transit time-to-porosity transform. In *SPWLA 21st Annual Logging Symposium* (pp. 1–12). Lafayette, Louisiana.

Rider, M. and Kennedy, M. (2011). *The geological interpretation of well logs* (Third). Sutherland, United Kingdom: Rider-French Consulting Limited.

Rutherford, S. R. and Williams, R. H. (1989). Amplitude-versus-offset variations in gas sands. *Geophysics*, *54*(6), 680–688. Retrieved from http://library.seg.org/doi/10.1190/1.1442696

Ryseth, A. (2014). Sedimentation at the Jurassic-Triassic boundary, south-west Barents Sea: Indication of climate change. *From Depositional Systems to Sedimentary Successions on the Norwegian Continental Margin*, 187–214.

Saadullah, N. (2015). *Reservoir quality of Jurassic sandstones in SW Barents Sea*. University of Oslo.

Sales, J. (1993). Closure vs. seal capacity- a fundamental control on the distribution of oil and gas. In A. G. Doré (Ed.), *Basin Modelling: Advances and applications.* (Special ed, pp. 399–414). Amsterdam: NPF.

Schulumberger Limited. (2017). Porosity. Retrieved January 4, 2018, from http://www.glossary.oilfield.slb.com/Terms/p/porosity.aspx

Sheriff, R. E. (2002). *Encyclopedic dictionary of applied geophysics*. (E. F. Scherrer, Ed.), *Society of exploration geophysics* (Fourth). Tulsa, Oklahoma: Society of Exploration Geophysicists.

Simm, R., White, R. and Uden, R. (2000). The anatomy of AVO crossplots. *The Leading Edge*, 150–155.

Smelror, M., Petrov, O. V., Larssen, G. B. and Werner, S. (2009). Atlas: Geological History of the Barents Sea Geological History of the Barents Sea, 1–138. Retrieved from http://issuu.com/ngu_/docs/atlas_-_geological_history_of_the_b/1?e=3609664/9026048

Statoil ASA. (2017). Johan Castberg. Retrieved December 1, 2017, from https://www.statoil.com/en/what-we-do/new-field-developments/johan-castberg.html

Stephenson, M.A., Guargena, C., Fjeldskaar, W., Michelsenc, J. . (1995). Integrated basin modeling for maturity predictions in the Bjørnøyrenna Fault Complex. *Norwegian Petroleum Society*, *4*, 287–304.

Storvoll, V., Bjørlykke, K. and Mondol, N.H. (2005). Velocity-depth trends in Mesozoic and Cenozoic sediments from the Norwegian Shelf. *AAPG Bulletin*, *3*, 359–381.

University of Oslo (UiO). (2016). Open hole wireline logging. Retrieved January 1, 2018, from http://www.uio.no/studier/emner/matnat/geofag/GEO4250/v08/Open_Hole_Wireline_logging.pdf

Williams, M.D. (1990). The Acoustic Log Hydrocarbon Indicator. In *31st Annual Logging Symposium* (pp. 1–23).

Worthington, P. F. and Cosentino, L. (2005). The Role of Cut-offs in Integrated Reservoir Studies. *SPE Reservoir Evaluation & Engineering*, *8*(4), 276–290. Retrieved from http://www.onepetro.org/doi/10.2118/84387-PA

Zhaolong, L. (2013). *Petroleum System Analysis in Skrugard Area , SW Barents Sea*. University of Trondheim.

Appendix A: Compaction Trends

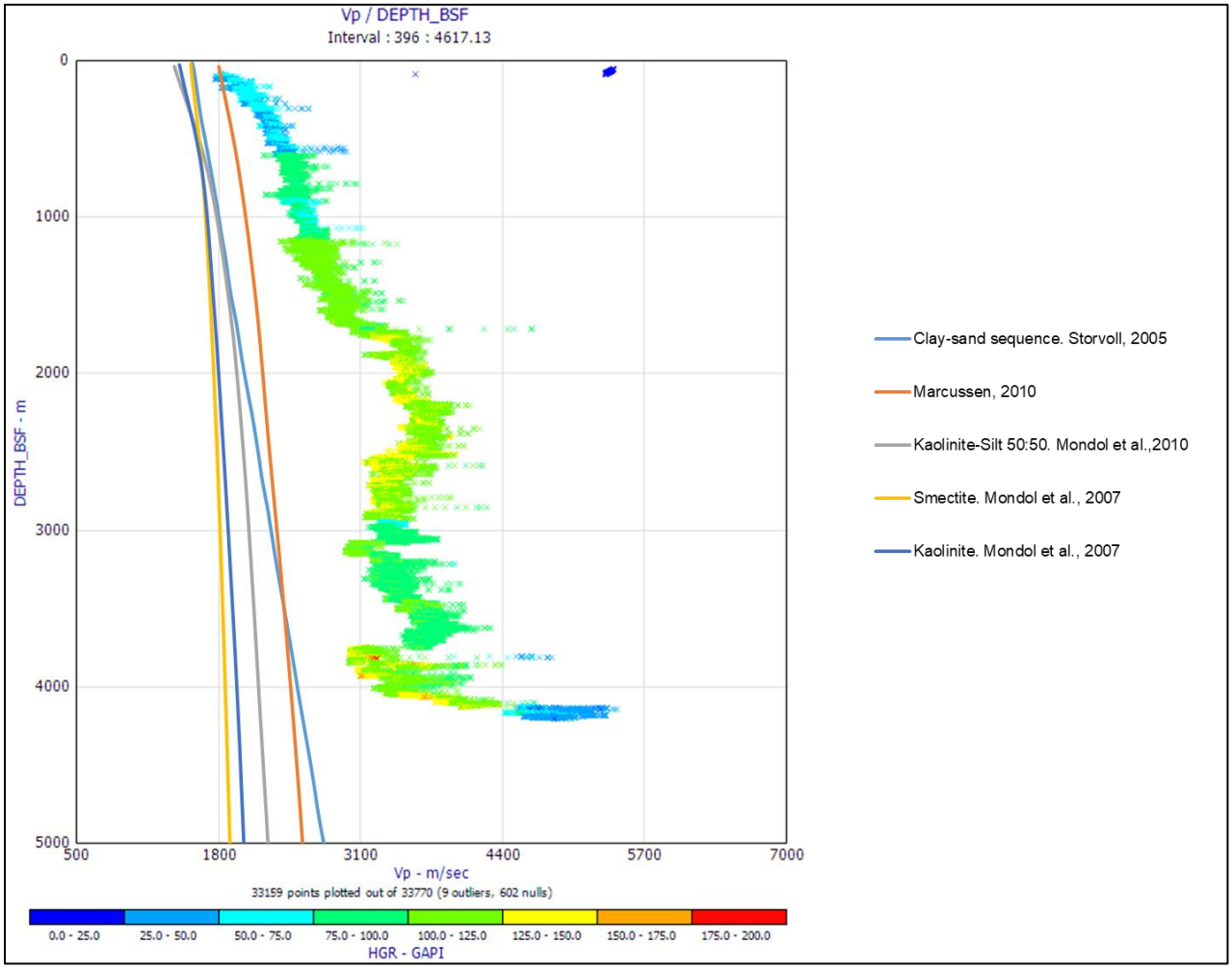

Figure A.1: Vp versus depth plot from well 7219/8-1 against published Vp-velocity trends. Data is color-coded in gamma ray.

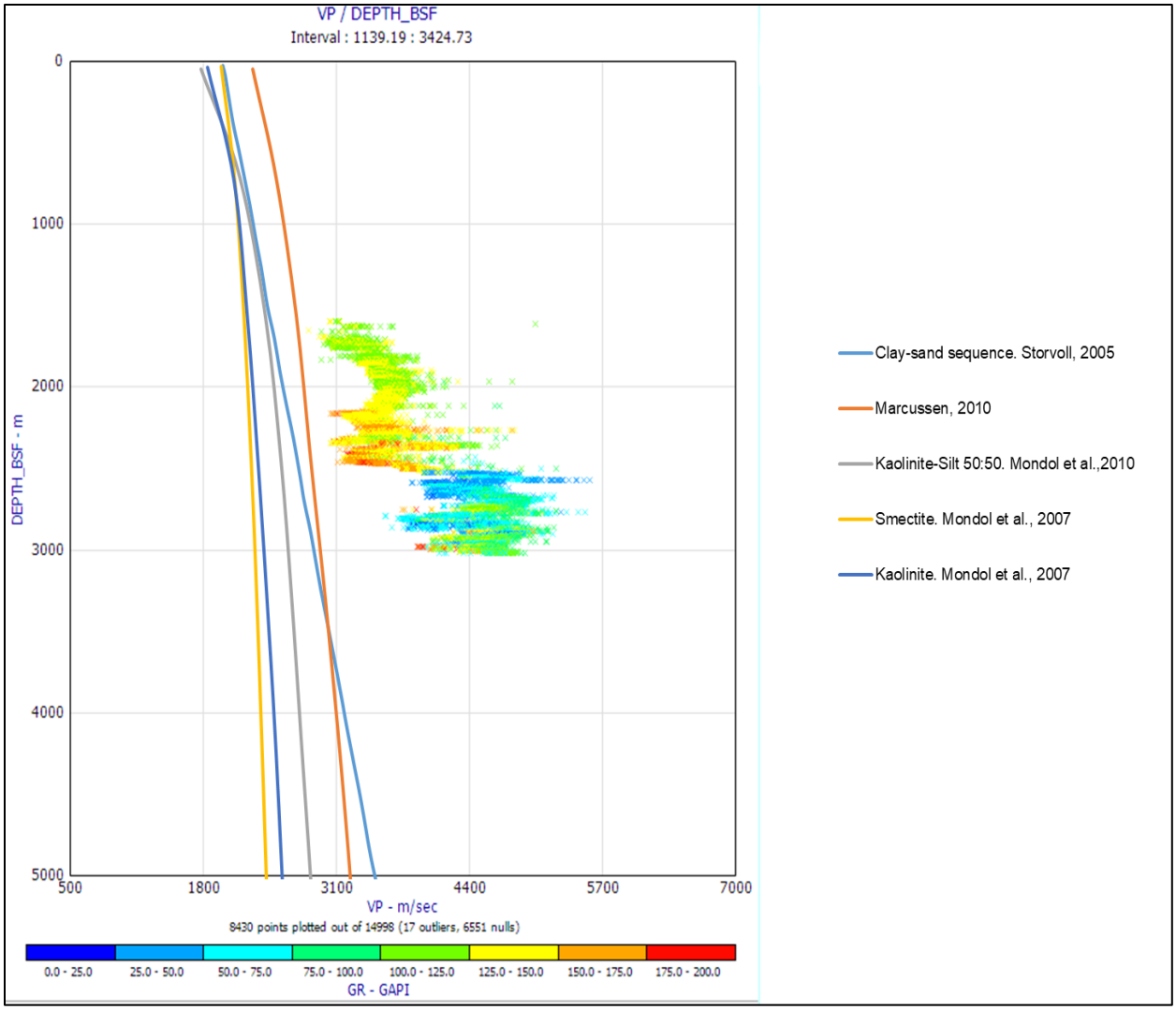

Figure A.2: Vp versus depth plot from well 7219/8-2 (Iskrystal) against published Vp-velocity trends. Data is color-coded in gamma ray.

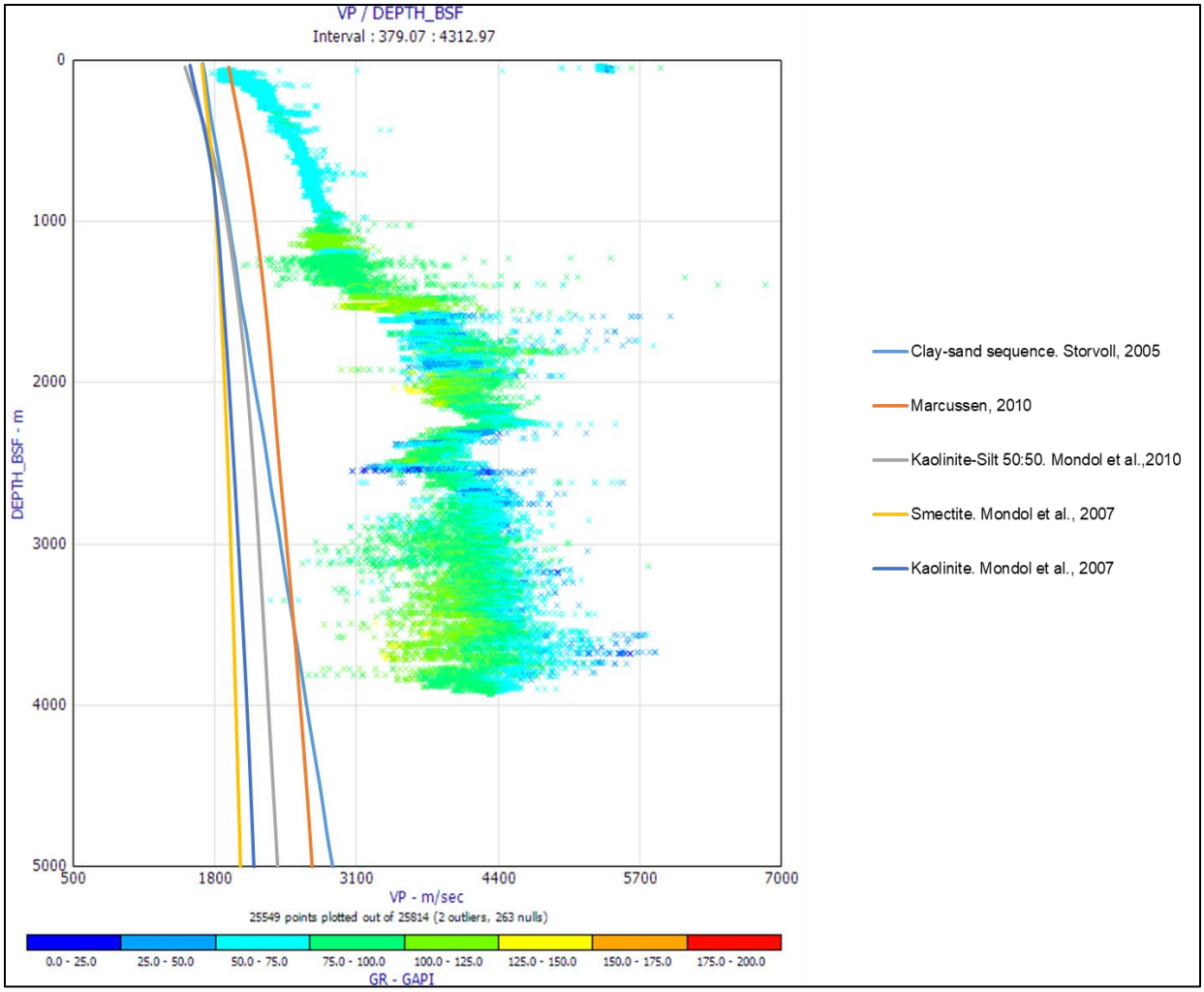

Figure A.3. Vp versus depth plot from well 7219/9-1 against published Vp-velocity trends. Data is color-coded in gamma ray.

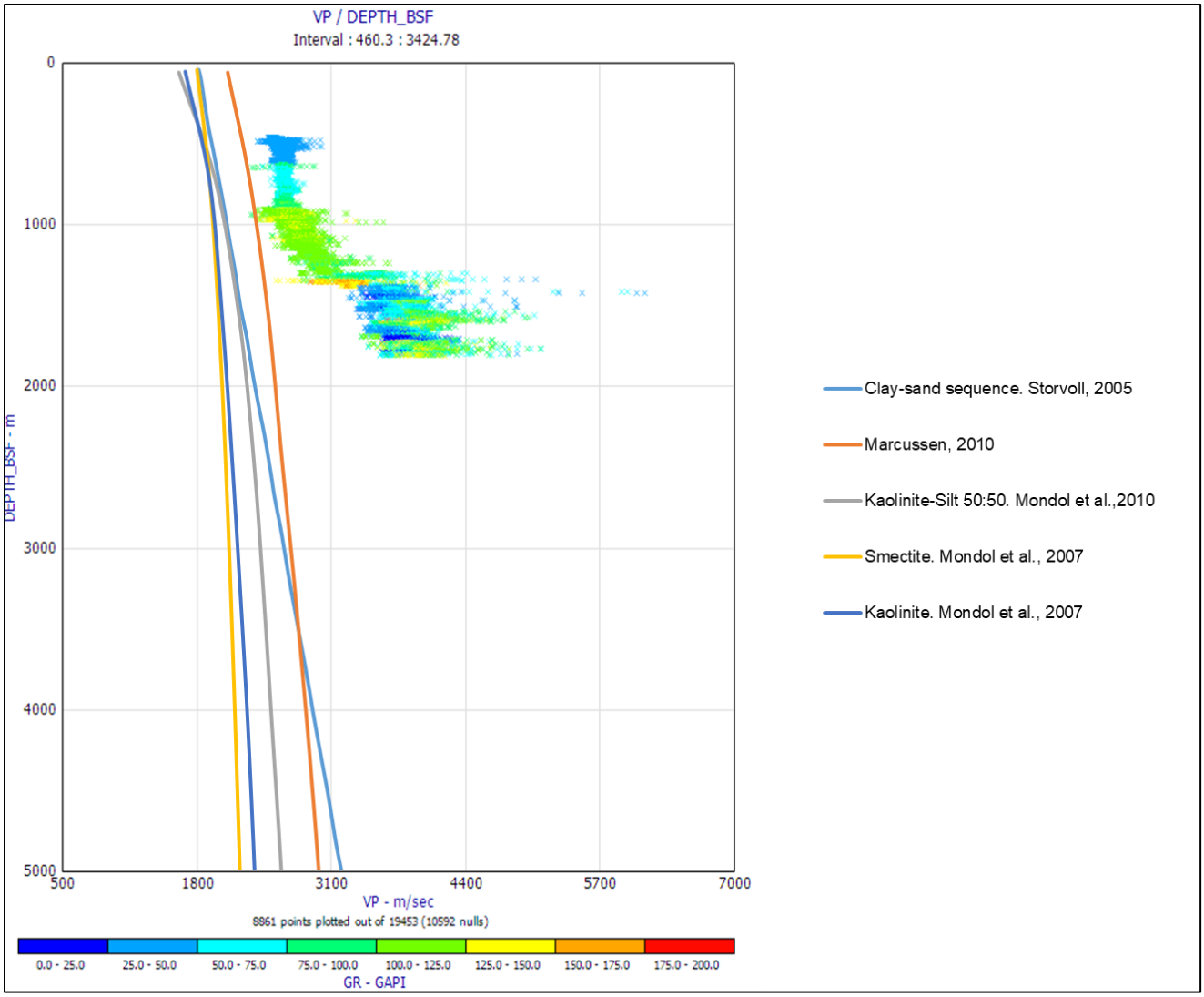

Figure A.4: Vp versus depth plot from well 7220/7-1(Havis) against published Vp-velocity trends. Data is color-coded in gamma ray.

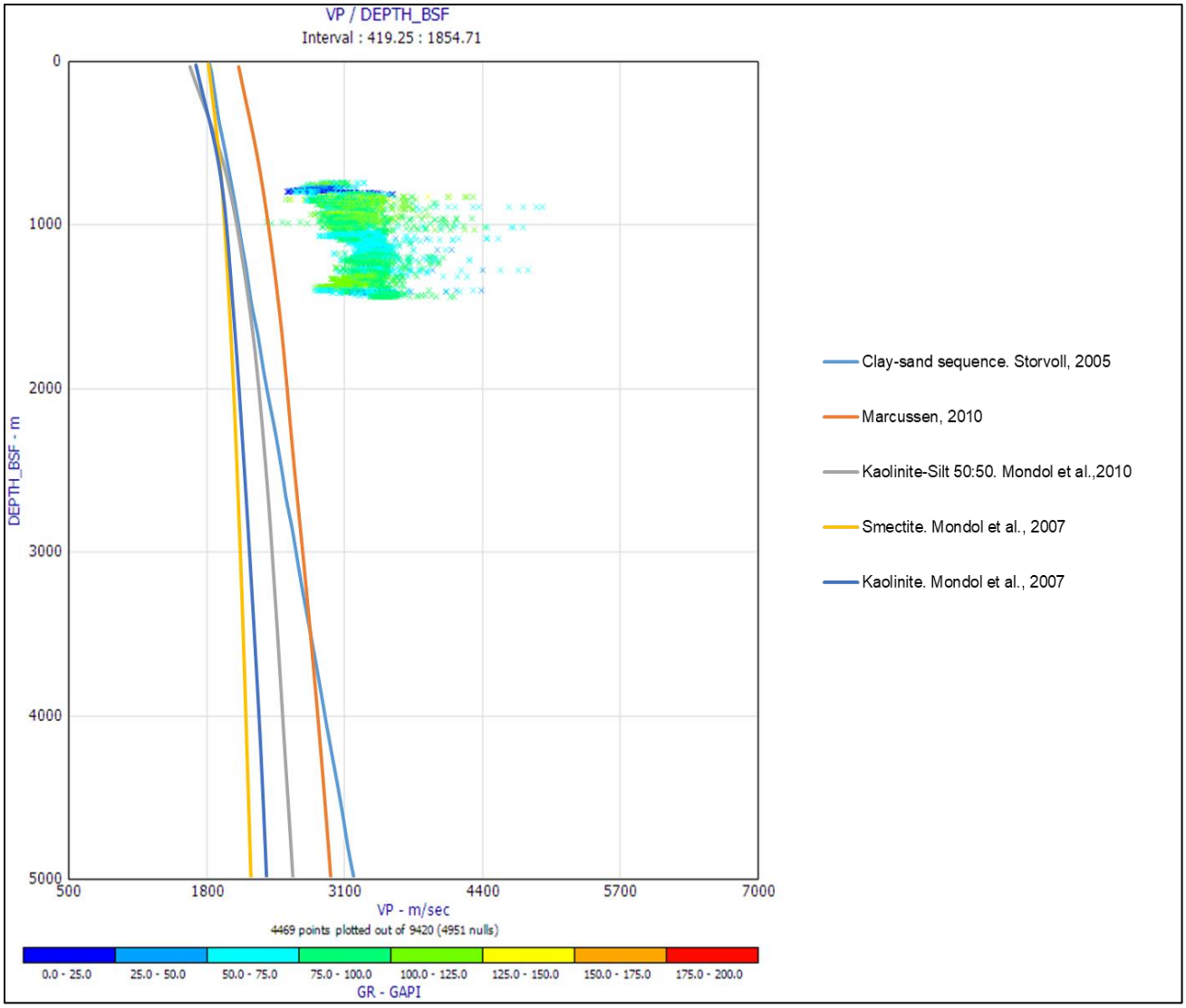

Figure A.5: Vp versus depth plot from well 7220/7-2 (Skavl) against published Vp-velocity trends. Data is color-coded in gamma ray.

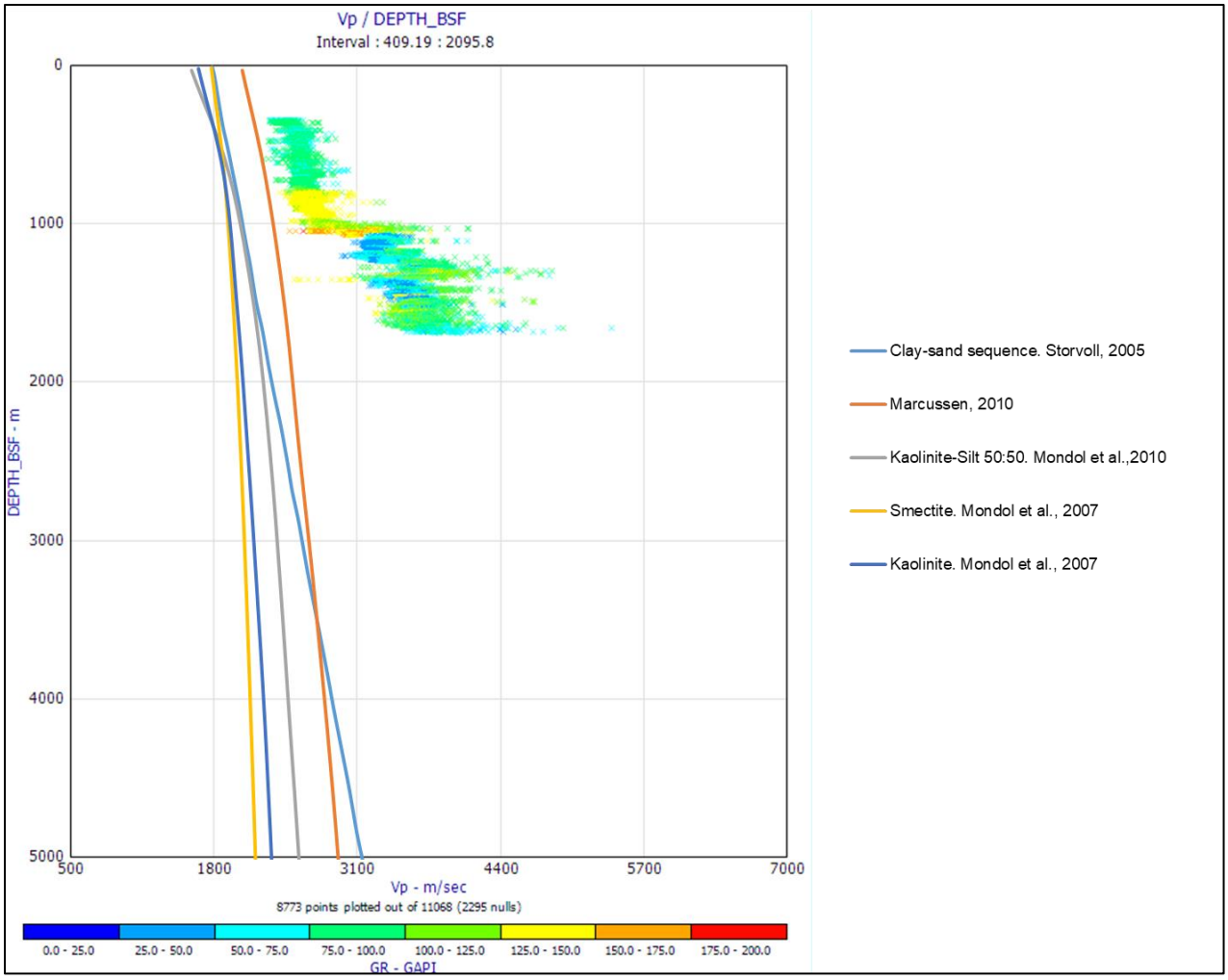

Figure A.6: Vp versus depth plot from well 7220/7-3 (Drivis) against published Vp-velocity trends. Data is color-coded in gamma ray.

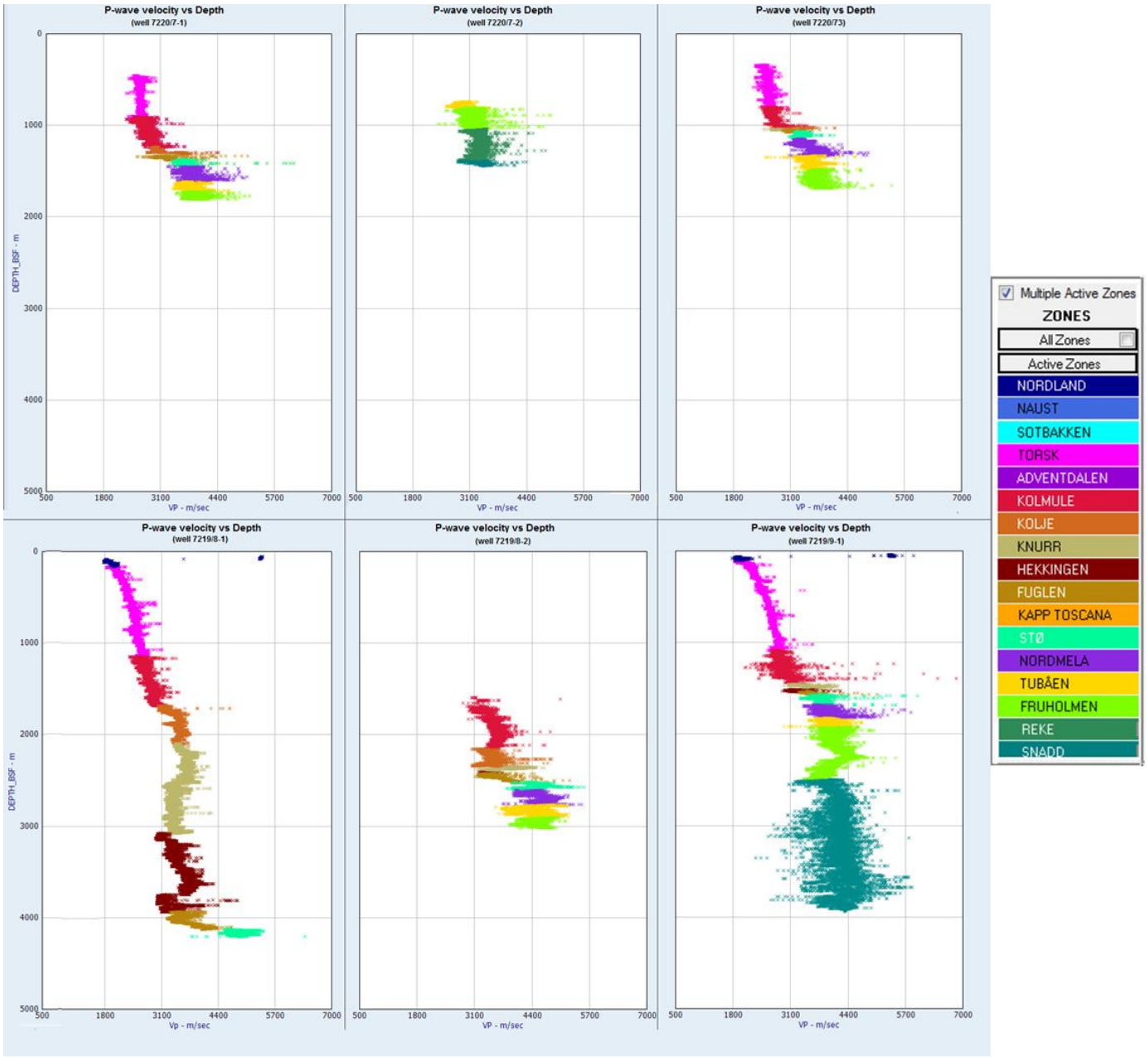

Figure A.7: Vp versus depth plot from all wells. The data is color-coded according to each of the penetrated formations.

Appendix B: Rock Physics Diagnostics

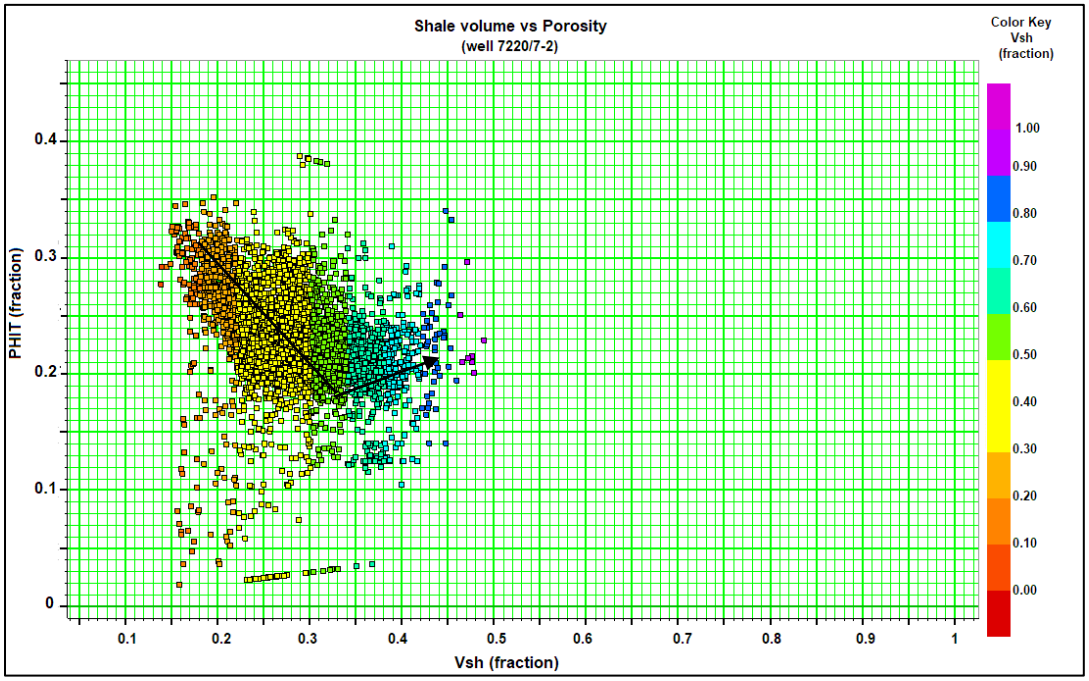

Figure B.1: Total porosity (PHIT) versus shale volume from the Fruholmen Formation in well 7220/7-2 (Iskrystall).

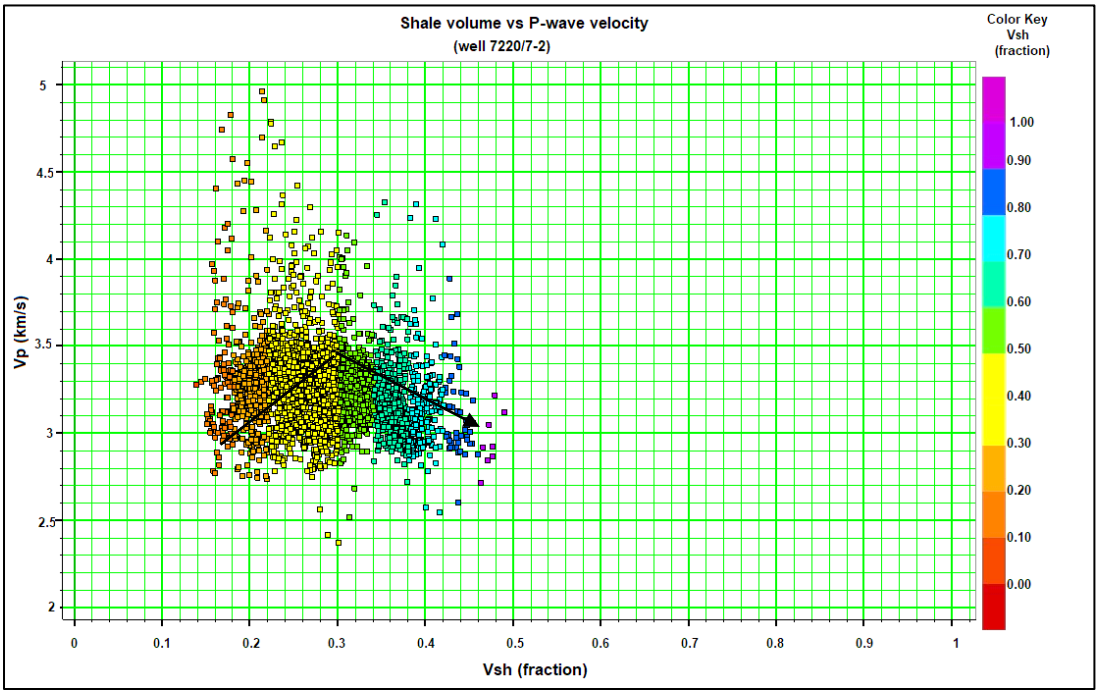

Figure B.2: Vp versus shale volume crossplot from the Fruholmen Formation in well 7220/7-2 (Iskrystall).

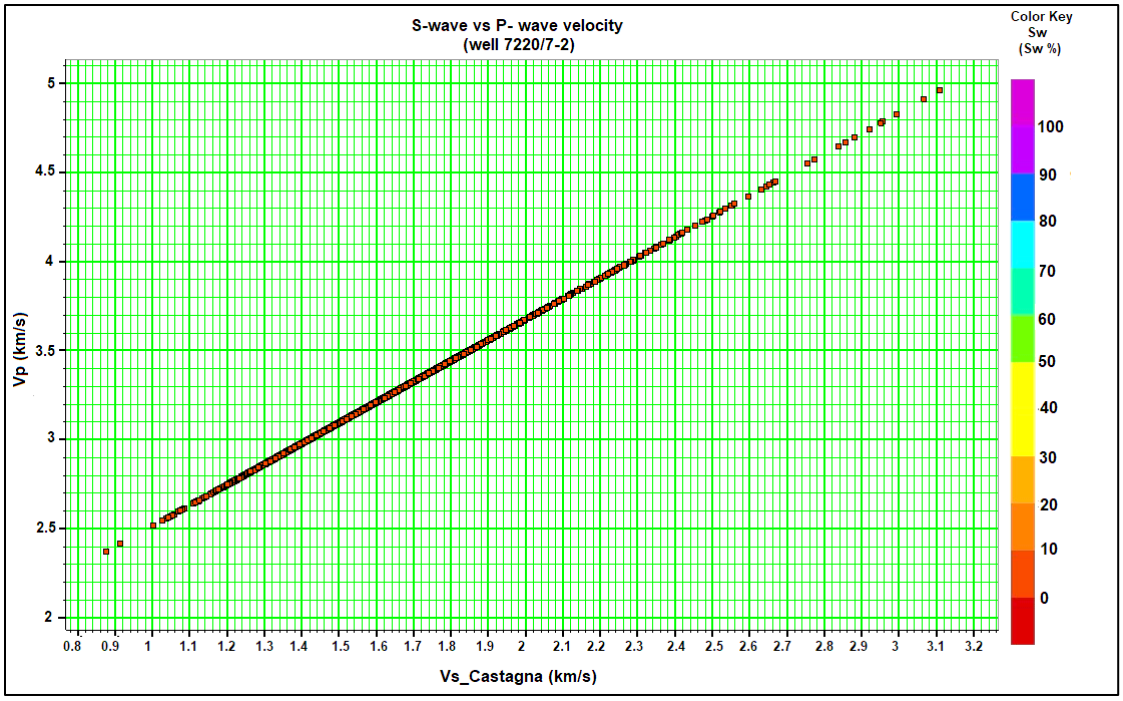

Figure B.3: Vs estimation using Castagna (1985) Vp-Vs relation on well 7220/7-2 (Iskrystall). A linear trend is observed in the crossplot been unable for proper fluid or lithology discrimination.

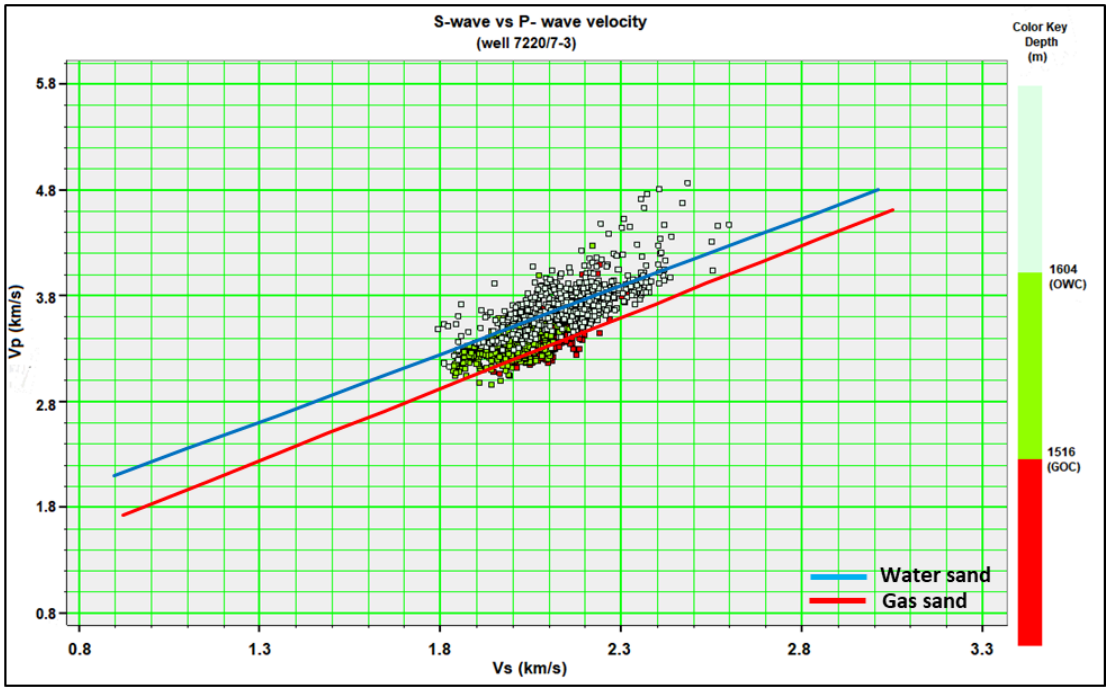

Figure B.4: Vp versus Vs crossplot showing the distribution of the fluids according to the contact depth in the Jurassic reservoir (Stø and Nordmela Formations) from well 7220/7-3 (Drivis). GOC: gas-oil contact, OWC: oil-water contact.

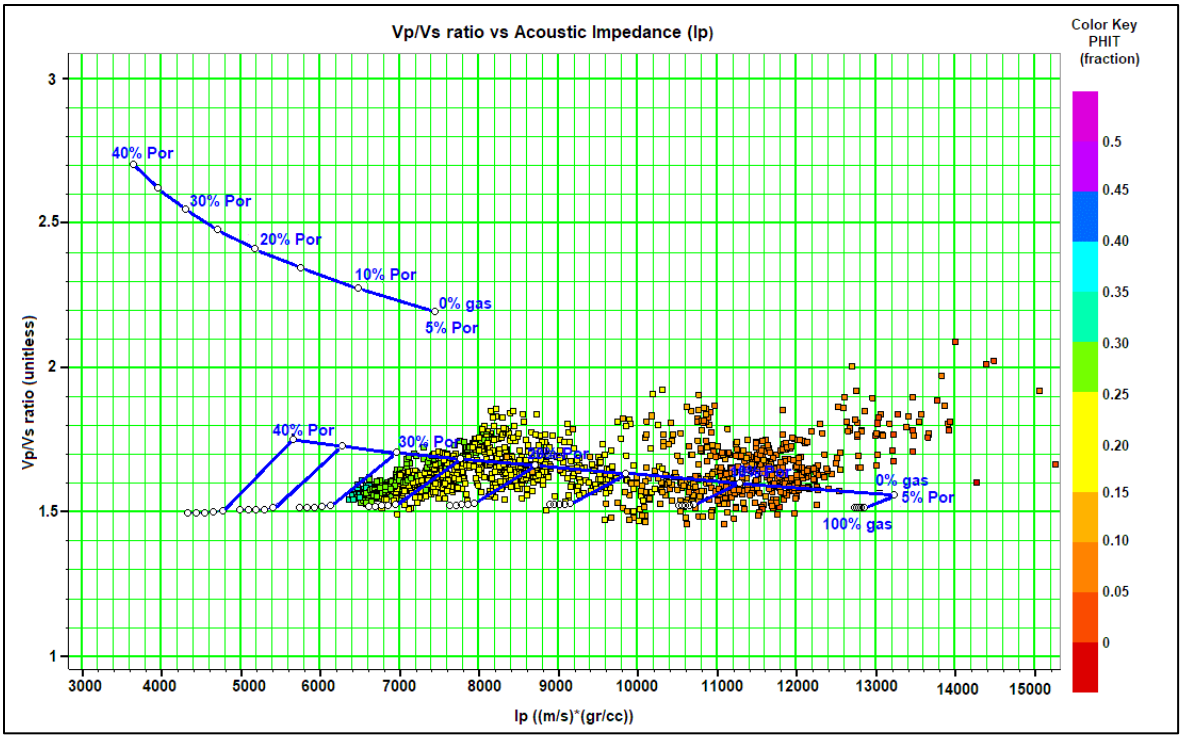

Figure B.5: Vp/Vs versus Acoustic impedance (Ip) of the Stø Formation from all the wells.

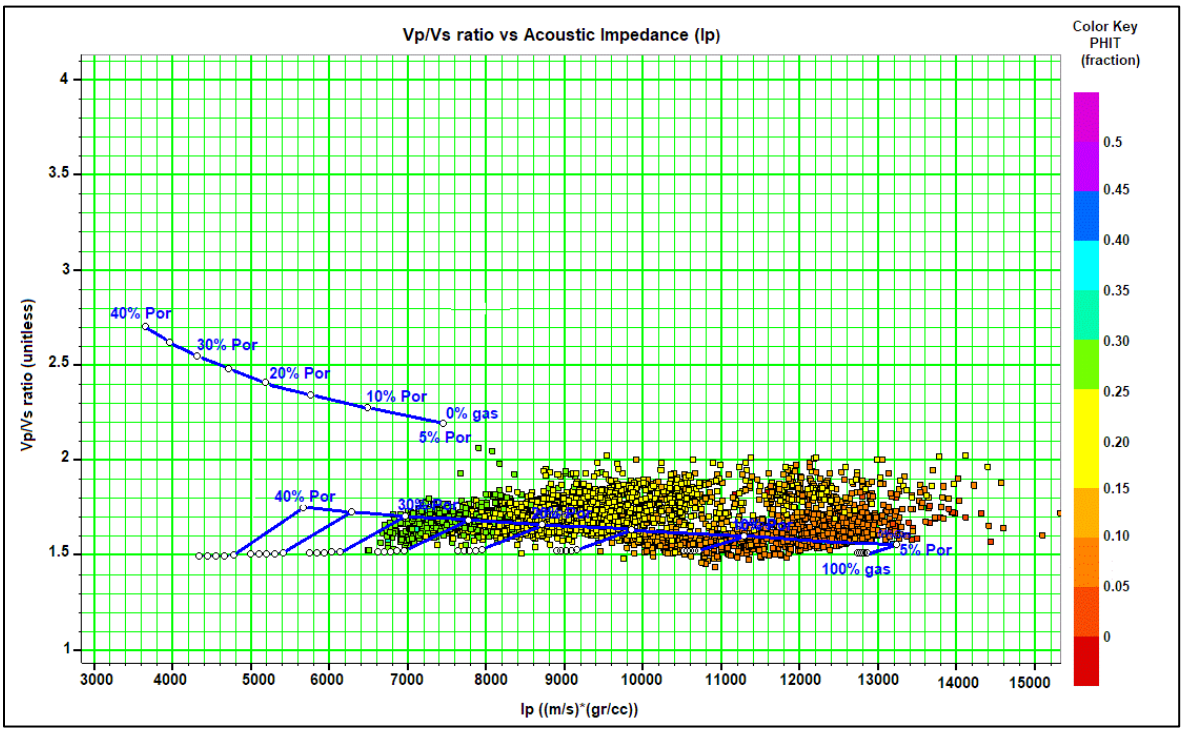

Figure B.6: Vp/Vs versus Acoustic impedance (Ip) of the Nordmela Formation from all the wells.

Appendix C: AVO forward modeling

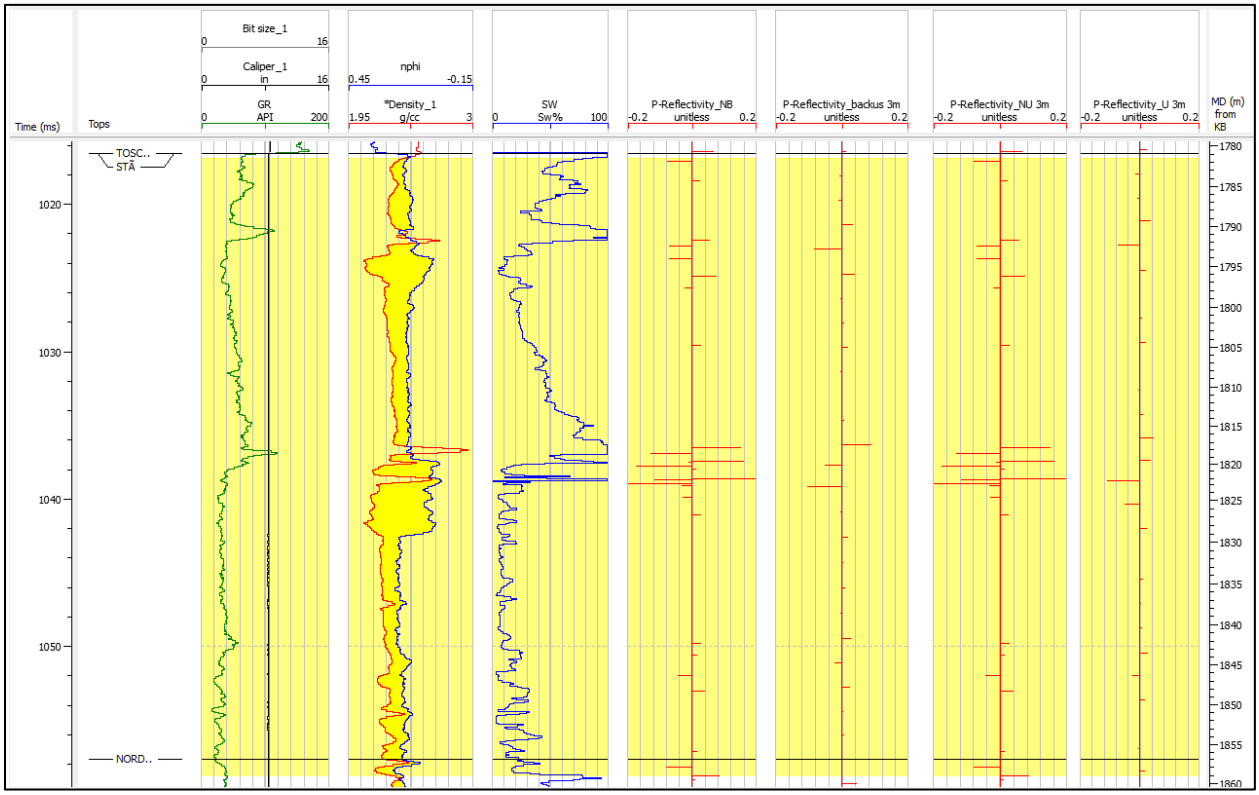

Figure C.1: P-wave reflectivity for the well 7220/7-1 from Backus average, Non-uniform and uniform methods for 3m window length. The highlighted zone corresponds to the hydrocarbon saturated interval, NB: non-blocked, NU: non-uniform and U: uniform.

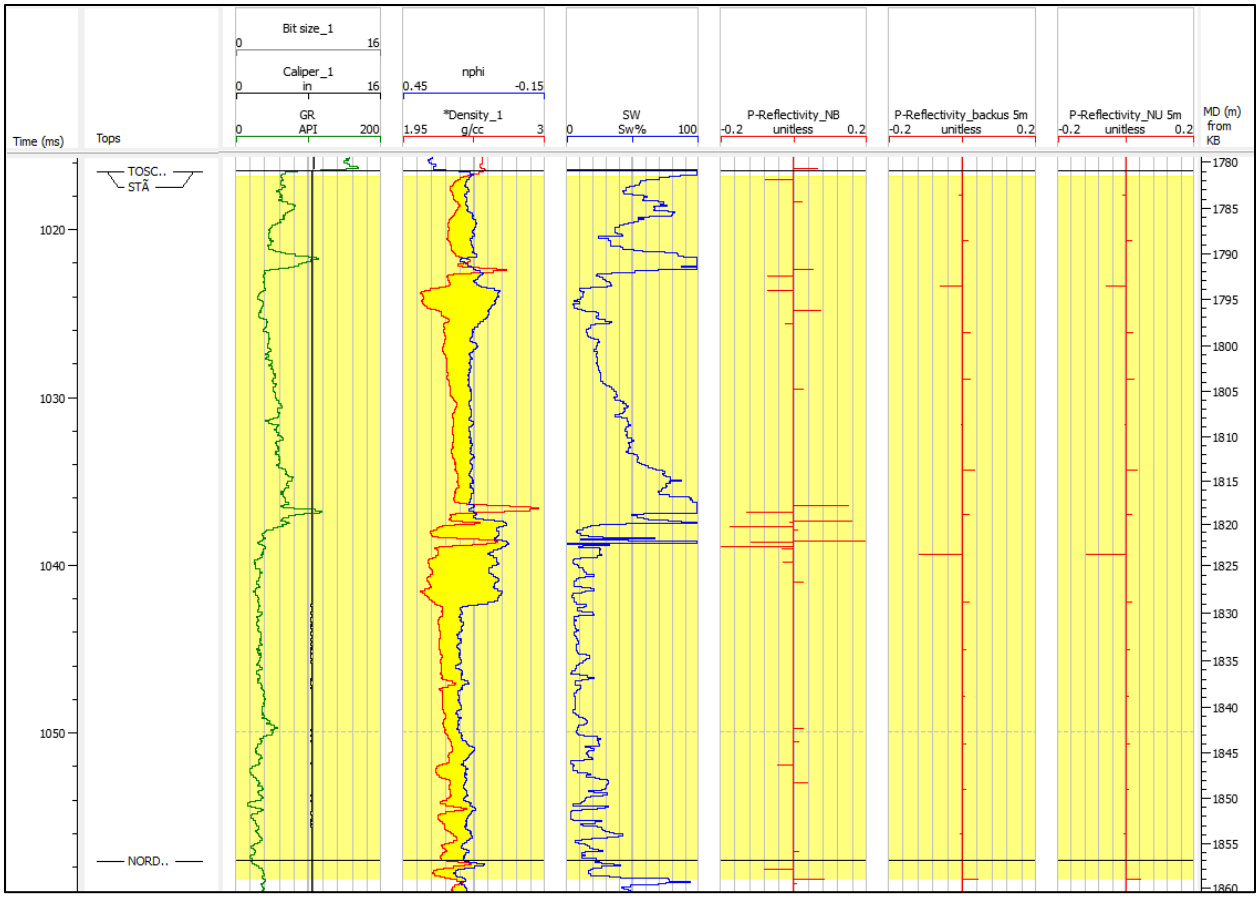

Figure C.2: P-wave reflectivity for the well 7220/7-1 from Backus average, Non-uniform and uniform methods for 5m window length. The highlighted zone corresponds to the hydrocarbon saturated interval, NB: non-blocked, NU: non-uniform and U: uniform.

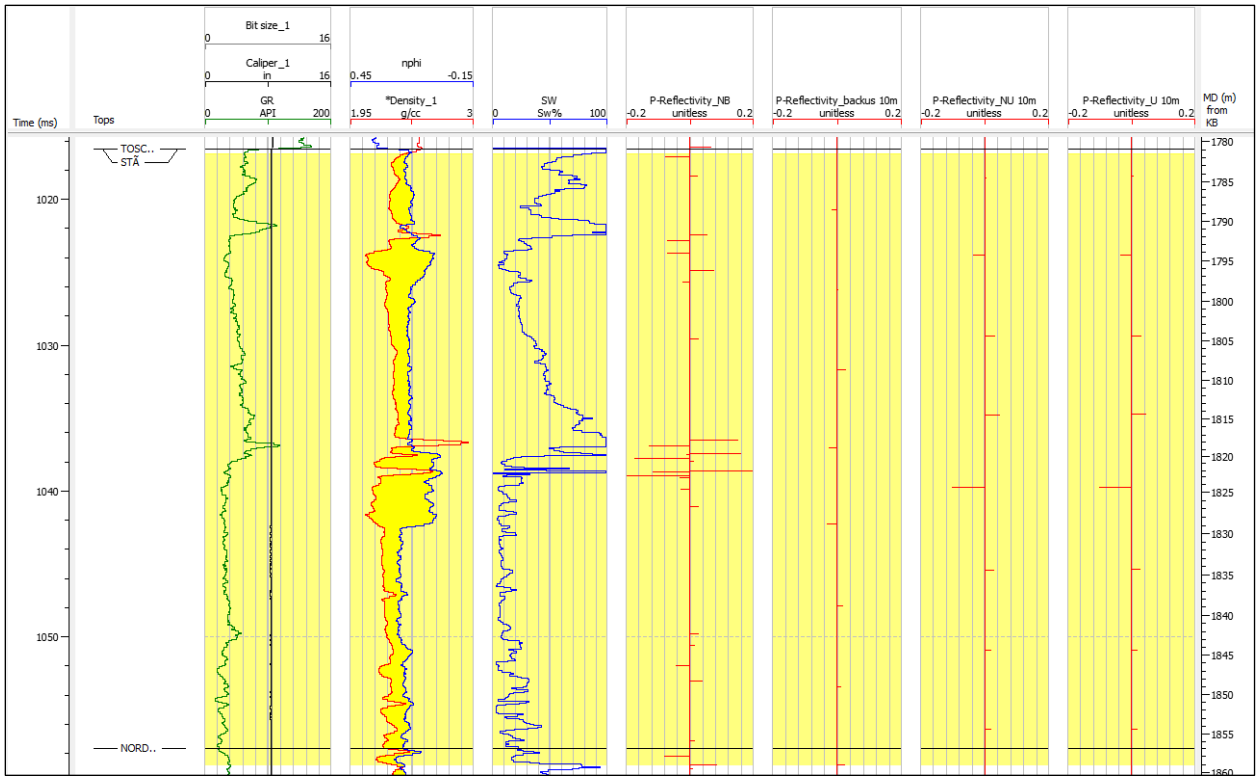

Figure C.3: P-wave reflectivity for the well 7220/7-1 from Backus average, Non-uniform and uniform methods for 10m window length. The highlighted zone corresponds to the hydrocarbon saturated interval, NB: non-blocked, NU: non-uniform and U: uniform.

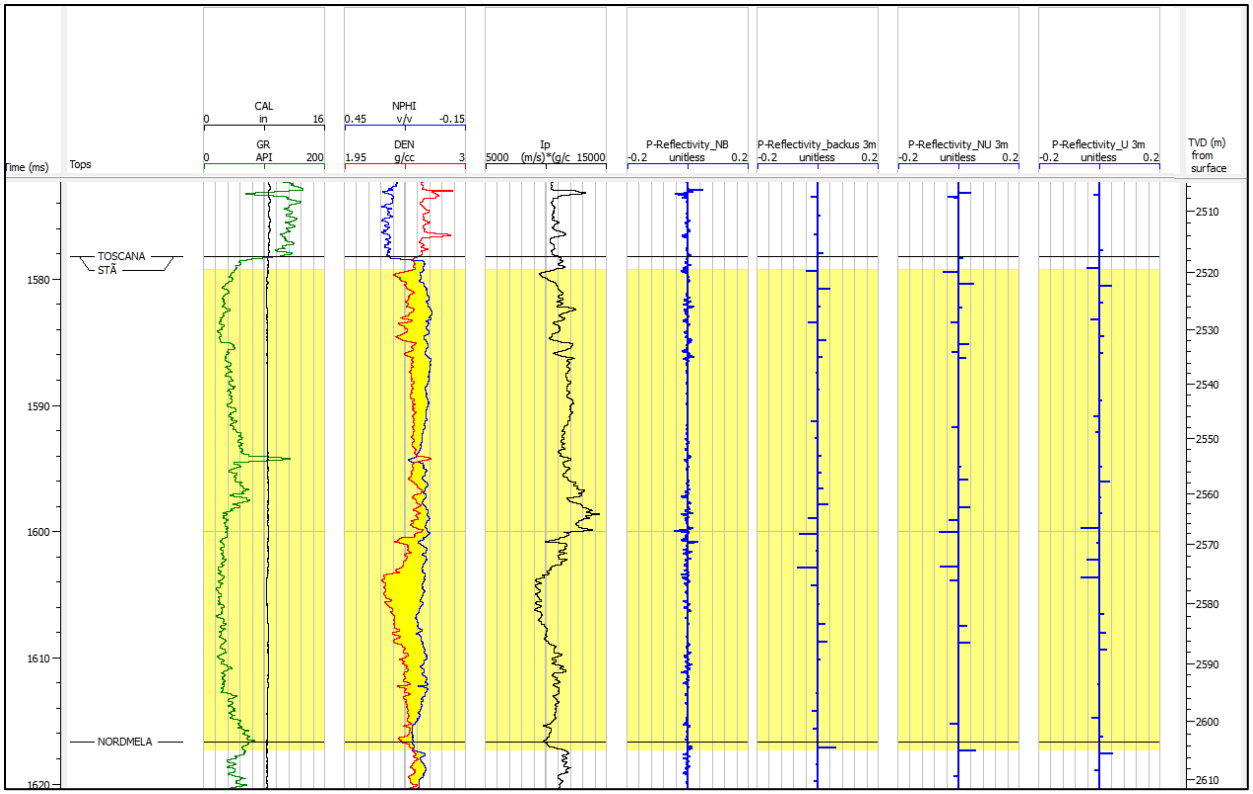

Figure C.4: P-wave reflectivity for the well 7219/8-2 from Backus average, Non-uniform and uniform methods for 3m window length. The highlighted zone corresponds to the hydrocarbon saturated interval, NB: non-blocked, NU: non-uniform and U: uniform.

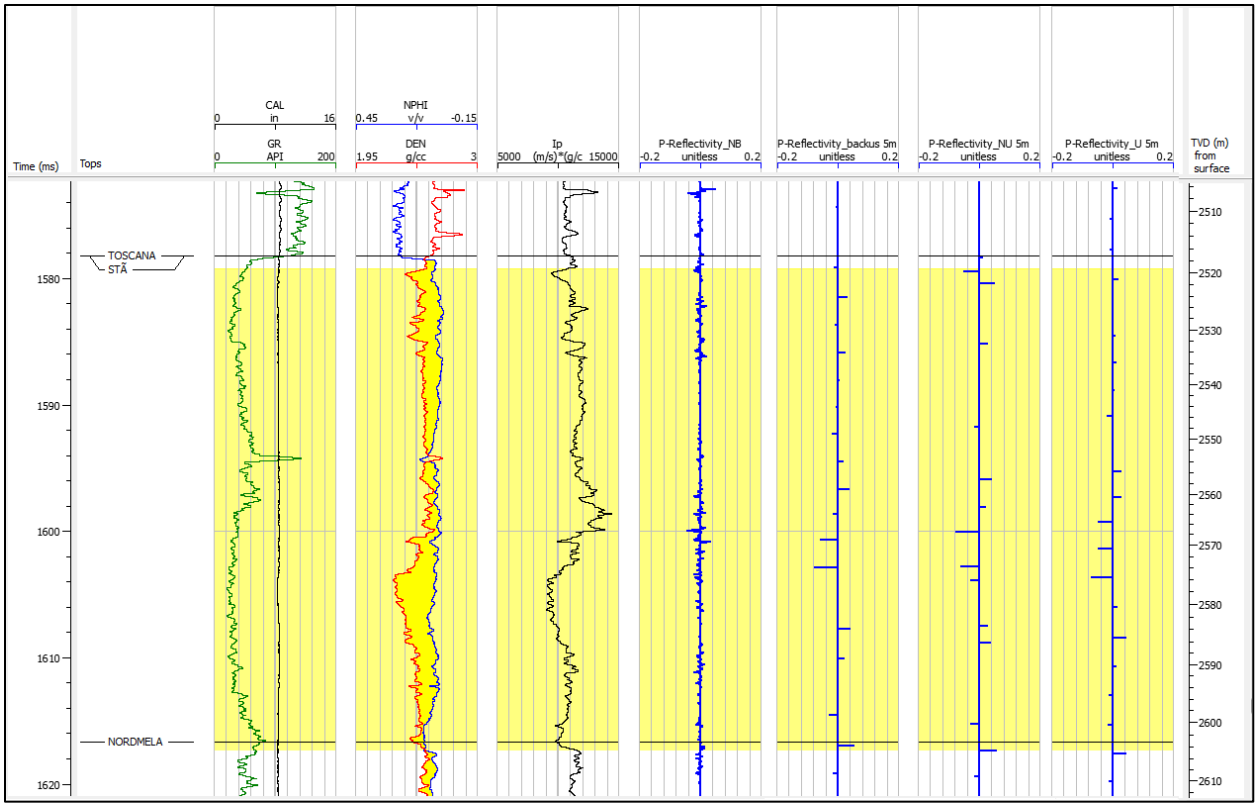

Figure C.5: P-wave reflectivity for the well 7219/8-2 from Backus average, Non-uniform and uniform methods for 5m window length. The highlighted zone corresponds to the hydrocarbon saturated interval, NB: non-blocked, NU: non-uniform and U: uniform.

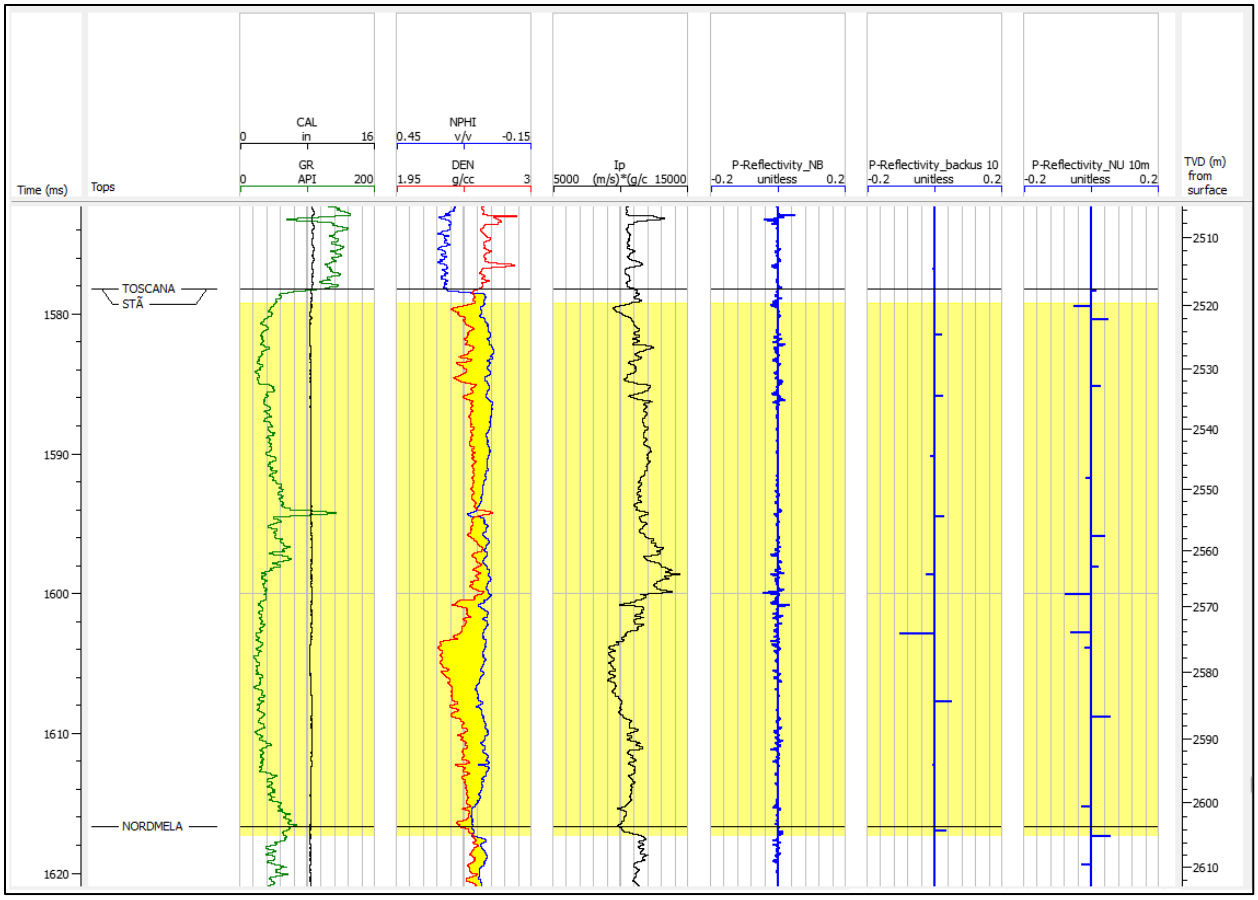

Figure C.6: P-wave reflectivity for the well 7219/8-2 from Backus average, Non-uniform and uniform methods for 10m window length. The highlighted zone corresponds to the hydrocarbon saturated interval, NB: non-blocked and NU: non-uniform.

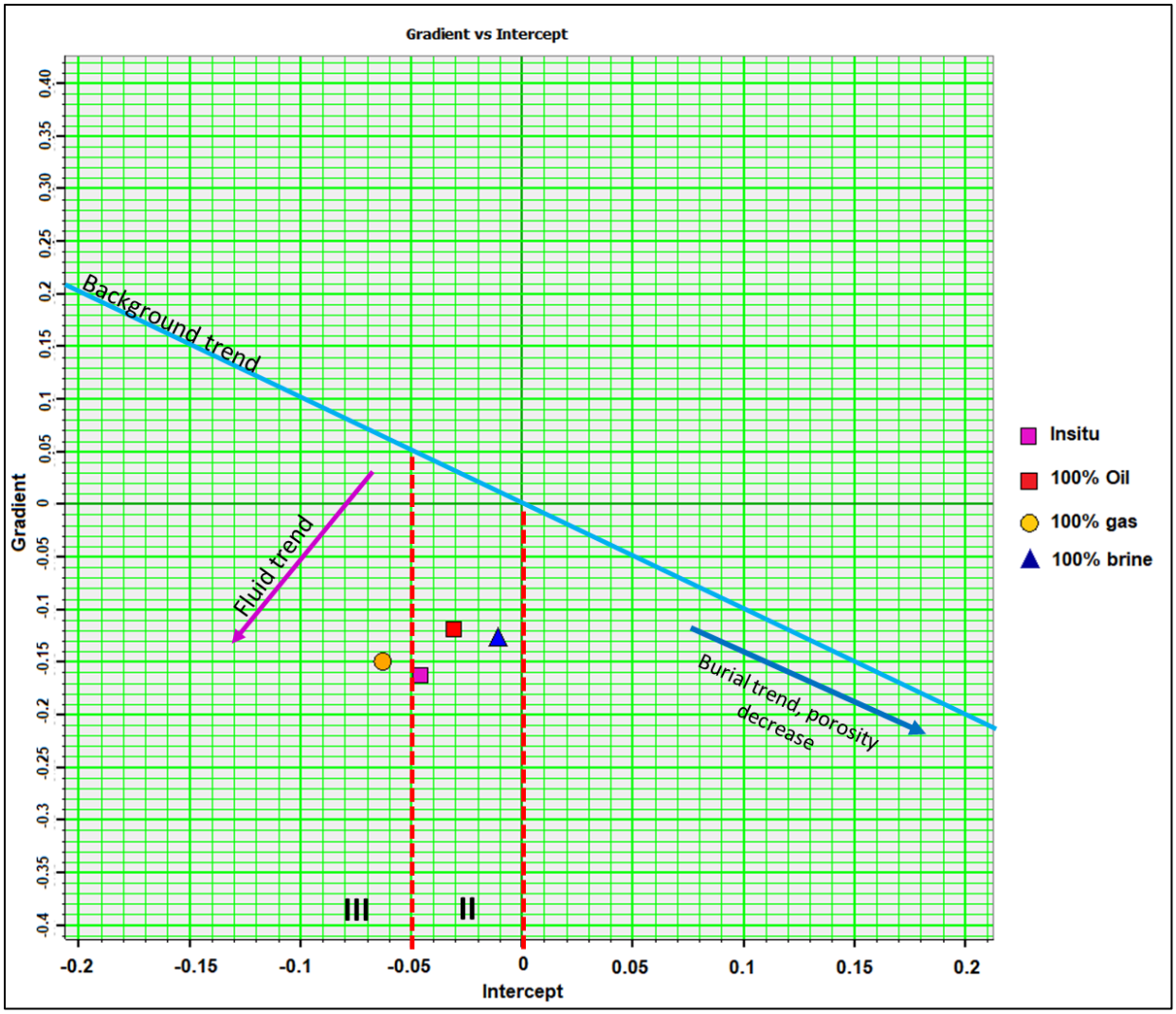

Figure C.7: Gradient vs intercept crossplot for all the fluid replacement scenarios on the well 7220/7-1 (Havis). The blue line represents the Vp/Vs=2 background trend, while the red dashed lines mark the limit of the gas sand classification.

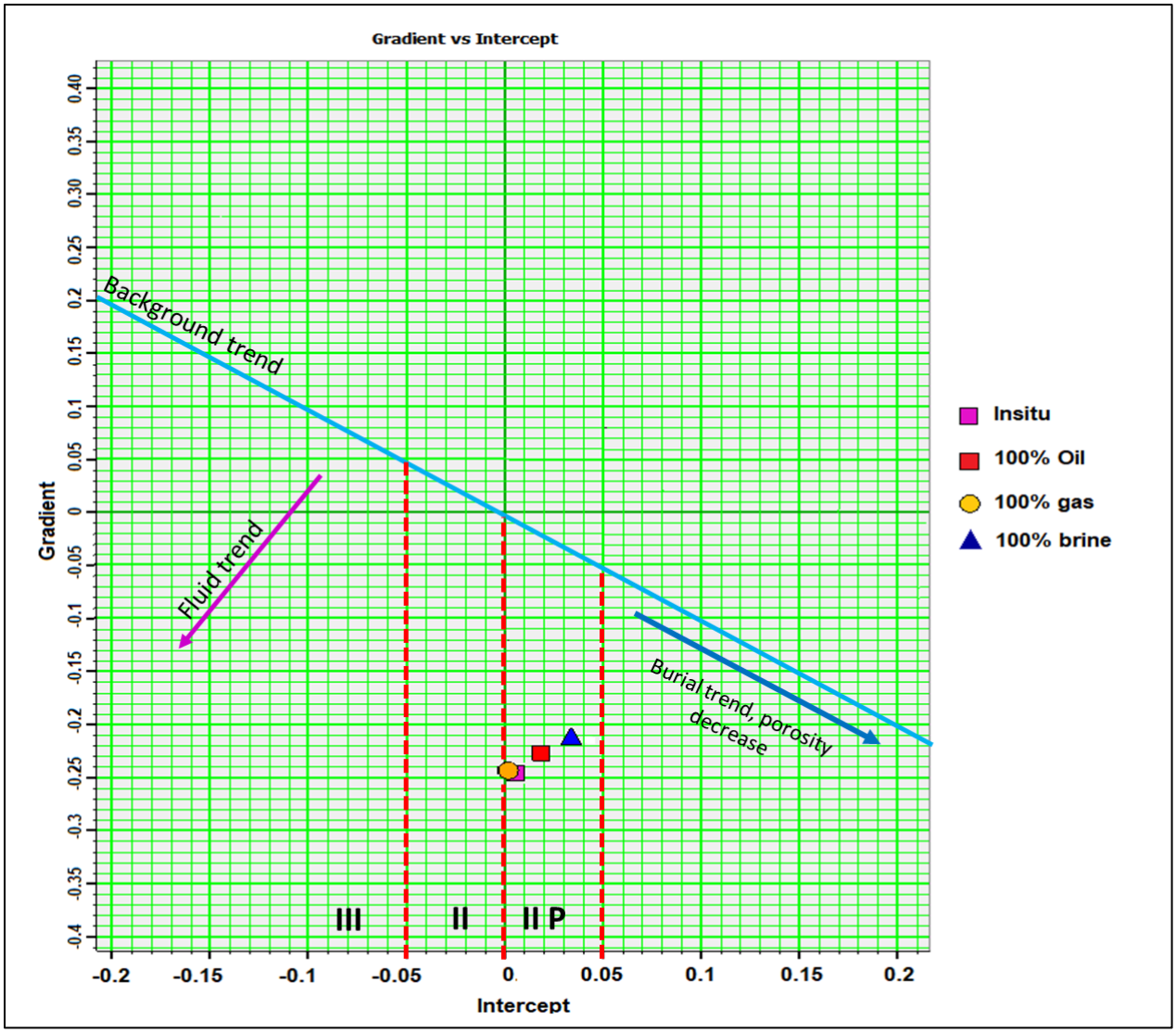

Figure C.8: Gradient vs intercept crossplot for all the fluid replacement scenarios on the well 7219/8-2 (Iskrystall). The blue line represents the Vp/Vs=2 background trend, while the red dashed lines mark the limit of the gas sand classification.

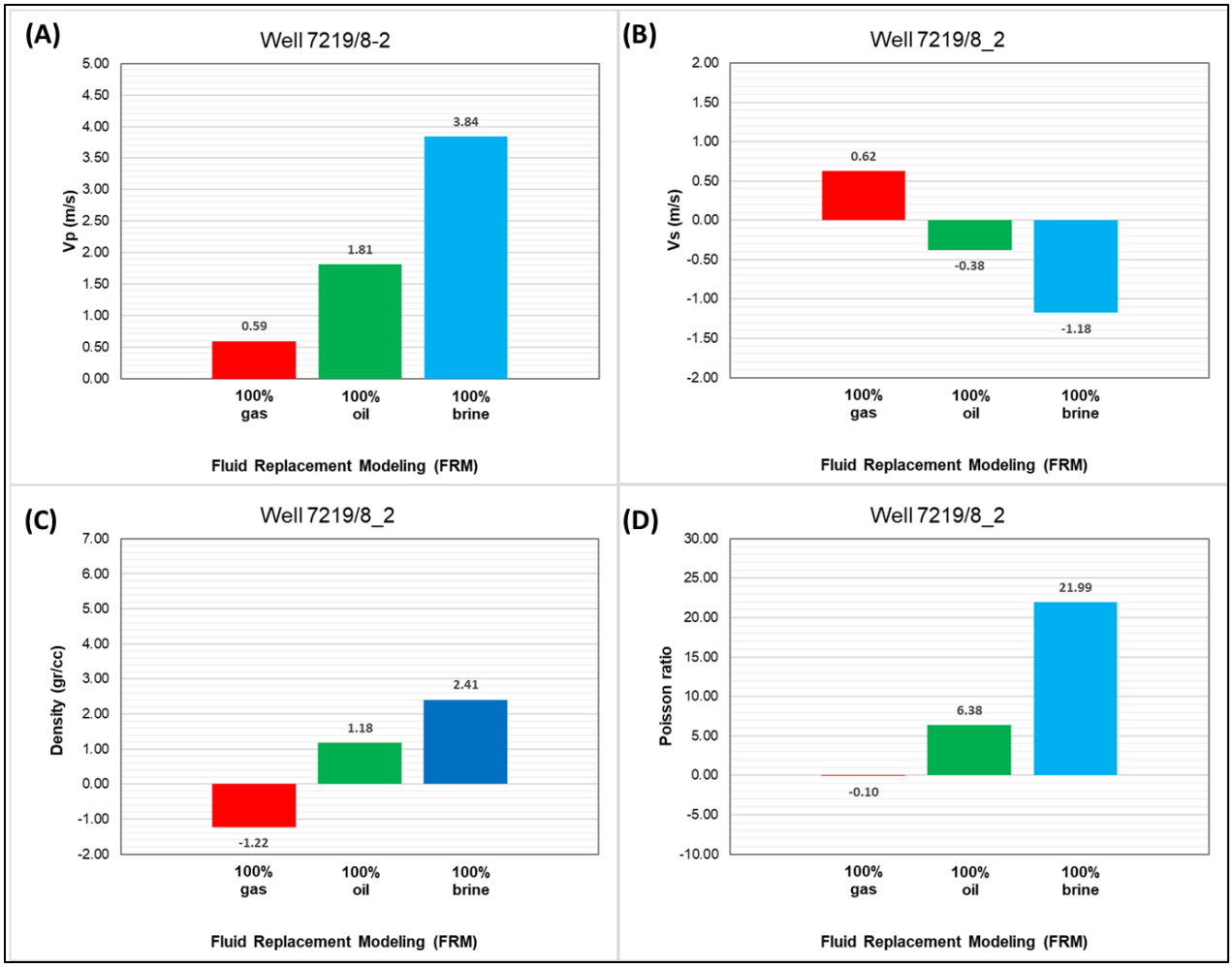

Figure C.9: Effect of replacing the in-situ fluid for 100% brine, oil and gas on the Vp (a), Vs (b), density (c) and Poisson's ratio (d) on the well 7219/8-2 (Iskrystall).

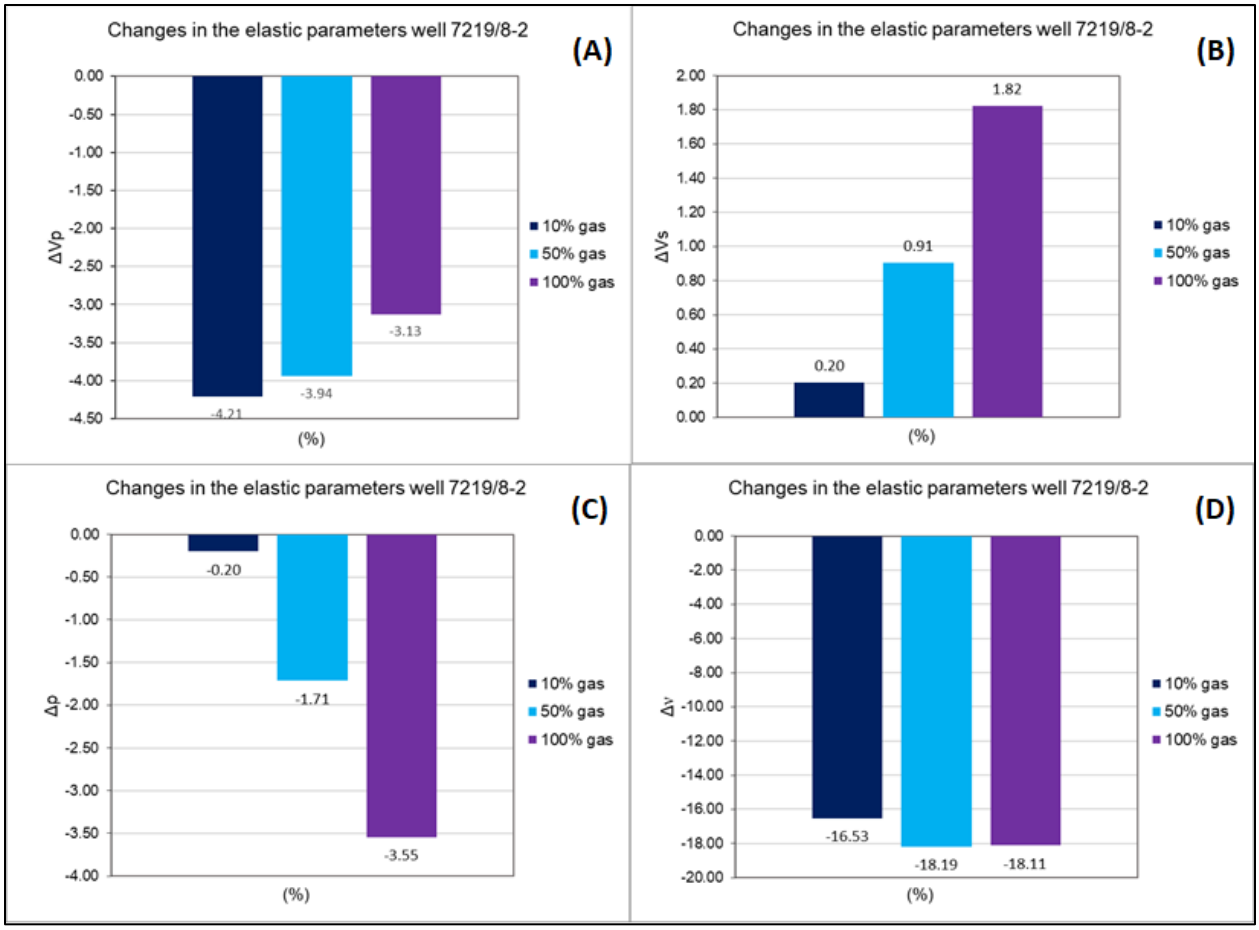

Figure C.10: Effect of replacing the in-situ fluid for 100% brine, oil and gas on the Vp (a), Vs (b), density (c) and Poisson's ratio (d) on the well 7219/8-2 (Iskrystall).